Fermilab FERMILAB-THESIS-1996-75

NORTHWESTERN UNIVERSITY

Coherent Nonlinear Longitudinal Phenomena in Unbunched Synchrotron Beams

A DISSERTATION

SUBMITTED TO THE GRADUATE SCHOOL
IN PARTIAL FULFILLMENT OF THE REQUIREMENTS

for the degree

DOCTOR OF PHILOSOPHY

Field of Physics

By

Linda Klamp Spentzouris

EVANSTON, ILLINOIS

December 1996

©Copyright by Linda Klamp Spentzouris 1996

All Rights Reserved

ABSTRACT

Coherent Nonlinear Longitudinal Phenomena in Unbunched Synchrotron Beams

Linda Klamp Spentzouris

Coherent nonlinear longitudinal phenomena are studied in proton and antiproton synchrotron beams. Theoretical development done in the field of plasma physics for resonant wave-wave coupling is applied to the case of a particle beam. Results are given from experiments done to investigate the nature of the weakly nonlinear three-wave coupling processes known as parametric coupling and echoes. Storage ring impedances are shown to amplify the parametric coupling process, underlining the possibility that machine impedances might be extracted from coupling events instigated by external excitation. Echo amplitudes are demonstrated to be sensitive to diffusion processes, such as intrabeam scattering, which degrade a beam. The result of a fast diffusion rate measurement using echo amplitudes is presented. In addition to the wave-wave interactions, observations of moderately nonlinear wave-particle interactions are also included. The manifestations of these interactions that are documented include nonlinear Landau damping, higher harmonic generation, and signs of the possible formation of solitons.

To my parents, with love.

ACKNOWLEDGMENTS

It would not have been possible for me to write this thesis without the broad base of support which I have been lucky to experience for many years. I have been blessed with the strength which comes from a loving family, the wonder of discovery which comes from inspired teachers, the stimulation which comes from an active, dedicated peer group, and the tools needed for the job which come from experts committed to technical excellence. My debt is large, and although I cannot explicitly name everyone who deserves my thanks, my gratitude to those people is not diminished.

This work is built on the inspiration of my thesis advisor, Dr. Patrick Colestock. He has met the ideal of what a thesis advisor should be, guiding me with his intellectual light, and investing hard work into every important aspect of my education. I have benefited from the scope of his vision, his mastery of both theoretical and experimental physics, and his sincere concern for my future success. Further, it is people such as Pat who make it possible for untraditional students such as myself to participate in the field of physics. His patience and support were unwavering as I joyfully entered marriage and became a mom.

I elected to work on a doctorate after being out of school for many years, during which time I worked in the Accelerator Division Operations group at Fermilab. My interest in beam physics was awakened by the many people at Fermilab who were my informal teachers, and who were ultimately responsible for nudging me back to school. I owe special thanks to Dr. David Finley, Dr. Don Edwards, Dr. Mike Syphers, Bob Mau, and the operations group.

Under the direction of Bob Mau, the people in the operations group were encouraged to maximally fulfill their potential, which created a dynamic, exciting daily work environment. Bob's dedication to the people who work for him, as well as his effort to maintain high standards in both the interest level of the job and in the abilities of the group, were responsible for my sustained interest in particle accelerators and storage rings. My motivated, creative fellow operators made sure that I did not fall victim to laziness. David Finley sharpened and directed my interest further, and put significant effort into satisfying my curiosity and into disciplining my thinking process. He has heroically struggled to improve the care and clarity of my work. The final push back to the University came from Don Edwards and Mike Syphers, who opened my horizons and directed me into the rich, rigorously academic side of beam physics.

Dr. Bruno Gobbi is my academic advisor on the Northwestern University staff, and has been a critical interface between myself and the formal requirements of the University. I owe him many thanks for the hours he has spent to insure my successful negotiation of the course work, and to safeguard my monthly stipend. I would also like to thank Dr. Heidi Schellman for guiding me through the jungle of error analysis and for her moral support when my knees were weak.

Upon returning to Fermilab to do my research I accrued more debt to the laboratory staff. Dr. Dave Wildman and John Reid graciously gave me access to their knowledge, time and equipment. Members of the pbar staff, such as Dr. Steve Werkema, Dr. Mike Church, and Dave Peterson helped me tackle the Accumulator ring. Brian Fellenz and the instrumentation group helped me cope with transfer function measurement madness. Dr. Gerry Jackson provided vital software, as well as

teaching me useful triggering tricks. The operations group was always there for me, down to unfreezing my car locks in the middle of the night so that I could go home.

Most graduate students rely on other graduate students and post docs for valuable discussion and practical help, and I was no exception. My thanks to Kathy Harkay, Ping-Jung Chou, David Olivieri, Donna Siergiej, Eric Colby, Dr. Saeed Assadi, and Dr. Peter Bagley.

Finally, my deepest thanks goes to my family without whom I would be bereft of spirit. My mom and dad, Margaret and Walter Klamp, have given me the wealth of resources needed to help me through all nature of difficulties. My sister and brother, Carolyn and Doug Klamp, have provided a constant source of strength and renewal, as well as listening ears and good counsel. My wonderful husband, Panagiotis Spentzouris, has supported me in every possible way, his loving encouragement enabling me to prosper.

Contents

1 Introduction **1**

1.1 Subject of research 1

1.2 Definition of terms 3

1.3 Stability in particle beams 5

1.4 Wave-wave coupling 7

1.4.1 Parametric coupling 9

1.4.2 Beam echoes 10

1.5 Nonlinear wave-particle interactions 11

1.6 Strongly nonlinear phenomena 13

1.7 Summary of material to be presented 14

2 Linear beam dynamics **16**

2.1 Coordinate Convention 16

2.2 Longitudinal Dynamics of Unbunched, Coasting Beams 17

2.3 Machine Impedance and Wakefields 21

2.4 Linear Stability Theory 24

2.4.1 Beam response to an external voltage 32

3 Accumulator beam transfer function measurements **36**

3.1 Introduction and overview 36

3.2 Experimental setup 39

3.3 Impedance measurements at the 2nd harmonic 44

3.4 Impedance measurements at the 84th harmonic 61

4 Main Ring beam transfer function measurements **66**

4.1 Introduction and overview 66

4.2 Experimental setup 68

4.3 Experimental results 72

5 Theory of parametric coupling **81**

5.1 Introduction and overview 81

5.2 Simple example of mechanical pendula 86

5.3 Method of multiple scales applied to a beam 93

5.4 Fourier transform method applied to a beam 100

5.5 Mode growth and conservation laws 103

6 Main Ring time domain results **109**

6.1 Introduction and overview 109

6.2 Experimental setup 113

6.3 Mode coupling cascades 117

6.4 The role of impedance in coupling 126

6.5 Threshold measurements 129

6.6 Nonlinear wave-particle effects 132

7 Theory of echoes **140**

7.1 Introduction and overview 140

7.2 Simple example of a collisionless neutral gas 144

7.3 Beam echoes without wakefields or collisions 147

7.4 Beam echoes with wakefields 154

7.5 Beam echoes with wakefields and collisions 161

8 Accumulator time domain results **169**

8.1 Introduction and overview 169

8.2 Experimental setup 172

8.3 Echo characteristics 175

8.4 Echo shape 180

8.5 Diffusion rate measurements 185

9 Conclusions **189**

9.1 The original objective 189

9.2 The experimental flow 190

9.3 Summary 193

A Beam transfer function measurements **196**

B Alternative derivation of the dispersion relation for parametric coupling **201**

C Demonstration of symmetry relations used in section ?? **209**

Bibliography **212**

List of Tables

3.1 Accumulator Beam Parameters 39

4.1 Main Ring Beam Parameters 68

List of Figures

2.1 Particle Accelerator Coordinate System 17

2.2 Typical accelerator impedances. 23

2.3 Three theoretical impedance curves generated by fixing the values of Im(Ω), while varying Re(Ω). 29

2.4 Theoretical stability boundary for the Accumulator beam. 31

2.5 Theoretical shift of the beam response due to an impedance. 35

3.1 Block diagram of Accumulator transfer function measurement setup. . 39

3.2 Technique for the ARF2 cavity fanback measurement 41

3.3 Measured frequency response of the ARF2 cavity. 42

3.4 Conceptual idea for a resistive wall current monitor 43

3.5 S21 measurement at $h = 2$ in the Accumulator 45

3.6 Uncalibrated impedance curve 46

3.7 Magnitude response of two independent, identical S21 measurements 48

3.8 Impedance curves from measured data fit to the stability boundary obtained from the dispersion relation. 49

3.9 Average of the square of the difference between a measured impedance curve and the theoretical stability boundary as a function of the applied offset to the measured curve. 51
3.10 Comparison of the theoretical stability boundary to impedance curves generated by applying different magnitude offsets to data from a beam transfer function measurement. 53
3.11 Comparison of magnitude response data taken with different machine impedances 54
3.12 A measurement of the ARF3 cavity impedance using beam transfer function measurements with the ARF3 cavity shorts in and out. . . . 55
3.13 Magnitude response of two independent, identical S21 measurements taken during a second study period 57
3.14 A second (independent) measurement of the ARF3 cavity impedance using beam transfer function measurements with the ARF3 cavity shorts in and out. 59
3.15 Calibrated Accumulator impedance curves at $h = 2$ taken with different beam sizes. 60
3.16 A noisy low power measurement of the ARF1 cavity impedance using beam transfer function measurements with the cavity shorts in and out 62
3.17 An attempt to fit a distorted impedance curve taken at $h = 84$ to the theoretical stability boundary. 63
3.18 A higher power distorted measurement of the ARF1 cavity impedance using beam transfer function measurements with the cavity shorts in and out 65

4.1 Block diagram of Main Ring transfer function measurement setup. . . 69
4.2 Measured frequency response of the Main Ring coalescing cavity . . . 70
4.3 Conceptual idea for a strip line beam current monitor 71
4.4 s21 measurement at $h = 106$ in the Main Ring 72
4.5 Main Ring magnitude response measurements with various horizontal tune settings 74
4.6 Comparison of two Main Ring magnitude response measurements taken with different horizontal tune settings 75
4.7 Main Ring magnitude response measurements with various chromaticity settings 77
4.8 Main Ring magnitude response measurements with various injected beam intensities 78
4.9 Typical Main Ring magnitude response and its mapping into the impedance plane 80

5.1 System of two parametrically coupled mechanical pendula 87

6.1 Block diagram of Main Ring time domain setup. 114
6.2 Main Ring 5 MHz cavity response to a .5 ms drive pulse 116
6.3 Frequency isolation of the Main Ring 5 MHz cavity 117
6.4 Power versus time at $h = 106$ in response to a .5 ms drive pulse . . . 118
6.5 Power versus time at $h = 105$ in reponse to a .5 ms drive pulse 119
6.6 Power versus time at all excited harmonics in response to a .5 ms drive pulse 120
6.7 Power versus time at odd harmonics in response to a .5 ms drive pulse 121

6.8 Peak power and time to peak power at harmonics excited during parametric coupling 123
6.9 Power in Main Ring stored beam at $h = 1$ 125
6.10 Comparison of beam power spectrum during parametric coupling with 5 MHz cavity bandwidth 127
6.11 Comparison of power at harmonics 102 and 110 as the drive pulse frequency is varied 128
6.12 Peak signal power versus drive level for excited harmonics 130
6.13 Peak signal power versus beam intensity for harmonics 105, 106, and 107. 131
6.14 Peak power at the higher harmonics of $h = 105$. 132
6.15 Peak signal power at higher order harmonics. 134
6.16 Power versus time at $h = 105$ as drive pulse width is varied 135
6.17 Two recorded traces of power versus time at $h = 105$, both with an 80 ms drive pulse 136
6.18 Power versus time at high, low, and center frequencies around $h = 5 \times 105$ 139

8.1 Block diagram of Accumulator time domain setup 173
8.2 Fast rise of a pulse applied to the Accumulator ARF2 cavity, as seen on the fanback signal. 175
8.3 ARF2 peak amplitude response at different harmonics, as seen on the cavity fanback signal 176
8.4 Longitudinal unbunched beam echo in the Fermilab Accumulator . . 177
8.5 Measured echo delay time versus separation of the drive pulses 179
8.6 Higher order echoes 181

8.7 Separation of the peaks within an echo versus beam energy spread . . 183
8.8 Three longitudinal beam echoes occurring in beams with different energy widths 184
8.9 Superposition of echoes with varying drive pulse separations 186
8.10 Peak echo response as a function of echo delay time 188

A.1 General two-port network 196
A.2 Network configuration for an impedance measurement 197
A.3 Comparison of the magnitude response from a beam transfer function measurement to the undisturbed frequency distribution of the beam . 200

Chapter 1

Introduction

1.1 Subject of research

The work presented here is an investigation of coherent nonlinear longitudinal dynamics in unbunched particle beams. In contrast to forces which may be experienced by a single particle, coherent wave motion in a beam is sensitive to the intensity. As particle density has been continuously increasing in synchrotrons in recent years, nonlinear wave motion is playing more of a role than ever in beam dynamics, and the consequences are often intrusive. It was just such an intrusion which not only triggered, but controlled the subsequent evolution of the studies presented in this work. In 1990, Colestock and Jackson undertook a standard measurement of linear stability in the Fermilab Tevatron proton synchrotron. The result could not be interpreted with the linear theory, as a weak nonlinearity manifested itself in the data. A study of this weak nonlinearity was undertaken, but it was to be just the first step in the exploration of nonlinear beam dynamics which followed. The results of one

investigation would point to the next, high intensity particle beams proving to be a workshop rich in nonlinear effects.

As technology improves and beam brightness increases, stability becomes more difficult to achieve, with nonlinear coherent processes taking a more dominant role in the evolution of particle motion. There has been considerable effort in other areas of physics to develop a theoretical framework for nonlinear wave dynamics. The work that has been done in plasma physics is particularly suited for adaption to particle beams, since a plasma is also a system of particles supporting coherent wave motion. There has so far been little systematic effort to apply the fruit of decades of labor in plasma physics to the case of a particle beam. The work presented here is an attempt to discuss nonlinear effects in a beam in the language of plasma physics, in the hope that such an application will prove useful in the years to come.

Many physical systems have been described in terms of the degree of nonlinearity of the dynamical processes governing their evolution. There is an available theoretical hierarchy spanning from the linear to the chaotic regimes. Between linearity and strong turbulence, there is a range of weak to moderately nonlinear processes. These have been categorized for plasmas by authors such as Sagdeev and Galeev [2]. In particular, in order of increasing nonlinearity, there are a nonlinear wave-wave interaction, where linearly-independent modes can couple; a quasilinear wave-particle interaction, in which fluctuation-induced diffusion can take place; and a nonlinear wave-particle interaction, where trapping or soliton-like behavior can occur. The main subject of this work is wave-wave coupling, the weakest of these nonlinearities, although some attention is devoted to the nonlinear wave-particle interaction as well. These will be described for the system of a stored particle beam in more detail below.

Although most of the experimental results presented are phenomenological in nature, already there are hints of potential practical uses for data taken under nonlinear beam conditions. A fast measurement of the diffusion rate in a stored beam using a technique based on weakly nonlinear dynamics was carried out, and will be discussed. The extraction of machine impedance from nonlinear data is also examined qualitatively. These are just the beginnings of a systematic investigation of new measurement techniques which might be developed.

1.2 Definition of terms

Particle beams support wave motion in all three coordinates. Transverse motion is defined to be in the plane perpendicular to the direction of beam motion. All of the discussion in this work pertains to the longitudinal coordinate, defined to be along the direction of beam motion. The beams used for these studies were at least initially spatially uniform in the longitudinal direction. In accelerator language, the unperturbed beams were unbunched. The longitudinal position of a particle in an unbunched circulating beam is given as the angular position (or phase) of the particle around the storage ring. The other degree of freedom in the longitudinal phase space is energy; specifically, the deviation from the design energy of the storage ring. The particle energy distribution in these studies approximated a Gaussian, the central energy being the design energy of the storage ring. The two phase space coordinates are to lowest order linearly related, an energy error causing an error in the phase of the particle. In other words, the relative position of two particles is dependent on their relative energies. Oscillations in the longitudinal plane are fluctuations of the particle density and particle energies.

Much of beam behavior in a storage ring may be described in terms of single particle dynamics, where the motion of the individual particles is governed by externally provided electromagnetic fields. The nonlinear motion of individual particles has long been an important factor in the design of particle accelerators. By the early 1950's, people such as Courant, Moser and Snyder were concerned with the impact of nonlinear magnetic field components on transverse particle motion in alternating-gradient synchrotrons [1]. Ultimately, not only has transverse nonlinear single particle motion been controlled, it has also been exploited, such as in the utilization of nonlinear resonances for the slow resonant extraction process.

While motion arising from externally applied fields may be examined on a single particle basis, motion due to electromagnetic fields generated by the beam itself cannot be understood without some knowledge of the beam density and shape. These self-generated fields may act back upon the beam in either a coherent or incoherent manner. An example of an incoherent effect is the space charge force, whereby a single uniformly charged beam is defocused by the repulsive fields its particles. The magnitude of this force varies depending on the location of a particle within the charge distribution.

Coherent effects are possible via a sustained self-generated electromagnetic interaction between the entire beam distribution and the physical structure of the storage ring through which the beam travels [8]. Once a beam is perturbed, the fluctuating current generates a field, which may be supported by the architecture of the storage ring. Positive feedback may develop between the beam and the stored field energy, enhancing the amplitude of the initial oscillation. This type of self-field is called a wakefield, because trailing particles experience the electromagnetic wake of leading

particles. Beam current traversing a wakefield will experience a voltage change, since particles are accelerated or decelerated by the longitudinal electric field component. Thus, it is equivalent to describe the effect of the wakefield in terms of the energy change of the particles due to the field strength, or in terms of the voltage change of the beam due to the impedance of the device storing the field.

The degree of nonlinearity in the wave motion of a beam may be characterized by the strength of the forces present acting to disrupt the particle distribution. As the amplitude of a wakefield becomes larger, more particles become trapped in the potential wells of the wave. The motion of particles remaining outside of these potential wells (or 'buckets' in accelerator physics terminology) approximates free-streaming motion. In the limit of no self-field generation, the entire beam approximates free-streaming motion, removing the necessity of a self-consistent treatment of the beam dynamics. In this case, an externally applied voltage would trigger a free-oscillation. Admission of self-fields into the problem requires a self-consistent analysis, although if coherent motion is initiated as a small oscillation, a perturbative treatment is still valid. Once large voltages are acting on the beam, the particle distribution may change significantly, and more traditional analysis techniques no longer apply.

1.3 Stability in particle beams

In the case of a particle beam, growth of the amplitude of coherent wave motion is normally undesirable, and when it occurs unintentionally, this growth is called an instability. Wakefields can drive the growth of a mode of oscillation, but there is also a mechanism for damping. The frequency with which a particle returns to the same location in its circular orbit is called its revolution frequency. Particles of differing

energies travel more or less quickly around the machine, so the energy spread of the particle distribution is proportional to the frequency spread of the distribution. The energy, or frequency, spread of a beam is responsible for providing damping of longitudinal oscillations [6, 7]. One aspect of longitudinal oscillation is compression and rarefaction of the particle density, so particle frequency dispersion due to energy differences will tend to damp these oscillations. When a particle beam is stable to perturbation, and still within the linear regime, its impulse response damps away with a time constant having a specific dependence on the beam energy spread. This characteristic damping time is called the linear Landau damping time.

Linear stability theory may be used to describe the competing mechanisms for mode damping and growth, and to find the boundary outside of which an initial perturbation results in the growth of coherent oscillation. An early treatment of linear stability in particle accelerators was published in 1965 by Neil and Sessler [3]. The analytic method for finding the linear stability boundary in a coasting beam was developed by Keil and Schnell, and is known as the Keil-Schnell criterion [5]. Investigation of the subject has continued, and linear stability theory has since been clearly presented by others such as Hofmann [4]. The growth of an instability in the linear regime is exponential, so that in the absence of nonlinear effects, the wave amplitude would quickly be beyond the physical boundaries of the storage ring. However, experience has shown that often mode growth saturates, usually at the expense of the particle density in phase space.

In an analysis using linear stability theory, each potential frequency component in a system is treated independently. A Fourier expansion is done on the function

which describes the particle distribution, along with a similar expansion of the driving mechanism. The undisturbed particle distribution is assumed large in comparison to the other terms in the frequency expansion, which are considered perturbations. For a particle beam, the linear theory is of primary importance, because the onset of instability is nearly always in the linear regime. However, as damping is characteristically weak in hadron machines, instabilities grow to large amplitudes and it is important to understand nonlinear effects which govern mode saturation and beam dilution.

1.4 Wave-wave coupling

Weakly nonlinear processes such as three-wave coupling are described using the same techniques as in linear stability theory, with the exception that a second-order frequency mixing term is now also included in the description of the dynamics. Keeping a frequency mixing product term allows the oscillation of waves at two different frequencies to generate coherent motion in a wave at yet a third frequency. The system is not strongly nonlinear in the sense that this coupling resonance is still considered a perturbation, not significantly changing the initial particle distribution. If the particle distribution were allowed to change (but on a slow timescale relative to the wave oscillation period) causing growth or decay of the external oscillation, the wave-particle interaction would be considered quasilinear.

This work focusses on manifestations of the 3-wave coupling resonance, known as echoes and parametric coupling. These phenomena, both being aspects of 3-wave coupling, are two views of the same underlying physics. The study of echoes examines the growth and decay of the wave amplitudes when it occurs sequentially,

with a time delay between the decay of one wave and growth of the next. The mathematical description of echoes is thus naturally based in the time domain. The study of parametric coupling examines the growth and decay of the waves when growth of one wave is occurring simultaneously with the decay of another. The mathematical description of parametric coupling is based in the frequency domain.

Each of the initial waves involved in the frequency mixing phenomena are coherent by virtue of a driving voltage. Externally applied excitations or wakefields are both possible sources of driving voltage. The echo experiments presented in this work were carried out in a low impedance storage ring, so that each of the initially excited modes had to be externally driven. The parametric coupling experiments presented in this work were carried out in a marginally stable storage ring with moderate impedances. Although the coupling was initiated with an external pulse, the subsequent evolution of mode growth was driven by machine impedance. It may be possible to extract information about machine impedances from such coupling measurements.

Particles undergoing longitudinal oscillation must change their phase by some multiple of 2π for every circuit around the machine. Thus, the longitudinal modes of oscillation supported by a stored beam are all harmonics of the same fundamental, f_{rev}, which is the particle revolution frequency. A feature of stored particle beams that is not present in all physical systems is that the longitudinal harmonics of the beam are also the entire set of eigenmodes for the system. It is not always the case that there is such regularity in a set of possible excitations.

The permittivity in a particle beam is given by the linear dispersion relation, which, except near a longitudinal resonance, is nearly one. This implies that there is little interference from the medium (the beam) in getting a clean measurement of

the coherent signals which it contains. This, together with the great regularity of the pattern of available modes, and extremely weak coupling between the longitudinal and transverse motion, make particle beams particularly suitable for the clear observation of three-wave coupling phenomena.

1.4.1 Parametric coupling

During parametric coupling, the energy of the coherent motion of two waves of differing frequencies gets transferred into the energy of coherent motion at a third frequency. This transfer of energy may behave as either a scattering process or as a decay process. In the case of a decay, the initial coherent motion of a wave at, say, frequency f_1 decays in favor of coherent motion at frequencies f_2 and f_3. In the case of a scattering process, the energy of coherent motion in waves with frequencies f_2 and f_3 gets transferred into a wave with frequency f_1. Both the decay and the scattering are inherently the same process known as parametric coupling. Frequency and mode number selection rules govern the coupling, namely, $f_1 = f_2 + f_3$, and $n_1 = n_2 + n_3$. These rules are alternative expressions of the conservation of energy and the conservation of momentum [2, 9, 10].

The number of phase oscillations per revolution experienced by a particle is equal to the harmonic number of the oscillation. For example, a particle oscillating at a frequency $f = n \times f_{rev}$ experiences $\phi = n \times 2\pi$ phase oscillations per revolution. Consequently, in the system of a stored particle beam, if the mode number selection rule of three-wave coupling is satisfied, then the frequency selection rule is automatically satisfied.

Parametric coupling has been studied extensively in areas such as electronics [41];

however, the theoretical development of 3-wave coupling in plasma physics is especially appropriate for particle beams. The parametric coupling resonance for the case of a plasma was analytically formulated in 1968 by Nishikawa [13]. There were also complete analyses done around this time by Sagdeev and Galeev [2], and also by Davidson [10].

1.4.2 Beam echoes

A temporal echo is the spontaneous growth (and subsequent decay) of coherent motion in a wave of frequency f_1 some time after separate, sequential excitations of waves at f_2 and f_3 have damped away. The frequency and phase selection rules mentioned previously are general properties of three-wave coupling, and they also hold for echo generation. The phenomena of echoes relies on the fact that the correlation between the energy and phase of the particles in the beam remains after the coherent oscillations have damped away. The frequency information from each of the excitations remains within the particle distribution, and the combined effect is to cause a recoherence at the difference frequency. The phase correlation of the particles may be destroyed by random processes such as small angle coulomb scattering. If randomizing effects are present, the phase correlation breaks down, decreasing the echo amplitude. Echo reconstruction is no longer possible if either the time delay to the echo or the scattering rate are sufficiently large. Since the time delay to the echo is dependent on the kick parameters, which are controlled, it is possible to measure the diffusion rate in a beam [11, 12].

Spin echoes in nuclear magnetic resonance experiments were seen as early as 1950 by E.L. Hahn [14]. The possibility of seeing echoes in a plasma was raised in 1967

by Gould, O'Neil and Malmberg [15, 16], who followed up with extensive analytical work as well as the first experimental observation in a plasma. The use of echoes to determine collisional damping rates was then discussed by Su, Oberman, and O'Neil [11, 16]. Echo generation also has some history in particle accelerators and storage rings. In 1983, transverse beam echoes were observed and utilized by Edwards, et al., in the Fermilab Tevatron proton synchrotron. These echoes were due to the modulation of a coherent transverse betatron oscillation by the synchrotron frequency, and so it was possible to use them to tune the chromaticity of the machine. Similar echoes were seen by Edwards, Syphers, and Gerig in 1987 in the Fermilab Main Ring proton synchrotron. Potential transverse echo generation in a beam has also been proposed by Kauffmann and Stupakov [17, 18], but in this case the mixing frequencies were to be supplied by external quadrupole kicks. Bunched beam longitudinal echoes have been observed by Colestock and Assadi [19].

1.5 Nonlinear wave-particle interactions

Large wakefields disrupt an initially smooth particle distribution, by trapping particles within the potential wells of their voltage waveforms. There are several observable aspects of this imposition of bunch structure onto the beam, and all are indications that the system is now decidedly nonlinear.

The particle motion decoheres with a time constant which is significantly longer than the Landau damping time of linear motion. Particles trapped within the potential well of the wakefield will oscillate about the equilibrium point, alternately gaining energy from the field or giving up energy to the field. This corresponds to

a rotation between energy and phase in the bunched beam phase space of the particles. The combination of the energy dispersion of the particles and the nonlinearity of the voltage waveform will cause phase mixing of the trapped particles. This phase mixing causes the particles to decohere within their potential wells, smearing out so that there is no longer any net energy exchange between the voltage wave and the particles. The decoherence time is longer than the bunch rotation period. The peak beam current goes down as the particle bunches decohere, and there is therefore also a concurrent reduction in the amplitude of the self-field. This nonlinear damping mechanism is called nonlinear Landau damping.

Considerable analysis and numerical work on nonlinear Landau damping has been done, beginning with Dawson in 1961 [6]. Since then, there have been many other treatments, among which are those by O'Neil in 1965 [7], Oei and Swanson in 1972 [20], and Canosa and Gazdag in 1974 [21]. Nonlinear Landau damping was first observed in plasmas by Malmberg and Wharton [22].

O'Neil, Winfrey and Malmberg have pointed out that the advent of particle bunching is accompanied by the appearance of power in higher harmonics of the fundamental frequency of the wakefield [23]. This is a natural result of the periodicity imposed on the spatial coordinate, with the harmonic content becoming richer as the bunch compresses. Higher order harmonic generation will necessarily be associated with the occurrence of moderately nonlinear phenomena, and was documented during both parametric coupling and echo studies. Since echoes were observed in the time domain, higher harmonic generation manifested itself there as higher order beam echoes.

1.6 Strongly nonlinear phenomena

The strongly nonlinear dynamic of soliton formation may arise under the special circumstance of a nonlinear equilibrium between the dispersive force in a system and nonlinearities in the field. The phenomenon of this pulselike nonlinear wave was observed hydrodynamically as early as 1834. Scott, Chu and McLaughlin include a description of this observation in their review paper, and go on to do a thorough mathematical analysis of the equations which may exhibit behavior engendering solitons [24]. Bisognano has since raised the possibility of seeing solitons in a particle beam subject to space charge forces [25]. As the necessary attribute of the nonlinear wave motion is steepening and braking of the wavefront, soliton formation in beams may also be expected when particles experience wakefield forces. The wavefront of a wakefield will steepen with particle compression, and particles may experience compression when the field gradient opposes the dispersive force. There may be a localized portion of the beam distribution where the particle compression strikes a balance with the dispersive force. Studies done for this work have revealed small islands of trapped particles in the phase space of the beam, which are reminiscent of generalized solitonic behavior. Further study of this nonlinear effect needs to be done, to better determine its true nature.

Beyond the moderately nonlinear regime lies turbulence, which is described by Davidson as the regime where many waves are present in the system, with phases that are considered random, requiring a statistical treatment of the problem [10]. A chaotic beam would have little regularity in the distribution, the particles within the distribution would fluctuate in energy and phase in an unpredictable way. Particle beams at present are not normally strongly turbulent.

1.7 Summary of material to be presented

Chapter 2 contains a review of relevant accelerator terminology, single particle longitudinal dynamics, and linear stability theory. This is the point of departure for the remainder of the thesis.

Results of beam transfer function measurements made in the Accumulator and in the Main Ring are found in chapters 3 and 4 respectively. These also contain descriptions of the hardware used for the studies presented throughout the thesis. The importance of the frequency domain measurements was in gaining an understanding of the stability properties of the storage rings used for the time domain studies presented in this thesis. The results show that the Accumulator is a stable, low impedance machine, while the Main Ring is marginally stable. Consequently, the Accumulator was used for echo studies, while the Main Ring was used to study parametric coupling and moderately nonlinear wave-particle effects.

The theoretical framework for parametric coupling is given in chapter 5, beginning with a heuristic example of coupled pendula. This is followed by a treatment appropriate for particle beams. The experimental observations of parametric coupling are described in chapter 6. The data are shown to conform to the behavior required of parametric coupling, as delineated by the theory. The role of machine impedance in the manifestation of parametric coupling is examined, with the background thought that perhaps machine impedances may eventually be derived from observations of coupling. This experimental results chapter also contains data showing evidence of moderately nonlinear phenomena, namely, nonlinear Landau damping, higher harmonic generation, and behavior suggestive of solitons.

The theoretical framework for beam echoes is given in chapter 7, beginning with a

heuristic example of a collisionless, neutral gas. This is followed by several treatments for particle beams, each being appropriate under different dynamical conditions. Observations of beam echoes are described in chapter 8. The data are shown to conform to the predicted behavior of echoes. There is also presentation of a measurement of the diffusion rate of the beam.

Chapter 2

Linear beam dynamics

The purpose of this chapter is to define the standard terminology and fundamental concepts of longitudinal particle motion in a storage ring. Both single particle dynamics and the linear stability theory for a beam will be discussed.

2.1 Coordinate Convention

A depiction of the coordinate convention for storage rings and multiple pass accelerators is shown in figure 2.1. The x and y directions define a plane perpendicular to the beam motion, and are called the coordinates of the transverse motion. The coordinate along the beam motion is the z, or sometimes s, direction. At any given point along the particle orbit, z is defined by the tangent to the orbit at that point. The z direction is called the coordinate of longitudinal motion. All of the studies and theoretical development in this work concern beam dynamics in the longitudinal plane only. Specifically, they were applied to unbunched, coasting beams.

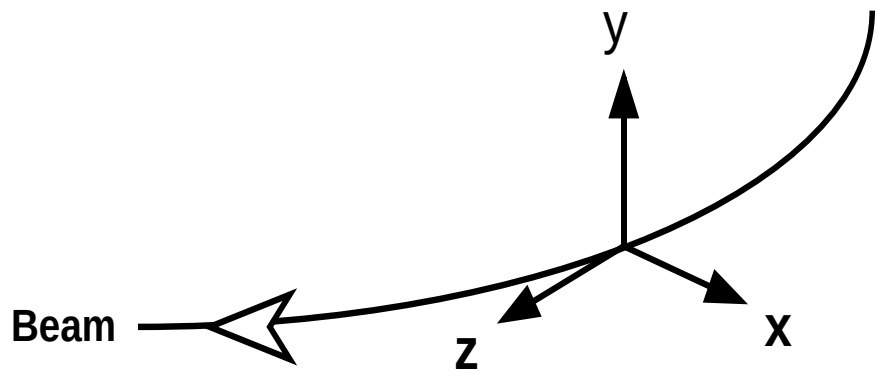

Figure 2.1: Particle Accelerator Coordinate System

2.2 Longitudinal Dynamics of Unbunched, Coasting Beams

A beam is said to be coasting if it is not undergoing acceleration, the particles remaining at a fixed average energy. The beam may also be unbunched, if in addition to not being accelerated, particles are also not captured in potential wells created by an externally applied sinusoidal electric field. In an unbunched beam, the particles are allowed to drift longitudinally with respect to each other, and will do so if they do not all have exactly the same energy.

A beam of particles will not all be at the design energy of the storage ring, but rather will have a (hopefully) tight distribution of energies around this ideal energy. Any given particle can be described in terms of its energy error, ε, from that of an ideal particle. Energy error is one of the degrees of freedom, and hence phase space variables, for longitudinal motion. The other degree of freedom is the angular position, θ, around the machine; a particle going through 2π radians in one circuit, or revolution. The distribution in phase of the particles in a beam is ideally uniform

in the available 2π, whereas a perfect beam would be monoenergetic. In practice, an unperturbed beam may be considered uniform in θ, but will generally be Gaussian in energy.

The particle revolution period, T, is the transit time for one circuit around the machine. Particles having different energies will have different revolution periods due to the fact that they may have different orbits (path lengths) around the machine, or different speeds, or both [26]. The relation between the energy error of a particle and its deviation from the ideal revolution period is given by,

$$\frac{\Delta T}{T_0} = \eta \frac{\Delta p}{p_0} = \frac{\eta}{\beta^2} \frac{\Delta E}{E_0} \tag{2.1}$$

where T_0 is the revolution period of an ideal particle, E_0 is the total energy of an ideal particle, p_0 is the momentum of an ideal particle, β is the relativistic beta factor $\beta \equiv v/c$, and η is a machine dependent function called the 'slip factor' which will be described shortly. Usually it is more convenient to deal with revolution frequency differences, in which case Eq. 2.1 would be written,

$$\frac{\Delta f}{f_0} = \frac{\Delta \theta}{\theta_0} = \frac{\Delta \omega}{\omega_0} = -\frac{\eta}{\beta^2} \frac{\Delta E}{E_0}$$

where f_0 is the revolution frequency of an ideal particle, θ_0 is the phase of an ideal particle, and ω_0 is the angular revolution frequency of an ideal particle. For later convenience, the proportionality constant between $\Delta\omega$ and ΔE will be called k_0,

$$k_0 \equiv -\frac{\eta \omega_0}{\beta^2 E_0} \tag{2.2}$$

The nature of the proportionality between the energy error of a particle and its error in revolution period is described by the slip factor η. Particles which are not very relativistic will have revolution period differences which are dominated by their difference in speed, whereas highly relativistic particles which are going nearly the same speed (the speed of light) will have revolution period differences which are dominated by their differences in path length. These orbital differences arise from the momentum dispersion of the bending magnets in the storage ring. Higher momenta particles experience less bending angle through a dipole field than do lower momenta particles. The cumulative effect of all dipoles in the ring is to cause higher momenta particles to travel on orbits of greater radius than the ideal orbit, and so these particles travel a greater distance every turn around the machine than do their low momenta cousins. The greater pathlength of a high momentum particle creates a transit time error of the opposite sense to that of an error caused by greater speed. Which factor dominates depends on the particle energy and the composition of dipoles in the machine, this information being contained in η. The η function is expressed as an expansion in $\frac{\Delta E}{E_0}$ since neither the particle velocity nor the path length of the ideal orbit is linear in $\frac{\Delta E}{E_0}$. The η function may be written [27],

$$\eta = \eta_0 + \eta_1 \frac{1}{\beta^2} \frac{\Delta E}{E_0} + \eta_2 \left(\frac{1}{\beta^2} \frac{\Delta E}{E_0} \right)^2 + \cdots \tag{2.3}$$

Normally the η function is approximated by the first term, and unless otherwise specified, throughout this work the assumption will be made that $\eta = \eta_0$. At a given

machine energy η_0 is a constant, and is defined by,

$$\eta_0 \equiv \frac{1}{\gamma_t^2} - \frac{1}{\gamma^2}$$

where γ is the standard relativistic gamma factor, and $\frac{1}{\gamma_t}^2$ is the average of the dispersion function around the storage ring divided by the radius of curvature of the ring. So, γ_t may be calculated by knowing the momentum dispersion generated by the magnets from which the machine is constructed.

For a highly relativistic particle, $v \rightarrow c$, so that $\gamma \rightarrow \infty$, and the dispersion of the ring magnets dominates the particle transit time, as one expects for particles all moving at nearly the same speed. The energy at which the two factors γ and γ_t are exactly balanced is called 'transition'. When a machine is at transition, to first order there is no relation between a particle's energy error and its phase slip relative to an ideal particle. When momentum dispersion effects dominate, a machine is said to be 'above transition', whereas when particle speed dominates a machine is said to be 'below transition'.

The dependence of transit time on particle energy provides a mechanism for the damping of coherent oscillations. A group of particles which are initially at the same location in the ring, will eventually spread out in phase due to their relative energy differences. A concentration of particles gives the beam a high peak current, so phase mixing will tend to damp the amplitude of a current oscillation.

2.3 Machine Impedance and Wakefields

Commonly, longitudinal beam instabilities arise from an unwanted electromagnetic interaction of the beam with the physical structure through which it travels. The machine environment typically consists of an evacuated chamber which is composed of straight beampipe, bore tube through magnetic devices, beam detection devices, accelerating cavities, and various connecting pieces between accelerator components. Under certain circumstances the beam deposits stored electromagnetic energy into a portion of the machine structure. Since beam continues to pass through this structure, the stored field may then act back on the beam. A positive feedback situation may arise whereby this self-field interaction acts to constructively reinforce an oscillation [28]. An electromagnetic field which persists after the passage of its generating charges is called a wakefield.

If a storage ring were made up only of cylindrically symmetric, perfectly smooth conducting beampipe, beam moving almost at the speed of light would not create wakefields. The $\vec{E}$ field lines radiating from a highly relativistic charge would be compressed into a pancake in the plane perpendicular to the motion of the particle, necessarily coming into contact with the conducting pipe at right angles. However, beampipe is usually somewhat resistive, causing the field lines to stream out some distance behind the passing charge [8]. The electric field excites image charges and currents in the beampipe walls, and if other particles are close enough behind the initial charge, they feel the resulting electromagnetic wake.

In addition to not being purely conductive, the chamber through which the beam passes often changes its size and shape. Of particular concern with respect to wakefields are resonant structures such as accelerating cavities. High Q devices have a

narrowband frequency response; once a cavity is filled with energy, the field persists for a much longer time than it would in a broadband device. In other words, a narrow response in the frequency domain corresponds to a broad response in the time domain. While field energy at the accelerating frequency is desirable, simple resonant cavities have the unfortunate feature of supporting other, higher order resonant modes [29]. These higher order modes (HOM) can be excited by the passage of beam through the cavity, provided the beam contains energy at these frequencies.

When a particle traverses a structure with a stored $\vec{E}$ field, it experiences a change in voltage given by the integral of the longitudinal electric field over the distance traveled through the field.

$$V = -\int_0^L E_z(z,t)dz$$

Alternatively, the voltage change can be expressed as the product of the beam current times the longitudinal impedance of the device.

$$V = -I(z,t)Z(\Omega)$$

The larger the impedance of the device, the larger V is, and the more strongly the beam is affected. An ideal accelerator would present no impedance to the beam. The amplitude versus frequency dependences of some typical kinds of accelerator impedances are shown in figure 2.2.

Wakefields and impedances are intimately related, wakefields being a time domain description of the interaction of a beam with its environment, and impedance being a frequency domain description. The electromagnetic force acting on a trailing

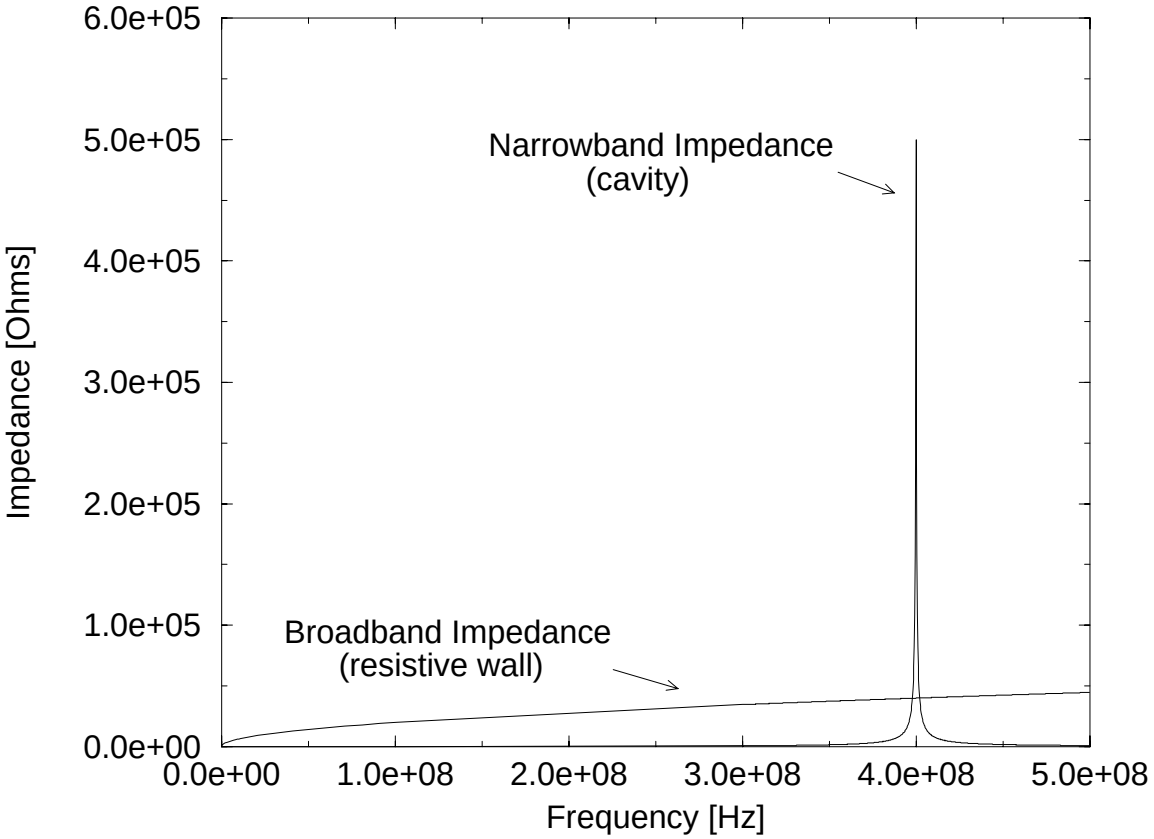

Figure 2.2: Typical accelerator impedances. The vertical scale of the broadband impedance has been exaggerated 100 times for clarity.

charge due to image currents in its surrounding environment is proportional to the wake function of the leading charge. The resulting impedance that a trailing charge experiences is the Fourier transform of the wake function [26, 8].

2.4 Linear Stability Theory

One method of investigating the stability of a beam is to examine its behavior in the presence of a small perturbation [4]. In an unstable situation, there is continued growth of the amplitude of coherent oscillation, even after the initial disturbance is removed. Instabilities are collective effects, and as such, need to be examined in light of the beam distribution as a whole, rather than in terms of the motion of individual particles.

The longitudinal distribution function of an unbunched, coasting beam will be symbolized by $f(\theta, \varepsilon)$. The total number of particles can be found by integrating the distribution function over the phase space variables,

$$N = \int_{-\infty}^{\infty} \int_{0}^{2\pi} f(\theta, \varepsilon)\, d\theta\, d\varepsilon \tag{2.4}$$

Once a beam is perturbed, the density may no longer be uniform in θ, but may vary around the machine as particles oscillate longitudinally. The number of particles per radian is,

$$n = \int_{-\infty}^{\infty} f(\theta, \varepsilon)\, d\varepsilon$$

The instantaneous beam current is found by multiplying the total number of particles

per radian by their angular velocity, ω_0 [rad/sec], and by e, their charge.

$$I(\theta) = e\omega_0 \int_{-\infty}^{\infty} f(\theta, \varepsilon)\, d\varepsilon \tag{2.5}$$

Assuming the total number of particles is conserved, then the total time rate of change of the particle distribution, $\frac{df}{dt}$, is zero. This is a reasonable assumption; due to the nature of the sources of instabilities, the response of the beam envelope to a disturbance is slow compared to the period of any mode supported by the beam. Thus, the initial development of an instability occurs with no concurrent beam loss. The transport equation is,

$$\frac{df}{dt} = 0$$

This is also a statement of Liouville's theorem, which says that although individual particles in the distribution change their phase space coordinates with time, the total area of the distribution in phase space is conserved. Since f is a function of θ and ε, the transport equation may be written,

$$\frac{\partial f}{\partial t} + \frac{\partial \theta}{\partial t}\frac{\partial f}{\partial \theta} + \frac{\partial \varepsilon}{\partial t}\frac{\partial f}{\partial \varepsilon} = 0$$

This is the Vlasov equation,

$$\frac{\partial f}{\partial t} + \dot{\theta}\frac{\partial f}{\partial \theta} + \dot{\varepsilon}\frac{\partial f}{\partial \varepsilon} = 0 \tag{2.6}$$

where $\dot{\theta} = \omega = \omega_0 + k_0\varepsilon$ is the revolution frequency of a particle with energy error ε. Again, the Vlasov equation is a suitable description of the beam dynamics as long as the time scale for growth or decay of an instability is slow compared to the period of the mode oscillations in the beam system.

A storage ring is a periodic system, a particle returning to the same location every revolution. The harmonics of the revolution frequency are the natural longitudinal modes of an unbunched beam. When a beam is undergoing oscillation, the frequency is conventionally specified by the mode number (for example $h = 2$), rather than by the corresponding number of cycles per second ($2 \times f_{rev} = 1.25$ MHz). Localized forces must be periodic at one of these revolution harmonics in order to interact resonantly with the beam, potentially causing growth of coherent motion. Due to the periodic nature of the motion, it is convenient to examine the stability issue in the frequency domain, writing f and $\dot{\varepsilon}$ in terms of their Fourier components. Fourier analysis is also suitable for a perturbative treatment of the Vlasov equation, since an excitation at one of the normal modes of the system begins as a small perturbation on the initially uniform beam distribution, f_0. Proceeding with this analysis, f is written,

$$f(\theta, \varepsilon) = f_0(\varepsilon) + \sum_{m \neq 0} f_m(\varepsilon) e^{i(m\theta - \Omega t)} \tag{2.7}$$

where f_0 is the unperturbed distribution, and the perturbative term is the expansion in longitudinal modes. The $m = 1$ term in the summation represents a modulation at the revolution frequency, the $m = 10$ term a mode at 10 times the revolution frequency, and so on.

The voltage change per turn due to a perturbation experienced by the beam is,

$$V = \sum_{m \neq 0} U_m e^{i(m\theta - \Omega t)} = -Z(\Omega) \sum_{m \neq 0} I_m e^{i(m\theta - \Omega t)} \tag{2.8}$$

where $I_m e^{i(m\theta - \Omega t)}$ is the perturbed current at mode m, and Z is an impedance present in the beam environment. Thus $\dot{\varepsilon}$, the energy change due to the perturbation is,

$$\dot{\varepsilon} = \frac{e\omega_0}{2\pi} \sum_{m \neq 0} U_m e^{i(m\theta - \Omega t)} \tag{2.9}$$

Equations 2.7 and 2.9 are substituted into the Vlasov equation (Eq. 2.6), which may then be written for a given mode m. By keeping only first order terms in the expansion parameter (which is on the order of the ratio of the perturbed to unperturbed portion of the particle distribution, $\frac{f_m}{f_0}$) the Vlasov equation is linearized,

$$(-i\Omega + im\omega) f_m + \frac{\partial f_0}{\partial \varepsilon} \frac{e\omega_0}{2\pi} U_m = 0$$

Rearranging,

$$f_m(\Omega) = \frac{e\omega_0}{i2\pi} U_m \frac{\frac{\partial f_0}{\partial \varepsilon}}{\Omega - m\omega} \tag{2.10}$$

A dispersion relation may be obtained from Eq. 2.10. By integrating over the energy error, the left hand side of this equation may be put in terms of I_m (see Eq. 2.5). Next, using the relation of Eq. 2.8, the U_m term on the right hand side of the equation may also be put in terms of the perturbed current I_m. Cancelling

$I_m e^{i(m\theta - \Omega t)}$ from both sides of Eq. 2.10 now results in the desired linear dispersion relation.

$$1 = \frac{i(e\omega_0)^2}{2\pi} Z(\Omega) \int \frac{\frac{\partial f_0}{\partial \varepsilon}}{\Omega - m\omega} \, d\varepsilon \tag{2.11}$$

The dispersion relation reveals an intrinsic relationship between complex frequencies generated in the beam and impedances present in the beam environment. Given any impedance, there is at least one complex frequency which satisfies the dispersion relation. This means that if the machine impedance is known, it can be determined whether or not growth will result from an initial perturbation of the beam. Examining the form of the perturbed beam current, $I_m e^{i(m\theta - \Omega t)}$, it is evident that as long as Ω is purely real, the motion of the perturbed current is purely oscillatory. However, in the case where Ω is complex, then $e^{-i\Omega t}$ either grows or decays exponentially. A curve representing the boundary between stable and unstable motion can be drawn in the complex impedance plane. Stability boundaries, such as the inner curve of figure 2.3, are generated using the dispersion relation to map a range of purely real frequencies into their associated impedances. When this is done for a Gaussian beam distribution, it can be verified that impedance values falling inside the stability boundary correspond to frequencies with a negative imaginary part. On the other hand, if an impedance lies outside of the stability curve, there is a frequency satisfying the dispersion relation which has a positive imaginary part. Thus, mapping out the stability boundary is a method for determining the range of storage ring impedances which do not lead to exponential growth of mode oscillations in the beam.

The stability boundary for a particular beam can be made by supplying eq. 2.11 with the appropriate beam parameters and a reasonable functional form for the beam

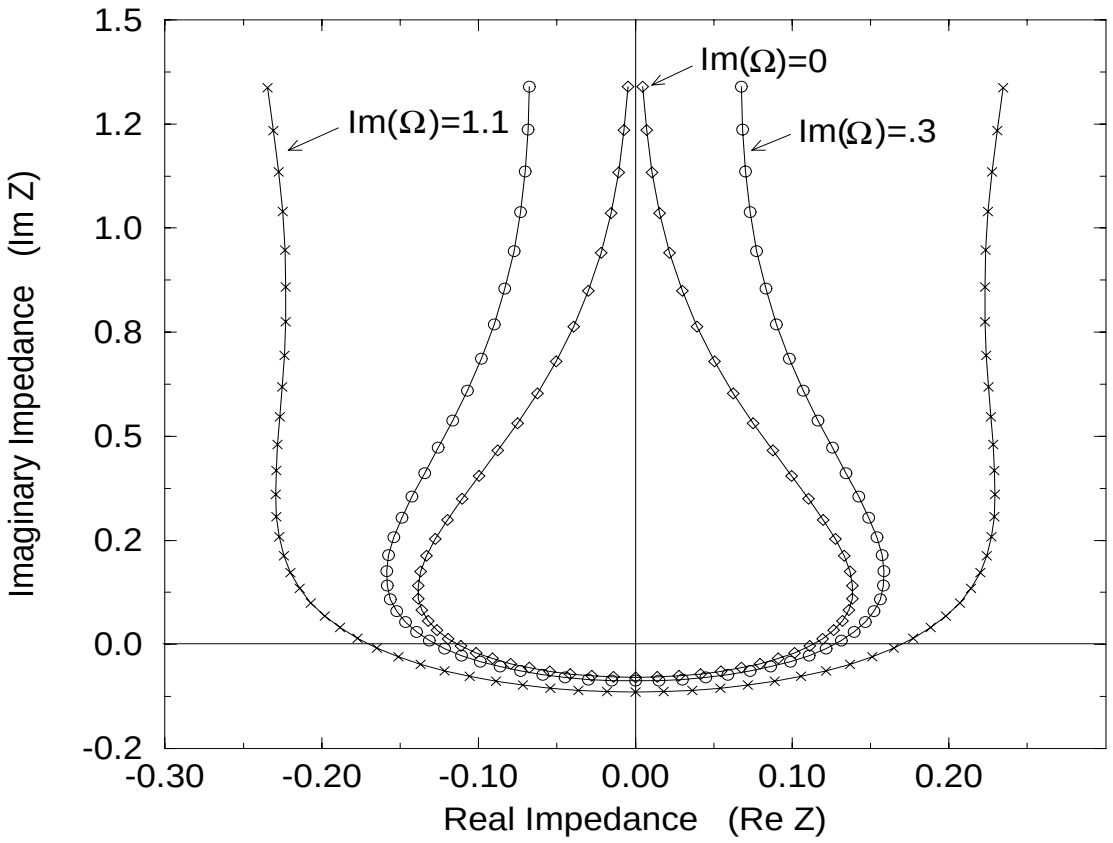

Figure 2.3: Impedance curves for three fixed values of $\mathrm{Im}(\Omega)$, while varying $\mathrm{Re}(\Omega)$. The inner curve represents the stability boundary. The beam distribution used was Gaussian in energy, and the beam parameters were arbitrary.

distribution. A realistic stability boundary for the Accumulator is shown in figure 2.4. The shape of the stability curve depends on the form of the beam distribution, a Gaussian distribution in energy is a good approximation for the Accumulator. The functional form of a Gaussian is given by,

$$f_0 = \frac{A}{\sqrt{2\pi}\,\sigma_\varepsilon}\, e^{-\frac{1}{2}\left(\frac{\varepsilon}{\sigma_\varepsilon}\right)^2}$$

The normalization constant A is found using equation 2.4,

$$f_0 = \frac{N}{(2\pi)^{\frac{3}{2}}\,\sigma_\varepsilon}\, e^{-\frac{1}{2}\left(\frac{\varepsilon}{\sigma_\varepsilon}\right)^2} \tag{2.12}$$

The derivative of the beam distribution with respect to energy error is then,

$$\frac{\partial f_0}{\partial \varepsilon} = -\frac{N}{(2\pi)^{\frac{3}{2}}\,(\sigma_\varepsilon)^3}\, \varepsilon e^{-\frac{1}{2}\left(\frac{\varepsilon}{\sigma_\varepsilon}\right)^2}$$

Now the dispersion relation can be written,

$$1 = \frac{I_0 \beta^2 Z}{i2m\eta\pi^{3/2}E_0[eV](\frac{\sigma_\varepsilon}{E_0})^2} \int dx \frac{x e^{-x^2}}{x-\xi}$$

where $\xi = \frac{-\beta^2}{\sqrt{2}m\eta(\frac{\sigma_\varepsilon}{E_0})}[\frac{\Omega}{\omega_0} - m]$. The η in the coefficient of the dispersion relation is the slip factor, and its sign depends on whether the machine is running at an energy above or below transition. The normal energy of the core of the beam in the Accumulator is 8.696 MeV, which is above transition. Above transition η is positive

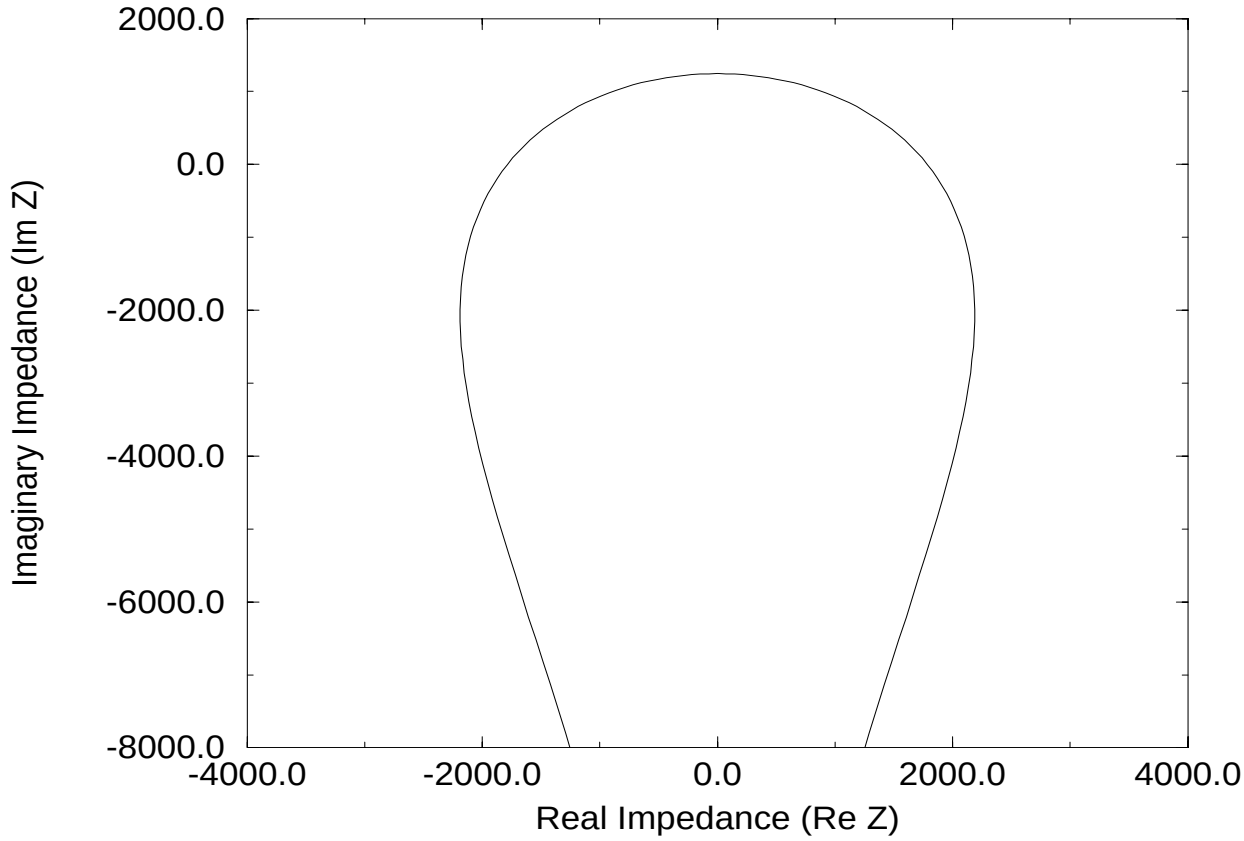

Figure 2.4: Stability boundary for the Accumulator beam. This curve was made using the following beam parameters: Beam Intensity $I_0 = 68.28$ mA, Beam Harmonic $m = 2$, Total Beam Energy $E_0 = 8.696$ GeV, Slip Factor $\eta = .023$, Relativistic Beta $\beta = .99416$, and Beam Energy Sigma $\sigma_\varepsilon = 1.59$ MeV. The beam distribution was assumed to be Gaussian in energy, which is a good approximation for the Accumulator. The curve is pointing downward because the Accumulator is above transition.

and purely inductive impedances are stable, whereas below transition η is negative and purely capacitive impedances are stable. Thus, stability curves for machines above transition will have their 'tails' along the negative imaginary axis rather than the positive imaginary axis [4].

Using the above dispersion relation, it is possible to determine that the area internal to the stability boundary will decrease as the beam intensity increases. For a given frequency, an increase in I_0 must result in a decrease of Z in order for the equation to still be satisfied. As a beam becomes more intense, there is a smaller range of machine impedances which are inside the region of stability. Similarly, as the energy spread of a beam goes up, the stable region increases. Note also that the scaling of the stability curve depends on the harmonic number, or frequency, in question. In order to avoid discussing a different stability boundary for every beam harmonic, it is conventional instead to refer to Z/n, where n is the harmonic number.

2.4.1 Beam response to an external voltage

The expected beam response to an excitation may be obtained theoretically [32]. The response to an applied driving voltage is given by $R = \frac{-V_0}{I_m}$, where V_0 is the driving voltage, and I_m is the perturbed current at the frequency of the driving voltage. The Vlasov formalism is used to express the perturbed current in terms of the driving voltage, the beam distribution, and the machine impedance; ultimately allowing the beam response to an external drive to be written in terms of the machine impedance and known quantities. Starting with a uniform, unbunched coasting beam, the energy

change due to the drive is,

$$\dot{\varepsilon} = \frac{e\omega_0}{2\pi}(V_0 - U_0)e^{i(m\theta - \Omega t)} = \frac{e\omega_0}{2\pi}(V_0 + I_m Z(\Omega))e^{i(m\theta - \Omega t)}$$

where $U_0 = -I_m Z(\Omega)$ is the self-field voltage initiated by the externally applied excitation. Substituting $\dot{\varepsilon}$ into the Vlasov equation and solving for f_m,

$$f_m = \frac{-i(e\omega_0)}{2\pi}(V_0 + I_m Z(\Omega))\frac{\frac{\partial f_0}{\partial \varepsilon}}{\Omega - m\omega}$$

Integrating over the distribution to get an expression containing I_m,

$$I_m = e\omega_0 \int f_m(\varepsilon)d\varepsilon = \frac{-i(e\omega_0)^2}{2\pi}(V_0 + I_m Z(\Omega))\int_{-\infty}^{\infty} \frac{\frac{\partial f_0}{\partial \varepsilon}}{\Omega - m\omega}d\varepsilon$$

Solving for I_m,

$$I_m = \frac{\frac{-i(e\omega_0)^2}{2\pi}V_0 \int_{-\infty}^{\infty} \frac{\frac{\partial f_0}{\partial \varepsilon}}{\Omega - m\omega}d\varepsilon}{1 + Z(\Omega)\frac{i(e\omega_0)^2}{2\pi}\int_{-\infty}^{\infty} \frac{\frac{\partial f_0}{\partial \varepsilon}}{\Omega - m\omega}d\varepsilon}$$

Then the measured response in terms of the ring impedance is,

$$R = \frac{-V_0}{I_m} = \frac{1}{\frac{i(e\omega_0)^2}{2\pi}\int_{-\infty}^{\infty} \frac{\frac{\partial f_0}{\partial \varepsilon}}{\Omega - m\omega}d\varepsilon} + Z(\Omega) \tag{2.13}$$

If there is no machine impedance at the frequency Ω of the applied voltage, then $Z(\Omega)$ in equation (2.13) is zero. Multiplying both sides by the denominator on the

right hand side,

$$1 = R\frac{i(e\omega_0)^2}{2\pi}\int_{-\infty}^{\infty}\frac{\frac{\partial f_0}{\partial \varepsilon}}{\Omega - m\omega}d\varepsilon$$

yields a result of the same form as the linear dispersion relation given by equation (2.11). Thus, in the absence of a machine impedance $Z(\Omega)$, and any nonlinear effects, the response curve obtained from a network analyzer measurement will match the stability boundary of the dispersion relation derived from the linearized Vlasov equation. When a machine impedance is present, $Z(\Omega) \neq 0$, and its effect is to shift the origin of the response curve by $Z(\Omega)$, as shown in figure 2.5. The experimentally measured beam response to an applied excitation can thus be used to determine the impedance of a storage ring. Such a measurement, which exhibits a shifted response curve due to an impedance, will be presented in the next chapter.

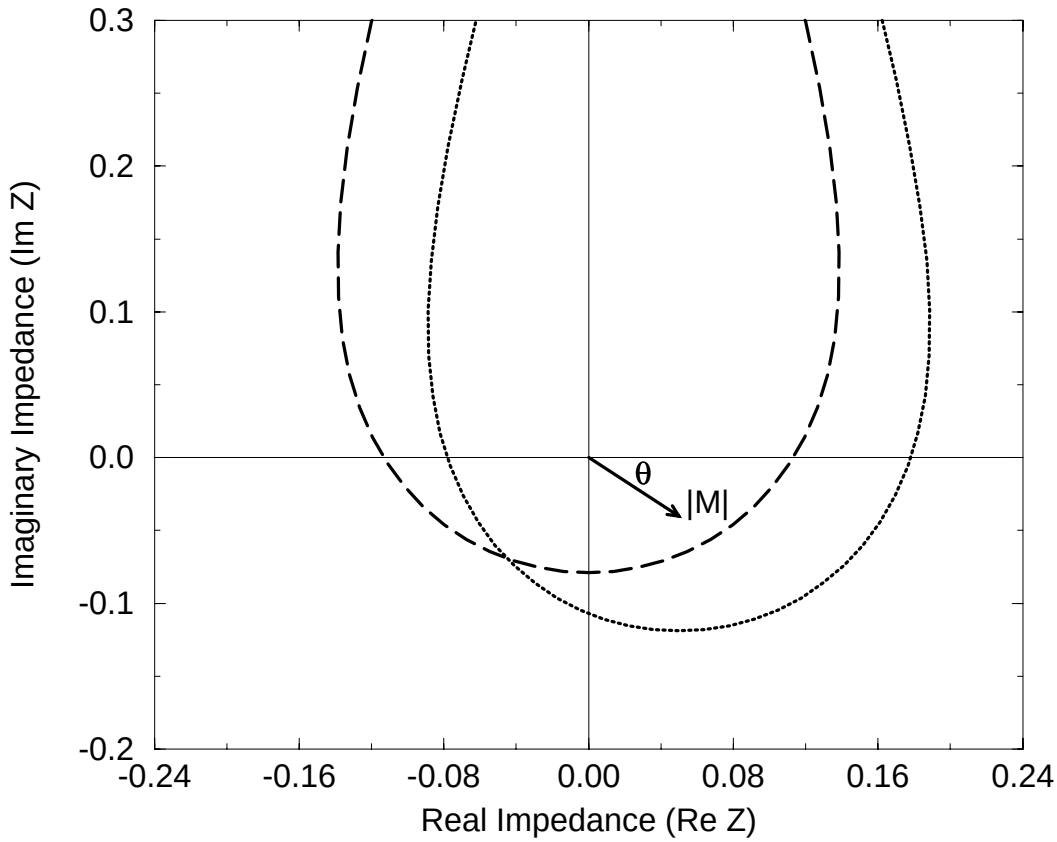

Figure 2.5: Theoretical shift of the beam response due to an impedance. The curve centered on the origin (dashed) is the response when there is no impedance, and the displaced curve (dotted) is the response when there is an impedance of $(Z_x, Z_y) = (.05, -.04)$. The magnitude of the impedance is $|\mathrm{M}| = \sqrt{Z_x^2 + Z_y^2} = .064\Omega$, and the phase is $\theta = -39°$. The beam distribution used was Gaussian in energy, and the beam parameters were arbitrary.

Chapter 3

Accumulator beam transfer function measurements

3.1 Introduction and overview

The original motivation for doing studies in the Fermilab Accumulator antiproton storage ring was a desire to investigate the weakly nonlinear parametric coupling phenomenon. For reasons which later became clear, it was difficult to initiate parametric coupling, and the experiments evolved into a study of beam echoes, which are another manifestation of weakly nonlinear wave-wave coupling. As a preliminary to the search for parametric coupling, the linear stability properties of the Accumulator were measured. This served as a baseline for understanding the measurement equipment and the properties of the machine. This turned out to be important, since the low impedance, stable nature of the Accumulator were exactly what made it difficult to trigger parametric coupling events in the machine.

This chapter is primarily concerned with presenting the results of the beam transfer function measurements that were done during the initial investigation of machine stability. Some important beam parameters that will be used throughout the thesis are listed in table 3.1 at the end of this section.

The experimental setup for the frequency domain measurements is documented in section 3.2. This section also has information about the hardware, given as a series of short descriptions of the devices used in acquiring data during studies. Some emphasis is placed on the frequency response, since this should be flat over the range of a given measurement, or over the range of measurements which are being compared. Standard cable does attenuate with frequency, but the frequency range of the measurements was small, so the response of devices which may behave resonantly is more of an issue.

Impedance measurements were done at many frequencies, but the frequencies of particular interest were the 2nd and 84th harmonics of the revolution frequency. The standard notation in accelerator physics for the frequency of the 2nd harmonic, $2 \times f_0$, is $h = 2$. Similarly for all other harmonics. The Accumulator has RF systems at $h = 2$ and $h = 84$, and the cavities are likely candidates for generating wakefields. Fortuitously, the cavities may be shorted, curtailing their resonant behavior. Besides the operational benefit, this provided the opportunity to directly determine the cavity impedance, by comparing measurements with the cavity shorts in and out.

Results of the $h = 2$ impedance measurements are presented in section 3.3. Calibration is always a delicate issue, as the response of each component in the measurement chain must be well-known to obtain the machine impedance from the measured data alone. However, it is possible to get a calibration by matching the data to a theoretically generated curve appropriate for the machine conditions at the time of

the measurement. This calibration technique is applied to cavity shorts in and cavity shorts out data, and a comparison of the scaled curves yields a reasonable value for the impedance of the cavity. At the end of section 3.3, a stability measurement comparing large and small beam sizes is presented in order to give a quantitative picture of how large energy spreads improve stability.

Results of the $h = 84$ impedance measurements are presented in section 3.4. Unfortunately, the measurements obtained at this frequency were either noisy, or worse, the excitation used for the measurement was not sufficiently perturbative, and so changed the nature of the beam distribution. It is possible to improve the experimental technique and get a better measurement, nevertheless, the results are presented. The data give a very rough idea of the machine behavior, and give graphic demonstration of nonlinear beam response to large voltages.

The Fermilab Accumulator is an antiproton storage ring, having a wide momentum aperture. Beam is injected on an outside orbit and moved to an inside orbit where the collected, stored beam circulates. During these studies the injection process was halted and data was taken using the stored beam, or 'core'. The beam in the core was not captured by an RF system, and so was unbunched. Table 3.1 lists typical Accumulator beam parameters [34]. Wherever the beam energy spread is written symbolically as $\frac{\sigma_\varepsilon}{E_0}$, as in table 3.1, σ_ε is the standard deviation of a distribution which is assumed to be Gaussian, and E_0 is the particle energy at the center of the distribution. The standard deviation is related to the full-width at half-maximum by the proportionality $fwhm = 2.354\sigma$.

Table 3.1: Accumulator Beam Parameters

Parameter	Value
Revolution Frequency f_0	628.955 kHz
Slip Factor η	.023
Total Particle Energy on Core Orbit E_0	8.696 GeV
Typical Beam Energy Spread σ_ε/E_0	$1-4\times10^{-4}$

3.2 Experimental setup

The hardware setup for the Accumulator beam transfer function measurements is shown in block diagram form in figure 3.1. The beam transfer function measure-

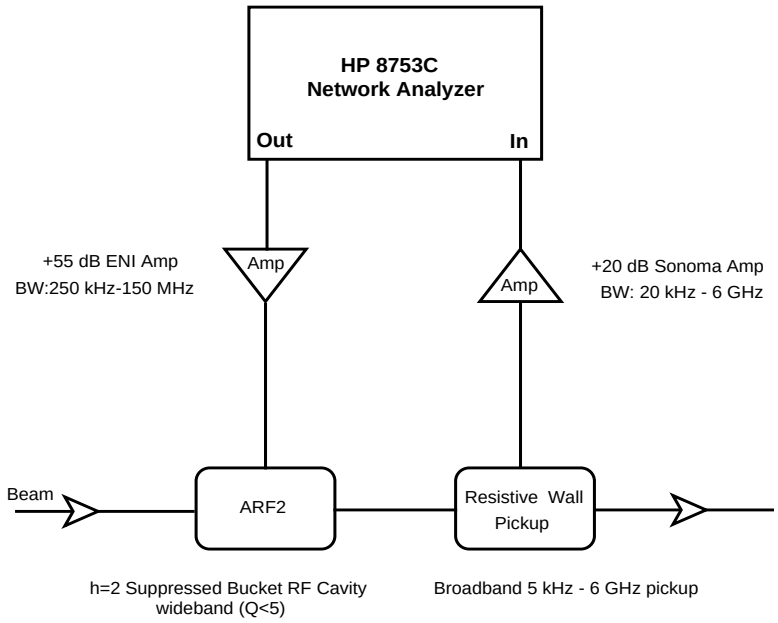

Figure 3.1: Block diagram of Accumulator transfer function measurement setup.

ments were S21 transmission coefficient measurements using a network analyzer with an attached S-parameter test set. Appendix A gives a general description of this

measurement technique. The network analyzer excited the beam longitudinally by applying a swept frequency sine wave to a broadband RF cavity. The resulting frequency content of the beam was monitored using a broadband longitudinal beam current monitor. The signal from this beam pick-up was directed to the return port of the network analyzer, completing the path needed for the measurement. The hardware components are described in more detail below.

The frequency source for the transfer function measurements was an HP 8753C network analyzer with a frequency range of 300 kHz - 3 GHz and an attached HP 85047A S-parameter test set. After a long cable run, necessary due to the distance between the beam kicker and the available signal from the beam detector, the voltage from the network analyzer was amplified by a 3100 LA +55 dB amplifier having a frequency range of .25-150 MHz. The output of this amplifier was connected directly to the drive cable for the ARF2 cavity; the normal cavity drive system was disconnected during these studies.

ARF2 is a broadband ($Q < 5$) suppressed bucket RF cavity, used to take antiprotons out of the core of the stored beam when they are needed for the physics program. The center frequency of the cavity is $h = 2$, or 1.25791 MHz. The ARF2 cavity is a ferrite loaded cavity with a low impedance (approximately 50Ω) gap.

The gap voltage of ARF2 may be monitored using the fanback signal. The result from a previous calibration at $h = 2$ was that for every volt on the fanback signal there are 273 volts across the gap [36]. Before commencing with the beam transfer function measurements, the frequency response of the cavity was examined by comparing the fanback signal to the input signal. The fanback signal was connected to the R port of the network analyzer, while the cavity drive signal, after passing through a 30 dB

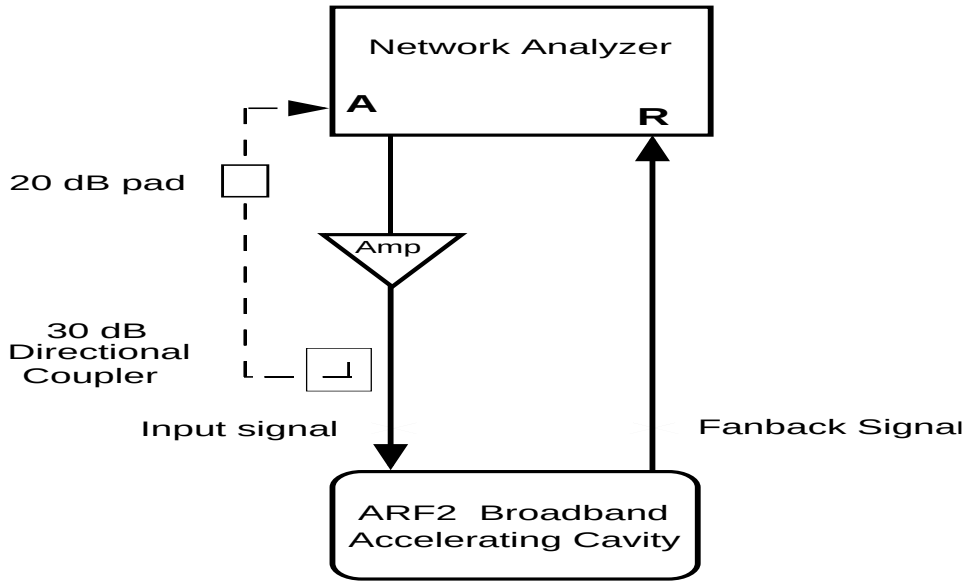

Figure 3.2: Technique for the ARF2 cavity fanback measurement

coupler and further attenuated by 20 dB, was connected to the A port of the network analyzer. A schematic of the measurement setup is shown in figure 3.2. It is best to try and compare the input signal to the fanback signal directly, preferably tapping at the locations shown by the x's in the diagram. Since this was not possible, some adjustments were made. The 30 dB coupler was measured over the frequency range of interest and the effect of the coupler as well as the 20 dB pad was subtracted from the final result. There were also long cables run back from the vicinity of cavity to the location of the network analyzer, both from the coupler and from the cavity fanback. As a rough approximation, the effect of these cables cancel each other in the A/R measurement, and so neither was subtracted from the measurement. The frequency response $R/(A - coupler - pad)$ is shown over three frequency ranges in figure 3.3. Note that at $h = 2$ the ratio measurement gives -49.65 dB. The result predicted by the fanback calibration is $20\log(1/273) = -48.72$ dB. So, this measurement of the

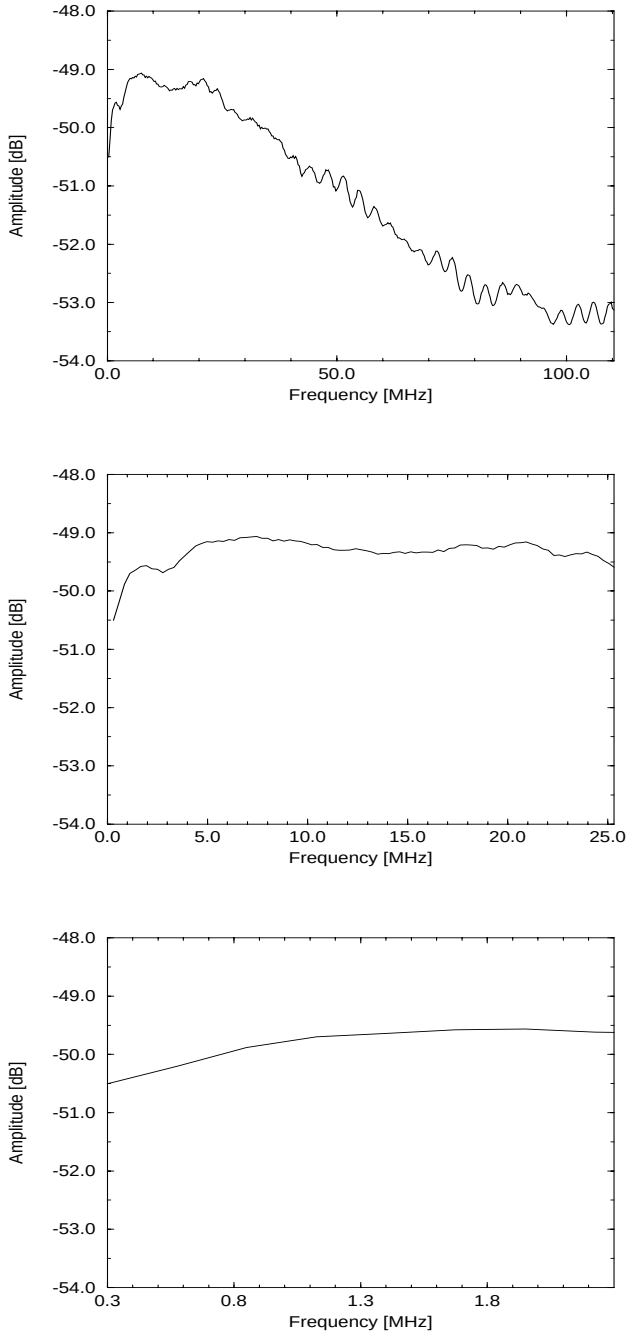

Figure 3.3: Measured frequency response of the ARF2 cavity.

frequency response of the cavity is good to about 10%.

The longitudinal beam pickup used was a resistive wall current monitor [37, 38] with a flat frequency response from 3 kHz to 6 GHz. The pickup is called a 'resistive wall' detector because of its construction. This type of detector relies on the principal that a particle beam will create an image current in the surrounding beampipe walls if they are made of conducting material. The continuity of the pipe is broken by a resistive gap which is in series with the wall. The image current flows through the gap resistance, some portion of which is combined into a 50 Ω line that carries the signal away for monitoring. Some care must be taken in the design to ensure broad-band response, insensitivity to beam position, and isolation from stray currents. A conceptual sketch of a wall current monitor is shown in figure 3.4. The gap resistance

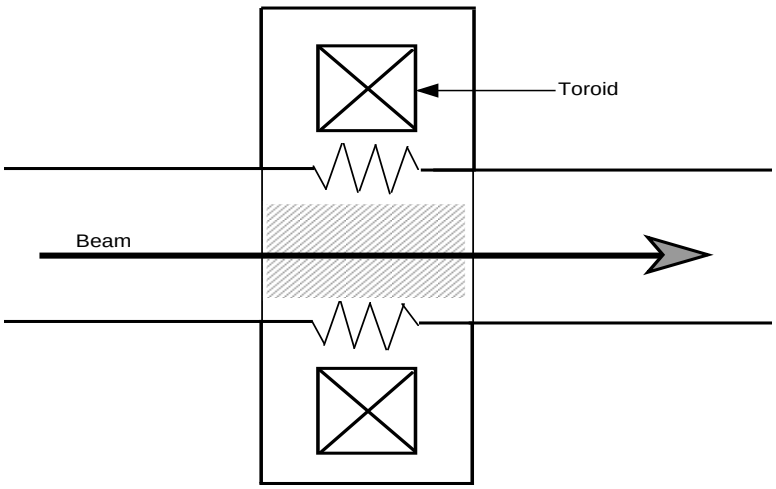

Figure 3.4: Conceptual idea for a resistive wall current monitor

of the actual detector is surrounded by a ferrite loaded cavity with several types of ferrite, whose purpose is to create a large shunt impedance thereby forcing the wall current to go through the gap resistance rather than around it. The combination of these various ferrites is responsible for realizing the flat frequency response up to

the several GHz range. Microwave absorbing material upstream and downstream of the detector, and an electric shield externally surrounding the ferrites, were installed to ensure that only current due to the instantaneous passage of beam goes through the gap resistance. There are eighty, 120 Ω resistors distributed around the gap circumference, providing a uniform gap resistance. This resistance, along with the inductance of the ferrite materials is responsible for the low frequency corner of the detector response. Four microstrip transmission lines are also evenly spaced around the gap circumference, substituting for gap resistors at those four locations. This distribution of transmission lines provides a position insensitive signal. The currents in the transmission lines are combined to make the single 50 Ohm output. A ceramic has been inserted into the break in the beampipe, so that the entire assembly of resistors and ferrites may be isolated from the storage ring vacuum.

The signal from the wall current monitor was passed through a +20 dB Sonoma amplifier with a bandwidth of 20 kHz to 6 GHz, before being connected to the return port of the network analyzer.

3.3 Impedance measurements at the 2nd harmonic

Figure 3.5 shows a typical beam transfer function measurement at $h = 2$ in the Accumulator. In order to be centered on the second revolution harmonic, the center frequency of the scan was $2 \times f_0 = 1.2579$ MHz. The frequency span was chosen to be just wide enough to completely encompass the frequency spread contained in the beam distribution. Frequencies outside this range are uninteresting, and opening up the frequency span may cause loss of resolution bandwidth.

Using equation A.1, this s21 measurement may be used to directly generate the

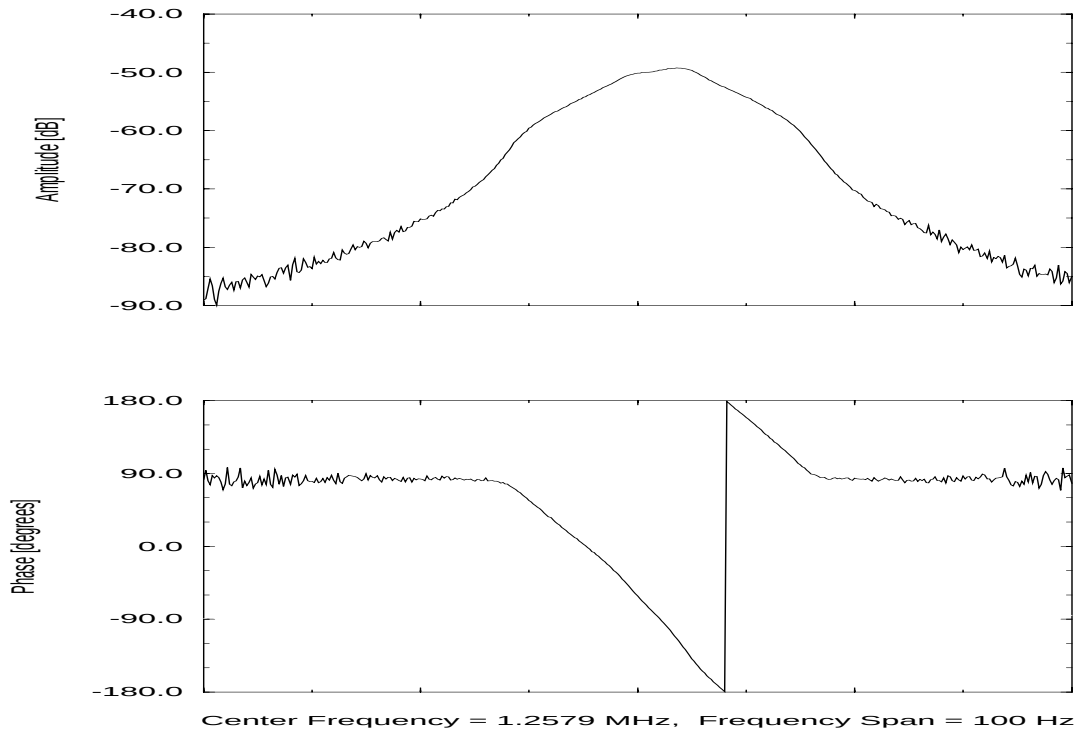

Figure 3.5: S21 measurement at $h = 2$ in the Accumulator. The top plot is the magnitude response, and the bottom plot is the phase response. Beam parameters: beam intensity 68 mA, and beam energy sigma 1.6 MeV. Network analyzer setup: 401 data points, sweep time 41 sec, and a resolution bandwidth of 10 Hz.

uncalibrated response curve of figure 3.6. As it stands, the network analyzer in figure 3.1 is set up to measure the transfer function of the beam, combined with the amplifiers, the cables, the cavity, and the pickup. There will also be an additional phase advance due to the distance between the kicker and the detector. In order to get solely the response of the beam in its normal machine environment, the transfer function of each component used in the measurement must be known and divided out of the total result (or subtracted if using a log scale). Unless these components were measured in isolation on the bench before installation into the storage ring, it

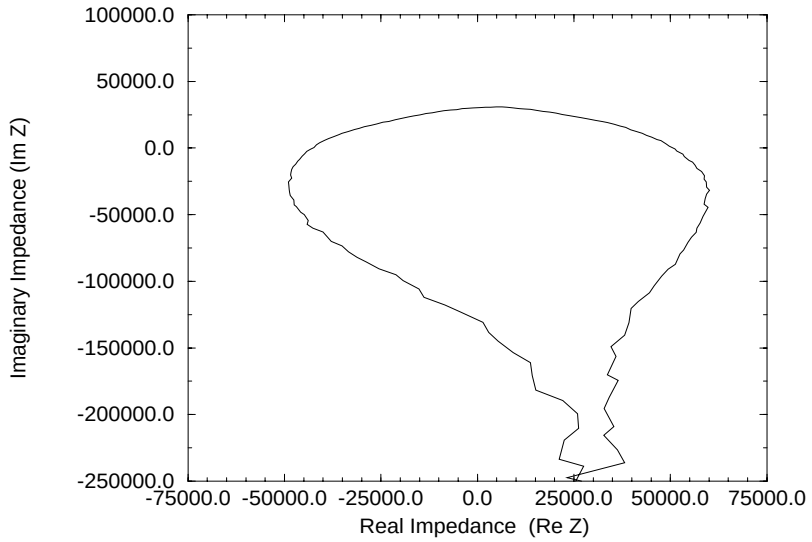

Figure 3.6: Uncalibrated response curve made using s21 data displayed in figure 3.5.

is difficult to untangle their individual contributions to the overall measurement.

Knowledge of the absolute magnitude of the frequency response of the equipment used during beam studies was not sufficient for an accurate brute force calibration of the beam transfer function measurements. However, if the frequency response of each piece of equipment is determined to be flat across the measurement span (thus leaving the shape of the total system response unchanged) then there is an alternative technique for calibrating the beam transfer function data. With knowledge of the beam parameters at the time of the measurement, the scale of the measured data can be set by matching it to the stability boundary obtained from the linear dispersion relation. In order to use this method, the form of the beam distribution function used in the dispersion relation must approximate the actual beam shape, at least in the center where most of the particles are located. Otherwise, it may be too difficult to

fit the shape of the measured curve to the stability boundary.

This alternative method allows calibration of the beam response data even when the response of individual measurement components is unknown. However, there will still be a statistical error on the measured curve, and possibly also some systematic errors. In addition, the curve given by the dispersion relation will have an associated error which depends on how well the beam parameters are known, since there is a product of these parameters in the coefficient of the integral.

Based on experimental data, there is reasonable confidence that the frequency response of each unwanted component in the Accumulator beam measurement chain was flat during any given scan. However, the systematic error on the beam transfer function measurements was greater than the statistical error, and is the limiting factor on the accuracy of a calibration. This can be seen in figure 3.7, in which the magnitude response of two identical measurements made during the same study period are overlaid. The top and bottom plots of the figure are the same, except that the amplitude of the top plot is shown on a log scale, while that of the bottom plot is shown on a linear scale. The beam parameters and network analyzer setup are the same as are listed in figure 3.5.

The calibrated impedance curves generated from the beam transfer function measurements of figure 3.7 are shown in figure 3.8. Note that while the middle portion of the measured and theoretical curves do match up pretty well, the portions which come down along the imaginary axis do not. The central regions of the curves correspond to the center of the beam distribution, while those parts along the extremes of the imaginary axis correspond to the tails of the distribution. So, while a Gaussian curve is a good match near the beam center, it breaks down at the beam edges. The

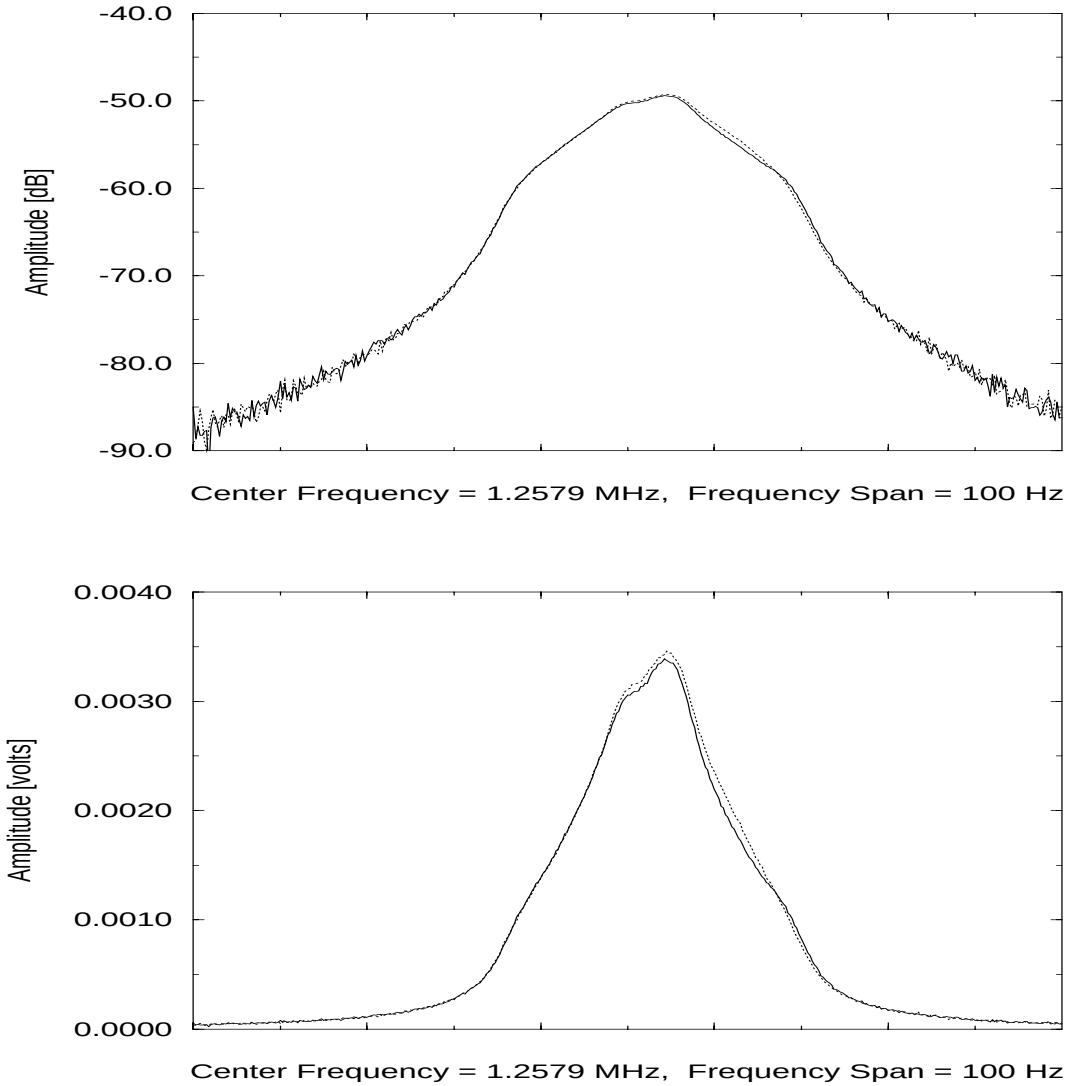

Figure 3.7: The Magnitude response of two independent, identical beam transfer function measurements taken during the same study period. The top plot shows the amplitude of the response on a log scale, while the bottom plot shows the response of the same measurements on a linear scale. The dashed curve was the second measurement, and so the discrepancy cannot be due to a small beam loss. The dashed curve is the same data as shown in figure 3.5.

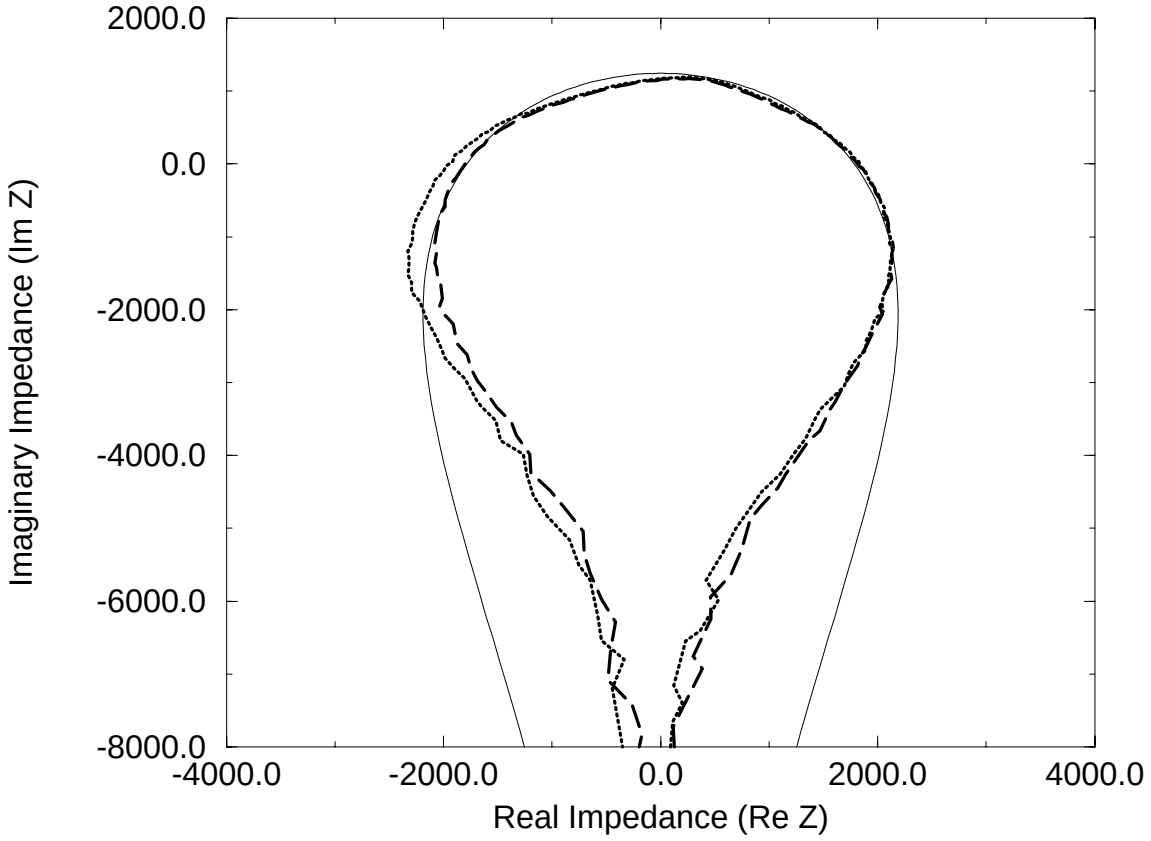

Figure 3.8: Impedance curves from two sets of measured data (dotted and dashed curves) fit to the stability boundary obtained from the dispersion relation (solid curve). The stability boundary here is the same as in figure 2.4, and the dashed impedance curve is the same as in figure 3.6, except for the calibration scale change and phase rotation. The same calibration was used for both measured curves. The beam parameters used to generate the stability boundary (listed in figure 2.4) were the actual conditions at the time of the measurement.

Accumulator has a beam cooling system (the Core Momentum Stochastic Cooling system) which actively works to compress the energy spread of the beam and narrow the distribution of particles. One manifestation of its operation is in the pinched tails of the actual response curves.

In order to get the match shown in figure 3.8, the measured curves were offset in magnitude by 28.23 dB and in phase by 8.5 degrees, before transforming into the impedance plane. These scale factors were found by comparing the magnitude and phase curves from one of the measurements (figure 3.5) to the magnitude and phase curves which generate the theoretical stability boundary. The necessary phase rotation can be easily determined by comparing the initial (or final) flat portion of the measured and theoretical phase curves, and then correcting the measured curve by the difference. The flat parts of the phase curve correspond to the tails on the stability diagram, and these orient the diagram.

The magnitude scaling is not as straightforward, but it turns out that using the difference between the magnitude of the measured and theoretical curves at the center frequency is usually a fairly good estimate of the required offset. This is supported by figure 3.9, which gives a measure of how well the two curves match up as a function of the applied offset. An estimate of the quality of the match is $\frac{1}{N-1}\sum_i[(xmeas_i - x_0) - xtheor_i]^2$; where $xmeas_i$ is the magnitude of the measured beam response at frequency i, x_0 is the offset in dB applied to the measured beam response, $xtheor_i$ is the magnitude of the theoretical beam response at frequency i, and N is the number of points included in the summation. Points from the center frequency out to the location where the theoretical curve falls by $.5\sigma$ were included in the summation used for figure 3.9. Note that the curve is smooth with the minimum located near 28.2 dB.

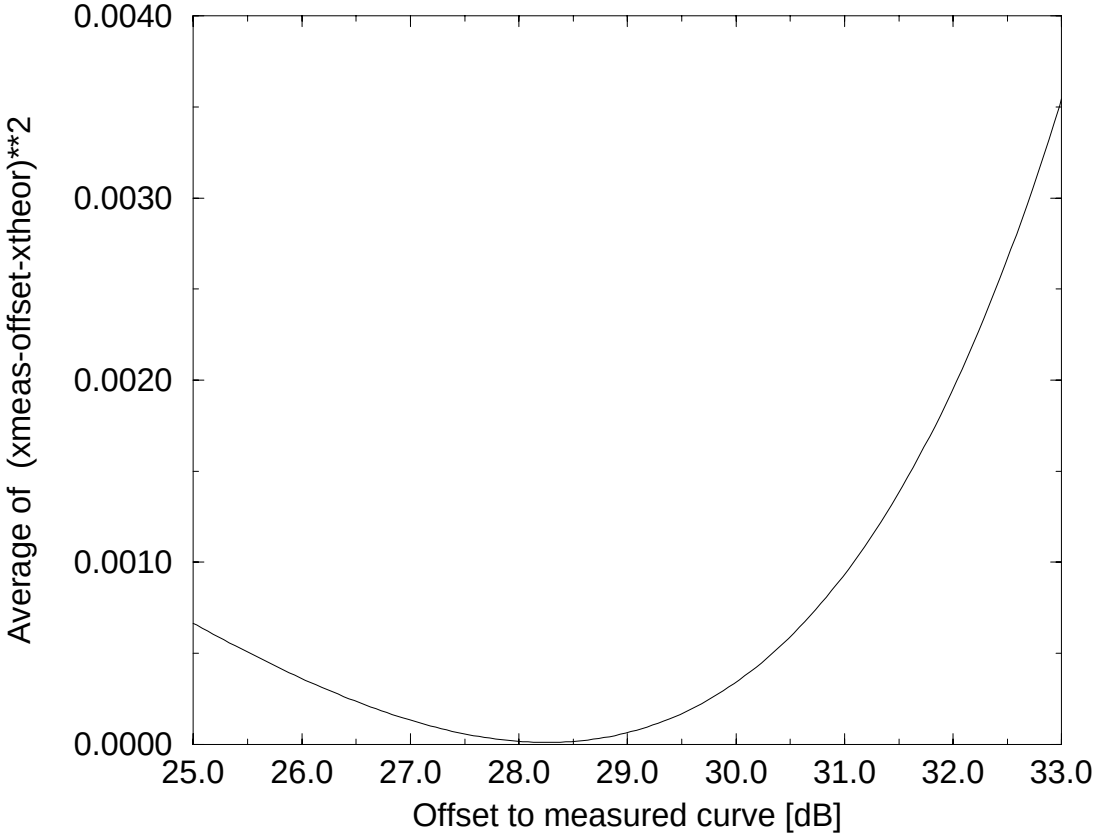

Figure 3.9: Average of the square of the difference between a measured impedance curve and the theoretical stability boundary as a function of the applied offset to the measured curve. Specifically, the plot is $f(x_0)$ vs. x_0, where $f(x_0) = \frac{1}{N-1}\sum_i[(xmeas_i - x_0) - xtheor_i]^2$.

The result that the magnitude difference between the theoretical and experimental beam response at the center frequency is close to the best overall scaling choice, can also be corroborated more loosely by visual inspection. Figure 3.10 compares the match between the stability boundary and three impedance curves which were generated using different magnitude offsets. The three offsets used were 28.23, and 28.23 ± 1 dB, with 28.23 giving the best match.

The experimental curves in figure 3.8 indicate that there was no significant machine impedance at $h = 2$ in the Accumulator at the time of the measurement. The effect of an impedance would have been to shift the origin of the measured response curve with respect to the origin of the stability boundary. The uncalibrated curve (shown in figure 3.6) had to be shrunk and rotated in order to be matched to the theoretical curve, but it did not have to be translated.

The Accumulator has two different RF systems at $h = 2$. One of these systems is ARF2, the cavity used as a kicker for these studies. The other system is ARF3, which was off during these studies. The ARF3 cavities are normally shorted (made non-resonant) when they are off, in order to remove them as a source of machine impedance. These cavity shorts can be removed without losing the beam, providing the opportunity to measure the impedance of ARF3. Figure 3.11 shows the magnitude portion of two sequential beam transfer functions, the only difference between the two being that the top trace was taken with the ARF3 cavity shorts in, while the bottom trace was taken with the shorts out. The impedance of ARF3 has non-uniformly enhanced the frequency response, as seen in the asymmetry of the bottom trace. As a result, the calculated impedance curve will no longer be centered on the origin in the impedance plane, but will in fact be shifted as expected theoretically. Figure 3.12

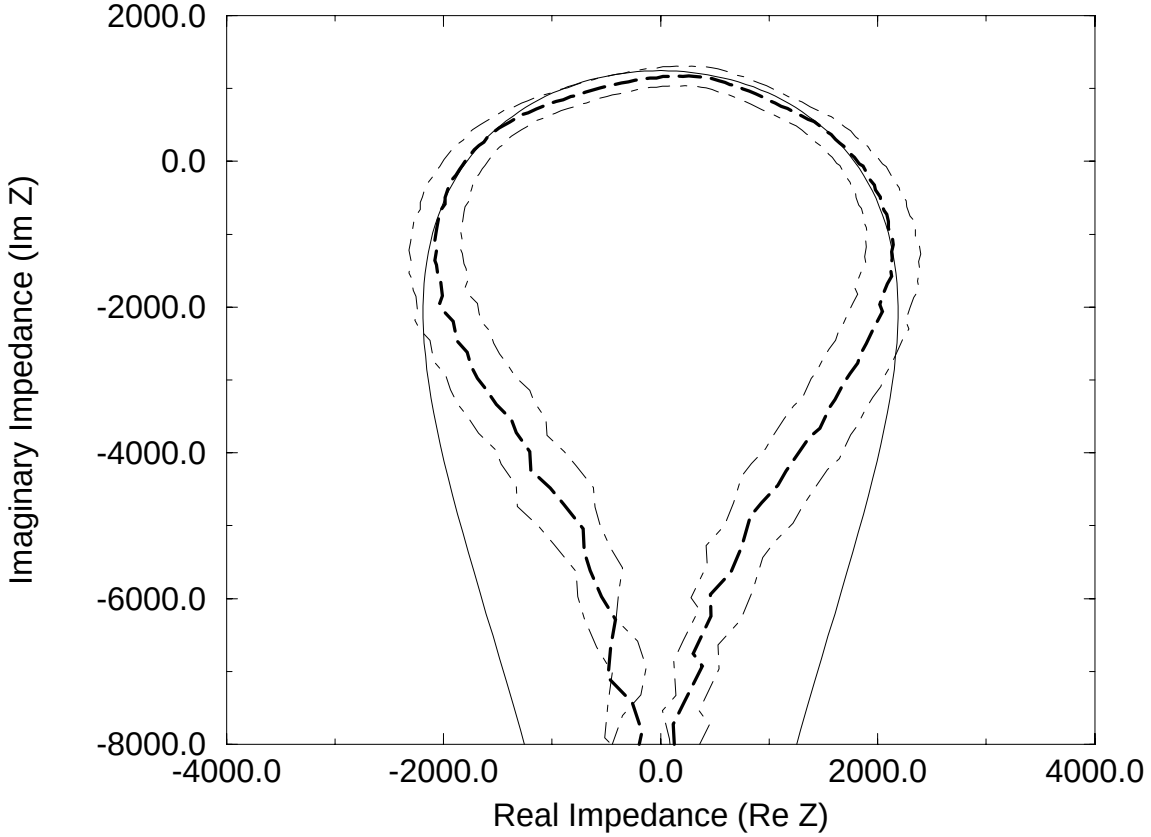

Figure 3.10: Comparison of the theoretical stability boundary (solid) to impedance curves generated by applying different magnitude offsets to data from a beam transfer function measurement (dashed). The scaling offsets used for the curves from inside to outside were 29.23, 28.23, and 27.23 dB.

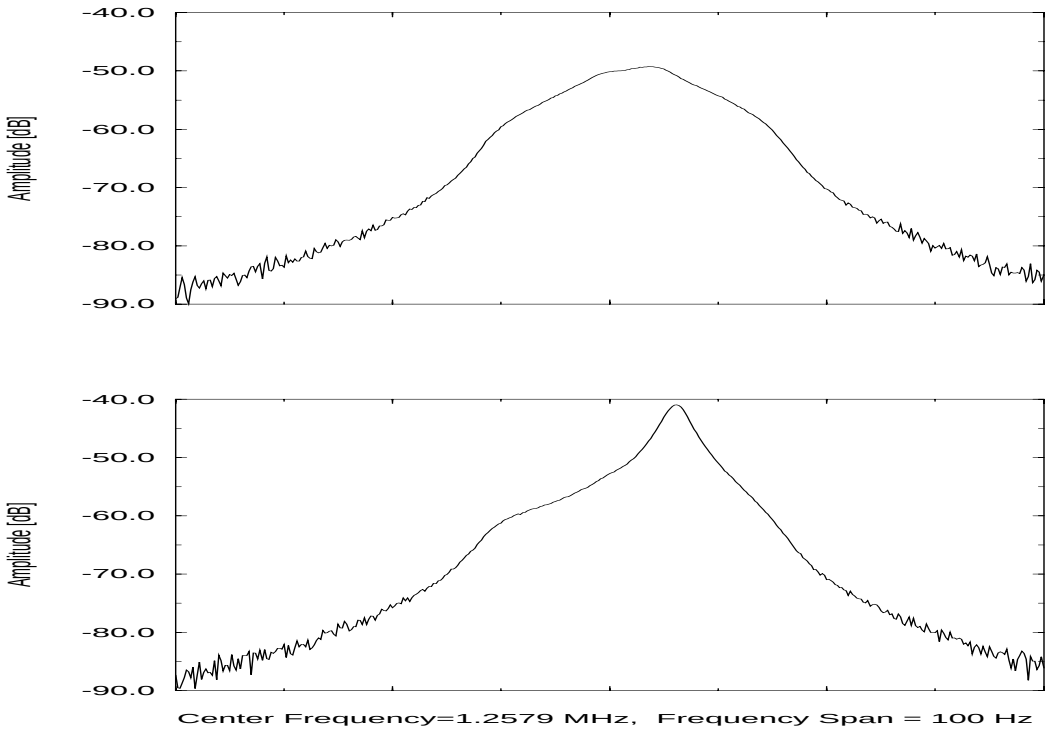

Figure 3.11: Comparison of magnitude portion of two beam transfer function (s21) measurements taken with different machine impedances. The top trace was taken with ARF3 cavity shorts in place, the bottom trace was taken with the ARF3 cavity shorts removed. Beam parameters: $I_0 = 68$ mA, $E_0 = 8.696$ GeV, $\eta = .023$, $\beta = .99416$, and $\sigma_\varepsilon = 1.6$ MeV. Network analyzer setup: center frequency at $h = 2$, 401 data points, sweep time 41 sec, and resolution bandwidth 10 Hz.

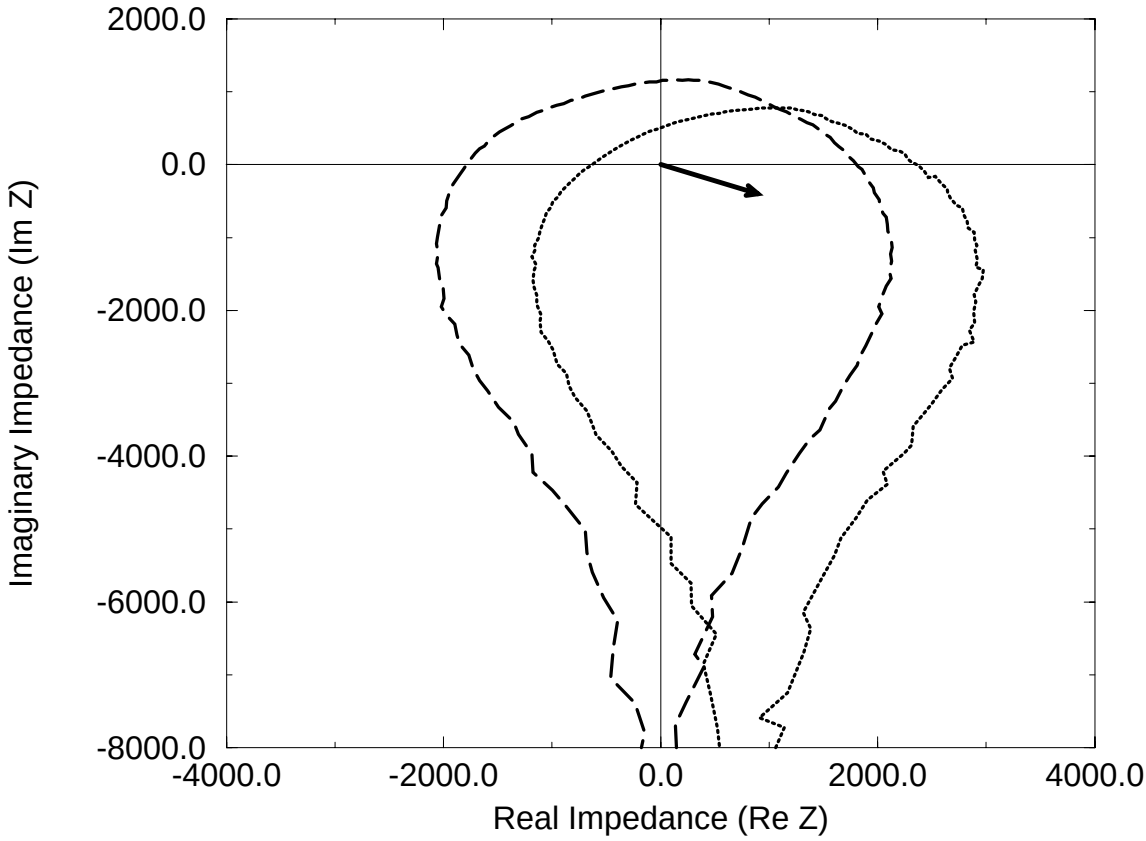

Figure 3.12: Calibrated impedance curves of measured data with ARF3 cavity shorts in (dashed curve) and with cavity shorts out (dotted curve). The origin of the response curve with the shorts out is shifted by approximately (x,y)=(900,-390), which gives an ARF3 cavity impedance of $Z/n = \sqrt{(900 \pm \sqrt{2} \times 170)^2 + 390^2}/2 = 490\Omega \pm 110$, at a phase angle of $-23°$.

shows the impedance curves calculated from the two transfer function measurements of figure 3.11. The curve for the case of 'cavity shorts in' was calibrated as shown in figure 3.8. Since this calibration must apply to all measurements made under the same beam conditions, the curve for 'cavity shorts out' was scaled identically. Again, no translation was done, only rotation and shrinking. Thus, the shift of the curves in figure 3.12 is a calibrated measure of the impedance of ARF3. The result for Z/n is $490 \pm 110\Omega$, which may be compared with a previous bench measurement for a comparable cavity ($\sim 480\Omega$) given in reference [33].

The uncertainty quoted on the machine impedance is due to the systematic error seen on the measured beam response. Examination of figure 3.8 shows that while the Z_y intercept and one of the Z_x intercepts are the same for the two measured curves, the other Z_x intercept differs by 170Ω. Assuming that either of the two measurements (shorts in and shorts out) could give Z_x different from the true value, the error is found by adding the possible systematic error for each curve in quadrature. Then, $\Delta Z_x = \sqrt{(\Delta Z_x^{in})^2 + (\Delta Z_x^{out})^2} = \sqrt{2} \times 170$, and $Z = \sqrt{(Z_x \pm \Delta Z_x)^2 + Z_y^2}$.

Another similar measurement of the machine impedance of ARF3 was done on a different day to check the reproducibility of the results. The systematic error during this study period was less, as can be seen in figure 3.13. Here the magnitude response of two independent, identical measurements are overlaid. The bottom plot of the figure shows the complete traces with the amplitudes on a linear scale, and the top shows only the central portion of the traces (also on a linear scale) in order to better show the difference between the two traces. While the same type of systematic error as shown in figure 3.7 is present, the effect is much less. Since the source of the systematic error is unknown, the cause of the reduction of systematic error during

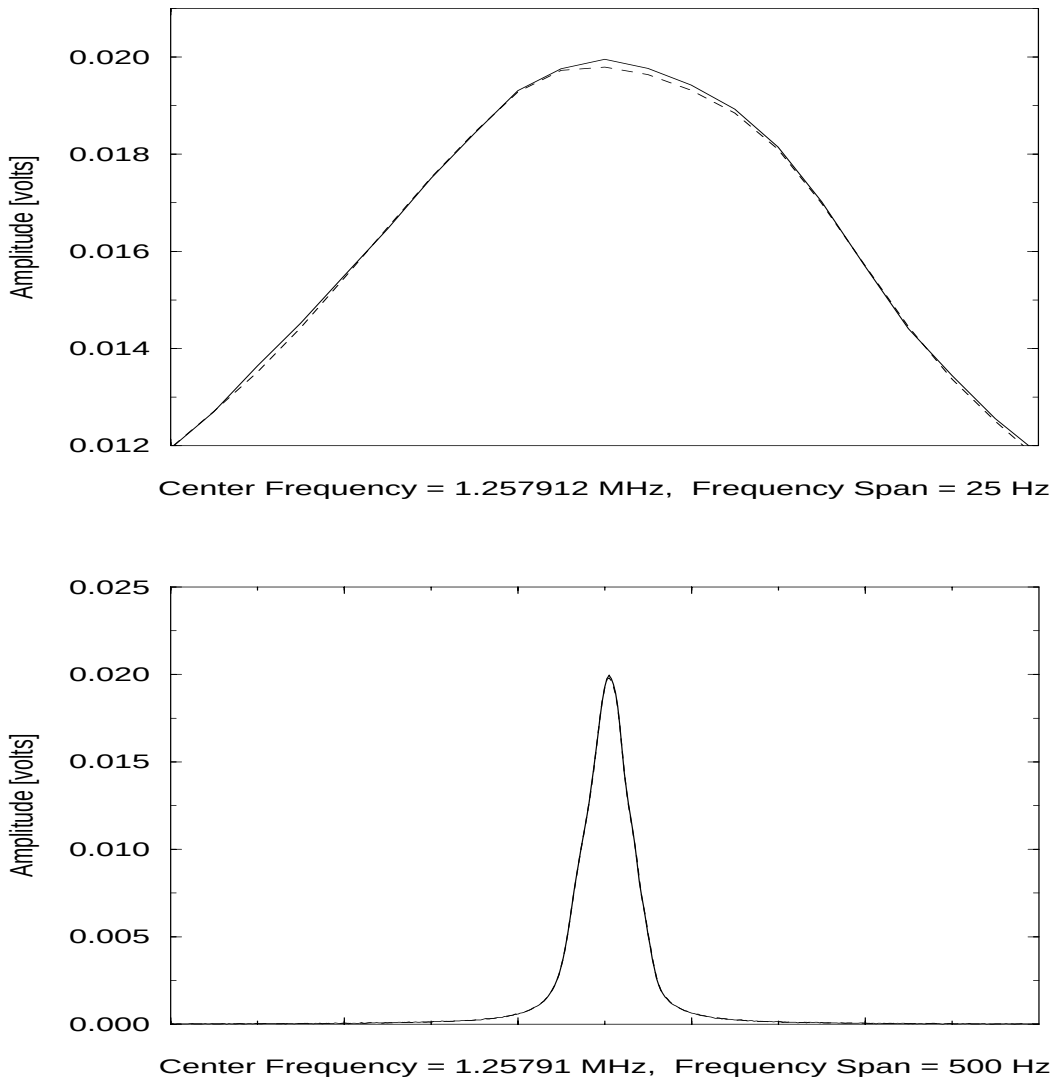

Figure 3.13: The Magnitude response of two independent, identical beam transfer function measurements taken during the same study period. The bottom plot shows the amplitude of the response on a linear scale, and the top plot is a close-up of the central region of the bottom plot. The curve from the first measurement is solid, and from the second measurement is dashed. At the time of these scans, the beam intensity was $I_0 = 81$ mA, and the beam energy sigma was $\sigma_\varepsilon = 2.5$ MeV.

the second study period is also unknown. The beam characteristics, the gain of the experimental setup, and the frequency span of the measurement are known differences between the first and second study period. During the second study period, there was more gain in the system, primarily due to the removal of a 20 dB attenuating pad from the network analyzer output. The beam intensity was higher (81 mA), and the energy spread of the beam larger (2.5 MeV). The frequency span of the network analyzer was 500 Hz instead of 100 Hz, but the number of measurement points in the scan remained the same.

Impedance curves for the cases of 'cavity shorts in' and 'cavity shorts out' obtained during the second study period are shown in figure 3.14. The theoretical stability boundary appropriate for the beam conditions is also shown. The results of the two study periods agree within the range of the systematic error.

The range of impedances for which a machine is stable depends on the beam size and intensity. A quantitative example of how beam size changes the range of allowable impedances in the Accumulator is shown in figure 3.15. There are two measured impedance curves in this figure, the inner one from a transfer function measurement taken under normal conditions, and the outer one from a measurement taken 1.33 hours after the core momentum stochastic cooling system had been turned off. The beam energy sigma with the cooling system on was $\sigma_\varepsilon = 2.74$ MeV, while with the cooling off it was $\sigma_\varepsilon = 4.86$ MeV. The larger, uncooled beam is much more tolerant of machine impedances. It is also more Gaussian, as indicated by the better fit between the measured curve and the calculated stability boundary.

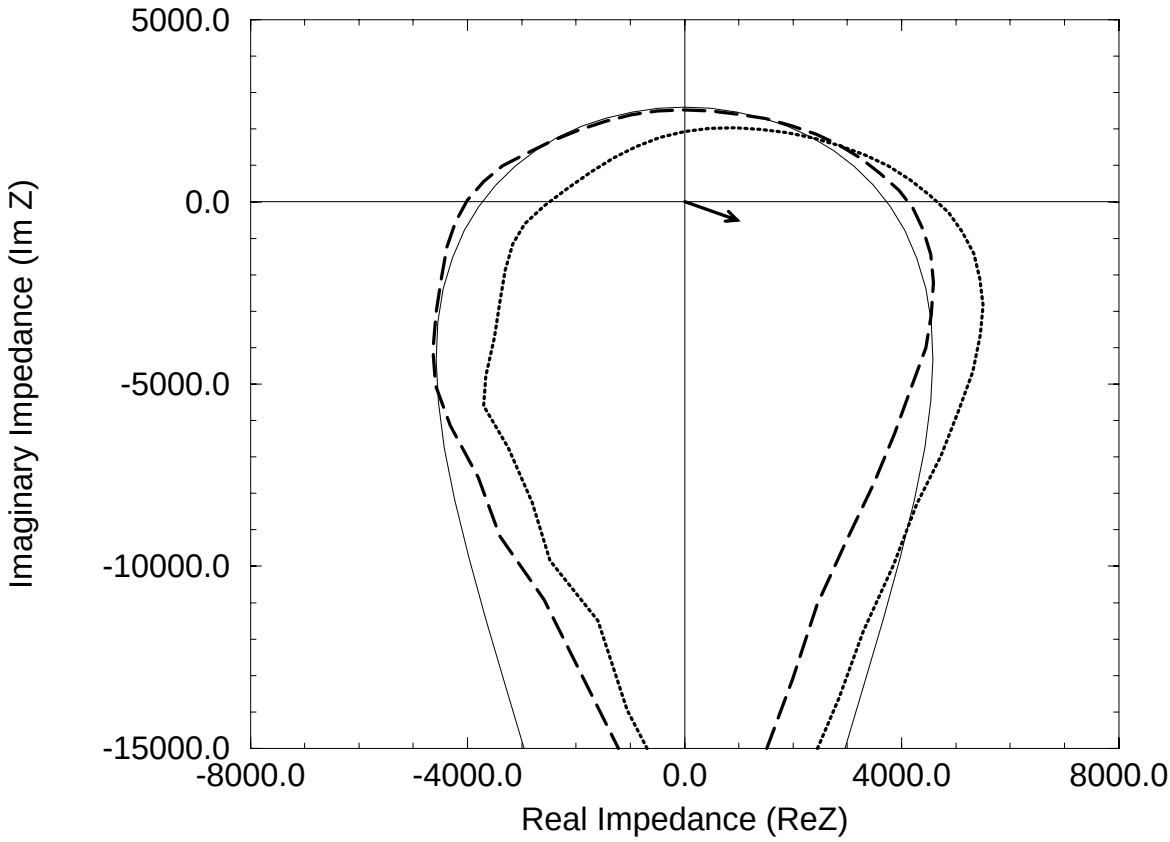

Figure 3.14: Calibrated impedance curves of measured data with ARF3 cavity shorts in (dashed curve) and with cavity shorts out (dotted curve). The solid curve is the stability boundary from the linear dispersion relation. The origin of the response curve with the shorts out is shifted by approximately (x,y)=(980,-490), which gives an ARF3 cavity impedance of $Z/n = \sqrt{(980 \pm \sqrt{2} \times 20)^2 + 490^2}/2 = 550 \pm 9\Omega$, at a phase angle of $-27°$.

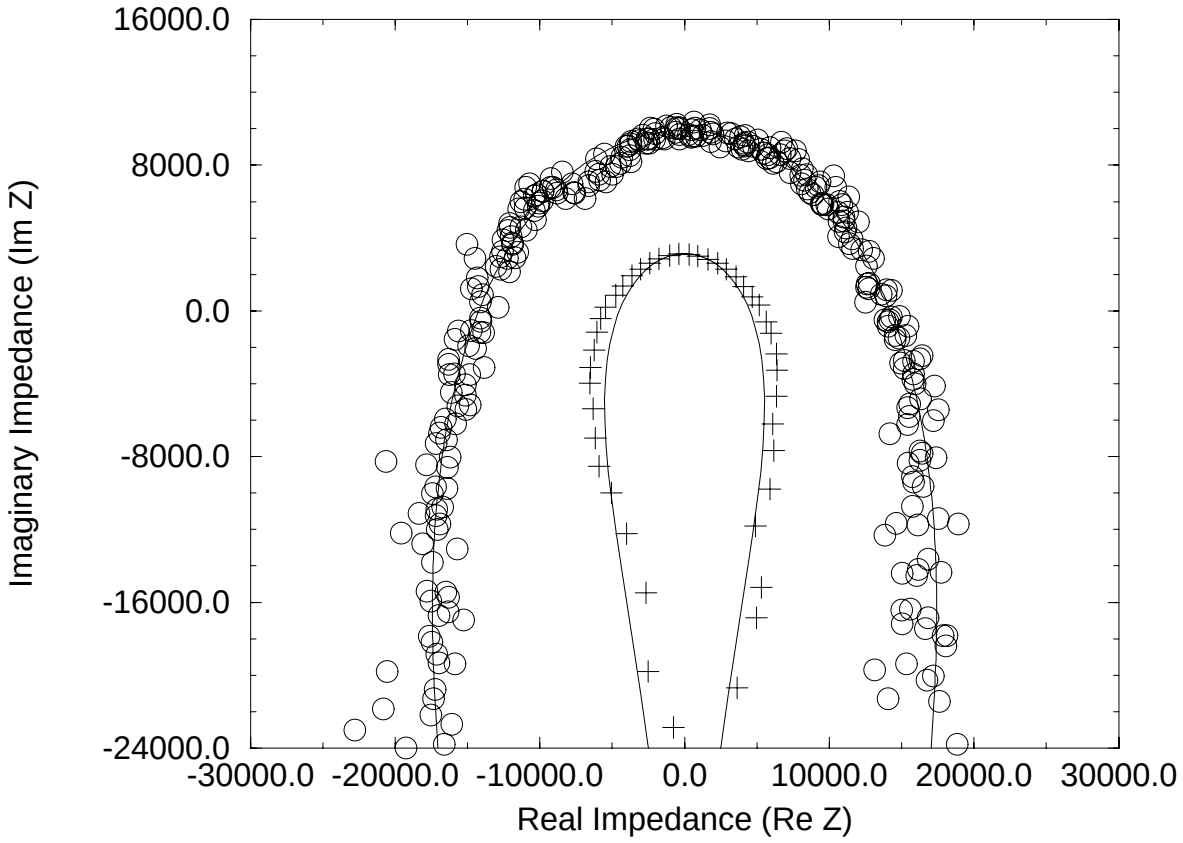

Figure 3.15: Calibrated Accumulator impedance curves at $h = 2$ measured when the momentum cooling was on (inner curve) and after it had been off for 1.33 hours (outer curve). When the cooling was on, the beam energy sigma was $\sigma_\varepsilon = 2.74$ MeV. When the cooling was off, $\sigma_\varepsilon = 4.86$ MeV. The beam intensity was 80 mA. The solid lines are the corresponding stability boundaries calculated from the dispersion relation.

3.4 Impedance measurements at the 84th harmonic

The Accumulator also has an RF system at $h = 84$, ARF1, which is off during the studies described in this work. However, ARF1 also has removable cavity shorts, allowing the opportunity to try to measure the cavity impedance with the same technique as used for ARF3. This is a more difficult measurement because ARF2 is still used as the kicker, and its frequency response has rolled off at $h = 84$ (see figure 3.3). Also, the signal to noise ratio gets worse at higher frequencies. Two preliminary attempts at this measurement were made. The first, shown in figure 3.16, was done with a low enough drive power on the kicker to avoid disturbing the beam distribution (as is usually done). The result was quite noisy, and multiple measurements should have been averaged for better precision. Since this was not the case, the calculated impedance is less reliable than the $h = 2$ measurement. The second measurement attempt was done with too much drive power, disturbing the beam distribution. As figure 3.17 shows, in this case the response curve does not fit the calculated stability boundary well. The same fitting technique was used, but the magnitude offset had to be a bit smaller than the difference at the center frequency, due to the small notch created in the center of the beam distribution at the time of the measurement. The notch was caused when some of the particles close to the center frequency were moved by the drive power to enhance one side of the beam distribution. This causes an asymmetry of the measured response with respect to the stability boundary which is not due to machine impedance. It may still be possible to sort out this asymmetry from the offset due to an impedance, since the lower power measurement shows the 'shorts in' response to be centered on the origin. However, since it is more difficult to do a reasonable fit to the stability boundary, the impedance result once again lacks

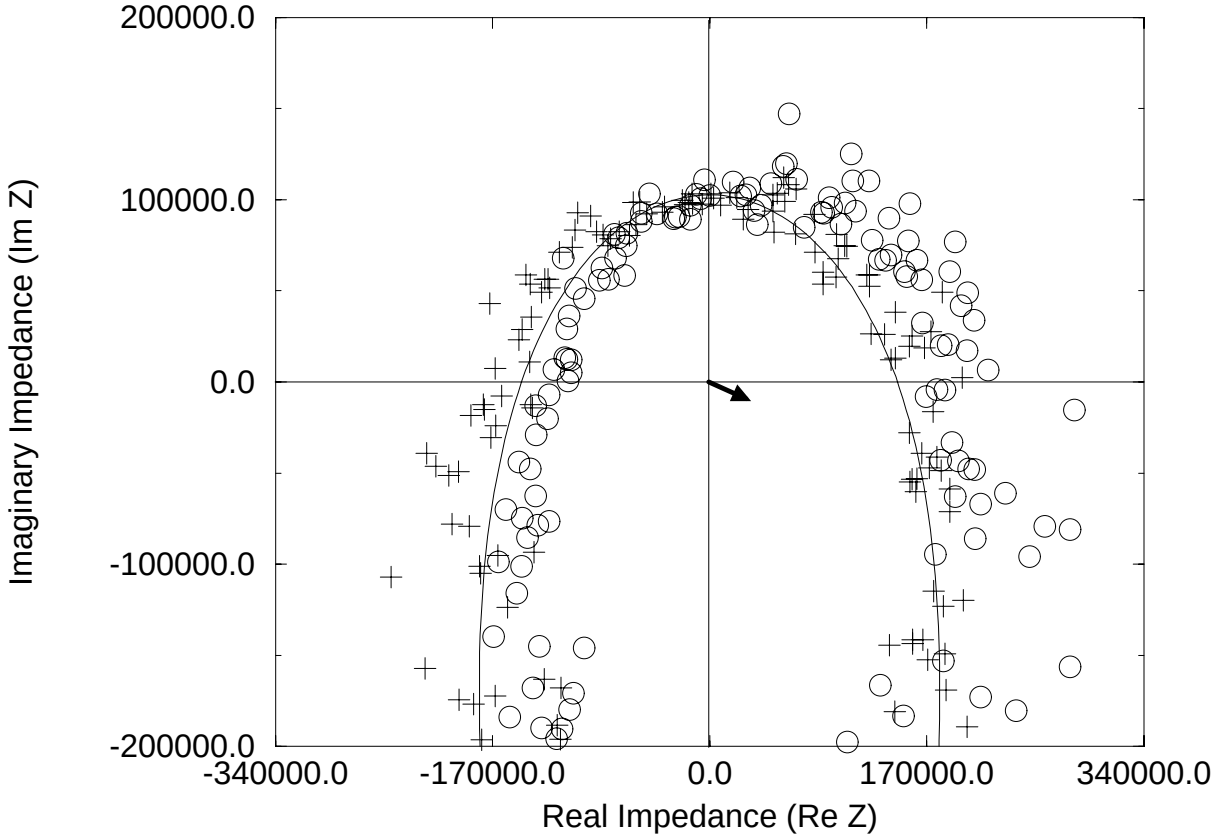

Figure 3.16: Noisy low power impedance measurement of ARF1. Calibrated response curves of measured data with ARF1 cavity shorts in (crosses) and with cavity shorts out (open circles). The solid curve is the stability boundary from the linear dispersion relation. The origin of the response curve with the shorts out is shifted by approximately (x,y)=(29700,-9400), which gives an ARF1 cavity impedance of $Z/n = \sqrt{29700^2 + 9400^2}/84 = 400\Omega$, at a phase angle of $-18°$.

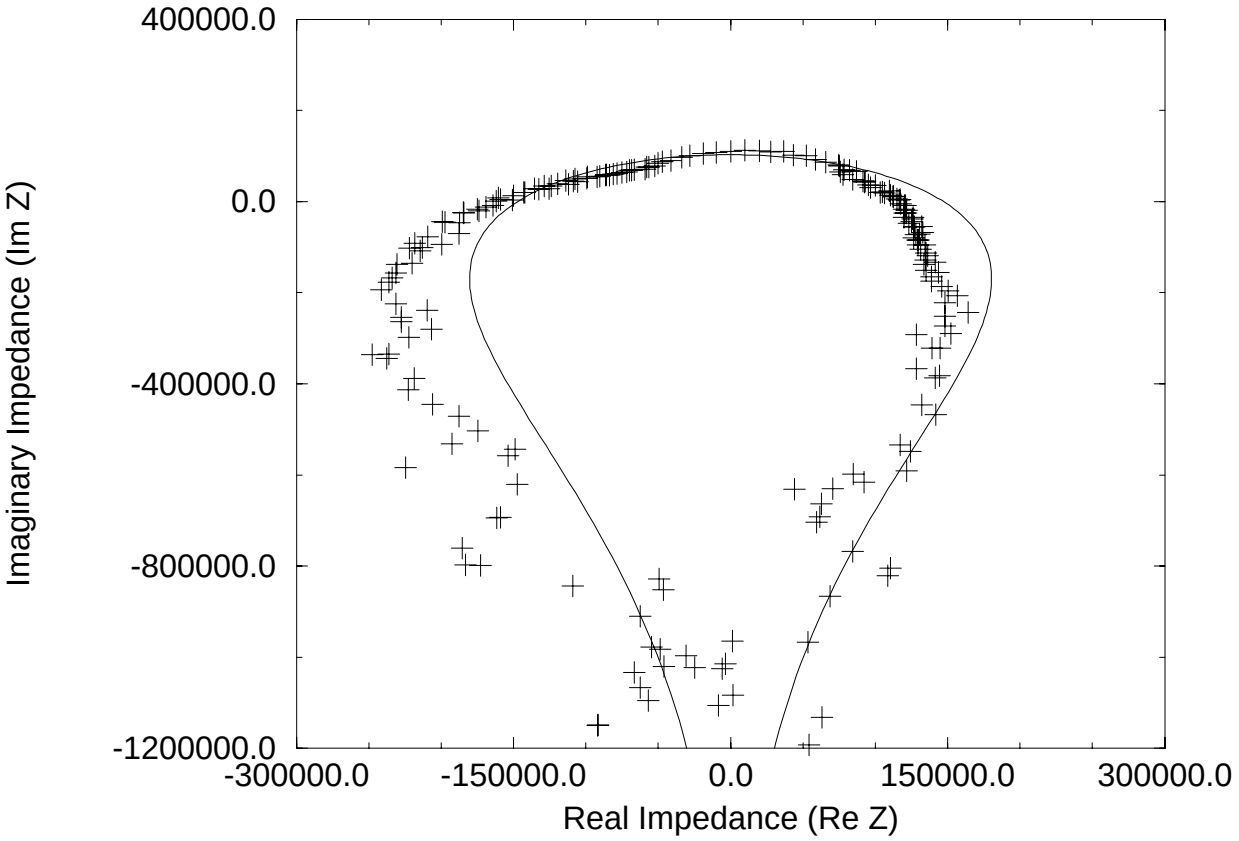

Figure 3.17: An attempt to fit a distorted response curve (crosses) taken at $h = 84$ to the theoretical stability boundary. The distortion was due to excessive drive power used for the measurement. Beam parameters: $I_0 = 81$ mA and $\sigma_\varepsilon = 2.4$ MeV.

precision. The higher power impedance measurement is shown in figure 3.18. The value for Z/n indicated by the higher power power measurement was 600Ω, that for the lower power measurement was 400Ω, while 760Ω was the value extracted from an R/Q measurement of the cavity [33]. The distortion of the beam distribution by the external voltage during the measurement is a good example of the relative ease with which nonlinearities can arise in a beam. There has been an energy exchange between the voltage wave and the particle distribution which resulted in heating of the distribution. Particles in the center of the distribution were matched in frequency to the applied voltage wave, which was directly on the harmonic. These particles were thus able to maintain a constant phase relationship with the voltage wave, and were consequently decelerated. Deceleration shifted the frequency of these particles upward (the Accumulator is above transition), leaving a notch at the vacated center frequency. Although in this case the voltage wave was externally applied, essentially the same dynamics occur when the nonlinear wave-particle interaction is due to a wakefield voltage.

Transfer function measurements of the Accumulator give every indication of a stable, low impedance machine. This helps clarify why it was difficult to trigger parametric coupling, on the one hand, and to get clean echo measurements on the other. As seen in chapter 4, measurements of this type paint a very different picture of stability in the Main Ring.

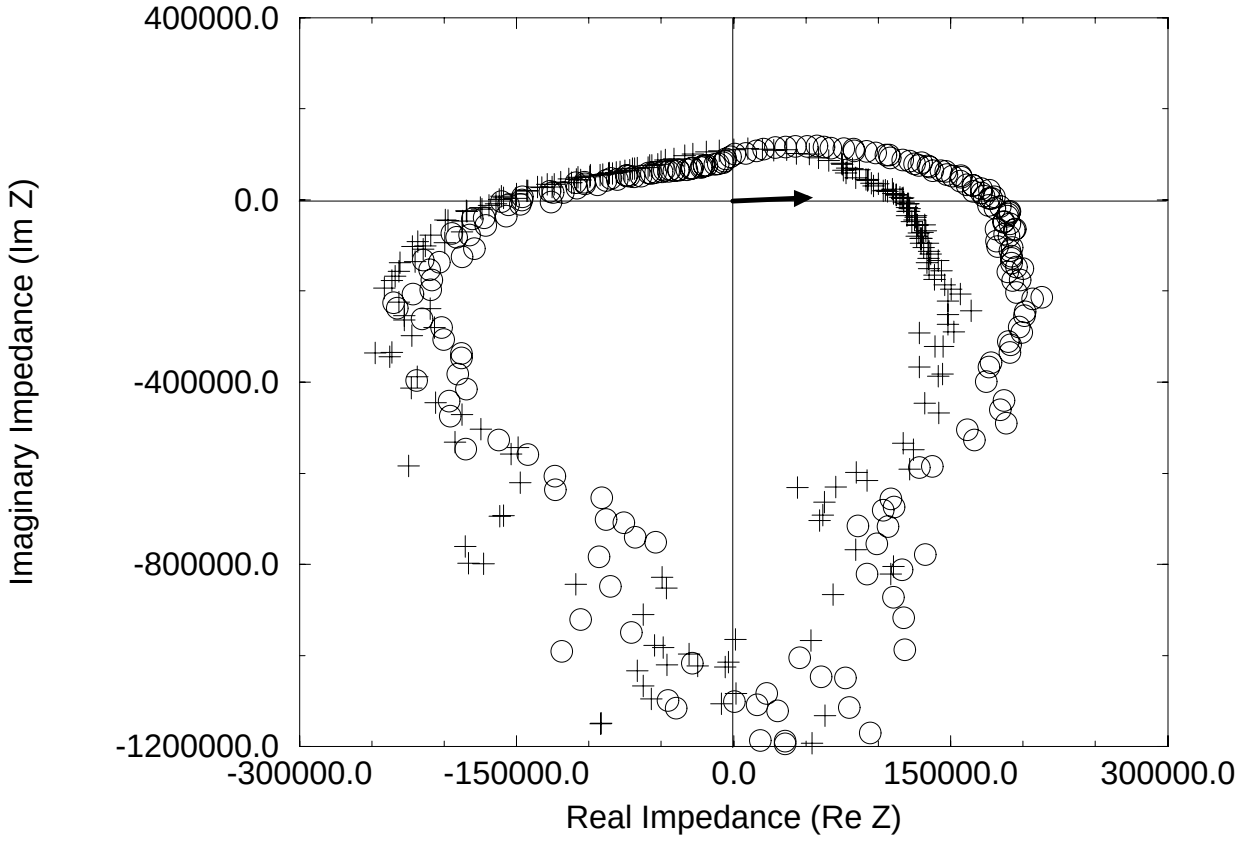

Figure 3.18: Higher power impedance measurement of ARF1. Calibrated response curves of measured data with ARF1 cavity shorts in (crosses) and with cavity shorts out (open circles). The origin of the response curve with the shorts out is shifted by approximately (x,y)=(51500,-6300), which gives an ARF1 cavity impedance of $Z/n = \sqrt{51500^2 + 6300^2}/84 = 600\Omega$, at a phase angle of $7°$.

Chapter 4

Main Ring beam transfer function measurements

4.1 Introduction and overview

Once it was determined that a spontaneous series of parametric coupling events was not easily triggered in the Accumulator, the investigation moved to the Main Ring. The original observation had been in the Fermilab Tevatron, during which time it was noted that the frequency distribution of the beam was not smooth during transfer function measurements. Instead, there appeared to be 'notches' cut into the distribution at various frequencies. It was postulated by the original investigators that these regions of depletion in the particle phase space might be caused by localized resonances. Thus, before embarking on the parametric coupling experiments in Main Ring, transfer function measurements were done to determine the nature of the beam distribution. Once again the notches appeared, and a small series of studies was done

to investigate their origin. Those results are presented in this chapter.

The experimental setup for the frequency domain measurements is reviewed in section 4.2. This section also has information about the hardware, given as a series of short descriptions of the devices used in acquiring data during studies. There is some discussion of the frequency response of the major hardware components.

The experimental results for the frequency domain measurements are presented in section 4.3. The shape of the beam profile, as given by the magnitude response of the transfer function measurement, is examined under various circumstances. Investigations were made of the notch pattern as a function of machine tune (number of transverse oscillations per revolution), chromaticity (tune dependence on particle energy), and beam intensity. It should be noted that the notches were examined as a function of the set values of the tune and chromaticity, rather than of measured values. Therefore, the results should be considered as relative dependences, with little confidence in the absolute numerical value of the tunes and chromaticities.

The Main Ring proton synchrotron is normally used as an accelerator, which requires bunched beam. However, during these studies the energy was held fixed at the injection level, allowing the use of a stored, unbunched beam. An unbunched beam was used for all studies presented in this work. The machine was still cycled, beam being regularly injected and extracted. Study pulses were anywhere between 2 to 12 seconds. Most of the studies were done at low intensity, so that beam intensity and losses were consistent from pulse to pulse. Table 4.1 lists typical Main Ring beam parameters [35]. Referring to table 4.1, σ_ε is the standard deviation of a distribution which is assumed to be Gaussian, and E_0 is the particle energy at the center of the distribution. The standard deviation is related to the full-width at half-maximum by

Table 4.1: Main Ring Beam Parameters

Parameter	Value
Revolution Frequency f_0	47.450 kHz
Slip Factor η	9.7E-3
Total Particle Energy E_0	8.938 GeV
Typical Beam Energy Spread σ_ε/E_0	$3-5\times10^{-4}$

the proportionality $fwhm = 2.354\sigma$.

4.2 Experimental setup

The hardware setup for the Main Ring transfer function measurements is shown in block diagram form in figure 4.1. The beam transfer function measurements were S21 transmission coefficient measurements using a network analyzer with an attached s-parameter test set. Appendix A gives a general description of this measurement technique. The analyzer excited the beam longitudinally by applying a swept frequency sine wave to a broadband RF cavity. The resulting frequency content of the beam was monitored using a strip line type of longitudinal detector. The signal from this beam pick-up was directed to the return port of the network analyzer, completing the path needed for the measurement.

The major components in figure 4.1 will be described here. The frequency source for the transfer function measurements was an HP 8753C network analyzer with a frequency range of 300 kHz - 3 GHz and an attached HP 85047A s-parameter test set. After a long cable run, necessary due to the distance between the beam kicker and

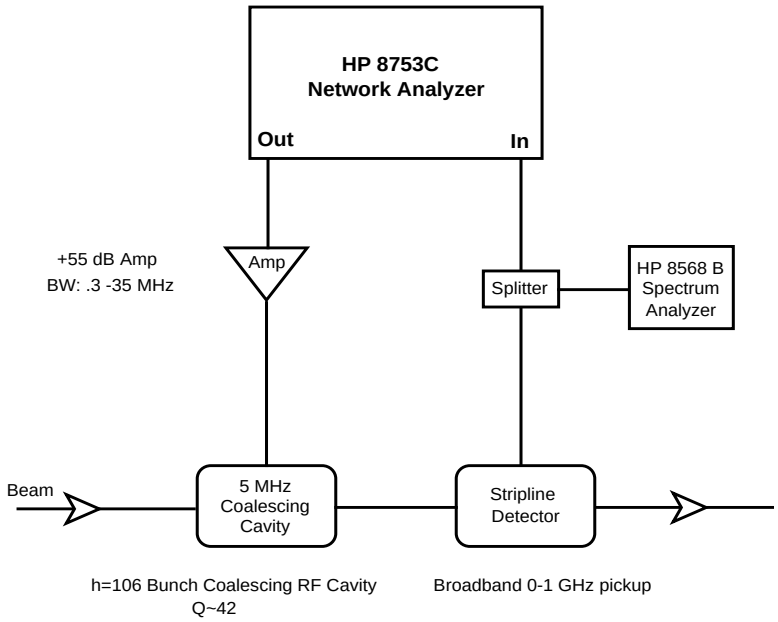

Figure 4.1: Block diagram of Main Ring transfer function measurement setup.

the available signal from the beam detector, the signal from the network analyzer was substituted for the normal 5 MHz signal at the input of the low level system for the cavity drive. The output of the low level system was amplified by a +55 dB amplifier having a frequency range of .3-35 MHz. This amplifier in turn drove the power amplifier and cavity in the accelerator enclosure.

The Main Ring 5 MHz coalescing cavity is a relatively broadband ($Q \sim 42$) RF cavity normally used in the process of combining 11 or so small 53 MHz bunches into one large 53 MHz bunch for collider physics [39, 40]. The center frequency of the cavity is $h = 106$, or 5.029 MHz. The cavity has 10 ferrites on either side of the accelerating gap. The gap is in parallel with a tunable capacitance, allowing fine control of the resonant frequency of the cavity. The +55 dB amplifier on the output of the low-level electronics drives a power amplifier, which in turn drives the 5 MHz

cavity to which it is attached.

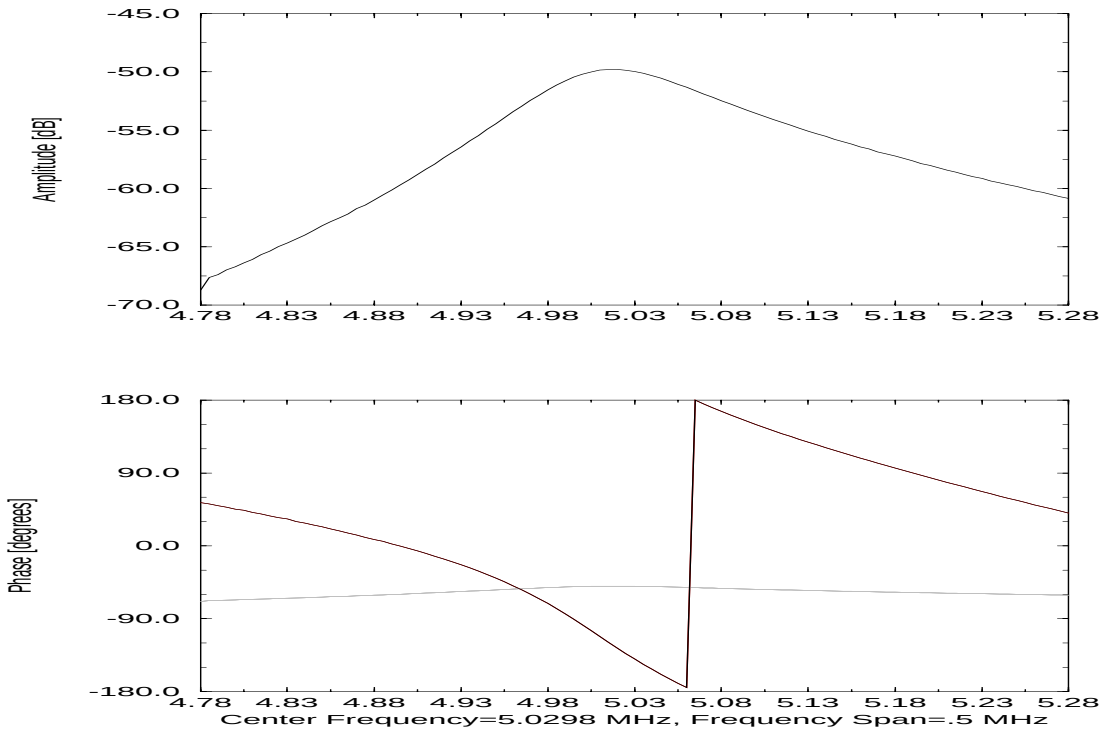

Figure 4.2: S21 measurement of coalescing cavity fanback, centered at h=106. Top plot is the magnitude response, and bottom plot is the phase response. Measurement made with no beam. Network analyzer setup: 30 dB attenuating pad on output, 101 data points, sweep time 10.4 sec, and resolution bandwidth 10 Hz.

The frequency response of the cavity was examined by doing a transfer function measurement where the output port of the network analyzer was used to drive the cavity, and the return port was the signal from the cavity fanback. The fanback calibration is 2031:1 accelerating volts to fanback volts [39]. The results of the transfer function measurement are shown in figure 4.2. The frequency span in this figure covers approximately 11 revolution harmonics. Although the coalescing cavity is relatively broadband, it does exhibit a resonant response, and so the Q of the cavity can be

determined from the s21 measurement. The bandwidth of the cavity response was found to be 119.6 kHz, giving $Q = f_0/BW = 42$.

The longitudinal beam pickup used was a quarter wave transmission line, consisting of two concentric stainless steel tubes [39]. Each end of the inner tube is connected to four signal ports via eight stainless steel connecting strips. Usually only the output terminals from one end are used to get a faster, shorter pulse. The quarter wave beam detector is 55.56 inches long, corresponding to a frequency of $f = c/\lambda = 53.1$ MHz. The detector impedance has nulls at $n\lambda/2$. The first null has an impedance of 3.2 Ohms, while the first maxima (at 53.1 MHz) has an impedance of 23.6 Ohms. Since there are 1113 harmonics between 0 and 53.1 MHz, the change in impedance over, say, 15 harmonics is small. The impedance of the detector increases linearly by .4 Ohms going from h=99 to h=113. The roll-off of the beam detector begins around 1.4 GHz.

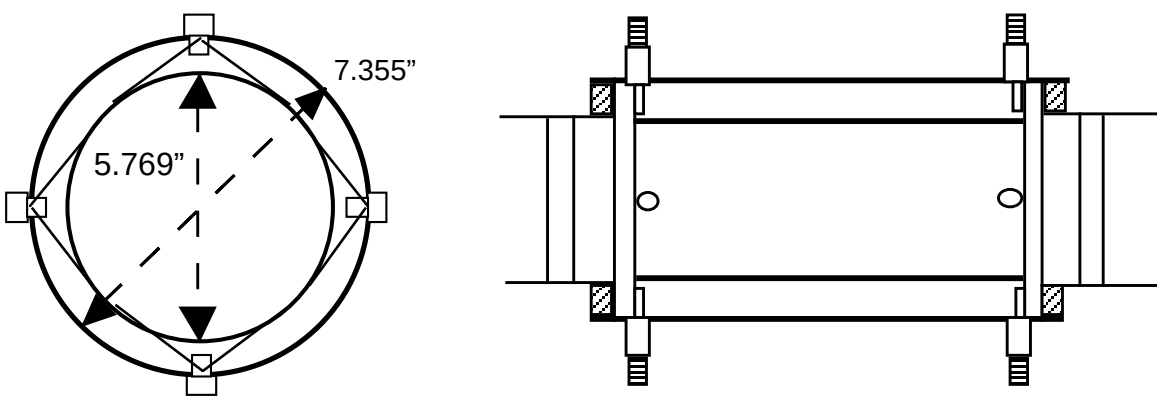

Figure 4.3: Conceptual idea for a strip line beam current monitor

4.3 Experimental results

Figure 4.4 shows a typical beam transfer function measurement at h=106 in the Main Ring. The center frequency of the scan was $106 \times f_0 \simeq 5.0298$ MHz. The

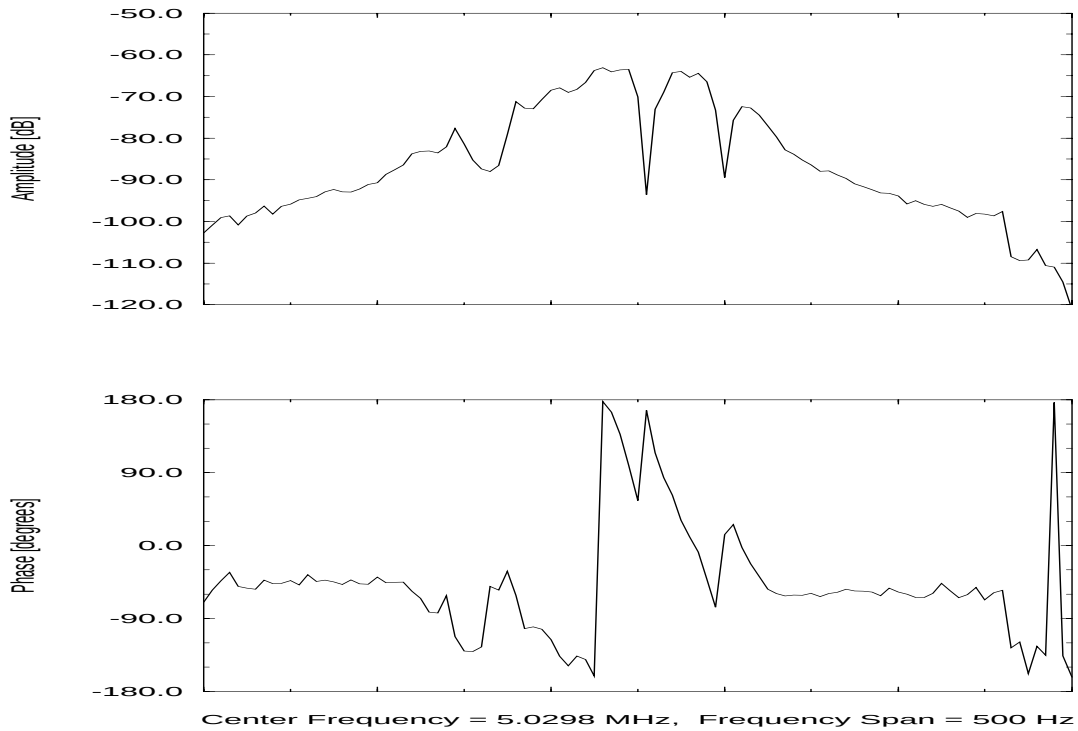

Figure 4.4: S21 measurement at $h = 106$ in the Main Ring. The top plot is the magnitude response, and the bottom plot is the phase response. The beam intensity was 1.85×10^{12} protons per pulse. Network analyzer setup: averaged 10 times, 101 data points, sweep time 10.41 sec, and a resolution bandwidth of 10 Hz.

magnitude response is not a nice, smooth curve such as one gets in the Accumulator (see figure 3.5). Here instead there are deep holes or notches at certain frequencies in the sweep. These notches are not manifestations of a noisy measurement, as they do not go away with averaging or as the power is increased. Thus, the notches

must correspond to regions of particle depletion in the beam distribution. The sharp drops in population occur at certain frequencies which, since the beam in unbunched, correspond to specific particle momenta. The momentum dependence of the notches implies that specific driving resonances are responsible for the depletion zones. These could easily be transverse resonances, since there is a correspondence between particle momentum and the number of transverse oscillations per circuit around the machine (betatron tune), due to chromatic effects from the magnets. An investigation to check whether the notches are related to particle tune was undertaken.

One study was to examine whether the pattern of notches was tune dependent by varying the horizontal tune setting and then taking transfer function measurements. As Main Ring is a pulsed machine, beam was re-injected after each tune change, so each scan reflects only one tune setting. There was a repeatable correlation between the tune setting and the pattern of notches. Transfer function measurements taken after adding various offsets to the base tune setting of 19.42 are shown in figure 4.5. There are four different plots showing the results of four tune offsets. Each of these plots has two traces made with the same tune offset, but taken during different study periods on different days. These results show that the shape of the curves was fairly reproducible, those with the same tune settings were similarly shaped. In contrast, as seen in figure 4.6, transfer functions taken at different tune offsets were often quite distinct. With some effort, perhaps specific resonances could be mapped to notches in the transfer function, providing an alternative to the standard technique for identifying coherent betatron frequencies present in the beam.

While the tune setting controls the average tune of the ensemble of particles comprising the beam, the chromaticity setting controls the spread in tunes within the

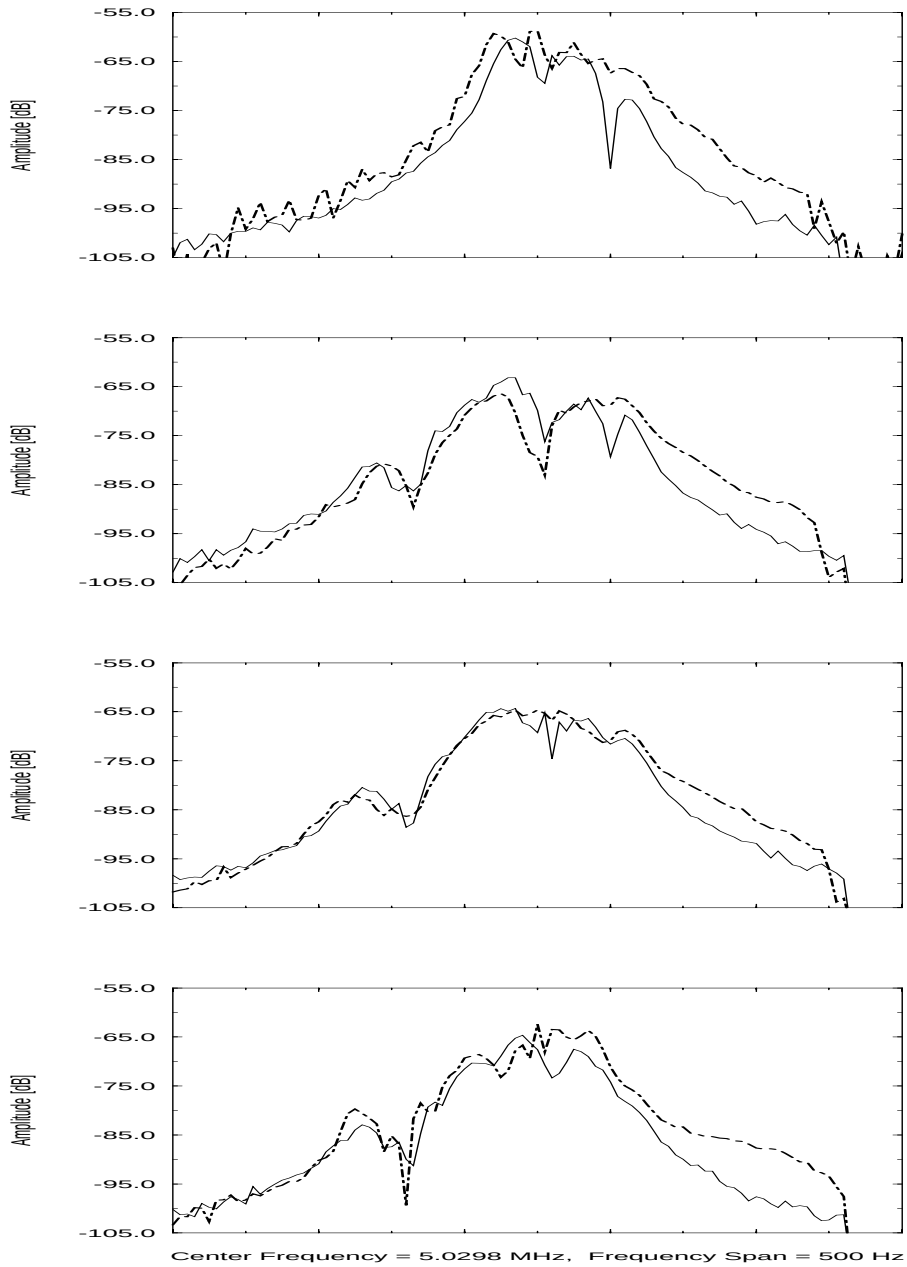

Figure 4.5: Magnitude response measurements taken in the Main Ring with various horizontal tune settings. From top to bottom, the tune offsets were +.04, +.02, 0, and -.04. The two traces of each plot were taken in different study periods.

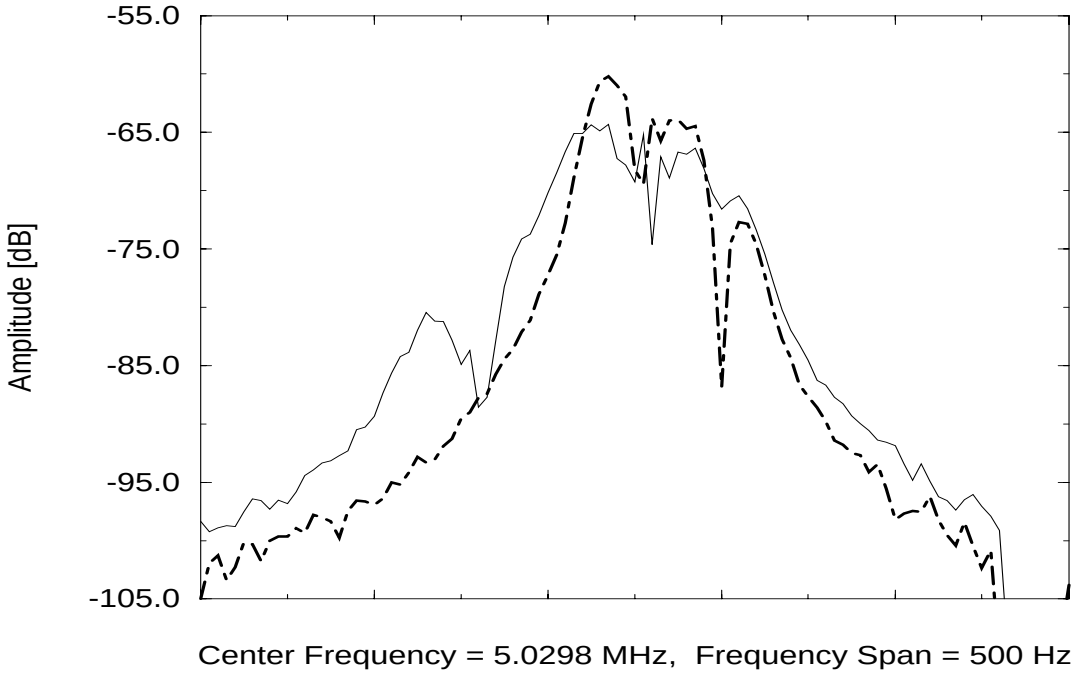

Figure 4.6: Magnitude response measurements taken in Main Ring with horizontal tune offsets +.04 (dashed line) and .00 (solid line) added to the normal tune setting. Network analyzer setup: 10 averages, 101 points, resolution bandwidth 10 Hz, sweep time 10.413 seconds.

distribution of particles. Chromaticity determines the proportionality between the momentum spread of the beam and its transverse tune spread. If each depletion region in the particle distribution corresponds to a different transverse driving resonance, then the chromaticity of the machine should affect the number of resonances which fall within the distribution.

A second study examined the relation between the chromaticity setting and the shape of the magnitude response of the beam transfer function. The results are shown in figure 4.7, where each of the four plots displays the magnitude response for different chromaticity settings. In the bottom plot, notches eat deeply into the beam distribution. The situation gets progressively better going from the bottom to the top plot of the figure. Although the injected beam intensity was the same in each case, the extracted beam intensity was greater when the magnitude response was cleaner, as expected if the notches are due to resonances. The average injected beam intensity was $I_{inj} = 3.3 \times 10^{12}$ protons per pulse (ppp), which is 25 mA of current (for the Main Ring $1 \times 10^{12} = 7.6$ mA). For the top plot, the horizontal and vertical chromaticity settings were $(C_H, C_V) = (+8, -8)$, and the average extracted beam intensity was $I_{ext} = 1.5 \times 10^{12}$ ppp. For the next three plots in order, the chromaticity settings were $(C_H, C_V) = (0, 0)$, $(C_H, C_V) = (-7, +6)$, and $(C_H, C_V) = (-15, +14)$; while the average extracted beam intensities were $I_{ext} = 1.4 \times 10^{12}$, $I_{ext} = .7 \times 10^{12}$, and $I_{ext} = .8 \times 10^{12}$ ppp.

In a third study, the magnitude of the response was examined as the injected beam intensity was varied, with all other machine conditions remaining the same. The results are shown in figure 4.8. The four plots from top to bottom had injected intensities of $I_{inj} = .6 \times 10^{12}$, $I_{inj} = 1.8 \times 10^{12}$, $I_{inj} = 2.2 \times 10^{12}$, and $I_{inj} = 3.0 \times 10^{12}$

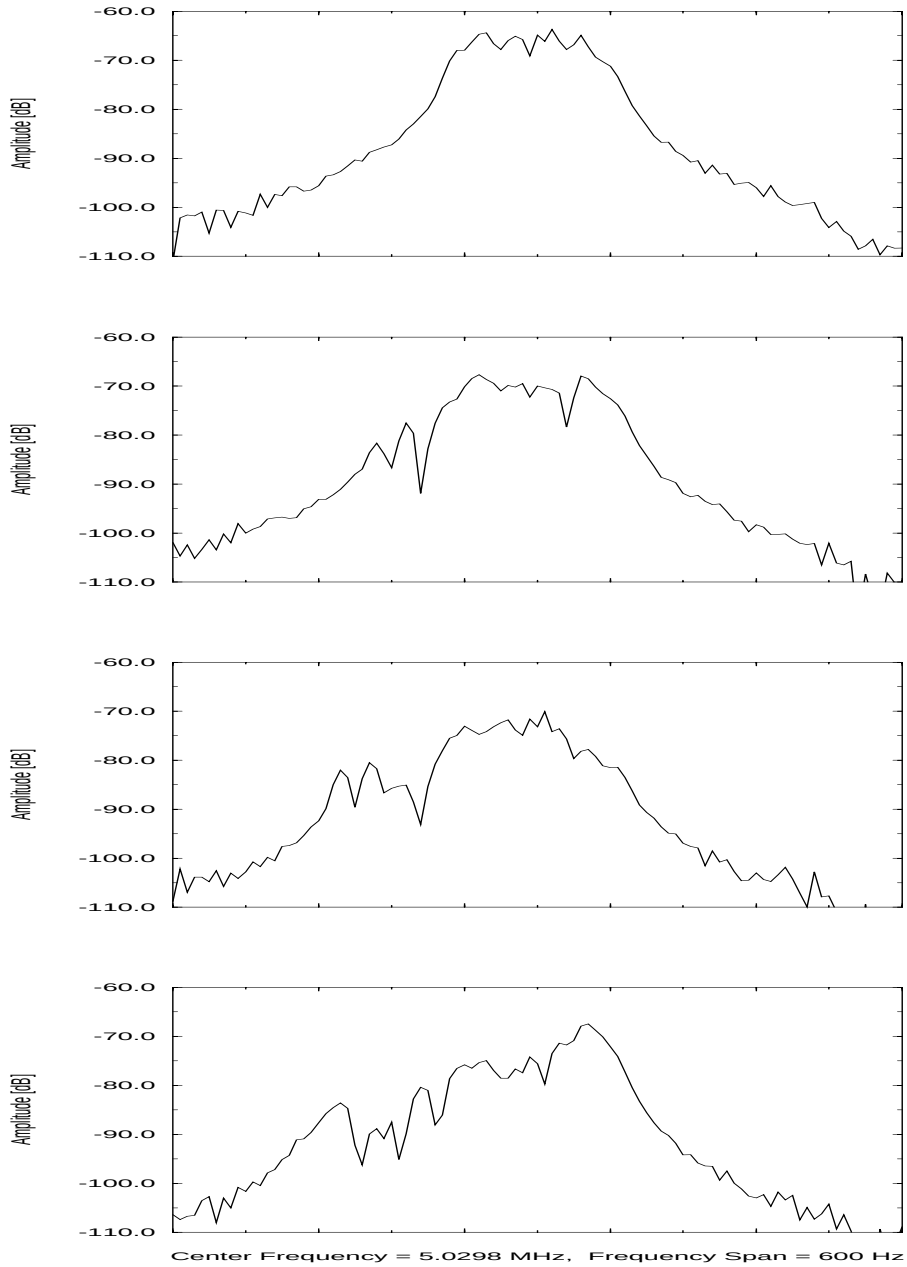

Figure 4.7: Magnitude response measurements taken in Main Ring with various chromaticity settings. From top to bottom: $(C_H, C_V) = (+8, -8)$, (0, 0), (-7, +6), and (-15,+14). These chromaticities were set, but not measured.

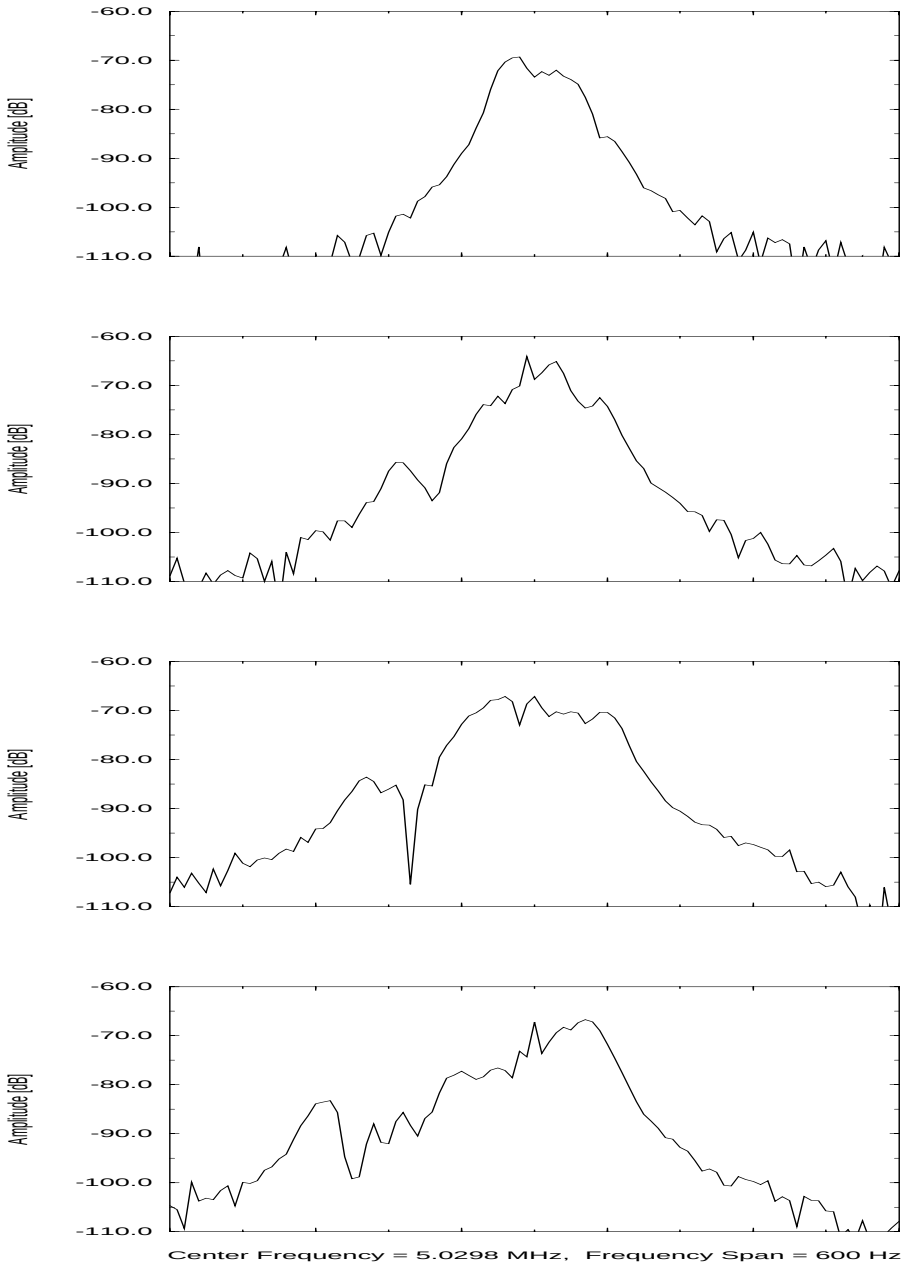

Figure 4.8: Magnitude response measurements taken in Main Ring with various injected beam intensities. From top to bottom: $I_{inj} = .6 \times 10^{12}$, $I_{inj} = 1.8 \times 10^{12}$, $I_{inj} = 2.2 \times 10^{12}$, and $I_{inj} = 3.0 \times 10^{12}$ ppp.

ppp; with efficiencies of 58%, 40%, 46%, and 26%. That the efficiencies went down as the injected intensities went up may be expected, but it is interesting to see what happened to the magnitude response. As the injection intensity increased, the momentum width of the beam also increased, and the notches became more pronounced and greater in number. Probably the additional resonances encompassed by the larger tune spread contibuted to beam loss. In addition to the increase of momentum width with intensity, the beam distribution became increasingly asymmetric. It is possible that an instability developed at the higher intensities, with the self-field voltage wave gaining energy by virtue of beam heating.

Since the momentum distribution of the particles in the beam is not smooth, the impedance curve generated from the transfer function measurement also is not smooth. The magnitude portion of a typical s21 measurement in Main Ring and the associated impedance curve is shown in figure 4.9. The points on the magnitude curve in the notches are marked with special symbols, and these map one to one into the corresponding symbols in the loops of the response curve in the impedance plane. These loops correspond to unstable regions in the longitudinal phase space, but longitudinal impedance does not drive these instabilities. It is no longer a simple matter to use the response curve as an indicator of machine impedance. As will be shown in the next chapter, according to the theory for parametric coupling, the likelihood of coupling occurring is highly sensitive to the momentum width of the beam. The presence of notches in the beam distribution considerably lowers the threshold for nonlinear, or parametric coupling.

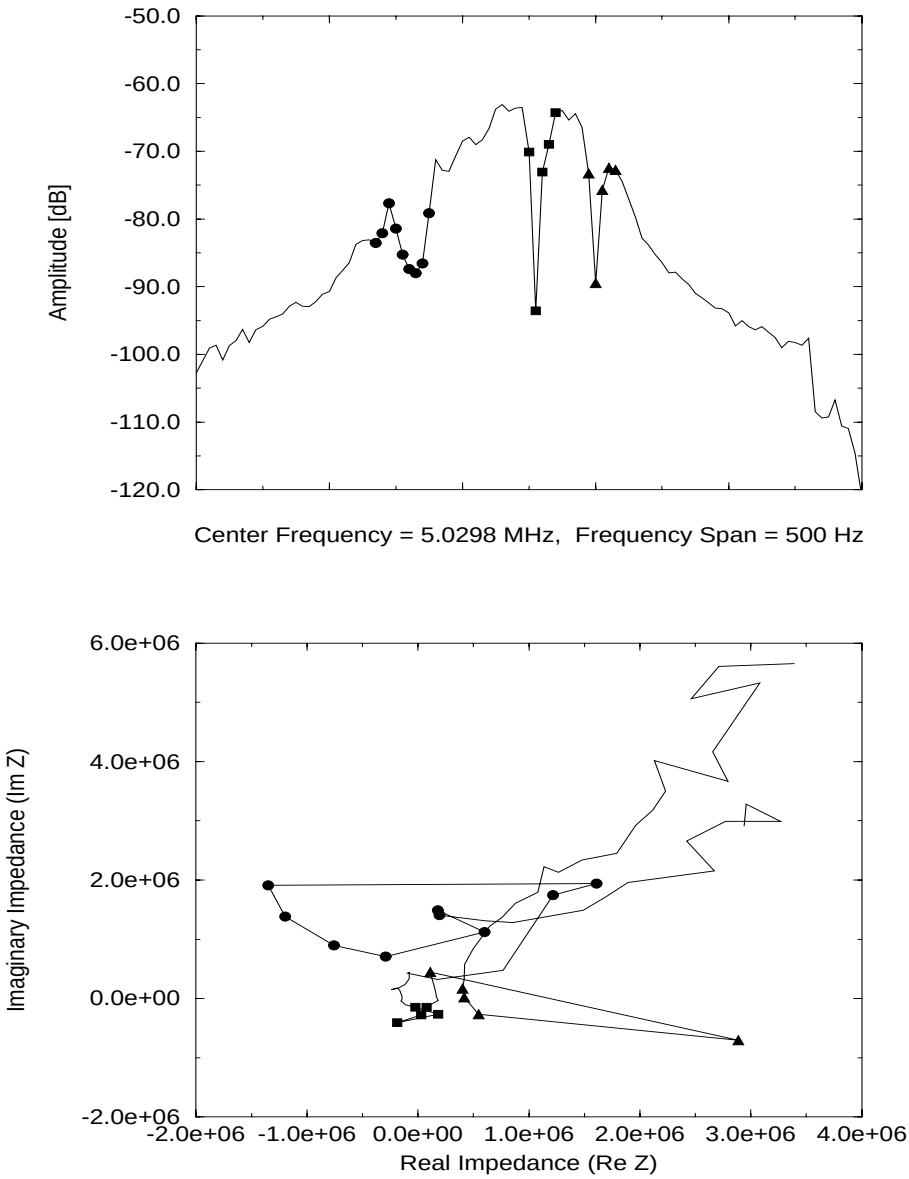

Figure 4.9: Magnitude response from a typical transfer function measurement in Main Ring (top plot) and its mapping into the impedance plane (bottom plot). The notches in the magnitude response (marked with symbols) map into loops in the impedance curve (marked with the same symbols).

Chapter 5

Theory of parametric coupling

5.1 Introduction and overview

Parametric coupling is, in essence, when energy supplied to a system at one frequency is converted into energy at another frequency through the agency of frequency mixing [41]. This wave-wave coupling is considered to be the first stage in the advent of coherent nonlinear phenomena in the system of a particle beam and storage ring. Parametric coupling is widespread and has been studied extensively in such disciplines as electronics and plasma physics. Parametric coupling has now also been observed in the realm of high energy beams; three-wave coupling of longitudinal modes has been seen in the Fermilab Main Ring. Power present in the beam at one frequency was transferred into coherent excitation at another frequency, via modulation from a third frequency. Once initiated, this three-wave coupling process happened multiple times, creating a cascade of coherent excitations at successively lower harmonics. The theoretical framework to describe parametric coupling in beams closely follows that

developed for plasma physics, as in both cases the Vlasov formalism is used to model the dynamics of the system.

The wave carrying the supplied energy is called the pump wave. In systems where damping exists, the energy supplied by the pump must cross a threshold if coupling is to occur. Once in progress, the parametric transfer of energy can deplete the energy available from the pump, and the system remains near threshold. There are other conditions which must be satisfied if resonant coupling is to occur. The frequencies and phases of the three waves involved must obey the following sum rules,

$$\omega_m = \omega_n + \omega_k \tag{5.1}$$

$$\phi_m = \phi_n + \phi_k \tag{5.2}$$

where m, n, and k are integers identifying the mode numbers of the three waves involved in the coupling. The phase matching condition, eq. 5.2, may be written as a simple integer relation ($m = n + k$ instead of $\phi_m = \phi_n + \phi_k$) due to the periodicity of a storage ring.

The interpretation of these sum rules depends on the physical situation. For example, the pump wave with frequency ω_m may decay parametrically, transferring energy into two daughter waves with frequencies ω_n and ω_k. Another possibility is that the pump wave with frequency ω_n combines with another coherent excitation of frequency ω_k to build up a third wave of frequency ω_m.

The sum rules are manifestations of fundamental conservation laws. The frequency sum rule is a consequence of the conservation of energy, while the phase sum rule is a consequence of the conservation of momentum. This relationship will

be demonstrated in section 5.5, following closely techniques used by Davidson and Sitenko [10, 9].

Three-wave coupling cannot be described by the first order linearized Vlasov equation. In a perturbative treatment of the Vlasov equation, a frequency mixing term of second order must be retained in order to have a valid description of these beam dynamics. Repeating the Vlasov equation here for reference,

$$\frac{\partial f}{\partial t} + \dot{\theta}\frac{\partial f}{\partial \theta} + \dot{\varepsilon}\frac{\partial f}{\partial \varepsilon} = 0$$

Proceeding as in section 2.4, the beam distribution function, f, and the energy change per turn, $\dot{\varepsilon}$, are written as longitudinal mode expansions,

$$\begin{aligned} f &= f_0(\varepsilon) + \sum_{m\neq 0} f_m(\varepsilon, t)e^{im\theta} \\ \dot{\varepsilon} &= \frac{e\omega_0}{2\pi}\sum_{m\neq 0} U_m e^{im\theta} \end{aligned}$$

where U_m is the amplitude of the voltage change per turn due to the perturbation at mode m, ω_0 is the angular revolution frequency, and e is the elementary charge. Upon substitution of these expansions into the Vlasov equation, an expression for a particular mode m is obtained. However, rather than linearizing the equation by keeping only first order terms, the frequency mixing term is now retained.

$$\frac{\partial f_m}{\partial t} + im\omega(\varepsilon)f_m + \frac{e\omega_0}{2\pi}\frac{\partial f_0}{\partial \varepsilon}U_m + \frac{e\omega_0}{2\pi}\sum_{n+k=m} U_n\frac{\partial f_k}{\partial \varepsilon} = 0 \tag{5.3}$$

where $\omega(\varepsilon) = (\omega_0 + k_0\varepsilon)$, with k_0 being the constant defined in eq. 2.2. The dynamics of mode m are described by eq. 5.3. The first two terms of this equation directly contain the mth harmonic of the beam distribution, f_m. The third term represents coupling between the unperturbed beam distribution and a voltage at the frequency of the mth harmonic. The last term represents coupling between a perturbation in the beam distribution at mode k and a voltage at the frequency of mode n. It is now evident that the phase sum rule, $m = n + k$, is an intrinsic requirement coming from the inclusion of the frequency mixing term.

The voltage in the coupling terms of eq. 5.3 can either be experimentally applied from an external source, or it can be present in the machine environment due to the existence of wakefields. If U_n is an externally applied voltage, then the frequency mixing term describes source-mode coupling; whereas if U_n is a wakefield voltage, then the frequency mixing term describes mode-mode coupling. While the initial instance of mode coupling in the Main Ring began with an externally applied voltage, the ensuing series of coupling events was enabled by wakefields.

The linear dispersion relation obtained from the linearized Vlasov equation predicts whether there will be growth of a single mode based on the machine impedance and beam properties. The dispersion relation is a central tool in evaluating stability. It is similarly beneficial in evaluating stability with respect to coupling resonances to derive a second order dispersion relation. The threshold for mode growth as well as the frequency selection rule are embedded in such a dispersion relation. The assumption of weak 3-wave coupling leads to a new dispersion relation built from the linear dispersion relations of individual modes.

A dispersion relation for the process at resonance can be obtained mathematically,

starting with eq. 5.3, and proceeding in either of two ways. The method of section 5.3 follows R.C. Davidson, utilizing a multiple time scale perturbation expansion, and solving coupled second order equations by normal mode analysis to obtain the desired dispersion relation [10]. A perturbation expansion in the dependent variables alone may not be valid for all times, as there is no systematic method for removing secularities which cause the solution to diverge. Even if an exact solution is bounded, an expansion to finite order may not be bounded, since not all secular terms are represented and thus cannot cancel. Expanding in the time variable as well allows the removal of secular terms order by order in the expansion, insuring a uniform solution at all times [42]. In our case, the secular terms are the interesting ones since parametric coupling is a resonance condition. Mode growth due to three-wave coupling is represented by the secular terms in the second order equation. Identification of these terms yields the frequency selection rule given by eq. 5.1. Setting the sum of these terms to zero gives an expression for the growth rate, and is the platform from which the resonant dispersion relation for parametric coupling is obtained. The strength of this technique is in the acquisition of the growth rate equation, and the ease with which the resonant terms are identified.

Alternatively, the result presented in section 5.4 derives from a method which follows D.G. Swanson [43]. This method, which is fully developed in appendix B, begins by taking the Fourier transform of eq. 5.3, and making direct substitutions until both sides of the equation are written in terms of a perturbed current at the same mode number. Cancellation of this perturbed current then gives the dispersion relation. This result is more general than the dispersion relation found in section 5.3, which is valid only directly at resonance. The general result is useful in that it

contains a coupling coefficient which gives the likelihood of a parametric coupling event based on the impedance as well as other beam and machine parameters. Directly on resonance the impedance dependence cancels out of the dispersion relation. As shown in appendix B, when the more general dispersion relation is expanded around the resonant frequency, it is formally identical to that found in section 5.3.

Before embarking on the derivation of the second order dispersion relation for parametric coupling in particle beams, section 5.2 gives a mathematically simpler example inspired by Sagdeev and Galeev [2]. Using a pair of parametrically coupled mechanical pendula, the purpose of this section is to conceptually demonstrate some of the techniques in the following sections. A dispersion relation is first found using coupled equations and doing normal mode analysis. Although a perturbation expansion is not done, the solution is assumed to have two characteristic time scales, the natural oscillation periods of the pendula, and the slower period of the growth of the oscillation amplitude. Next, the dispersion relation is found by doing a Fourier transform of the equations of motion and using direct substitution to get an equation in one dependent variable. The equivalence of the dispersion relations at resonance is demonstrated. It may be useful to go through these mathematical methods without the additional symbolic overhead of the self-consistent Vlasov formulation. Since later material is not based on section 5.2, it may be skipped with no ill effect.

5.2 Simple example of mechanical pendula

Parametric coupling can occur in simple systems such as two mechanical pendula connected with a spring of variable spring constant. In this section, a dispersion

relation for the system depicted in figure 5.1 will be derived using two different methods. Two pendula, each having bob of mass m, are connected by a weak spring of

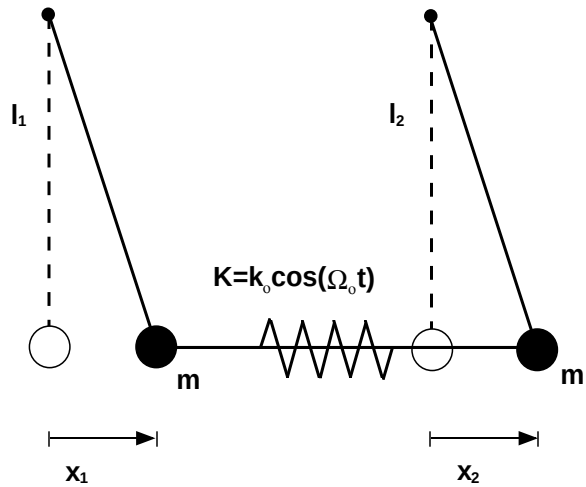

Figure 5.1: System of two parametrically coupled mechanical pendula

variable spring constant $k_0 \cos(\Omega_0 t)$. The first pendulum has length l_1 and its displacement from equilibrium is given by x_1. The second pendulum has length l_2 and its displacement is given by x_2. The Lagrangian for this system is the following,

$$\mathcal{L} = T - V = \frac{m}{2}(v_1^2 + v_2^2) - \frac{m}{2}(\frac{g}{l_1}x_1^2 + \frac{g}{l_2}x_2^2) - \frac{k_0}{2}cos(\Omega_0 t)(x_1 - x_2)^2 \tag{5.4}$$

The frequency of the first pendulum, ω_1 is given by $\omega_1^2 = \frac{g}{l_1} + \frac{k_0}{m}\cos(\Omega_0 t) \simeq \frac{g}{l_1}$, where the change in the natural frequency of the pendulum due to the spring is small and will be neglected. Similarly for ω_2. The equations of motion are given by Lagrange's equations,

$$\frac{d}{dt}\left(\frac{\partial \mathcal{L}}{\partial \dot{q_k}}\right) - \frac{\partial \mathcal{L}}{\partial q_k} = 0$$

For this system the equations of motion are then,

$$\begin{aligned}\frac{d^2x_1}{dt^2}+\omega_1^2x_1 &= \frac{k_0}{m}\cos(\Omega_0 t)x_2\\ \frac{d^2x_2}{dt^2}+\omega_2^2x_2 &= \frac{k_0}{m}\cos(\Omega_0 t)x_1\end{aligned} \tag{5.5}$$

Since the parametric coupling between the pendula is small, each pendulum will oscillate about its equilibrium position at its natural frequency, but the amplitude of the oscillation may change slowly due to the spring. Then the displacements of the pendula are of the form,

$$x_j = A_j(t)e^{i\omega_j t} + A_j^*(t)e^{-i\omega_j t} \tag{5.6}$$

Using the expression given by eq. 5.6, and writing the cosine function of the spring as $\cos(\Omega_0 t) = \frac{e^{i\Omega_0 t}+e^{-i\Omega_0 t}}{2}$, the first of equations 5.5 becomes,

$$\begin{aligned}\frac{d^2A_1}{dt^2}+2i\omega_1\frac{dA_1}{dt} &= -\left[\frac{d^2A_1^*}{dt^2}-2i\omega_1\frac{dA_1^*}{dt}\right]e^{-2i\omega_1 t}\\ &+\frac{k_0}{2m}A_2e^{i(\Omega_0+\omega_2-\omega_1)t}\\ &+\frac{k_0}{2m}A_2^*e^{i(\Omega_0-\omega_2-\omega_1)t}\\ &+\frac{k_0}{2m}A_2e^{i(-\Omega_0+\omega_2-\omega_1)t}\\ &+\frac{k_0}{2m}A_2^*e^{i(-\Omega_0-\omega_2-\omega_1)t}\end{aligned} \tag{5.7}$$

The result is similar for the second of equations 5.5, the only difference being that the indices are swapped.

The amplitudes A_j and A_j^* are more interesting than the free oscillations, since these envelope functions contain the mode growth information. If eq. 5.7 is averaged over the rapid time scale of the natural oscillations of the system, then only the time evolution of the envelope functions remain. The exponential terms on the RHS will average to zero, unless the sum of the frequencies in one of the exponents is zero. When some combination of the frequencies ω_1, ω_2, and Ω_0 sum to zero, there is a resonant condition which allows transfer of energy between the pendula. Unless this condition is met, the averaged equations are uncoupled. This is the manifestation of the frequency selection rule of parametric coupling for this system.

Suppose the frequency selection rule $\Omega_0 = \omega_1 - \omega_2$ is satisfied, then the averaged equations of motion become,

$$\begin{aligned} \frac{d^2A_1}{dt^2} + 2i\omega_1\frac{dA_1}{dt} &= \frac{k_0}{2m}A_2 \\ \frac{d^2A_2}{dt^2} + 2i\omega_2\frac{dA_2}{dt} &= \frac{k_0}{2m}A_1 \end{aligned} \tag{5.8}$$

In order to do normal mode analysis on these equations, let the envelope functions of the displacements be $A_1(t) = ae^{\nu t}$ and $A_2(t) = be^{\nu t}$. Upon substitution into equations 5.8, the constants a and b may be eliminated to find the dispersion relation,

$$\begin{vmatrix} \nu^2 + 2i\omega_1\nu & \frac{k_0}{2m} \\ \frac{k_0}{2m} & \nu^2 + 2i\omega_2\nu \end{vmatrix} = 0$$

Working to lowest order in $\frac{\nu}{\omega_j}$, the dispersion relation for the system of weakly parametrically coupled pendula takes the following simple form,

$$\nu = i\frac{\frac{k_0}{4m}}{(\omega_1\omega_2)^{\frac{1}{2}}} \tag{5.9}$$

As a consequence of satisfying the frequency selection rule $\Omega_0 = \omega_1 - \omega_2$, the envelope frequency ν has turned out to be imaginary (ω_1 and ω_2 are defined as positive). Since the functions $A_1(t)$ and $A_2(t)$ are then purely oscillatory, there is no growth of the motion. If, on the contrary, the selection rule $\Omega_0 = \omega_1 + \omega_2$ is satisfied, then the motion will grow. This can be seen by deriving the dispersion relation from the new averaged equations of motion. Proceeding from there as previously, the dispersion relation corresponding to this selection rule is the following,

$$\nu = \frac{\frac{k_0}{4m}}{(\omega_1\omega_2)^{\frac{1}{2}}}$$

In this case ν is real, and values of the envelope functions increase with time. It is significant that the selection rule resulting in mode growth is $\Omega_0 = \omega_1 + \omega_2$. Since all frequencies are defined as positive, Ω_0 is greater than ω_1 and ω_2. Unless this condition holds, the spring cannot transfer energy to the pendula. In other words, this is a process of parametric decay; there cannot be mode growth at frequencies higher than the pump frequency. This example is analogous to photon decay, which cannot occur unless the frequencies of the decay products sum to the frequency of the original photon.

There is an alternative technique for finding the dispersion relation, eq. 5.9, which will now be demonstrated. The first step is to take the Fourier transform of the

equations of motion (eq. 5.5). To facilitate the procedure, write the cosine term on the RHS as the sum of exponential functions. Then it can be seen that a modulation in time causes a frequency shift in the argument of the transformed variable. The transformed equations of motion are as follows,

$$(-\Omega^2 + \omega_1^2)X_1(\Omega) = \frac{k_0}{2m}[X_2(\Omega - \Omega_0) + X_2(\Omega + \Omega_0)] \tag{5.10}$$

$$(-\Omega^2 + \omega_2^2)X_2(\Omega) = \frac{k_0}{2m}[X_1(\Omega - \Omega_0) + X_1(\Omega + \Omega_0)] \tag{5.11}$$

All of the terms in eq. 5.10 must explicitly contain X_1 rather than X_2, so that X_1 can be eliminated from the equation. The required substitutions are found by shifting the frequency in eq. 5.11, letting $\Omega \to \Omega - \Omega_0$ to get $X_2(\Omega - \Omega_0)$, and $\Omega \to \Omega + \Omega_0$ to get $X_2(\Omega + \Omega_0)$.

Since only $X_2(\Omega - \Omega_0)$ is resonant, the contribution from $X_2(\Omega + \Omega_0)$ is not significant, and this term may be discarded. In order to determine the strength of these terms, consider the following. Assuming that the first pendulum is being driven near its resonant frequency sets the value for Ω, namely, $\Omega \simeq \omega_1$. The frequency sum rule driving the coupling resonance requires $\Omega_0 = \omega_1 - \omega_2$, where ω_2 is the resonant frequency of the second pendulum. Therefore, $X_2(\Omega - \Omega_0) \simeq X_2(\omega_2)$ is near resonance and makes a large contribution to the motion of the first pendulum compared to $X_2(\Omega + \Omega_0) \simeq X_2(\omega_2 + 2\Omega_0)$. The latter term could be kept until the final dispersion relation is evaluated near resonance, at which time it is explicit that its contribution is small. Selecting the dominant terms based on their strength is equivalent to the phase averaging which was done in the time domain.

Find $X_2(\Omega - \Omega_0)$ by shifting the frequency in eq. 5.11,

$$[-(\Omega - \Omega_0)^2 + \omega_2^2]X_2(\Omega - \Omega_0) = \frac{k_0}{2m}[X_1(\Omega - 2\Omega_0) + X_1(\Omega)]$$

The $X_1(\Omega - 2\Omega_0)$ is non-resonant and will be dropped. Then,

$$X_2(\Omega - \Omega_0) = \frac{\frac{k_0}{2m}}{[-(\Omega - \Omega_0)^2 + \omega_2^2]}X_1(\Omega) \tag{5.12}$$

Upon substitution of eq. 5.12 into eq. 5.10, $X_1(\Omega)$ may be eliminated to yield the dispersion relation,

$$1 = \frac{\left(\frac{k_0}{2m}\right)^2}{[-(\Omega - \Omega_0)^2 + \omega_2^2][-\Omega^2 + \omega_1^2]} \tag{5.13}$$

This will be shown to be equivalent to the result of the normal mode analysis technique by doing an expansion around the resonant frequency. Assume the frequency is nearly resonant, $\Omega = \omega_1 - i\nu$, where ν is small compared to ω_1. Then the two terms in the denominator of eq. 5.13 can be written,

$$\begin{aligned} -\Omega^2 + \omega_1^2 &= \quad -\omega_1^2 + 2i\omega_1\nu + \nu^2 + \omega_1^2 \quad &= 2i\omega_1\nu + \nu^2 \\ -(\Omega - \Omega_0)^2 + \omega_2^2 &= -[(\Omega_0 + \omega_2 - i\nu) - \Omega_0]^2 + \omega_2^2 &= 2i\omega_2\nu + \nu^2 \end{aligned}$$

Giving the resonant dispersion relation,

$$1 = \frac{\left(\frac{k_0}{2m}\right)^2}{-4\omega_1\omega_2\nu^2 + 2i\omega_1\nu^3 + 2i\omega_2\nu^3 + \nu^4}$$

$$= \frac{\left(\frac{k_0}{2m}\right)^2}{-4\omega_1^2\omega_2^2\left[\left(\frac{\nu}{\omega_1}\right)\left(\frac{\nu}{\omega_2}\right) - \frac{1}{2}\left(\frac{i\nu}{\omega_1}\right)\left(\frac{\nu^2}{\omega_2^2}\right) - \frac{1}{2}\left(\frac{\nu^2}{\omega_1^2}\right)\left(\frac{i\nu}{\omega_2}\right) - \frac{1}{4}\left(\frac{\nu^2}{\omega_1^2}\right)\left(\frac{\nu^2}{\omega_2^2}\right)\right]}$$

To lowest order in $\frac{\nu}{\omega_j}$, the resonant dispersion relation for the coupled pendula has the same form as that which resulted from the method using normal mode analysis.

$$\nu = i\frac{\frac{k_0}{4m}}{(\omega_1\omega_2)^{\frac{1}{2}}}$$

5.3 Method of multiple scales applied to a beam

While the principal of parametric coupling is the same in a particle beam as it is for a pair of mechanical pendula, the modes of oscillation in a beam are macroscopic averages of the motion of a very large number of particles. Consequently, the coupling will be described using a perturbative treatment of the Vlasov equation, beginning with eq. 5.3 which was developed in the introduction of this chapter.

When three-wave coupling is sufficiently weak, the multiple time scale expansion technique can be used to get a resonant dispersion relation for the process [10, 42]. This method is suitable for the parametric coupling observed in Main Ring, since the normal modes oscillate rapidly compared to the slower time scale for the growth or decay of power in these modes. Treating the time scales as independent variables allows the time derivative $\frac{\partial}{\partial t}$ to be expanded in powers of λ, where λ is on the order of the ratio of the time scales. The dependent variables are also expanded, using λ as the expansion parameter for convenience.

$$\frac{\partial}{\partial t} = \frac{\partial}{\partial \tau_0} + \lambda\frac{\partial}{\partial \tau_1} + \lambda^2\frac{\partial}{\partial \tau_2} + \cdots$$

$$
\begin{aligned}
f_m &= \lambda f_m^1 + \lambda^2 f_m^2 + \lambda^3 f_m^3 + \cdots \\
U_m &= \lambda U_m^1 + \lambda^2 U_m^2 + \lambda^3 U_m^3 + \cdots
\end{aligned} \tag{5.14}
$$

Where,

$$
\begin{aligned}
f_m^1 &= \hat{f_m}(\tau_1) e^{-i\omega_m \tau_0} \\
U_m^1 &= \hat{U_m}(\tau_1) e^{-i\omega_m \tau_0}
\end{aligned}
$$

The envelope of f_m^1 is given by $\hat{f_m}(\tau_1)$, τ_1 being the timescale for its growth or decay. The period of oscillation of f_m^1 is τ_0, with $\tau_0 << \tau_1$. Similarly for U_m^1.

Substituting expansion 5.14 into eq. 5.3, the first order equation in λ is found by collecting the first order terms,

$$
\frac{\partial f_m^1}{\partial \tau_0} + im\omega(\varepsilon) f_m^1 + \frac{e\omega_0}{2\pi} \frac{\partial f_0^0}{\partial \varepsilon} U_m^1 = 0 \tag{5.15}
$$

With,

$$
I_m^1 = e\omega_0 \int_{-\infty}^{\infty} f_m^1 \, d\varepsilon \tag{5.16}
$$

The first order equation in λ leads to the linear dispersion relation. Rearranging the terms of eq. 5.15, and using $U_m^1 = -Z_m I_m^1$ together with eq. 5.16 gives the familiar result,

$$
1 = \frac{i(e\omega_0)^2}{2\pi} Z_m(\omega_m) \int_{-\infty}^{\infty} \frac{\frac{\partial f_0^0}{\partial \varepsilon}}{\omega_m - m\omega(\varepsilon)} \, d\varepsilon
$$

The second order dispersion relation is needed to describe the three-wave coupling resonance. The derivation begins with the second order equation in λ, which is found by substituting expansions 5.14 into eq. 5.3 and collecting the second order terms,

$$\frac{\partial f_m^2}{\partial \tau_0} + im\omega(\varepsilon) f_m^2 + \frac{e\omega_0}{2\pi} U_m^2 \frac{\partial f_0^0}{\partial \varepsilon} =$$

$$-\frac{e\omega_0}{2\pi} U_m^1 \frac{\partial f_0^0}{\partial \varepsilon} + \frac{ie\omega_0}{2\pi} \frac{\frac{\partial f_0^0}{\partial \varepsilon}}{\omega_m - m\omega(\varepsilon)} e^{-i\omega_m \tau_0} \frac{\partial \hat{U}_m^1}{\partial \tau_1}$$

$$+\frac{i(e\omega_0)^2}{(2\pi)^2} \sum_{n+k=m} U_n^1 U_k^1 e^{-i(\omega_n+\omega_k)\tau_0} \frac{\partial}{\partial \varepsilon} \left(\frac{\frac{\partial f_0^0}{\partial \varepsilon}}{\omega_k - k\omega(\varepsilon)} \right) \tag{5.17}$$

Only the most weakly nonlinear dynamical process will be considered here, and the unperturbed portion of the beam distribution will not be allowed to change. Therefore, the first term on the RHS of eq. 5.17 will be dropped.

The sum of the secular terms is next set to zero, which is equivalent to carrying out phase averaging. There is no envelope growth of the non-resonant terms, so they will phase average to zero, leaving only the secular terms which describe the resonant behavior of three-wave coupling. The secular terms in eq. 5.17 are more easily identified by taking the Laplace transform,

$$[s + im\omega(\varepsilon)] \int_0^\infty f_m^2 e^{-s\tau_0}\, d\tau_0 + \frac{e\omega_0}{2\pi} \frac{\partial f_0^0}{\partial \varepsilon} \tilde{U}_m^2(s, \tau_1) =$$

$$\frac{ie\omega_0}{2\pi} \frac{\frac{\partial f_0^0}{\partial \varepsilon}}{[s + i\omega_m][\omega_m - m\omega(\varepsilon)]} \frac{\partial \hat{U}_m^1}{\partial \tau_1}$$

$$+i\frac{(e\omega_0)^2}{(2\pi)^2} \sum_{n+k=m} \hat{U}_n^1 \hat{U}_k^1 \frac{1}{s + i(\omega_n + \omega_k)} \frac{\partial}{\partial \varepsilon} \left(\frac{\frac{\partial f_0^0}{\partial \varepsilon}}{\omega_k - k\omega(\varepsilon)} \right) \tag{5.18}$$

Both terms on the LHS of eq. 5.18 may be put in terms of $\tilde{U_m^2}$ using the relation,

$$\begin{aligned}\tilde{U_m^2} &= \int_0^\infty U_m^2 e^{-s\tau_0}\, d\tau_0 \\ &= -Z_m e\omega_0 \int_{-\infty}^{\infty} d\varepsilon \int_0^\infty f_m^2 e^{-s\tau_0}\, d\tau_0\end{aligned}$$

Then,

$$\begin{aligned}&\tilde{U_m^2}\left\{1 - Z_m \frac{(e\omega_0)^2}{2\pi}\int_{-\infty}^{\infty}\frac{\frac{\partial f_0^0}{\partial\varepsilon}}{s+im\omega(\varepsilon)}\, d\varepsilon\right\} = \\ &-Z_m e\omega_0 \int_{-\infty}^{\infty}\frac{d\varepsilon}{s+im\omega(\varepsilon)}\left\{\frac{ie\omega_0}{2\pi}\frac{\frac{\partial f_0^0}{\partial\varepsilon}}{[s+i\omega_m][\omega_m - m\omega(\varepsilon)]}\frac{\partial \hat{U_m^1}}{\partial\tau_1}\right. \\ &\left. +i\frac{(e\omega_0)^2}{(2\pi)^2}\sum_{n+k=m}\hat{U_n^1}\hat{U_k^1}\frac{1}{s+i(\omega_n+\omega_k)}\;\frac{\partial}{\partial\varepsilon}\left(\frac{\frac{\partial f_0^0}{\partial\varepsilon}}{\omega_k - k\omega(\varepsilon)}\right)\right\} \qquad (5.19)\end{aligned}$$

The term in curly brackets on the LHS is just the linear dispersion relation for mode m, $D_m(s)$, written as a function of s, the Laplace transform variable, instead of $-i\omega_m$.

The frequency selection rule is a natural consequence of identifying the secular terms in eq. 5.19. If both sides of the equation are divided by $D_m(s)$, it can be seen that $\tilde{U_m^2}$ will be larger as the dispersion relation is closer to zero. The root of the dispersion relation occurs when $s = -i\omega_m$, with $\omega_m = m\omega_0$ being the frequency of the mth normal mode. Independent of D_m, the first term on the RHS of eq. 5.19 will also be larger when $s = -i\omega_m$ due to the doubly resonant denominator. On simple physical grounds, if $\tilde{U_m^2}$ is large, then an oscillation at ω_m must be present in the beam. Thus, the first term on the RHS of eq. 5.19 is necessarily secular. The second term

on the RHS will be secular when $\omega_n + \omega_k = \omega_m$, due to the $s + i(\omega_n + \omega_k)$ term in the denominator. Thus, the frequency selection rule of parametric decay is a consequence of the condition for the secularity of this second term. Using the phase selection rule $k = m - n$, the frequency selection rule may also be written $\omega_n + \omega_{m-n} = \omega_m$. Setting the secular terms to zero,

$$\frac{ie\omega_0}{2\pi}\frac{\partial \hat{U}_m^1}{\partial \tau_1}\int_{-\infty}^{\infty}\frac{d\varepsilon\frac{\partial f_0^0}{\partial \varepsilon}}{[s+im\omega(\varepsilon)][s+i\omega_m][\omega_m - m\omega(\varepsilon)]}$$

$$+i\frac{(e\omega_0)^2}{(2\pi)^2}\sum_n \hat{U}_n^1 \hat{U_{m-n}^1}\int_{-\infty}^{\infty}\frac{d\varepsilon}{[s+im\omega(\varepsilon)][s+i(\omega_n+\omega_{m-n})]}\frac{\partial}{\partial\varepsilon}\left(\frac{\frac{\partial f_0^0}{\partial \varepsilon}}{\omega_{m-n}-(m-n)\omega(\varepsilon)}\right)$$

$$= 0 \tag{5.20}$$

Now that the secular terms have been identified and the equation describing resonant coupling has been obtained, take the inverse Laplace transform of eq. 5.20 to return to the time domain,

$$\frac{ie\omega_0}{2\pi}\frac{\partial \hat{U}_m^1}{\partial \tau_1}\int_{-\infty}^{\infty}\frac{d\varepsilon\frac{\partial f_0^0}{\partial \varepsilon}}{\omega_m - m\omega(\varepsilon)}\int_{c-i\infty}^{c+i\infty}\frac{ds\, e^{s\tau_0}}{[s+im\omega(\varepsilon)][s+i\omega_m]} =$$

$$-i\frac{(e\omega_0)^2}{(2\pi)^2}\sum_n \hat{U}_n^1 \hat{U_{m-n}^1}\int_{-\infty}^{\infty}d\varepsilon\frac{\partial}{\partial\varepsilon}\left(\frac{\frac{\partial f_0^0}{\partial \varepsilon}}{\omega_{m-n}-(m-n)\omega(\varepsilon)}\right)$$

$$\times\int_{c-i\infty}^{c+i\infty}\frac{ds\, e^{s\tau_0}}{[s+im\omega(\varepsilon)][s+i(\omega_n+\omega_{m-n})]}$$

The evaluation of the s integrals is expedited by doing a partial fraction expansion

on the arguments of the integrals. Then,

$$\frac{e\omega_0}{2\pi}\frac{\partial \hat{U}_m^1}{\partial \tau_1}\int_{-\infty}^{\infty}\frac{\frac{\partial f_0^0}{\partial \varepsilon}}{[\omega_m - m\omega(\varepsilon)]^2}\,d\varepsilon =$$

$$-\frac{(e\omega_0)^2}{(2\pi)^2}\sum_n \hat{U}_n^1 \hat{U_{m-n}^1}\int_{-\infty}^{\infty}\frac{\partial}{\partial \varepsilon}\left(\frac{\frac{\partial f_0^0}{\partial \varepsilon}}{\omega_{m-n} - (m-n)\omega(\varepsilon)}\right)\frac{1}{[\omega_n + \omega_{m-n} - m\omega(\varepsilon)]}\,d\varepsilon \quad (5.21)$$

Equation 5.21 may be simplified by doing an integration by parts on the energy integral on the RHS,

$$\frac{e\omega_0}{2\pi}\frac{\partial \hat{U}_m^1}{\partial \tau_1}\int_{-\infty}^{\infty}\frac{\frac{\partial f_0^0}{\partial \varepsilon}}{[\omega_m - m\omega(\varepsilon)]^2}\,d\varepsilon =$$

$$\frac{(e\omega_0)^2}{(2\pi)^2} m k_0 \sum_n \hat{U}_n^1 \hat{U_{m-n}^1}\int_{-\infty}^{\infty}\frac{\frac{\partial f_0^0}{\partial \varepsilon}}{[\omega_{m-n} - (m-n)\omega(\varepsilon)][\omega_n + \omega_{m-n} - m\omega(\varepsilon)]^2}\,d\varepsilon \quad (5.22)$$

In order to examine the circumstance where the response at mode m is due to mode mixing with an externally applied voltage, let U_n be a driving voltage of the form,

$$U_n = V_0 e^{i(n\theta - \Omega_0 t)} + V_0^* e^{-i(n\theta - \Omega_0 t)} \quad (5.23)$$

where V_0 is the amplitude of the applied voltage, and $\Omega_0 = n\omega_0$ is the frequency of the applied voltage. Once mode m is specified in eq. 5.22, if U_n is replaced with the expression given by eq. 5.23, then the summation reduces to two terms. These describe the coupling of mode m to modes $m - \Omega_0$ and $m + \Omega_0$ via the driving voltage. In other words, each term represents a different selection rule, $\omega_m = \omega_n + \omega_{m-n}$ and

$\omega_m = -\omega_n + \omega_{m+n}$. For example, suppose that the mode driven by the coupling resonance is $m = 105$, and that the drive frequency is $n = 106$. Then there are two possible third waves involved. The selection rule $105 = 106 + \omega_k$ requires $\omega_k = -1$, while the selection rule $105 = -106 + \omega_k$ requires $\omega_k = 211$. Each of these coupling terms may be considered separately, as in general modes 211 and -1 will not both be present. For the sake of simplicity, the $m + n$ term will be discarded.

$$\frac{e\omega_0}{2\pi}\frac{\partial \hat{U}^1_m}{\partial \tau_1}\int_{-\infty}^{\infty}\frac{\frac{\partial f_0^0}{\partial \varepsilon}}{[\omega_m - m\omega(\varepsilon)]^2}\,d\varepsilon =$$

$$\frac{(e\omega_0)^2}{(2\pi)^2} m k_0 V_0 \hat{U^1_{m-n}}\int_{-\infty}^{\infty}\frac{\frac{\partial f_0^0}{\partial \varepsilon}}{[\omega_{m-n} - (m-n)\omega(\varepsilon)][\Omega_0 + \omega_{m-n} - m\omega(\varepsilon)]^2}\,d\varepsilon \quad (5.24)$$

When m is excited, there will also be a response at mode $m - n$ due to the frequency mixing of ω_m with Ω_0. Swapping m and $m - n$ in eq. 5.24 and letting $\Omega_0 \to -\Omega_0$, produces the second of the pair of coupled equations. Proceeding with normal mode analysis, the envelope functions for mode growth, $\hat{U}^1_m(\tau_1)$ and $\hat{U^1_{m-n}}(\tau_1)$, are replaced with $ae^{\nu\tau_1}$ and $be^{\nu\tau_1}$, where a and b are constants, and ν is the envelope frequency.

$$\frac{e\omega_0}{2\pi} a\nu\int_{-\infty}^{\infty}\frac{\frac{\partial f_0^0}{\partial \varepsilon}}{[\omega_m - m\omega(\varepsilon)]^2}\,d\varepsilon =$$

$$\frac{(e\omega_0)^2}{(2\pi)^2} m k_0 V_0 b\int_{-\infty}^{\infty}\frac{\frac{\partial f_0^0}{\partial \varepsilon}}{[\omega_{m-n} - (m-n)\omega(\varepsilon)][\Omega_0 + \omega_{m-n} - m\omega(\varepsilon)]^2}\,d\varepsilon \quad (5.25)$$

$$\frac{e\omega_0}{2\pi} b\nu\int_{-\infty}^{\infty}\frac{\frac{\partial f_0^0}{\partial \varepsilon}}{[\omega_{m-n} - (m-n)\omega(\varepsilon)]^2}\,d\varepsilon =$$

$$\frac{(e\omega_0)^2}{(2\pi)^2}(m-n)k_0V_0^*a\int_{-\infty}^{\infty}\frac{\frac{\partial f_0^0}{\partial\varepsilon}}{[\omega_m-(m)\omega(\varepsilon)][-\Omega_0+\omega_m-(m-n)\omega(\varepsilon)]^2}\,d\varepsilon \quad (5.26)$$

Eliminating the constants a and b in equations 5.25 and 5.26, the second order dispersion relation at resonance is found,

$$\nu^2\int_{-\infty}^{\infty}\frac{\frac{\partial f_0^0}{\partial\varepsilon}}{[\omega_m-m\omega(\varepsilon)]^2}\,d\varepsilon\int_{-\infty}^{\infty}\frac{\frac{\partial f_0^0}{\partial\varepsilon}}{[\omega_{m-n}-(m-n)\omega(\varepsilon)]^2}\,d\varepsilon =$$

$$\frac{(e\omega_0)^2}{(2\pi)^2}V_0V_0^*m(m-n)k_0^2\int_{-\infty}^{\infty}\frac{\frac{\partial f_0^0}{\partial\varepsilon}}{[\omega_m-m\omega(\varepsilon)]^2[\omega_{m-n}-(m-n)\omega(\varepsilon)]}\,d\varepsilon$$

$$\times\int_{-\infty}^{\infty}\frac{\frac{\partial f_0^0}{\partial\varepsilon}}{[\omega_m-m\omega(\varepsilon)][\omega_{m-n}-(m-n)\omega(\varepsilon)]^2}\,d\varepsilon \quad (5.27)$$

The relation $\omega_m = \Omega_0 + \omega_{m-n}$ has been used to simplify the form of the result.

5.4 Fourier transform method applied to a beam

The dispersion relation for parametric coupling can be found using an alternative technique to that used in section 5.3. The method is to Fourier transform eq. 5.3, and then to express all terms as products of the perturbed current I_m. This allows I_m to be cancelled out of the equation, resulting in the second order dispersion relation. The detailed procedure is carried out in appendix B, and only the result will be discussed here. The form of the dispersion relation obtained using this Fourier transform method is somewhat more general than the result found in section 5.3, since it is not based on normal mode analysis where the system is implicitly being treated

near resonance. In order to support the validity of both methods, appendix B shows the equivalence of the two dispersion relations when the system is near resonance.

The response of the beam at mode m due to parametric coupling of modes n and $k = m - n$, may be described by the second order dispersion relation derived in appendix B,

$$\begin{aligned} D_m(\Omega)D_{m-n}(\Omega-\Omega_0) &= \frac{(e\omega_0)^6}{(2\pi)^4} V_0 V_0^* m(m-n)k_0^2 Z_m(\Omega)Z_{m-n}(\Omega-\Omega_0) \\ &\times \int_{-\infty}^{\infty} \frac{\frac{\partial f_0}{\partial \varepsilon}}{[\Omega - m\omega(\varepsilon)][\Omega-\Omega_0-(m-n)\omega(\varepsilon)]^2}\, d\varepsilon \\ &\times \int_{-\infty}^{\infty} \frac{\frac{\partial f_0}{\partial \varepsilon}}{[\Omega - m\omega(\varepsilon)]^2[\Omega-\Omega_0-(m-n)\omega(\varepsilon)]}\, d\varepsilon \quad (5.28) \end{aligned}$$

where V_0 is the amplitude of the applied voltage, $\Omega_0 = n\omega_0$ is the frequency of the applied voltage, D_m represents the linear dispersion relation for mode m (similarly for D_{m-n}), and other symbols in the equation are consistent with previous definitions.

When it is feasible to assume a Gaussian beam distribution of the form given by eq. 2.12, then the dispersion relation may be written in terms of generally available beam parameters,

$$\begin{aligned} D_m(\Omega)D_{m-n}(\Omega-\Omega_0) &= \frac{I_0^2 Z_m(\Omega)Z_{m-n}(\Omega-\Omega_0)V_0V_0^*\beta^8}{64\pi^5 m^2(m-n)^2\eta^4\left(\frac{\sigma_\varepsilon}{E_0}\right)^8 (E_0[eV])^4} \\ &\times \int_{-\infty}^{\infty} \frac{xe^{-x^2}}{[\varepsilon-\xi_1][\varepsilon-\xi_2]^2}\, dx \\ &\times \int_{-\infty}^{\infty} \frac{xe^{-x^2}}{[\varepsilon-\xi_1]^2[\varepsilon-\xi_2]}\, dx \quad (5.29) \end{aligned}$$

where $x = \frac{\varepsilon}{\sqrt{2}\sigma_\varepsilon}$, $\xi_1 = \frac{1}{\sqrt{2}\sigma_\varepsilon mk_0}(\Omega - m\omega_0)$, $\xi_2 = \frac{1}{\sqrt{2}\sigma_\varepsilon (m-n)k_0}(\Omega - \Omega_0 - (m-n)\omega_0)$, and the other variables are as previously defined. The coefficient to the integrals can be considered a coupling coefficient; the larger the coefficient, the more likely parametric coupling is to occur. The general character of the dependences are as one might expect. For example, the likelihood of this coupling goes up with beam intensity, applied driving voltage, or impedance, while it goes down as the momentum width of the beam increases. However, the level of sensitivity to these parameters is less intuitive, particularly the dependence on the momentum width of the beam, which goes as σ_ε^{-8}.

The coupling coefficient is an indication of why parametric coupling readily occurs in a marginally stable machine such as the Main Ring, while it is difficult to stimulate in a stable machine such as the Accumulator. First, there is an absence of coupling impedance available in stable machines. Secondly, the effective beam width in the Main Ring was much narrower than the actual beam width, due to the depletion within the beam distribution. These depletion regions caused deep notches to be visible in the magnitude response of the transfer function measurements. In contrast, Accumulator transfer function measurements showed a beam distribution with a smoothly varying particle population.

One significant difference between the simple case of a system of parametrically coupled pendula and the analysis for a beam, is that in the system of pendula there was no mechanism for damping. There is damping in the beam case, which is contained mathematically in the complex denominators in the integrands of the dispersion relation, and is due physically to the energy spread of the beam. Damping in the parametric coupling process in a beam is due to a combination of the resonant

denominators in the linear dispersion relations of the individual modes. Thus, the relative stability of each of the independent modes also determines the beam stability with respect to the coupling resonance. This might be expected, as the parametric coupling process is weakly nonlinear. The waves are essentially scattering off each other without changing the distribution of particle energies in the beam.

5.5 Mode growth and conservation laws

The frequency sum rule for parametric coupling and conservation of energy for the process are mutually implied [2, 9, 10]. The time rate of change of the total wave energy density per mode number of the three-wave system will be shown to be zero, provided that the frequencies of the three modes sum to zero. This will be shown only for a weakly dissipative system, with the additional restriction that the impedance is a constant. The method used here follows one given by Davidson [10] for a plasma, with a departure being that the conserved quantity in the beam case is wave energy density per mode number, rather than wave energy density. Also, for a beam, the coefficient of the interaction matrix V_{mnk} is written in terms of the machine impedance and the revolution frequency, whereas in the plasma case the coefficient is written in terms of the plasma frequency and the wave number. Although it is not treated here, consideration of the general case would be useful, for this more complete accounting of the energy flow should allow for the extraction of the frequency dependent machine impedance from a parametric coupling event.

The mode number sum rule for parametric coupling and conservation of momentum for the process are also mutually implied. They can be linked using the same

formal technique as the one shown below, except that the definition of wave momentum is used in place of the definition for wave energy density.

The wave energy density per mode number of mode m, symbolized by $\frac{W_m}{m}$, and the wave momentum per mode number of mode m, symbolized by $\frac{P_m}{m}$, are given in MKSA units by,

$$\begin{aligned} \frac{W_m}{m} &= \frac{1}{4m}\epsilon_0\omega_m\frac{\partial D_m}{\partial\omega_m}|U_m|^2 \\ \frac{P_m}{m} &= \frac{1}{4}\epsilon_0\frac{\partial D_m}{\partial\omega_m}|U_m|^2 \end{aligned}$$

where m is the mode number, ω_m is the frequency of the mode, ϵ_0 is the permittivity of free space, U_m is the the wakefield voltage per turn at mode m, and the linear dispersion relation D_m is equivalent to the dielectric coefficient. These relations may also be written,

$$\frac{W_m}{m} = \frac{1}{m}s_m\omega_m|A_m|^2 \tag{5.30}$$

$$\frac{P_m}{m} = s_m|A_m|^2 \tag{5.31}$$

where A_m is the wave amplitude $A_m = \frac{1}{2}\sqrt{\epsilon_0}\left|\frac{\partial D_m}{\partial\omega_m}\right|^{\frac{1}{2}}\hat{U}_m e^{i\phi_m}$, and $s_m = \mathrm{sgn}\left(\frac{\partial D_m}{\partial\omega_m}\right)$, with $s_m = \pm 1$, depending on whether the wave is a positive or negative energy wave.

Wave energy density per mode number is conserved if the following holds,

$$\frac{d}{dt}\left[\sum_m \frac{W_m}{m}\right] = 0$$

Using eq. 5.30, the change in the wave energy density per mode number can be expressed,

$$\begin{aligned}\frac{\partial}{\partial t}\left(\frac{W_m}{m}\right) &= \frac{1}{m}s_m\omega_m\left[A_m^*\frac{\partial A_m}{\partial t}+A_m\frac{\partial A_m^*}{\partial t}\right]\\ &= \frac{1}{m}s_m\omega_m 2\mathrm{Re}\left[A_m^*\frac{\partial A_m}{\partial t}\right] \qquad (5.32)\end{aligned}$$

where,

$$\frac{\partial A_m}{\partial t}=\frac{1}{2}\sqrt{\epsilon_0}\left|\frac{\partial D_m}{\partial \omega_m}\right|^{\frac{1}{2}}\left[\frac{\partial \hat{U}_m}{\partial t}\right]e^{i\phi_m}$$

The time rate of change of mode amplitude m, $\frac{\partial \hat{U}_m}{\partial t}$, is found by rearranging eq. 5.21 and dropping the multiple time scale perturbation notation,

$$\frac{\partial \hat{U}_m}{\partial t}=\frac{-\hat{U}_n\hat{U}_k\frac{(e\omega_0)^2}{(2\pi)^2}\int_{-\infty}^{\infty}\frac{\partial}{\partial\varepsilon}\left(\frac{\frac{\partial f_0^0}{\partial\varepsilon}}{\omega_k-(k)\omega(\varepsilon)}\right)\frac{1}{[\omega_n+\omega_k-m\omega(\varepsilon)]}\,d\varepsilon}{\frac{e\omega_0}{2\pi}\int_{-\infty}^{\infty}\frac{\frac{\partial f_0^0}{\partial\varepsilon}}{[\omega_m-m\omega(\varepsilon)]^2}\,d\varepsilon} \qquad (5.33)$$

The denominator of eq. 5.33 has nearly the same form as $\frac{\partial D_m}{\partial \omega_m}$,

$$\frac{\partial D_m}{\partial \omega_m}=i\frac{(e\omega_0)^2}{2\pi}Z\int_{-\infty}^{\infty}\frac{\frac{\partial f_0}{\partial\varepsilon}}{[\omega_m-m\omega(\varepsilon)]^2}\,d\varepsilon$$

The growth rate of the wave amplitude can be cast in the form,

$$\frac{\partial A_m}{\partial t} = -s_m e^{i\phi_m}\left(\frac{1}{2}\sqrt{\epsilon_0}\left|\frac{\partial D_n}{\partial \omega_n}\right|^{\frac{1}{2}}\hat{U}_n\right)\left(\frac{1}{2}\sqrt{\epsilon_0}\left|\frac{\partial D_k}{\partial \omega_k}\right|^{\frac{1}{2}}\hat{U}_k\right)$$

$$\times \frac{\frac{i2(e\omega_0)^3}{\sqrt{\epsilon_0}(2\pi)^2} Z \int_{-\infty}^{\infty} \frac{\partial}{\partial \varepsilon}\left(\frac{\frac{\partial f_0^0}{\partial \varepsilon}}{\omega_k - (k)\omega(\varepsilon)}\right) \frac{1}{[\omega_m - m\omega(\varepsilon)]}\, d\varepsilon}{\left|\frac{\partial D_m}{\partial \omega_m}\right|^{\frac{1}{2}} \left|\frac{\partial D_n}{\partial \omega_n}\right|^{\frac{1}{2}} \left|\frac{\partial D_k}{\partial \omega_k}\right|^{\frac{1}{2}}} \tag{5.34}$$

Equation 5.34 may be written more compactly,

$$\frac{\partial A_m}{\partial t} = s_m e^{i\phi} V_{mnk} A_n A_k \tag{5.35}$$

where the matrix element of the interaction has been symbolized as V_{mnk}, and is defined by eq. 5.34 as the following,

$$V_{mnk} = \frac{-i\frac{2(e\omega_0)^3}{\sqrt{\epsilon_0}(2\pi)^2} Z \int_{-\infty}^{\infty} \frac{\partial}{\partial \varepsilon}\left(\frac{\frac{\partial f_0^0}{\partial \varepsilon}}{\omega_k - (k)\omega(\varepsilon)}\right) \frac{1}{[\omega_m - m\omega(\varepsilon)]}\, d\varepsilon}{\left[\left|\frac{\partial D_m}{\partial \omega_m}\right| \left|\frac{\partial D_n}{\partial \omega_n}\right| \left|\frac{\partial D_k}{\partial \omega_k}\right|\right]^{\frac{1}{2}}} \tag{5.36}$$

Substituting eq. 5.35 into eq. 5.32 and carrying out the summation over modes,

$$\begin{aligned} \frac{d}{dt}\left[\sum_m \frac{W_m}{m}\right] &= \sum_m \frac{1}{m} s_m \omega_m 2\mathrm{Re}\left\{s_m V_{mnk} A_m^* A_n A_k\right\} \\ &= 2\mathrm{Re}\left\{\sum_m \omega_m \frac{V_{mnk}}{m} A_m^* A_n A_k\right\} \end{aligned} \tag{5.37}$$

Equation 5.37 is invariant under permutation of the indices on the RHS. Performing two such permutations, and adding the three resulting equivalent expressions, allows the RHS to be of eq. 5.37 to be re-written,

$$\frac{d}{dt}\left[\sum_m \frac{W_m}{m}\right] = \frac{2}{3}\mathrm{Re}\left\{\sum_m \omega_m \frac{V_{m,n,k}}{m} A_m^* A_n A_k\right.$$

$$+\sum_n \omega_{-n}\frac{V_{-n,-m,k}}{-n}A^*_{-n}A_{-m}A_k$$

$$+\sum_k \omega_{-k}\frac{V_{-k,n,-m}}{-k}A^*_{-k}A_nA_{-m}\Bigg\}$$

In order to complete the proof, use is made of the following equalities,

$$\begin{aligned}\omega_{-m} &= -\omega_m \\ A_{-m} &= A^*_m\end{aligned}$$

The first equality is true since the normal mode frequencies of a storage ring are given by $\omega_m \equiv m\omega_0$, where ω_0 is the revolution frequency of the ring. The second equality can be seen by letting $m \to -m$ in the definition of the wave amplitude A_m, and making use of the fact that $\phi_m \equiv m\theta$ in a ring.

The following symmetry relations, which are demonstrated in appendix C, are also needed:

$$\frac{V_{m,n,k}}{m} = \frac{V_{-n,-m,k}}{-n} = \frac{V_{-k,n,-m}}{-k}$$

Then,

$$\frac{d}{dt}\left[\sum_m \frac{W_m}{m}\right] = \frac{2}{3}\mathrm{Re}\left\{\sum_m(\omega_m - \omega_n - \omega_k)\frac{V_{mnk}}{m}A^*_mA_nA_k\right\}$$

Thus, the total change in energy density per mode number of the system is zero,

provided that the frequency sum rule $\omega_m = \omega_n + \omega_k$ is satisfied. Proof of the relation between the conservation of wave momentum and the mode number sum rule follows the same steps as the preceding proof, except that it begins with eq. 5.31, the definition for wave momentum.

While this derivation does not apply in the presence of significant dissipative effects, its importance lies in the realization that the wave-wave coupling process is governed by conservation of energy. The requirements of energy conservation determine which combinations of wave coupling will be allowed in the system. If the analysis is extended to include dissipation and a more generalized machine impedance, it may prove useful for extracting the impedance from measurements of a beam in the weak to moderately nonlinear regime.

Chapter 6

Main Ring time domain results

6.1 Introduction and overview

The observations motivating this study of parametric coupling of longitudinal modes in coasting beams were made in the Tevatron [44, 45], a high energy proton synchrotron at Fermilab. These observations showed growth of multiple modes after a single drive frequency had been applied to the beam. There was an indication that these modes were sequentially excited from higher to lower frequencies in a cascade. Further, this multiple frequency response occurred only after the applied voltage had crossed a certain threshold. The evidence suggested a classic second-order frequency mixing effect, known as parametric coupling. This led to the studies presented here, which were done in the Main Ring proton synchrotron, whose purpose was to determine and document the nature of this process. Once it was established that the parametric coupling process was indeed an aspect of beam dynamics in the Main Ring, new studies were initiated to investigate beam behavior under more strongly

nonlinear conditions.

One possible way to characterize a system is by its degree of nonlinearity. There is a continuous spectrum of possibilities, from linear to chaotic. The first level of nonlinearity after the linear regime are weakly nonlinear processes such as parametric coupling. This 3-wave coupling process is analyzed using the same techniques as used in linear stability theory, with the exception that now besides the linear terms a second order frequency mixing term is retained in the description of the beam dynamics. This coupling resonance is not strongly nonlinear in the sense that it is still considered a perturbation, not significantly changing the initial particle distribution.

The experimental setup for the study of parametric coupling is described in section 6.2. Experimental results are reviewed in section 6.3. These results show that a single frequency excitation can produce a multiple frequency cascade from higher to lower harmonics. The mode coupling is single-sided, only those modes lower than the pump frequency were excited. The timing of growth at the different harmonics relative to a short initial drive pulse was determined, giving evidence of the frequency selection rules which were in operation. The data provide confirmation that the phenomenon being studied was indeed parametric coupling.

The role of machine impedance in the parametric coupling process is examined in section 6.4, where it is shown to enhance coupling. Since the strength of parametric coupling depends on the machine impedance, perhaps ultimately the impedance could be extracted from a coupling measurement. If machine conditions are conducive to parametric coupling, then the nonlinear response to an excitation would make it difficult to get a clear impedance measurement using conventional methods. In order to get an accurate measurement out of the coupling process, a more quantitative

analysis of power flow in the system is needed.

An investigation of the Main Ring threshold for parametric coupling is presented in section 6.5. Unlike the case of the Tevatron, parametric coupling occurred in the Main Ring as soon as there was any detectable perturbation of the beam at the drive frequency. Main Ring is a marginally stable machine (see chapter 4), with plenty of available coupling impedance. In addition, the Tevatron has a stiffer beam, coasting at 150 GeV as opposed to 8.9 GeV in the Main Ring. These factors strengthen the coupling coefficient which governs the parametric process in the Main Ring (see chapter 5).

The dynamics of a particle beam become moderately nonlinear as the strength of the wakefields increase, and the initial particle distribution is disrupted. Some of the signatures of moderate nonlinearity are a longer, nonlinear Landau damping time for the decay of coherent motion, higher harmonic generation, and asymmetric particle clumping across the beam distribution. These processes are described briefly below. All of these characteristics have been observed experimentally in the Main Ring. In order to enhance nonlinearities, the power delivered by the drive pulse was increased, primarily by increasing the length of the pulse. Results of experiments in the moderately nonlinear regime are summarized in section 6.6.

When wakefield voltages increase beyond a perturbative level, coherent mode oscillations decay with a nonlinear Landau damping time that may be long compared to the linear Laundau damping time [7, 20, 21]. As a wakefield amplitude increases, more particles become trapped in the potential well of its voltage waveform, which causes them to travel on nonlinear orbits. This bunching of particles in energy (and phase) modifies the particle distribution. The coherent beam motion, which consists

of the phase oscillations of the trapped particles, may sustain itself as a result of energy exchange between the voltage wave of the wakefield, and the coherent oscillation of the trapped particles.

The phase relation of the bunched particles and the voltage wave is such that the particles in turn gain energy by acceleration from the voltage wave, and then due to this energy gain, slip in phase so that the voltage wave then takes energy back out of the particle bunch. This rotation of the particle bunch between energy and phase causes a 'bouncing' or modulation of the mode power during its decay. The decay itself is due to the energy spread of the trapped particles and the nonlinearity of the voltage wave. Energy dispersion causes the particles to be at different relative phases on the wave, and the nonlinearity of the wave then causes phase mixing of the particles. This phase smearing dilutes the trapped particles, thus reducing the peak current of the coherent oscillation, damping the coherent motion. In addition, the decrease in peak current will in turn decrease the amplitude of the self-field.

Higher harmonic generation refers to the phenomena whereby not only the cascade of modes directly excited by the pump frequency become coherent, but also higher multiples of these modes [23]. For example, besides supporting $h = 105$, the beam would also have a coherent response at $h = 2 \times 105$, $h = 3 \times 105$, and so on. Like nonlinear Landau damping, higher harmonic generation is a result of particle bunching by wakefield voltages. The periodic fluctuation of the particle density in the spatial coordinate produces harmonics of the fundamental frequency of the fluctuation.

There are specific circumstances under which nonlinear phenomena not generally present may occur. One example is soliton formation [24, 25, 48]. Normally the coherent motion of a group of trapped particles will damp as the particles disperse

due to their relative energy differences and the nonlinearities in the field. However, under some circumstances, the particles may interact with the machine in such a way as to steepen the wavefront of the wakefield. The wavefront may change enough so that the nonlinear driving force of the field comes to a balance with the dispersion. In this case, the particles will remain clumped together, caught in this nonlinear equilibrium.

Asymmetric particle clumping across the beam distribution has been observed. Particle clumping, or the formation of pockets of trapped particles into bunchlets, on only one side of the beam distribution was indicated by a particle tracking simulation, and then verified experimentally. The simulation modeled a longitudinal coasting beam experiencing a machine impedance [46, 47]. Power in the higher order harmonics was found to be modulated with a bunchlet rotation frequency on only the high energy side of the beam distribution. This high frequency grouping of a subset of particles, which are selected on the basis of their energies, may be an indication of a generalized soliton-like behavior.

The importance of studying and understanding nonlinear effects lies in the fact that although beam instabilities (mode growth) begin in the regime of linear stability theory, if the motion is unstable, the beam dynamics move quickly into nonlinearity. Emittance dilution and saturation of mode growth are nonlinear phenomena, and are increasingly important in the era of high intensity beams.

6.2 Experimental setup

The experimental setup used for time domain measurements in the Main Ring is shown in block diagram form in figure 6.1. An impulse excitation was applied to

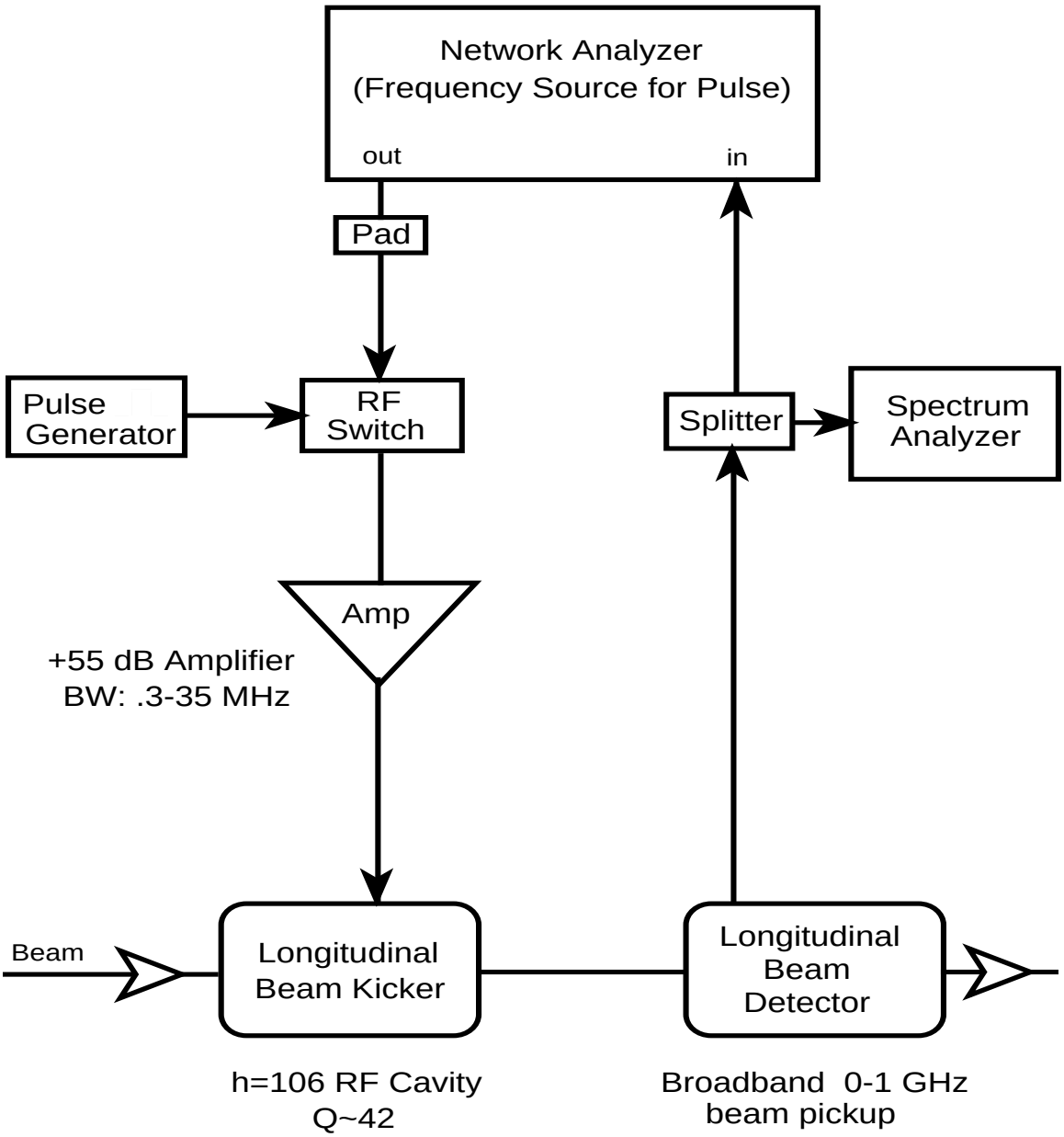

Figure 6.1: Block diagram of Main Ring time domain setup.

the beam via the 5 MHz coalescing cavity, which was used as a longitudinal kicker. The frequency and width of the pulse were both adjustable. The beam response to the excitation was monitored via a quarter wave transmission line pickup, which operates as a broadband longitudinal beam detector. More complete descriptions of the hardware may be found in section 4.2.

The signal from the beam detector was monitored with an HP 8568B 100 Hz-1.5 Gz spectrum analyzer. The spectrum analyzer was set up in such a way as to determine the time development of power at selected frequencies. This is done by setting the center frequency of the sweep to the frequency of interest, and the frequency span to 0 Hz. Power at the selected frequency will then be recorded over the sweep time of the instrument. The setting for the frequency resolution determines how wide the monitored frequency band will be. The spectrum analyzer traces were stored on a VAX using a GPIB interface. The beam kicker, beam pickup, and amplifier were the same as those used for the frequency domain measurements.

The frequency source for the pulse was the HP 8753C network analyzer, with a continuous wave sweep at a fixed frequency. The frequency was chosen to be somewhere within the band of the 5 MHz cavity, the typical selection being the center frequency $h = 106$, or 5.029805 MHz. The output of the network analyzer was gated onto the beam kicker for a short time using an RF power switch with a single, triggerable gate pulse. The gate, with a typical width of .5 ms, was supplied by an HP 8011A pulse generator operating with an external trigger. Unlike studies conditions in the Accumulator, the beam in the Main Ring did not coast indefinitely, but was dumped anywhere between 3-12 seconds after injection. For this reason, the instruments were all triggered externally by available timing pulses which had

adjustable delays from the beginning of the Main Ring beam cycle.

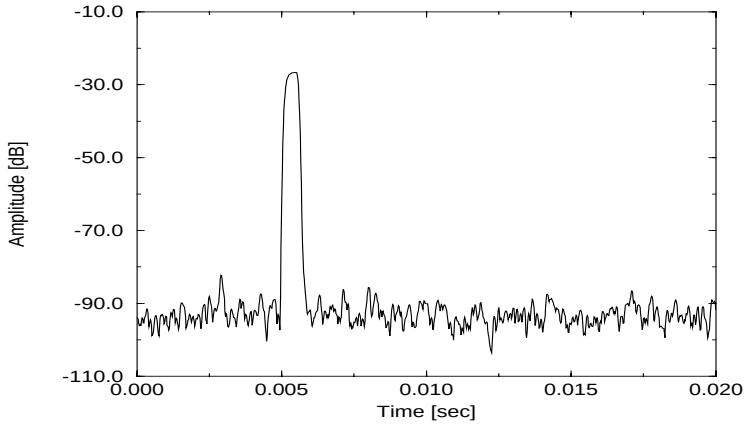

Figure 6.2: Fanback signal when a .5 ms drive pulse is applied to the Main Ring 5 MHz cavity. Spectrum analyzer setup: Center frequency at h=106, Frequency span=0 Hz, Resolution bandwidth=10 kHz, Sweep time=20 ms.

There was no significant distortion of a driving pulse applied to the Main Ring 5 MHz coalescing cavity. This can be seen in figure 6.2, which shows the cavity fanback signal while the drive pulse was being applied to the cavity. The drive pulse was at frequency h=106, and the spectrum analyzer trace in figure 6.2 shows the power level of the fanback signal at the same frequency.

In order to determine the quality of the frequency isolation, nearby harmonics were also examined while driving the cavity at h=106. The results are shown in figure 6.3. Most of the unwanted power was in the adjacent harmonics which were down by 20 dB. While this is not perfect isolation, it was sufficient for the nature of the studies undertaken.

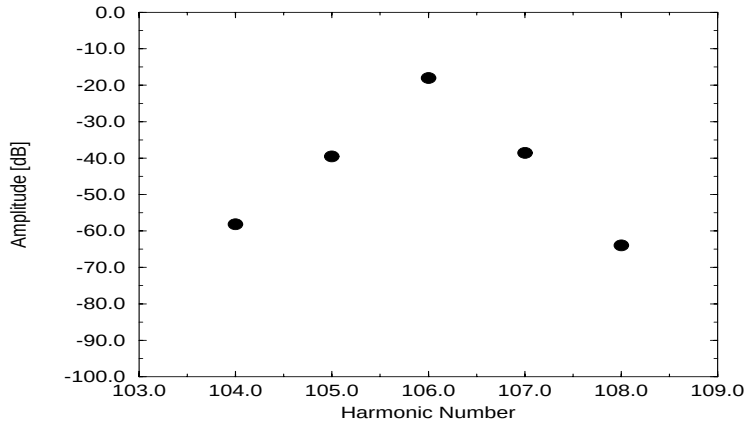

Figure 6.3: Examination of the frequency isolation of the 5 MHz cavity: amplitude of the Main Ring cavity fanback signal at several harmonics while driving the cavity at h=106.

6.3 Mode coupling cascades

Longitudinal mode growth after a short, single frequency excitation develops in time as a cascade from higher to lower harmonics. Studies, whose results will be presented here, show that after a drive pulse at $h = 106$, coherent motion occurs first at $h = 106$, and then downward through a succession of additional harmonics. There seems to be no significant coupling of the motion to the high frequency side of mode 106.

The drive pulse, with a duration of .5 ms, together with the beam response at the drive frequency, are shown in figure 6.4. Both curves are spectrum analyzer traces of power at harmonic 106 versus time. The trace of the drive pulse was obtained by looking at the cavity fanback as the pulse was applied to the cavity, while the trace of the beam response came from the longitudinal beam detector. The two curves are overlaid, but the relative timing is correct, since in both cases the same trigger and sweep time were used.

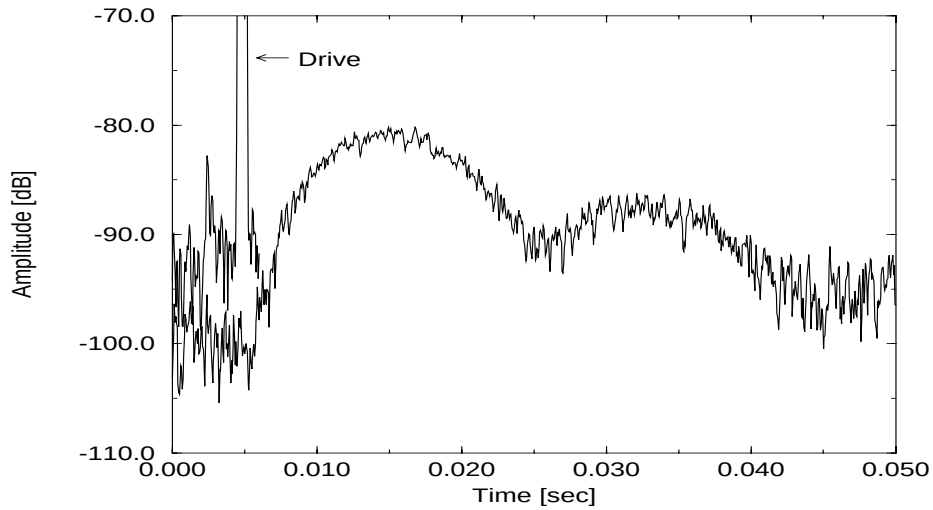

Figure 6.4: Power versus time at $h = 106$ in response to a .5 ms drive pulse. There are two overlaid traces in this figure, each was taken with the same trigger and with the same sweep time. One trace is the power versus time at $h = 106$ as seen on the longitudinal detector signal. The other is the cavity fanback signal at $h = 106$.

As seen in figure 6.4, the peak response of the beam at $h = 106$ occurs about 10 ms after the drive pulse is over. In addition, rather than exhibiting a smooth rise and decay of signal power, the trace shows a 'bouncing' effect. The application of voltage to the cavity acts to bunch some fraction of the beam. There is an ensuing rotation of these particles in the bunched beam phase space in which particle clumping in the time dimension evolves into clumping in the energy dimension. As particle clumping in time increases, the instantaneous beam current passing through the detector increases, causing a larger signal. The exchange between energy and time creates an apparent modulation on the overall decline of power in the beam. In spite of the short drive pulse, the evidence shows that mode 106 is subject to nonlinear Landau damping. The coherent oscillation damps significantly more slowly than the linear Landau damping

time, which is $\tau_{landau} = .011$, according to eq. 7.7. This result is expected in light of the bunch structure modulation, which indicates that the initial beam distribution has been significantly altered.

Figure 6.5 has been included since it shows signal modulation due to bunching particularly clearly. It also shows coherent motion lasting long after the drive pulse had terminated, which requires the presence of wakefields. Notice that as the peak power in the signal declines, the 'bounce' frequency decreases, an indication that the wakefield voltage is also decreasing.

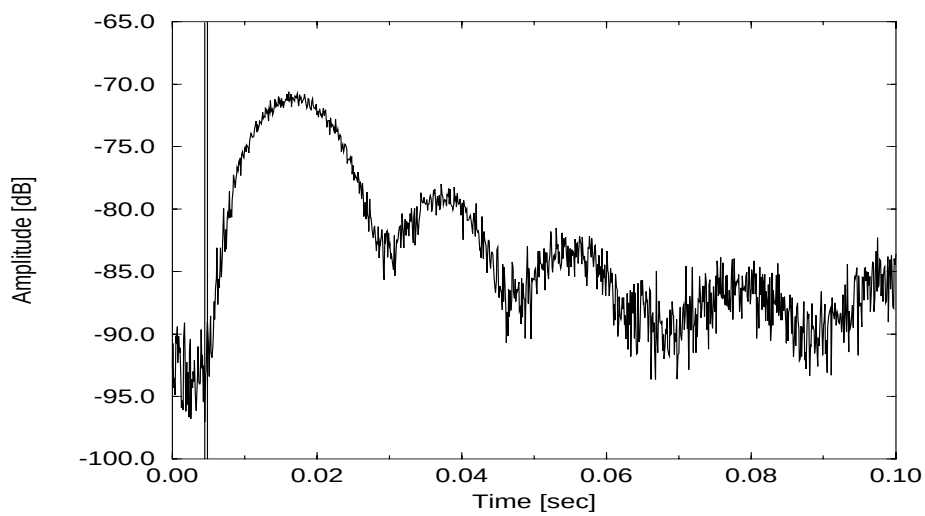

Figure 6.5: Power versus time at $h = 105$ in response to a .5 ms drive pulse. The placement of the drive pulse has been drawn in for reference (located at .005 sec).

The cascade of mode excitation occurring after the drive pulse is shown in figure 6.6. Eight traces of the evolution of power in harmonics 106-99, having the correct relative timing are displayed. Since the complete figure is complex, the power evolution in only the odd harmonics is shown in figure 6.7. It can be seen in either of

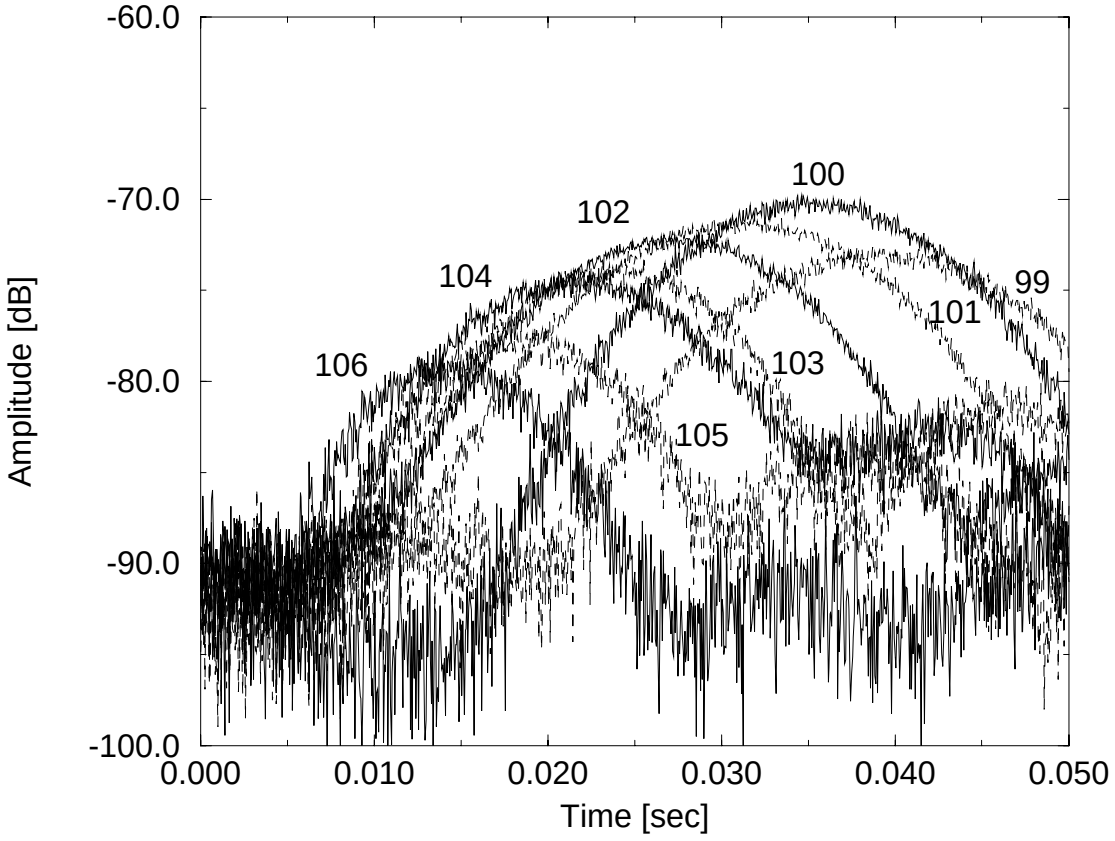

Figure 6.6: Power in all excited harmonics versus time in response to a .5 ms drive pulse. Even harmonics are represented by a solid line, odd harmonics by a dashed line.

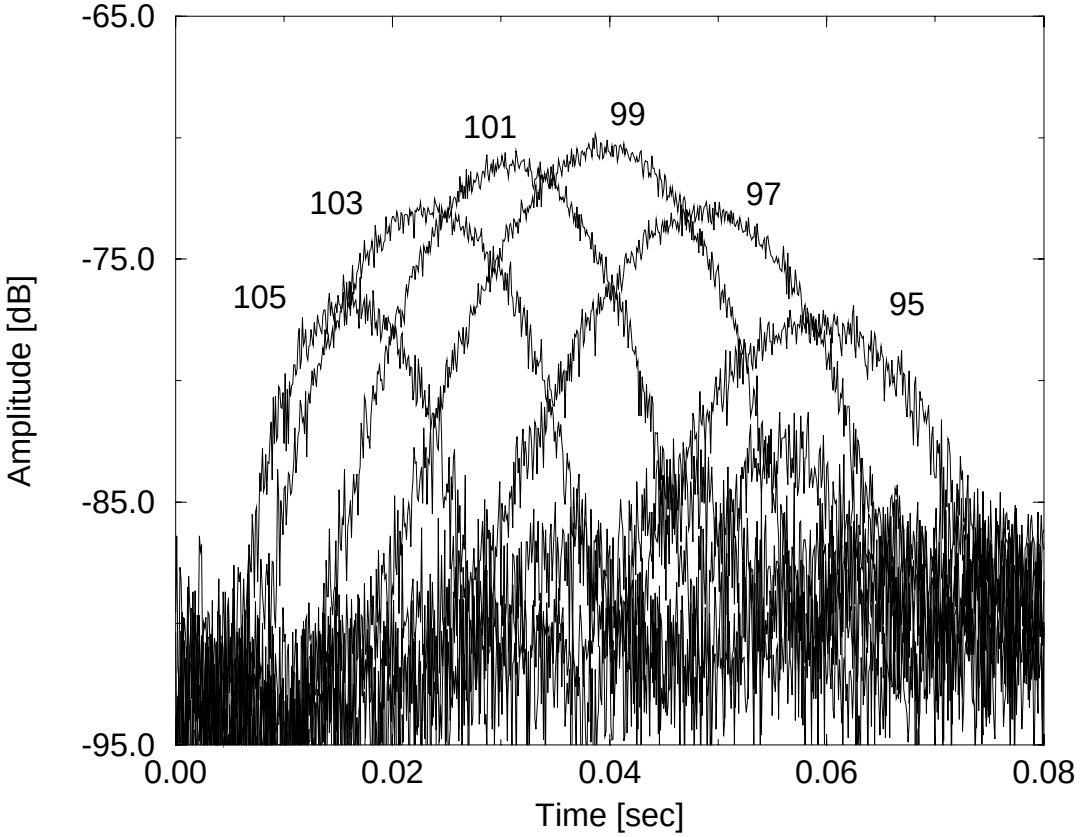

Figure 6.7: Power versus time at odd harmonics in response to a .5 ms drive pulse

figures 6.6 or 6.7, that the mode growth is sequentially downward, with each mode reaching its peak and then declining as lower harmonics grow in their turn. Each mode peaks at a different power level, the level of the peak increasing from $h = 106$ to $h = 100$. Afterwards, the peak power decreases again down through $h = 95$, which is close to the last mode to be excited with this short drive pulse.

One purpose of figure 6.8 is to demonstrate the single sided nature of the growth of the coupled modes. The top plot of the figure shows peak power versus harmonic number, while the bottom plot shows the time to reach peak power versus harmonic number. Only those harmonics whose peak power was arguably above the noise floor have been plotted. As can be seen in figures 6.6 and 6.7, the noise floor is somewhere around -95 dB. While there was a slight increase in power in a few of the harmonics above $h = 106$, the peak power in these harmonics was only slightly above the noise, and may have been due to imperfect frequency isolation in driving the cavity. The conclusive evidence that these higher harmonics were not coupled into $h = 106$ in the same way as the lower harmonics, can be seen in the bottom plot of figure 6.8. The time to the peak power for harmonics 107 and 108 was roughly the same as for harmonic 106. In contrast, all harmonics lower than 106 reached their peaks later and in sequence.

Assuming that frequency mixing was responsible for the excitation of multiple harmonics, the orderly cascade of energy through the lower modes suggests that $h = 1$ was the third wave in each of these coupling events. Depending on the initial distribution of power, each instance of coupling may have been either a wave scattering or decay. The high frequency wave could have decayed into two lower frequency waves,

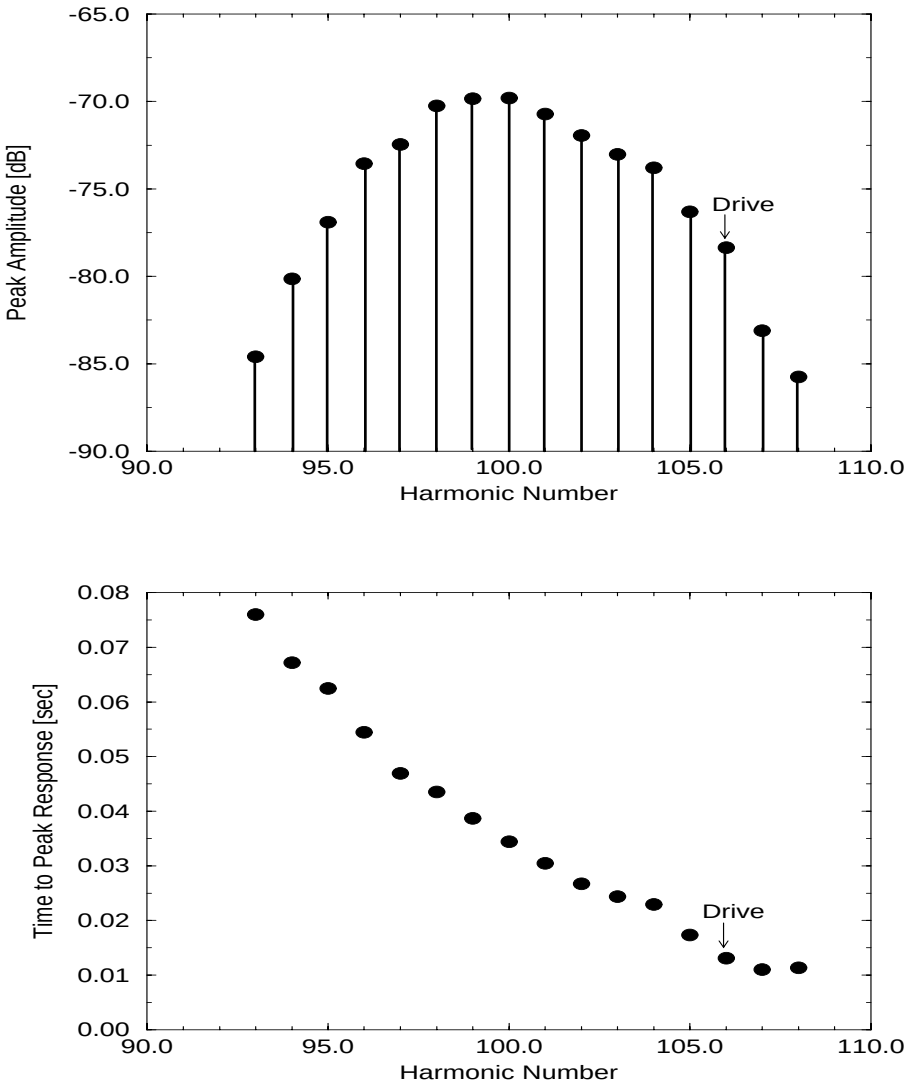

Figure 6.8: The top plot shows peak power at the harmonics excited during parametric coupling. The bottom plot shows time to peak power at these harmonics. The drive voltage was a .5 ms pulse applied at $h = 106$.

one of which was the $h = 1$ mode. Symbolically,

$$\begin{aligned} \omega_{106} &\rightarrow \omega_{105} + \omega_1 \\ \omega_{105} &\rightarrow \omega_{104} + \omega_1 \\ &\vdots \end{aligned}$$

Alternatively, the high frequency wave could have scattered with a wave at $h = 1$, producing the next lower harmonic. Symbolically,

$$\begin{aligned} \omega_{106} - \omega_1 &\rightarrow \omega_{105} \\ \omega_{105} - \omega_1 &\rightarrow \omega_{104} \\ &\vdots \end{aligned}$$

In either case, the pattern of excitation is consistent with the frequency selection rule required for parametric coupling. The distinction between scattering and decay can only be made by understanding the direction of power flow. The scattering process would require that the $h = 1$ mode be initially coherent, and remain coherent throughout the time of the cascade. In principal, conservation of energy could be used to make this determination, since power in the $h = 105$ mode would be greater if energy were flowing in from both the $h = 106$ and $h = 1$ modes. However, the actual storage ring has dissipation which removes energy from the system, and impedance which enhances the wave motion. These effects have not been quantified..

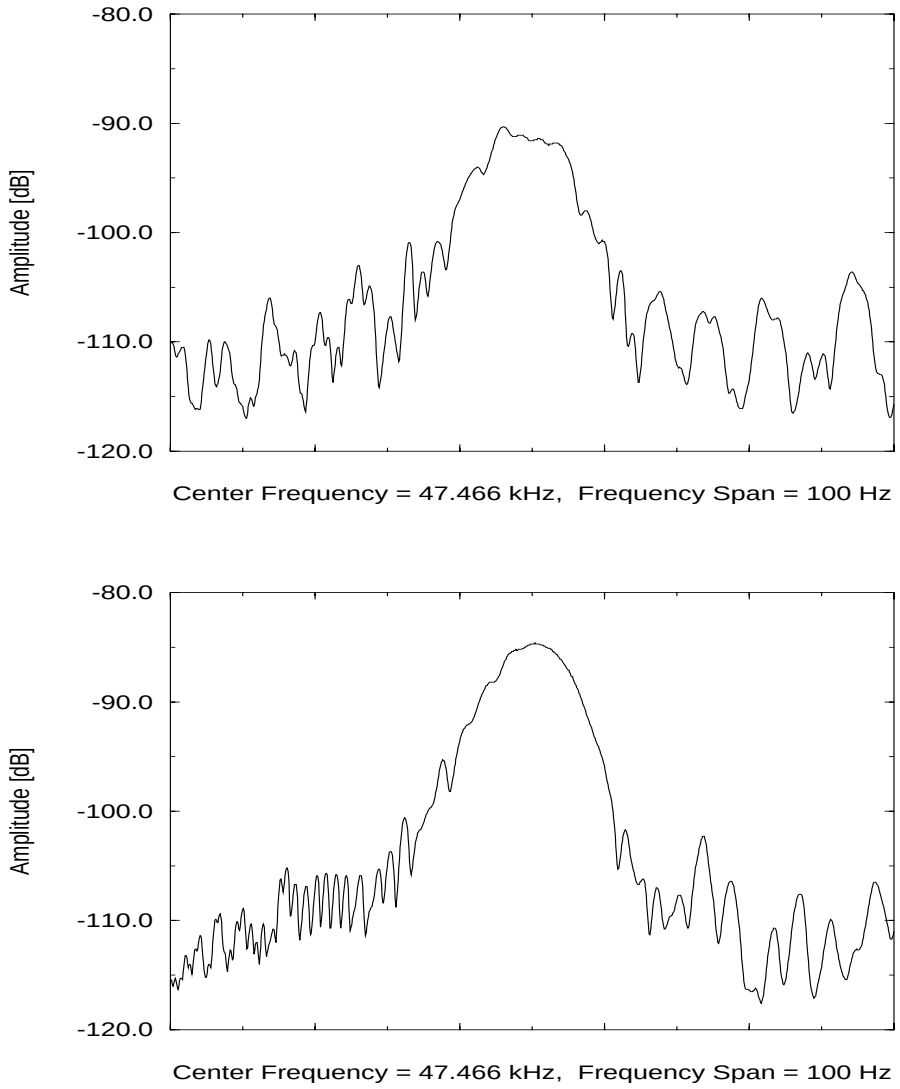

Figure 6.9: The top spectrum analyzer trace shows power at $h = 1$ when the beam was unbunched, and the bottom trace shows power at $h = 1$ for a bunched beam. The sweep time was 3 seconds and the resolution bandwidth was 10 Hz.

Power measurements at $h = 1$ indicate that wave scattering is possible in the Main Ring. Even with an unbunched, low intensity beam, there was enough power in the $h = 1$ mode that the signal was significantly above the noise floor. The two spectrum analyzer traces in figure 6.9 show power measured at $h = 1$ for bunched and unbunched beams. The intensity during the scan was 3.6E11 ppp. The power at $h = 1$ versus time was also measured. Although the power did decrease slowly by about 20 dB from the level at injection, at the end of the beam cycle the signal was still 15-20 dB above the noise floor. The $h = 1$ mode was also examined during the parametric process, with no detectable change in the signal level. It is possible that the additional energy gain from a parametric decay was too small to be resolved, but it seems more likely that $h = 1$ is continuously coherent, providing an available partner for frequency mixing.

6.4 The role of impedance in coupling

Parametric coupling can only transfer coherent energy between different modes, it cannot cause damping or amplification of the total mode energy of the system. There must be other sources to drive coherent oscillations. Although a .5 ms drive pulse was provided to initiate mode growth during the coupling experiments, the effect of the pulse was enhanced by wakefields.

Although the coalescing cavity was being used as the beam kicker, it also provided impedance which amplified the mode coupling. After an initial perturbative impulse, the cavity supports wakefield generation, which in turn causes the self-bunching responsible for coherent signals. The role of the cavity during the parametric coupling cascade is shown in figure 6.10, where the frequency response curve of the cavity is

superimposed on the power spectrum of the beam during parametric coupling.

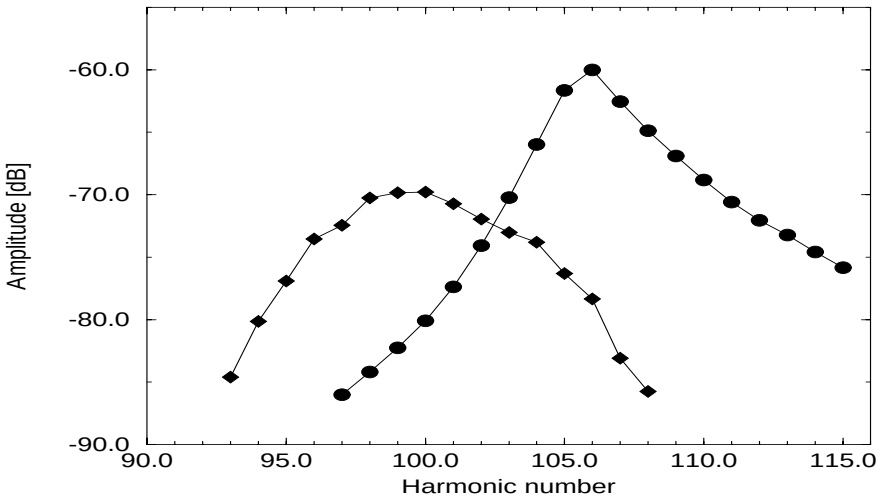

Figure 6.10: Superposition of maximum power spectrum of beam after .5 ms drive pulse (diamonds), and the frequency response of the cavity (circles). The absolute scale of the y-axis corresponds to the curve for the beam spectrum, the cavity response curve has been offset by -60 dB for viewing convenience.

The peak signal level of modes within the cavity bandwidth grows from harmonic to harmonic in the direction of the power flow. Energy at the driving frequency gets coupled into $h = 105$, where the cavity supports mode growth. There is then more energy available for transfer into $h = 104$, which also grows due to the cavity impedance. This continues, the mode growth slowing down as the frequency shifts away from the center frequency of the cavity. Once outside the cavity bandwidth, the peak signal level of successive harmonics then declines as the coherent mode energy dissipates away. When the initial driving signal approximates an impulse, the shape of the cascade of parametric coupling events is determined by the machine impedance (plus dissipative effects and the cumulative effect of the contribution from $h = 1$).

The slope of the energy change during the cascade gives a good qualitative picture of the nature of the machine impedance.

Additional evidence as to the role of the cavity impedance is shown in figure 6.11. The peak power in two selected harmonics is plotted as a function of the frequency

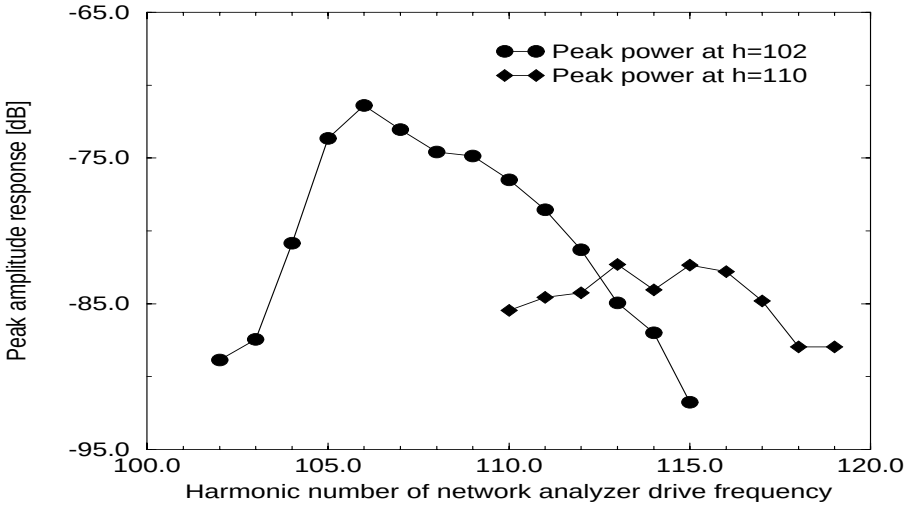

Figure 6.11: Peak power at harmonics 102 (circles) and 110 (diamonds) as the frequency of the driving pulse is varied.

of the driving pulse, which is varying for this particular study. The two harmonics chosen for monitoring were on the upper and lower side of the center frequency of the cavity (lower:106-4=102, upper:106+4=110). Due to the single-sided nature of the mode coupling, the lower harmonic (102) could receive energy when the drive frequency fell within the center of the cavity bandwidth, while the higher harmonic (110) could only receive energy when the drive frequency fell on the tail of the cavity bandwidth. The mode growth at $h = 102$ could be fully amplified by the cavity impedance, while that at $h = 110$ could not.

During the majority of the parametric coupling studies, the beam was stimulated by a short perturbative pulse. The coherent response of the beam quickly dissipated once the coupling reached harmonics outside the range of the cavity impedance, as shown in figure 6.10. However, during one study a continuous voltage wave was applied, rather than a gated pulse. In this case, the parametric coupling was seen to continue down through many harmonics outside the range of the cavity impedance.

6.5 Threshold measurements

There were a few studies aimed at addressing the question as to whether there is a threshold condition for the parametric process in the Main Ring. One of these was to slowly increase the power in the driving voltage while looking for mode growth. Power was increased by changing the attenuation on the drive signal. As seen in figure 6.12, even before a coherent signal is discernible at the drive frequency ($h = 106$), mode growth is detectable at the coupled frequencies.

Another study was to lower the beam intensity in an attempt to drop below the coupling threshold. The power of the mode response for harmonics 105, 106, and 107 versus the beam intensity is shown in figure 6.13. Even at the lowest beam intensity, there was evidence of the coupling resonance.

Based on these studies, the Main Ring is already above the threshold for parametric coupling.

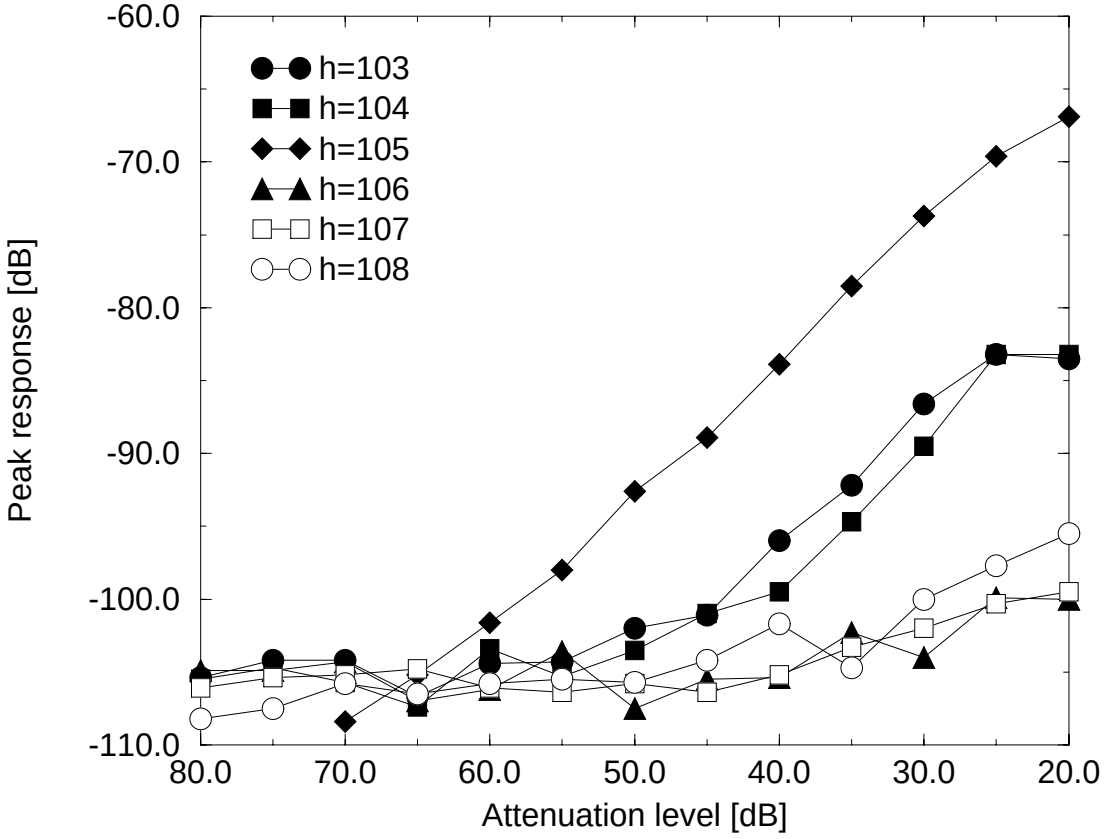

Figure 6.12: Peak signal power versus drive level for excited harmonics

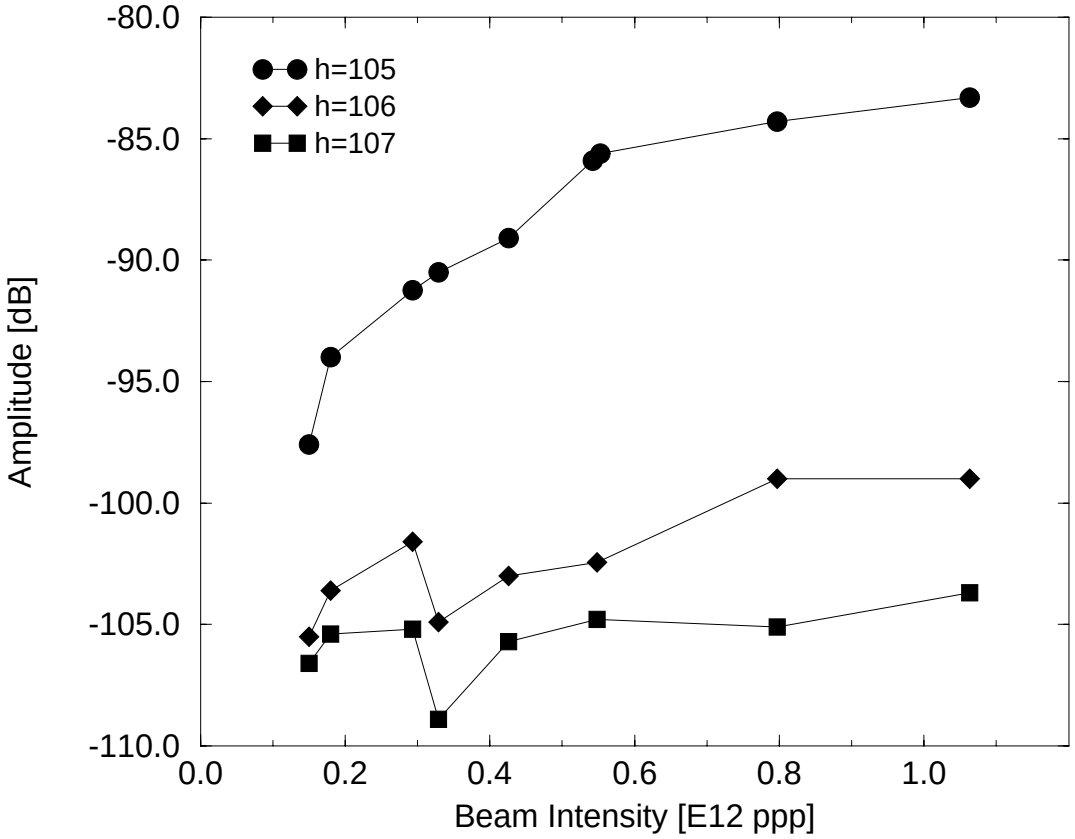

Figure 6.13: Peak signal power versus beam intensity for harmonics 105, 106, and 107.

6.6 Nonlinear wave-particle effects

Observation of 'bouncing' in the power signals of excited modes, along with the particle clumping and filamentation effects seen in a particle tracking simulation [46, 47], were invitations to experiment with greater driving voltages. The trapping of particles into bunchlets is an inherently nonlinear process, and for the case of low energy electron beams, has been demonstrated by O'Neil, Winfrey, and Malmberg [23] to generate a response at higher harmonics of the fundamental bunching frequency. The higher order harmonics are naturally coherent as a result of the newfound periodicity of the particle density, and are not due to an energy transfer from lower harmonics.

With sufficient driving voltage, higher harmonics of the parametrically coupled modes were detected in the Main Ring experiments. For example, with a 45 ms pulse, harmonics of up to 40 times $h = 105$ were excited. The relative power levels in several of these harmonics are plotted in figure 6.14. During this study, there was actually

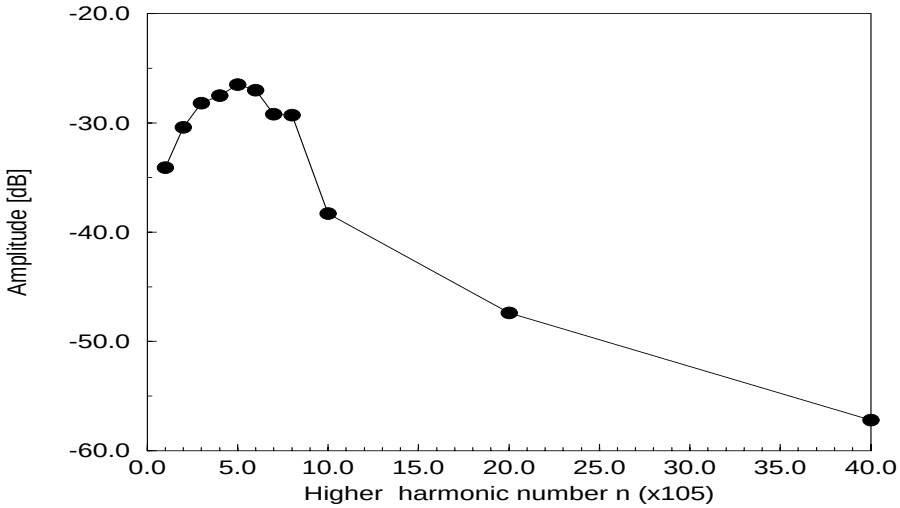

Figure 6.14: Peak power at the higher harmonics of $h = 105$.

more power in some of the higher harmonics of $h = 105$ than at the fundamental. These higher harmonics must be generated from nonlinear voltages which result from the bunching process itself, rather than through some type of higher order mode generation of the cavity. Evidence of this lies in the fact that the power spectrum of the higher order modes is consistent with the power spectrum of the beam at low frequencies (see figure 6.15). For example, $h = 107$ is not excited due to the single-sided nature of parametric coupling, and there are no higher harmonics of $h = 107$.

Another interesting investigation was to examine the effect that the width of the drive pulse had on the parametrically coupled modes. The magnitude response of $h = 105$ versus time for pulse widths of 10, 20, 40, and 80 ms is shown in figure 6.16. As the initial drive pulse increased, not only did the coherent motion due to the self-field persist for much longer, the synchrotron period of the bunched particles also increased. (Synchrotron period is accelerator physics terminology for the period of rotation between energy and phase of the particles in a bunched beam.) Note that for the responses shown in figure 6.16, the synchrotron period approximately doubles as the width of the initiating pulse is doubled. However, this series of measurements was somewhat fortuitous, as the evolution of the particle trapping and subsequent motion is also dependent on initial conditions, such as the energy spread of the beam. This can be seen in figure 6.17, where two identical 80 ms drive pulses initiated a different response pattern at the same harmonic. A different arrangement of trapped particles in phase space must be the cause of these variations in the signal modulation.

Particle tracking simulations with a machine impedance built into the beam dynamics suggested the possibility of an asymmetry in wakefield induced bunchlets

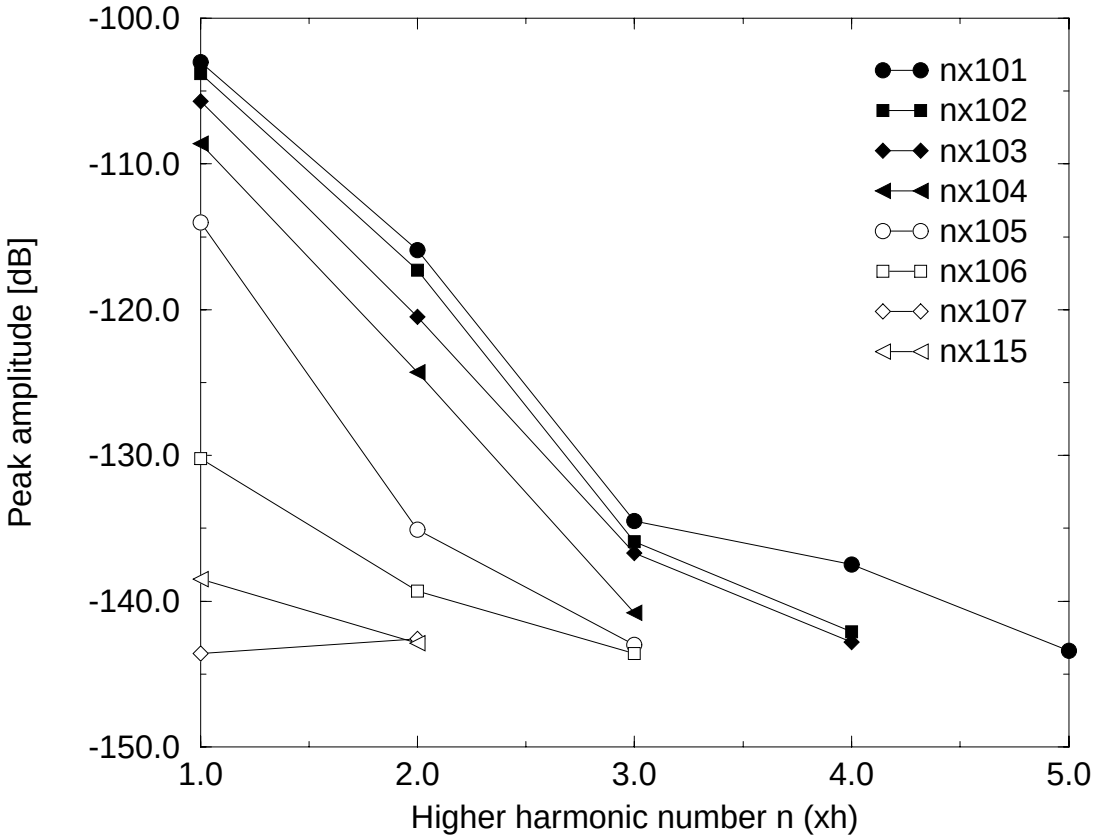

Figure 6.15: Peak signal power at higher order harmonics.

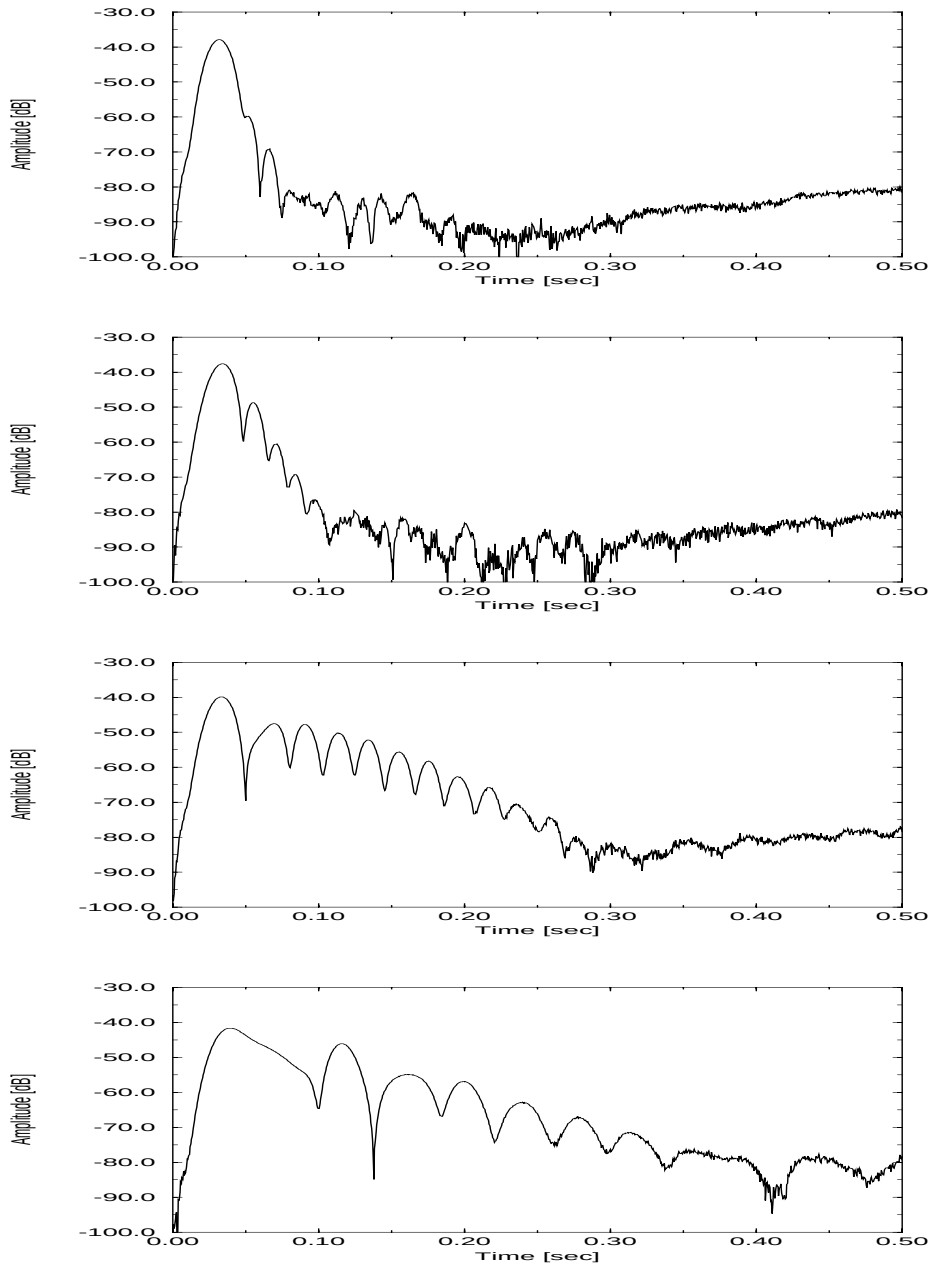

Figure 6.16: Power versus time at $h = 105$. Each trace was taken with a different drive pulse width. From top to bottom the pulse widths were 10ms, 20ms, 40ms, and 80ms.

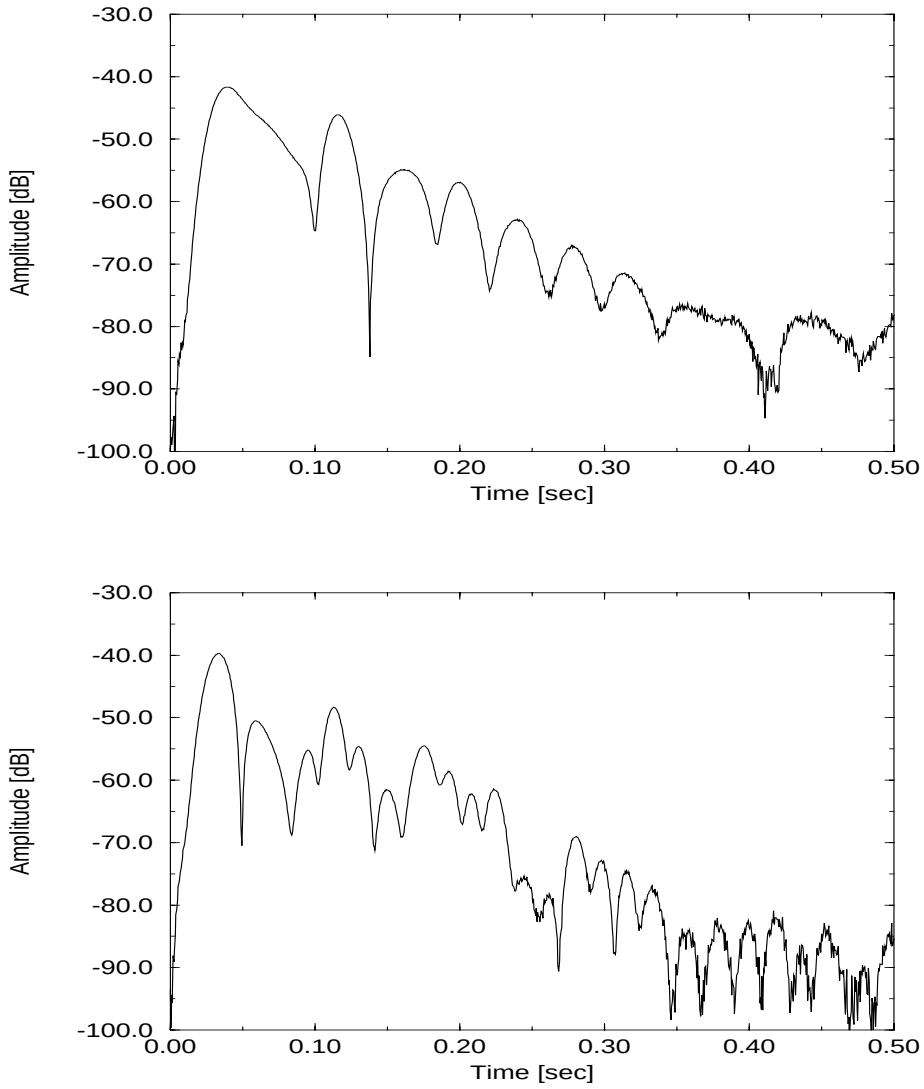

Figure 6.17: Power versus time at $h = 105$. Both traces were taken with an 80 ms drive pulse.

across the beam distribution. This asymmetry is a consequence of the impedance, which may have both resistive and reactive components. The phase evolution of particles on the high energy side of the beam distribution has the opposite sense with respect to an ideal particle than that of the particles on the low energy side. Particles on one side of the distribution or the other may be able to resonantly interact with the impedance. Whether it will be the higher or lower energy particles that experience a frequency shift due to energy exchange with the field, depends on whether the field is capacitive or inductive. It is possible for the combination of the nonlinearity of the wakefield voltage and the particle dispersion to trap a subset of particles. This coherent clump of particles may then undergo deceleration depending also on the resistive component of the wakefield.

It was feasible to look for the asymmetry demonstrated by the simulation, since the spectrum analyzer being used allowed resolution bandwidths down to 10 Hz. By setting the center frequency at different points across the frequency distribution of the beam, and then narrowing down the resolution bandwidth of the instrument, it was possible to monitor the time development of power in various fractions of the beam. Upon following this procedure at some of the higher harmonics (for example, h=5x105) the posited asymmetry was discovered. One such scan is shown in figure 6.18, where the three traces represent three frequency slices of the beam. The middle trace resulted when the center frequency of the spectrum analyzer was set to the center frequency of the chosen harmonic, which was 5x105. The center frequency of the upper trace was offset by +500 Hz, while that of the lower trace was offset by -500 Hz. The resolution bandwidth of the spectrum analyzer was set to 300 Hz.

Note that since the Main Ring was below transition in these studies, the high frequency side of the beam distribution corresponds to the high energy side of the beam distribution.

The power evolution of the high frequency side of the beam distribution exhibited a modulation which was not present at the center frequency or on the low frequency side. This modulation is reminiscent of the bunch rotation modulation seen on power signals exhibiting nonlinear Landau damping (discussed in section 6.3). This suggests that there were indeed small islands of particles in phase space, or bunchlets, that only developed on one side of the energy spectrum. The phase of the wakefield is indicated by the particular side of the energy spectrum on which the bunching occurs.

In order for groups of particles to remain clumped into bunchlets, there must be a nonlinearly generated voltage which at least compensates for the natural tendency of energy dispersion. If these bunches do not become narrower with time, then perhaps the nonlinear force of the wakefield is just balancing the energy dispersion effect. This behavior is similar to that of solitons, which have been studied in other areas of physics, and may be a fruitful area of future study.

This concludes the description of the nonlinear studies which were carried out in the Fermilab Main Ring. Attention will now be turned to another manifestation of weak wave-wave coupling that may be seen in particle beams, namely, beam echoes.

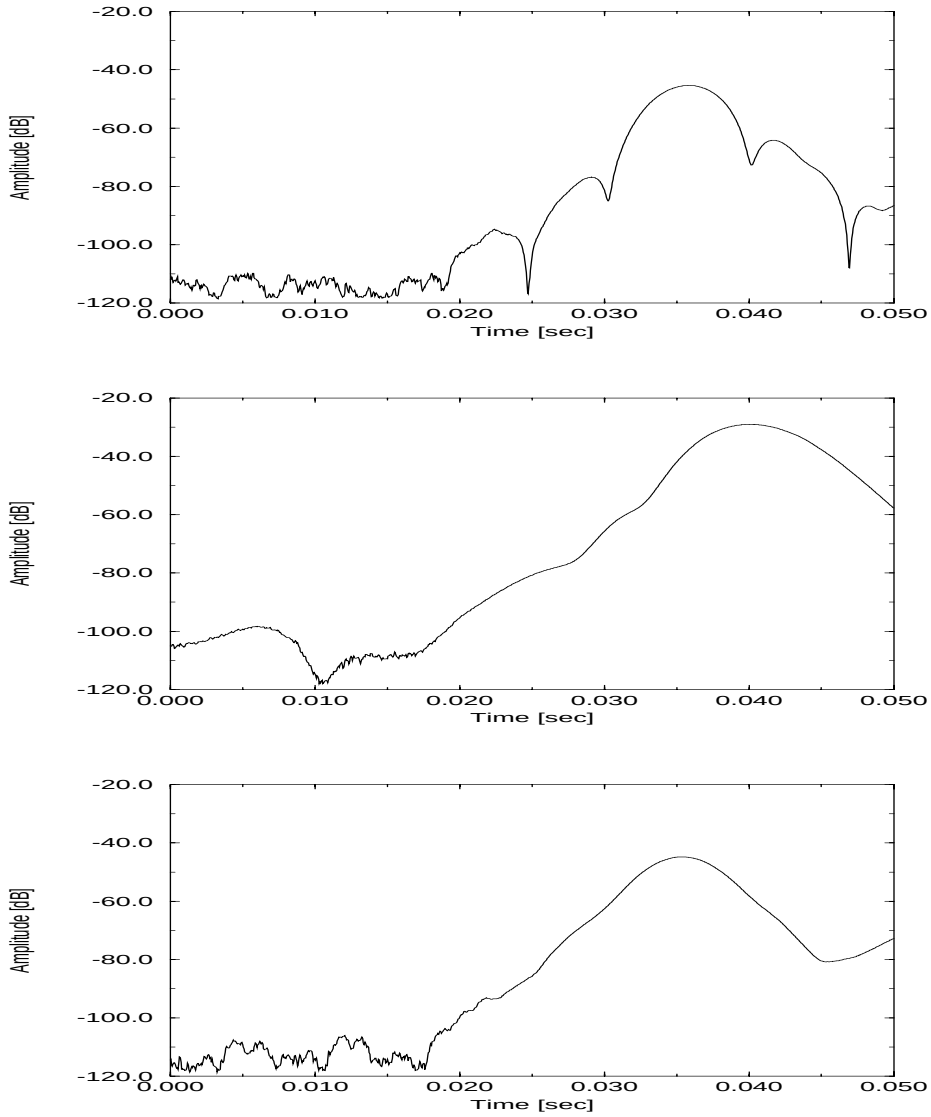

Figure 6.18: Power versus time in cross-sectional frequency slices of the beam. In the middle plot the center frequency is $h = 5 \times 105 = 24.9$ MHz, while in the top plot cf=$(5 \times 105) + 500$ Hz (this is the higher energy side of the distribution), and in the bottom plot cf=$(5 \times 105) - 500$ Hz. The resolution bandwidth of the spectrum analyzer was set to 300 Hz.

Chapter 7

Theory of echoes

7.1 Introduction and overview

An echo in a particle beam is a coherent current oscillation, occurring with some delay after a sequence of two independent pulse excitations. The beam response to a longitudinal kick naturally decoheres, with a decoherence time that is inversely proportional to the energy spread of the particles in the beam. Damping due to a spread in the natural frequencies of a system is generally called Landau damping. A key characteristic of Landau damping is that although the coherent motion damps, the phases of the particles remain correlated. Due to this correlation, the phase evolution of the decoherence is reversible. An echo is a partial reconstruction of the particle phase relations present during the coherent motion from the initial kicks. This reconstruction normally occurs some time after the beam response to the kicks has damped away, the coherent motion of the echo growing in the absence of direct excitation.

Echoes are enabled by frequency mixing of the two initial pulse excitations. As such, echo phenomena are directly related to parametric 3-wave coupling, although they are best described with time domain analysis. Echoes arise from a specific temporal flow of events; the phase evolution of the particles following the first kick is modified by the action of the second kick in such a way as to reconstruct a coherent oscillation at the mixing frequency. Echoes have been observed and studied in other areas such as nuclear magnetic resonance [14] and plasma physics [15]. It is also possible to study beam echoes in transverse phase space [17, 18], as well as in the longitudinal phase space of a bunched beam [19].

Longitudinal echoes in an unbunched beam have been seen with good clarity in the Fermilab Accumulator. The frequency of these echoes was the difference frequency of the applied excitations. Both the timing of the echo and its amplitude can be theoretically predicted. The time delay to the echo has a simple linear dependence on the frequencies and the pulse separation of the applied excitations. The amplitude dependence is more complicated, and in some cases depends on factors other than the kick parameters. Echo generation relies on the phase relationship of the particles not becoming disrupted. Processes such as small angle coulomb scattering (intrabeam scattering) will decrease the echo amplitude, completely eradicating it if either the collision rate is high enough, or the echo delay is long enough. The measurement of the decay of the echo amplitude thus allows the opportunity to determine the diffusion rate in a beam.

As delineated in Lifshitz and Pitaevskii [48], one of the simplest physical systems allowing the presence of echoes is a collisionless, neutral gas. Section 7.2 goes through this example for the purpose of presenting the basic features of the echo mechanism

with a minimum of complication. The gas particle density is modulated by two purely sinusoidal continuous excitations of differing wave numbers. One of the excitations starts with some delay after the other. This example shows that although the particle distribution retains information from the modulations on a microscopic level, the macroscopic perturbations of the gas density damp with characteristic damping rates. The coherent response due to the frequency mixing of the two excitations happens at a specific time, t_{echo}. This is calculated and shown to depend on the wave numbers of the two excitations, and on the time delay to the start of the second excitation. The physical principles as well as the form of the result for t_{echo} are the same as those in the later particle beam examples.

The extent of the mathematical treatment of echo generation in high energy particle beams depends on what dynamical processes are playing a role in the particle motion. The simplest situation is that in which the initial particle distribution is affected only by the externally applied excitations. The distribution then evolves in a free-streaming manner since no self-fields are generated, and the self-consistent Vlasov treatment is not necessary. A treatment of beam echoes neglecting wakefields and particle collisions is given in section 7.3, which follows the method used by T.M. O'Neil [16]. The external excitations used for the beam studies in this work were short kicks approximating impulse excitations. Although the analytic method in section 7.3 is similar to Lifshitz and Pitaevskii, the nature of the applied excitations is more suitable for the beam case. In order to examine the perturbed beam current at a certain frequency, a Laplace transform of the beam distribution is done to pick out the desired mode. The kicks, while still sinusoidal, are of finite duration and cause a discrete phase change, which then evolves accordingly. The damping time constant,

or Landau damping time, of the coherent beam response to a single kick is calculated.

The response at the echo frequency is examined in some detail. The dependence found for t_{echo} is the same as in the example of section 7.2, but the amplitude of the echo now has a Bessel function dependence. In addition, as a consequence of the short pulse lengths, higher order echo generation is also possible. These higher order echoes have frequencies which are combinations of multiples of the frequencies of the driving pulses. If the applied kicks are sufficiently weak, then this general result may be simplified for the perturbative case, by approximating the Bessel function dependence with the first term of the expansion.

A treatment of beam echoes which includes wakefield effects was done by P. Colestock and is presented in section 7.4. Analysis allowing for wakefields begins with the Vlasov equation. Since echoes are a frequency mixing effect, in a perturbative treatment, the second order equation is required. Barring any collisional terms, this equation would be the same as eq. 5.3. The result for the echo current amplitude obtained with this method is favorably compared in the limit of no wakefields to the result of section 7.3 for weak kicks.

Finally, in section 7.5 the continued analysis of P. Colestock which includes both wakefields and collisional effects on the beam dynamics is examined. In order to include diffusion in the beam dynamics, collisional terms (which can be represented by the Fokker-Planck operator [12]) are added to the Vlasov equation. This transport equation which includes collisions is now called the Boltzmann equation [50]. A calculation of the echo current amplitude beginning with the Boltzmann equation is done in 7.5. The analysis technique is the same as that used in section 7.4, only somewhat more cumbersome due to the extra collision terms in the initial equation.

The disadvantage of this treatment is that the Boltzmann equation cannot be easily solved analytically without a perturbative expansion of the dependent variables. As long as the kick strength is small enough, the results of this method are valid.

Once the general solution for the echo current is found, it is then examined in the limit of no wakefields. Wakefields were not a significant factor in the Accumulator echo experiments presented in this work. Neglecting wakefields in the solution for the echo current curtails the work needed to extract relationships for specific measurable parameters, such as t_{echo}, and the diffusion rate. In chapter 8, these analytic results are compared with the experimental data.

7.2 Simple example of a collisionless neutral gas

Echoes can occur in a gas of uncharged particles which are not undergoing collisions. The echo mechanism is purely kinematic and may be investigated in a single plane having phase space variables x and p. The gas is initially spatially uniform with a Maxwellian distribution in momentum,

$$f_0(p) = A_0 e^{-\frac{p^2}{2mk_BT}} = A_0 e^{-(\frac{\alpha}{2m})^2 p^2}$$

In general, the distribution function is integrated over momentum to give the number of particles per length,

$$n = \int_0^\infty f(x,p)\,dp$$

A sinusoidal perturbation with wave number k_1 is applied at $t = 0$, modulating the unperturbed particle distribution,

$$f(x,p) = A_1 \cos\left[k_1(x - \frac{1}{m}pt)\right] f_0(p)$$

The applied perturbation also produces a modulation of the density of the gas. Although f remains oscillatory, the density perturbation damps,

$$\begin{aligned} n &= A_1 \mathrm{Re}\left[e^{ik_1 x}\int_0^\infty e^{-i\frac{k_1}{m}tp} e^{-(\frac{\alpha}{2m})^2 p^2}\, dp\right] \\ &= a\mathrm{Re}\left[e^{ik_1 x} e^{-\frac{k_1^2 t^2}{\alpha^2}}\right] \end{aligned}$$

The oscillation is damped by an exponential in t^2, with a damping time constant of $\frac{\alpha}{k_1}$. This damping, or decoherence, of the density fluctuation is considered to be Landau damping in the free-streaming limit, where there is no exchange of energy between the particles and an external wave. A second perturbation with a different wave number, k_2, is applied at $t = \Delta t$. This second perturbation modulates the already modulated particle distribution,

$$\begin{aligned} f &= A_2 \cos\left[k_2(x - \frac{1}{m}p(t-\Delta t))\right] A_1 \cos\left[k_1(x - \frac{1}{m}pt)\right] f_0(p) \\ &= \frac{1}{2}A_1 A_2 f_0(p)\left\{\cos\left[(k_2 - k_1)x - (k_2 - k_1)\frac{p}{m}t + k_2\frac{p}{m}\Delta t\right]\right. \\ &\quad \left. + \cos\left[(k_2 + k_1)x - (k_2 + k_1)\frac{p}{m}t + k_2\frac{p}{m}\Delta t\right]\right\} \end{aligned} \tag{7.1}$$

The trigonometric angle sum and difference relations have been used to write the product of cosines as the sum of two cosine terms. This is a mathematical statement that the presence of excitations at wave numbers k_1 and k_2 produces modulations of the gas at the mixing frequencies, $k_2 - k_1$ and $k_2 + k_1$. Normally, macroscopic fluctuations of the gas density at these frequencies would not be detectable, since each of the oscillatory terms time-averages to zero. However, the time oscillation of the first cosine term vanishes under the following condition,

$$t = \frac{k_2}{(k_2 - k_1)}\Delta t \tag{7.2}$$

When eq. 7.2 is satisfied, there is no time dependent portion in the first cosine term of eq. 7.1, and this in turn removes any damping effect on the density function. Thus, a large coherent response is enabled in the gas at a specific time, t_{echo}, which is given by eq. 7.2. The time of the echo is dependent on the wave numbers of the two excitations, as well as on their relative timing. If the wave numbers are assumed to be positive, then in order to have an echo, k_2 must be greater than k_1 (otherwise t_{echo} will be negative).

When the wave numbers are positive, under no circumstance can the second cosine term of eq. 7.1 cause an echo. In order for the time dependent part of this oscillation to vanish, the following condition must be met,

$$t = \frac{k_2}{(k_2 + k_1)}\Delta t$$

This gives an echo time which comes before the second excitation, since $\frac{k_2}{(k_2+k_1)}$ is less than one.

This neutral gas has demonstrated several important features of echo generation which are characteristic of the echo mechanism itself, holding broadly for different systems and forms of excitation. An echo is enabled through frequency mixing, hence the echo frequency is the difference frequency of the applied excitations. The time of the echo is given by eq. 7.2, where k_1 and k_2 will in general be the harmonic numbers of the excitations. The coherent particle density fluctuation which is the echo occurs even when the response to the initial excitations has damped away.

7.3 Beam echoes without wakefields or collisions

This section will explore the nature of longitudinal echoes in a particle beam, when the dynamics are unaffected by wakefields or diffusion effects. In a beam, it is more feasible to create temporal, rather than spatial, echoes. Temporal echoes require short pulse excitations, which are impulse approximations. Since the kicks are narrow bursts, higher harmonics are also present, allowing the generation of higher order echoes. Having a short pulse rather than a continuous excitation gives the echo amplitude response a Bessel function dependence. Experimental conditions in the Accumulator were such that the echo width was much shorter than the time scale associated with the first zero of the Bessel function. Multiple echoes at different echo times were necessary to determine larger scale structure such as a Bessel function dependence.

A pair of applied kicks will alter the phase development of particles within the beam. In the absence of any external excitation, the phase evolution of a particle is

given by,

$$\begin{aligned}\theta &= \theta_i + \omega_i(\varepsilon)t \\ &= \theta_i + (\omega_0 + k_0\varepsilon)t\end{aligned}$$

where θ_i is the initial phase, and ω_i is the initial frequency. The initial frequency is the revolution frequency, plus a small deviation which depends on the particle energy error, and on the constant scaling factor, k_0 (defined in eq. 2.2). A kick applied at $t = 0$ causes an energy change of $(\Delta\varepsilon)_1$, and a second kick applied at $t = \Delta t$ causes an energy change of $(\Delta\varepsilon)_2$. Now the phase evolution of a particle after the first kick is given by,

$$\theta(t) = \theta_i + \omega_i t + k_0(\Delta\varepsilon)_1 t$$

The phase evolution after the second kick is given by,

$$\theta(t) = \theta_i + \omega_i t + k_0(\Delta\varepsilon)_1 t + k_0(\Delta\varepsilon)_2(t - \Delta t)$$

This may be written as the sum of the initial phase at the time of the second kick, $\theta_{\Delta t}$, and the phase development thereafter,

$$\theta(t) = \theta_{\Delta t} + \omega_i(t - \Delta t) + k_0(\Delta\varepsilon)_1(t - \Delta t) + k_0(\Delta\varepsilon)_2(t - \Delta t) \tag{7.3}$$

where $\theta_{\Delta t} = \theta_i + \omega_i \Delta t + k_0 (\Delta\varepsilon)_1 \Delta t$. It is useful to express the time development of the phase in this way. If a kick is short enough, then the energy change due to the kick is dependent only on the particle phase at the time of the kick, not on the energy error of the particle at the time of the kick. An energy error causes the particle phase to slip, but if this phase shift is small during the kick, it may be neglected.

Let the kicks be short pulse excitations, both of duration ΔT_p, with each kick singular in frequency, and each having amplitude V_0. If the first kick is applied at the kth harmonic, and the second kick applied at the nth harmonic, the resultant energy changes are given by,

$$\begin{aligned}(\Delta\varepsilon)_1 &= \dot{\varepsilon}_1 \Delta T_p = \frac{e\omega_0}{2\pi} V_0 \Delta T_p \cos(k\theta_i) \\ (\Delta\varepsilon)_2 &= \dot{\varepsilon}_2 \Delta T_p = \frac{e\omega_0}{2\pi} V_0 \Delta T_p \cos(n\theta_{\Delta t})\end{aligned}$$

The perturbed particle density at a given harmonic, m, is given by,

$$n_m(t) = \int d\theta \int f(\theta, \varepsilon, t) e^{-im\theta(t)} \, d\varepsilon \tag{7.4}$$

The density perturbation after the first kick is then,

$$n_m = \int d\theta_i \int f_0(\varepsilon_i) e^{-im\left[\theta_i + \omega_i t + k_0 \frac{e\omega_0}{2\pi} V_0 \Delta T_p \cos(k\theta_i) t\right]} \, d\varepsilon_i \tag{7.5}$$

In order to evaluate eq. 7.5, use the following Bessel function identity,

$$e^{-iA\cos\vartheta} = \sum_l (-i)^l J_l(A) e^{-il\vartheta} \tag{7.6}$$

where ($l = 0, \pm 1, \pm 2, \ldots$). It is in this mathematical step where higher order harmonics come into the analysis. Now there are multiple sinusoidal terms at different frequencies, each of which eventually might contribute to echo generation.

Assume the beam distribution function is a Gaussian,

$$f_0(\varepsilon) = \frac{N}{(2\pi)^{\frac{3}{2}}\sigma_\varepsilon} e^{-\frac{1}{2}(\frac{\varepsilon_i}{\sigma_\varepsilon})^2}$$

The expression for n_m may be written,

$$\begin{aligned} n_m &= \frac{N}{(2\pi)^{\frac{3}{2}}\sigma_\varepsilon} e^{-im\omega_0 t} \sum_l (-i)^l J_l(m\frac{e\omega_0}{2\pi} k_0 V_0 \Delta T_p t) \\ &\times \int e^{-i(m+lk)\theta_i}\, d\theta_i \int e^{-imk_0\varepsilon_i t} e^{-\frac{1}{2}(\frac{\varepsilon_i}{\sigma_\varepsilon})^2}\, d\varepsilon_i \end{aligned}$$

The density fluctuation vanishes, and there is no perturbed current, unless $lk = -m$. In other words, when a kick acts on an unperturbed beam, the kick can only result in a perturbed current at harmonics of the mode number of the kick. In this analysis it can be assumed that the harmonic number k is positive with no loss of generality, since the Bessel function index multiplier l may be either positive or negative. If

$l = -1$, then $k = m$, and the instantaneous beam current at mode m is,

$$I_m(\theta) = iI_0 J_1(m\frac{e\omega_0}{2\pi}k_0 V_0 \Delta T_p t)e^{-im\omega_0 t}e^{-\frac{1}{2}(m\omega_0 \frac{\eta}{\beta^2}\frac{\sigma_\varepsilon}{E_0})^2 t^2}$$

where $I_0 = \frac{eN\omega_0}{2\pi}$ is the unperturbed beam current. Once again, the result is that in the absence of wakefields, the coherent oscillation resulting from a kick damps away. When an energy kick at mode m is applied to a beam, the damping time is,

$$\tau_{landau} = \frac{\sqrt{2}\beta^2}{m\omega_0 \eta \frac{\sigma_\varepsilon}{E_0}} \tag{7.7}$$

This expression for the damping time is useful in time domain measurements for gaining a qualitative idea of beam stability. If the motion from a kick decoheres within this characteristic time, it is evidence that self-field effects at this frequency are negligible. As the machine impedance at the kick frequency increases, so does the decay time of the coherent response.

The perturbed particle density at harmonic m after the second kick is found by again using eq. 7.4, but this time $\theta(t)$ is the phase evolution after the second kick (given by eq. 7.3),

$$\begin{aligned} n_m &= \int d\theta_i \int f_0(\varepsilon_i) e^{-im[\theta_{\Delta t} + \omega_i(t-\Delta t) + k_0(\Delta\varepsilon)_1(t-\Delta t) + k_0(\Delta\varepsilon)_2(t-\Delta t)]}\, d\varepsilon_i \\ &= \int d\theta_i \int f_0(\varepsilon_i) e^{-im(\theta_i + \omega_i t)} e^{-imk_0 tA\cos(k\theta_i)} e^{-imk_0(t-\Delta t)A\cos(n\theta_{\Delta t})}\, d\varepsilon_i \end{aligned}$$

where $A = \frac{e\omega_0}{2\pi}V_0 \Delta T_p$, is the energy amplitude of the kicks. Assuming a Gaussian

beam and using eq. 7.6, the expression for n_m becomes,

$$
\begin{aligned}
n_m &= \frac{N}{(2\pi)^{\frac{3}{2}}} \sum_{l_2} (-i)^{l_2} J_{l_2}(mk_0 A[t-\Delta t]) \\
&\times \sum_{l_3} (-i)^{l_3} J_{l_3}(mk_0 At) \sum_{l_4} (-i)^{l_4} J_{l_4}(l_2 n k_0 A \Delta t) \\
&\times \int e^{-i(m+l_2 n+(l_3+l_4)k)\theta_i} e^{-i\omega_0(mt+nl_2\Delta t} d\theta_i \int e^{-ik_0\varepsilon_i(mt+l_2 n\Delta t)} e^{-\frac{1}{2}(\frac{\varepsilon_i}{\sigma_\varepsilon})^2} d\varepsilon_i
\end{aligned}
$$

Notice that since the indices of the Bessel functions go up as the order of the echo harmonic; the amplitude of the beam response should be correspondingly smaller for the higher order echoes. Let $l_1 = l_3 + l_4$, and rewrite the expression for the echo current density using the following identity,

$$
J_\nu(u \pm v) = \sum_\mu J_{\nu\mp\mu}(u) J_\mu(v)
$$

Then,

$$
\begin{aligned}
n_m &= \frac{N}{(2\pi)^{\frac{3}{2}}\sigma_\varepsilon} \sum_{l_2} (-i)^{l_2} J_{l_2}(mk_0 A[t-\Delta t]) \sum_{l_1} (-i)^{l_1} J_{l_1}(k_0 A[mt + l_2 n\Delta t]) \\
&\times \int e^{-i(m+l_2 n+l_1 k)\theta_i} e^{-i\omega_0(mt+nl_2\Delta t)} d\theta_i \int e^{-ik_0\varepsilon_i(mt+l_2 n\Delta t)} e^{-\frac{1}{2}(\frac{\varepsilon_i}{\sigma_\varepsilon})^2} d\varepsilon_i \quad (7.8)
\end{aligned}
$$

Unless the argument of the θ exponent under the first integral in eq. 7.8 is zero, the density fluctuation will average to zero. Thus, to have an echo of any order, the

following phase matching condition must be satisfied,

$$m + l_1 k + l_2 n = 0$$

The last integral in eq. 7.8 produces a damping term, unless the argument of the sinusoidal term under this integral is zero. The time when there is no damping is the time of the echo. This is,

$$t_{echo} = -\frac{l_2 n \Delta t}{m} = \frac{l_2 n \Delta t}{l_1 k + l_2 n} \tag{7.9}$$

Again, it may be assumed that the mode numbers k and n are are positive, letting the indices l_1 and l_2 determine the signs of $l_1 k$ and $l_2 n$. Equation 7.9 for t_{echo} then says that in order to have an echo, l_1 and l_2 must be of opposite signs.

Suppose that $l_1 = -1$ and $l_2 = 1$, then the phase matching condition becomes $m = k - n$, and the time of the echo is given by,

$$t_{echo} = -\frac{n}{m}\Delta t = \frac{n}{n-k}\Delta t$$

This result for the echo time is the same as that found in the system of gas particles described in section 7.2.

After two initial pulses at modes k and n, the instantaneous beam current is given by,

$$I_m(\theta) \quad = \quad \left(\frac{eN\omega_0}{2\pi}\right) J_1(\frac{e\omega_0}{2\pi} k_0 V_0 \Delta T_p[mt - m\Delta t]) J_1(\frac{e\omega_0}{2\pi} k_0 V_0 \Delta T_p[mt + n(\Delta t)])$$

$$\times \exp\{-i\omega_0(mt + n(\Delta t)\} \exp\{-\frac{1}{2}(k_0\sigma_\varepsilon)^2(mt + n\Delta t)^2\} \tag{7.10}$$

This result is similar to that obtained by Brüning [49]. For small kicks the Bessel functions may be approximated, and the echo current then becomes,

$$I_m(\theta) = I_0 \left[\frac{1}{2}\frac{e\omega_0}{2\pi}V_0(\Delta T_p)k_0\right]^2 m[t - \Delta t][mt + (k - m)(\Delta t)]$$

$$\times \exp\{-i\omega_0[mt + (k - m)\Delta t]\} \exp\{-\frac{1}{2}(k_0\sigma_\varepsilon)^2[mt + (k - m)\Delta t]^2\} \tag{7.11}$$

where $I_0 = \frac{eN\omega_0}{2\pi}$ is the unperturbed beam current. During the Accumulator echo studies, the time independent portion of the argument of the Bessel functions typically had a value of .49, so the small kick approximation roughly held. Notice that at exactly t_{echo}, the echo current goes to zero, which describes the notches observed in the center of the beam echo.

7.4 Beam echoes with wakefields

In a treatment of beam echoes when there are wakefields present, the self-consistent Vlasov approach must be taken. In a perturbative treatment, the second order Vlasov equation must be used, since beam echoes are enabled through frequency mixing. This is the same point of departure as in the development of parametric coupling, but the description will diverge when a specific form for the voltages are chosen; namely short, externally applied pulses. Although there are explicitly applied external voltages in this analysis that do create a beam echo; in principal, these pulses could also generate

wakefields. The voltages from the wakefields would modify the beam response, and change the shape of the echo. The analysis begins with the perturbatively expanded second order Vlasov equation,

$$\frac{\partial f_m}{\partial t} + im\omega(\varepsilon)f_m = -\frac{e\omega_0}{2\pi}\frac{\partial f_0}{\partial \varepsilon}U_m - \frac{e\omega_0}{2\pi}\sum_{n+k=m} U_n \frac{\partial f_k}{\partial \varepsilon} \tag{7.12}$$

The symbolic definitions in this equation are consistent with previous usage (see section 2.4). Equation 7.12 describes the dynamics of mode m, where this mode will be taken to be that of the echo. The first term on the RHS represents coupling between the unperturbed beam distribution and a voltage at the frequency of the mth harmonic.

The second term on the RHS of eq. 7.12 is the frequency mixing term, and represents coupling between a perturbation in the beam distribution at mode k and a voltage at the frequency of mode n. This frequency mixing is derived from the effect of the second excitation on a beam already perturbed by the first excitation. In other words, the perturbation f_k arose from the voltage at mode k of the first pulse; and U_n is the voltage due to the second pulse. The total voltage change per turn at mode n experienced by the beam due to the drive pulse is the sum of the self-field voltage initiated by the external excitation, and the driving voltage itself.

$$U_n = V_n^{ext} + e\omega_0 Z_n \int_{-\infty}^{\infty} f_n \, d\varepsilon \tag{7.13}$$

The expression given by eq. 7.13 also holds for mode k of the first excitation.

There are several steps which facilitate the solution of eq. 7.12. A Laplace transform is done to remove the time derivative. The first order terms of the equation are

grouped together in such a way as to get the product of the perturbed current and the linear dispersion relation. The terms in the linear dispersion relation may then be written symbolically as $\tilde{D_m}(s)$, freeing attention for the second order term. First order solutions for the transformed quantities $\tilde{F_k}$ and $\tilde{U_n}$ may be used in the second order term, since $\tilde{F_k}$ and $\tilde{U_n}$ themselves are not generated through frequency mixing. Beginning with the Laplace transform,

$$\begin{aligned}[s + im\omega(\varepsilon)]\tilde{F_m}(\varepsilon, s) &= -\frac{e\omega_0}{2\pi}\frac{\partial f_0}{\partial \varepsilon}\tilde{U_m} \\ &\quad -\frac{e\omega_0}{2\pi}\frac{1}{2\pi i}\int_{c-i\infty}^{c+i\infty}\sum_{n+k=m}\tilde{U_n}(s-s')\frac{\partial \tilde{F_k}(s')}{\partial \varepsilon}\,ds' \quad (7.14)\end{aligned}$$

The summation in the third term on the RHS of eq. 7.14 may be dropped, since the echoes being investigated arise from a single frequency mixing event. Due to the $m = n + k$ condition on the summation, it will be understood that $k = m - n$, but this substitution will not be made until later for notational convenience. Also of importance to note is that in this analysis all three mode indices, m, k, and n may be either positive or negative. Next, the terms are rearranged and the equation is integrated over ε, for the purpose of writing the linear terms as $\tilde{I_m}\tilde{D_m}$,

$$\tilde{I_m}(s)\tilde{D_m(\varepsilon, s)} = -\frac{(e\omega_0)^2}{2\pi}\frac{1}{2\pi i}\int_{c-i\infty}^{c+i\infty}\tilde{U_n}(s-s')\,ds'\int_{\infty}^{\infty}\frac{d\varepsilon}{[s+im\omega(\varepsilon)]}\frac{\partial \tilde{F_k}(s')}{\partial \varepsilon} \quad (7.15)$$

A first order solution for $\tilde{F}_k$ may be found by Solving the linearized Vlasov equation,

$$\tilde{F}_k(\varepsilon, s) = -\frac{e\omega_0}{2\pi}\tilde{U}_k(s)\frac{\frac{\partial f_0}{\partial \varepsilon}}{[s + ik\omega(\varepsilon)]} \tag{7.16}$$

This may also be written,

$$\tilde{F}_k(\varepsilon, s) = -\frac{e\omega_0}{2\pi}\tilde{U}_k(s)\frac{\partial f_0}{\partial \varepsilon}\int_0^\infty \exp\{[s + ik\omega(\varepsilon)]\tau\}\, d\tau \tag{7.17}$$

For later convenience, define the integral portion of eq. 7.17 as $\mathcal{F}$

$$\begin{aligned} \mathcal{F}_k &\equiv \frac{1}{[s + ik\omega(\varepsilon)]} \\ &= \int_0^\infty \exp\{[s + ik\omega(\varepsilon)]\tau\}\, d\tau \end{aligned} \tag{7.18}$$

Having obtained a first order solution for $\tilde{F}_k$, a first order solution for $\tilde{U}_n$ is needed. This can be done beginning with the Laplace transformation of eq. 7.13, and writing the second term on the RHS as a function of $\tilde{U}_n$. The desired substitution is obtained by integrating eq. 7.16 over ε and multiplying by $e\omega_0\tilde{Z}_n$. Then,

$$\begin{aligned} \tilde{U}_n &= \tilde{V}_n^{\,ext} - \frac{(e\omega_0)^2}{2\pi}\tilde{U}_n(s)\tilde{Z}_n(s)\int_{-\infty}^\infty \frac{\frac{\partial f_0}{\partial \varepsilon}}{[s + in\omega]}\, d\varepsilon \\ \tilde{U}_n &= \frac{\tilde{V}_n^{\,ext}}{\tilde{D}_n(s)} \end{aligned} \tag{7.19}$$

Substituting for $\tilde{F}_k$ and $\tilde{U}_n$ in eq. 7.15, gives the expression for the perturbed current at the echo frequency,

$$\begin{aligned} I_m(s) &= -i\left(\frac{e\omega_0}{2\pi}\right)^3 \int_{c-i\infty}^{c+i\infty} ds' \frac{V_n^{ext}(s-s')V_k^{ext}(s')}{D_n(s-s')D_k(s')D_m(s)} \\ &\quad \times \int_{-\infty}^{\infty} d\varepsilon \mathcal{F}_m(\varepsilon,s)\frac{\partial}{\partial\varepsilon}\left[\frac{\partial f_0}{\partial\varepsilon}\mathcal{F}_k(\varepsilon,s')\right] \end{aligned}$$

Doing an integration by parts on the energy integral, and substituting the expression given by eq. 7.18 for $\mathcal{F}_m$ and $\mathcal{F}_n$,

$$\begin{aligned} I_m(s) &= \left(\frac{e\omega_0}{2\pi}\right)^3 mk_0 \int_{c-i\infty}^{c+i\infty} ds' \frac{V_n^{ext}(s-s')V_k^{ext}(s')}{D_n(s-s')D_k(s')D_m(s)} \\ &\quad \times \int_{-\infty}^{\infty} d\varepsilon \frac{\partial f_0}{\partial\varepsilon} \int_0^{\infty} \tau \exp\left[-(s+im\omega)\tau\right] d\tau \\ &\quad \times \int_0^{\infty} \exp\left[-(s'+ik\omega)\tau'\right] d\tau' \end{aligned} \tag{7.20}$$

If the applied excitations can be considered pulses of a single frequency, then the external voltages may be written,

$$\begin{aligned} V_k^{ext}(s') &= A\exp[-s'\tau_1] \\ V_n^{ext}(s-s') &= A\exp[-(s-s')\tau_2] \end{aligned}$$

where τ_1 is the start time of the first pulse, and τ_2 is the start time of the second pulse. Assuming that the excitations approach an impulse, the amplitude of the

applied pulses, A, is found by proper normalization to be $\frac{1}{2}V_0(\Delta T_p)$, where V_0 is the peak voltage of the kick, and ΔT_p is the time duration of the kick.

An expression for the perturbed current in the time domain may be obtained by doing an inverse Laplace transform on eq. 7.20. Using the explicit form for the external voltages, doing the inverse transform, and changing the order of integration, $I_m(t)$ is then,

$$I_m(t) = -i\left(\frac{e\omega_0}{2\pi}\right)^3 \frac{mk_0}{2\pi} A^2 \int_{-\infty}^{\infty} d\varepsilon \frac{\partial f_0}{\partial \varepsilon} \int_0^{\infty} \tau\, d\tau \int_0^{\infty} d\tau' \exp[-i\omega(\varepsilon)(m\tau + k\tau')]$$

$$\times \int_{c-i\infty}^{c+i\infty} ds' \int_{c-i\infty}^{c+i\infty} ds \frac{\exp(-s\tau)\exp(-s'\tau')\exp(st)\exp[-(s-s')\tau_2]\exp(-s'\tau_1)}{D_n(s-s')D_k(s')D_m(s)}$$

This result for the perturbed current at mode m includes wakefield effects. If the wakefield effects are neglected, this solution should agree with the small kick approximation of section 7.3, where wakefields were not considered. Assuming that there is sufficient Landau damping to ignore the poles in the the linear dispersion relations, allows their contribution to the integrand to be neglected, and is equivalent to assuming that wakefields are unimportant. Proceeding in this manner, the fact that the applied voltages are pulse excitations considerably simplifies evaluation of the integrals. Doing the s and s' integrations first yields delta functions in τ and τ'. The evaluation of the remaining integrals is then straightforward. After evaluating the integrals in s, s', τ, and τ', the expression for the echo current becomes,

$$\begin{aligned} I_m(t) &= -i\frac{(e\omega_0)^3}{(2\pi)^2} k_0 m(t-\tau_2)[\frac{1}{2}V_0(\Delta T_p)]^2 \int_{-\infty}^{\infty} d\varepsilon \frac{\partial f_0}{\partial \varepsilon} \\ &\quad \times \exp\{-i(\omega_0 + k_0\varepsilon)[k(\tau_2-\tau_1) + m(t-\tau_2)]\} \end{aligned}$$

The energy integral will average to zero unless the sinusoidal dependence in the integrand is removed. The condition for its removal determines when the echo will occur. The echo time is then given by,

$$t_{echo} - \tau_1 = \frac{(m-k)(\tau_2 - \tau_1)}{m}$$

If the first pulse is applied at $t = 0$, then $\tau_1 = 0$. Also, the time between applied pulses is $\Delta t = \tau_2 - \tau_1 = \tau_2$, and $m = k + n$ holds because of the frequency matching condition. The echo time can then also be written,

$$\begin{aligned} t_{echo} &= \frac{n}{m}\Delta t \\ &= \frac{n}{n+k}\Delta t \end{aligned}$$

Although there is a sum, rather than a difference, in the denominator of the expression for t_{echo}, all mode numbers may be either positive or negative. It is then a requirement that n and k have opposite signs in order for an echo to be generated.

Assuming the beam distribution is a Gaussian, then the energy integral may also be evaluated,

$$\begin{aligned} I_m(\theta) &= I_0 \left[\frac{1}{2}\frac{e\omega_0}{2\pi}V_0(\Delta T_p)k_0\right]^2 m[t-\Delta t][mt + (k-m)(\Delta t)] \\ &\quad \times \exp\{-i\omega_0[mt + (k-m)(\Delta t)]\} \exp\{-\frac{1}{2}(k_0\sigma_\varepsilon)^2[mt + (k-m)(\Delta t)]^2\} \end{aligned}$$

where $I_0 = \frac{eN\omega_0}{2\pi}$ is the unperturbed beam current. This result agrees with that from the small kick approximation in section 7.3 (given by eq. 7.11).

7.5 Beam echoes with wakefields and collisions

A full treatment of beam echoes, including collisional effects, uses the same analysis techniques as the previous section (7.4), but begins with the Boltzmann equation, which contains the Fokker-Planck operator to model diffusion. The Fokker-Planck terms describe the slow relaxation processes which play a role in the evolution of the particle distribution, and these are added to the Vlasov equation to get a full description of the beam evolution. The coefficients of these terms represent average characteristics of the collisional processes [48]. Again, in a perturbative treatment, the second order term frequency mixing term present in the Boltzmann equation must be retained. Beam echoes are a consequence of frequency mixing, whether or not a diffusion mechanism is present. For a more detailed account of the following analysis, refer to the previous section. Adding collisional terms to eq. 7.12,

$$\begin{aligned} \frac{\partial f_m}{\partial t} + im\omega(\varepsilon) f_m &= -\frac{e\omega_0}{2\pi}\frac{\partial f_0}{\partial \varepsilon} U_m - \frac{e\omega_0}{2\pi} \sum_{n+k=m} U_n \frac{\partial f_k}{\partial \varepsilon} \\ &\quad + \nu \frac{\partial(\varepsilon f_m)}{\partial \varepsilon} + 2\nu\sigma_\varepsilon^2 \frac{\partial^2 f_m}{\partial \varepsilon^2} \end{aligned} \tag{7.21}$$

where σ_ε is the rms beam energy spread, ν is the collision rate, the quantity $2\nu\sigma_\varepsilon^2$ is called the coefficient of diffusion, and the other terms have been defined elsewhere (see section 2.4). The last two terms on the RHS are the Fokker-Planck terms which

represent the effects of the random collisional processes. The third term on the RHS represents a collisional drag force, whereas the last term is the diffusion term describing such processes as intrabeam scattering. If both terms are kept throughout the analysis, it can be seen that the decorrelation time associated with the drag term is significantly longer than the decorrelation time due to the diffusion term. Since the diffusion term dominates, the drag term will be neglected in this analysis.

Taking the Laplace transform of eq. 7.21, and dropping the summation with the understanding that $m = n + k$,

$$\begin{aligned}[s + im\omega(\varepsilon)]\tilde{F}_m(\varepsilon, s) &= -\frac{e\omega_0}{2\pi}\frac{\partial f_0}{\partial \varepsilon}\tilde{U_m} + 2\nu\sigma_E^2\frac{\partial^2 \tilde{F}_m(\varepsilon, s)}{\partial \varepsilon^2} \\ &\quad -\frac{e\omega_0}{2\pi}\frac{1}{2\pi i}\int_{c-i\infty}^{c+i\infty}\tilde{U_n}(s - s')\frac{\partial \tilde{F}_k(s')}{\partial \varepsilon}\,ds' \qquad (7.22)\end{aligned}$$

Proceeding in a manner similar to that of section 7.4, all terms save the second order mixing term will be grouped together, eventually being manipulated into the form $\tilde{I_m}\tilde{D_m}$. Since the collision term is included in this exercise, now D_m represents a new dispersion relation which takes collisions into account. Similarly, the expressions which are to be substituted for $\tilde{U_n}$ and $\tilde{F_k}$ are also modified.

Writing eq. 7.22 without the mixing term, the differential equation for $\tilde{F_k}$ is now given by the following,

$$-2\nu\sigma_E^2\frac{\partial^2 \tilde{F}_k(\varepsilon, s)}{\partial \varepsilon^2} + [s + ik\omega_0 + ikk_0\varepsilon]\tilde{F}_k(\varepsilon, s) = -\frac{e\omega_0}{2\pi}\frac{\partial f_0}{\partial \varepsilon}\tilde{U_k}(s) \qquad (7.23)$$

This equation can be solved for $\tilde{F_k}$, using a method first outlined for the case of a

plasma by Su and Oberman [51, 11, 52]. The solution is given by,

$$\tilde{F}_k(\varepsilon, s) = -\frac{e\omega_0}{2\pi}\frac{\partial f_0}{\partial \varepsilon}\tilde{U}_k(s)\int_0^\infty d\tau \exp\left\{-(s+ik\omega)\tau - \frac{2\nu k^2 k_0^2 \sigma_\varepsilon^2 \tau^3}{3}\right\} \tag{7.24}$$

Define the integral portion of eq. 7.24 as $\mathcal{F}$,

$$\mathcal{F}_k(\varepsilon, s) = \int_0^\infty d\tau \exp\left\{-(s+ik\omega)\tau - \frac{2\nu k^2 k_0^2 \sigma_\varepsilon^2 \tau^3}{3}\right\}$$

Allowing for diffusion has modified $\mathcal{F}$ such that there is now a damping term in the exponent (compare with eq. 7.18). The coefficients of the damping terms in $\mathcal{F}_k$ and $\mathcal{F}_m$ define the particle phase correlation time constant.

The first order solution for $\tilde{U}_n$ is found as before, except that now the $\mathcal{F}_n$ in the dispersion relation $\tilde{D}_n{}'$ is altered due to the collisional term.

$$\begin{aligned} \tilde{U}_n &= \tilde{V}_n^{ext} - \frac{(e\omega_0)^2}{2\pi}\tilde{U}_n(s)\tilde{Z}_n(s)\int_{-\infty}^\infty \frac{\partial f_0}{\partial \varepsilon}\, d\varepsilon \mathcal{F}_n \\ \tilde{U}_n &= \frac{\tilde{V}_n^{ext}}{\tilde{D}_n{}'(s)} \end{aligned} \tag{7.25}$$

Equation 7.22 can be manipulated so that all terms except for the mixing term are incorporated into $\tilde{I}_m\tilde{D}_m{}'$. Once this is done, substituting the expression given by eq. 7.24 for $\tilde{F}_k$ and the expression given by eq. 7.25 for $\tilde{U}_n$, and doing an integration by parts on the energy integral, gives the following result,

$$I_m(s) = i\left(\frac{e\omega_0}{2\pi}\right)^3 \int_{c-i\infty}^{c+i\infty} ds' \frac{V_n^{ext}(s-s')V_k^{ext}(s')}{D_n'(s-s')D_k'(s')D_m'(s)}$$

$$\times \int_{-\infty}^{\infty} d\varepsilon \frac{\partial f_0}{\partial \varepsilon} \int_0^{\infty} (-imk_0\tau) \exp\left[-(s+im\omega)\tau - \frac{2\nu m^2 k_0^2 \sigma_\varepsilon^2 \tau^3}{3}\right] d\tau$$

$$\times \int_0^{\infty} \exp\left[-(s'+ik\omega)\tau' - \frac{2\nu k^2 k_0^2 \sigma_\varepsilon^2 \tau'^3}{3}\right] d\tau' \tag{7.26}$$

Applying excitation pulses of a single frequency, the external voltages may be written,

$$V_k^{ext}(s') = A\exp[-s'\tau_1]$$

$$V_n^{ext}(s-s') = A\exp[-(s-s')\tau_2]$$

where τ_1 is the start time of the first pulse, and τ_2 is the start time of the second pulse.

An expression for the perturbed current in the time domain may be obtained by doing an inverse Laplace transform on eq. 7.26. Using the explicit form for the external voltages, doing the inverse transform, and changing the order of integration, $I_m(t)$ is then,

$$I_m(t) = -i\left(\frac{e\omega_0}{2\pi}\right)^3 \frac{mk_0}{2\pi} A^2 \int_{-\infty}^{\infty} d\varepsilon \frac{\partial f_0}{\partial \varepsilon} \int_0^{\infty} \tau\, d\tau \int_0^{\infty} d\tau'$$

$$\times \exp[-i\omega(\varepsilon)(m\tau + k\tau')] \exp\left[-\frac{2\nu k_0^2 \sigma_\varepsilon^2}{3}(m^2\tau^3 + k^2\tau'^3)\right]$$

$$\times \int_{c-i\infty}^{c+i\infty} ds' \int_{c-i\infty}^{c+i\infty} ds \frac{\exp(-s\tau)\exp(-s'\tau')\exp(st)\exp[-(s-s')\tau_2]\exp(-s'\tau_1)}{D_n'(s-s')D_k'(s')D_m'(s)}$$

Except for the assumption of relatively weak driving pulses and linear energy dependence, this result for the perturbed current at mode m is general, taking into account both wakefields and collisional effects. At this point, the assumption will be made that there is sufficient Landau damping to ignore the poles of the linear dispersion relations. This takes the calculation out of the realm of large self-field effects, and implies that the decay of coherent oscillation due to the driving pulses is fast relative to the time between pulses. This condition was met during the Accumulator studies. Neglecting wakefields in the calculation is expeditious for understanding the collisional effects, which were present in the Accumulator. The beam current at the echo frequency is then,

$$I_m(t) = -i\frac{(e\omega_0)^3}{(2\pi)^2}k_0 m(t-\tau_2)A^2\int_{-\infty}^{\infty} d\varepsilon \frac{\partial f_0}{\partial \varepsilon}$$

$$\times \exp\{-i(\omega_0 + k_0\varepsilon)[k(\tau_2-\tau_1) + m(t-\tau_2)]\}$$

$$\times \exp\{-\frac{2\nu k_0^2\sigma_\varepsilon^2}{3}[k^2(\tau_2-\tau_1)^3 + m^2(t-\tau_2)^3]\} \tag{7.27}$$

The $\frac{\partial f_0}{\partial \varepsilon}$ in the integrand causes the echo current to go to zero in the center of the echo, creating a notch in the echo. If the beam distribution is smooth and peaks in the center, then the slope of the distribution function must be zero at the center of the echo. Echoes previously observed in plasmas did not have detectable notches, while notches were clearly present in the particle beam echoes observed in the Accumulator. The dispersion relation for a stored beam plays the role of the dielectric function in a plasma. When wakefields are not a significant factor, and the free-streaming calculation is valid, the value of the dispersion relation is nearly one. In contrast, the

dielectic function in a plasma is large, and may be responsible for filling in the notch in a plasma echo.

The separation of the peaks of the echo on either side of the central notch may be calculated. By finding the times of the maxima of the echo current and subtracting, the expression for the peak separation is found to be of the form,

$$(\Delta t)_{peak} = \frac{\beta^2}{\pi f_{rev} |\eta| \frac{\sigma_\varepsilon}{E_0}} \tag{7.28}$$

The time delay to the echo, t_{echo}, can be found by examining eq. 7.27,

$$t_{echo} = \frac{n}{m} \Delta t$$

where the time between applied pulses is $\Delta t = \tau_2 - \tau_1$, the first pulse occurs at $t = 0$, and the relationship $m = k + n$ holds because of the frequency matching condition.

As a consequence of including collisions in the beam dynamics, there is now a damping factor on the amplitude of the echo current. At the time of the echo, $t_{echo} = \frac{n}{m} \Delta t$, the damping factor is,

$$e^{-\left[\frac{2\nu\sigma_\varepsilon^2}{3} k^2 |1 - \frac{k}{m}|\right] (\Delta t)^3}$$

There are two competing time dependences acting on the amplitude of the perturbed current. Since t_{echo} is linearly dependent on Δt, the damping decrement goes as t_{echo}^3. For the free-streaming case in the absence of collisional damping, as seen in eq. 7.27,

the peak echo amplitude grows linearly with t_{echo}. If the pulse amplitude were non-perturbative, then the echo amplitude goes as a Bessel function (see eq. 7.10). In either case, the effect of collisions is to damp out the normal amplitude dependence on t_{echo}, until at some time determined by the collision rate, echoes are no longer possible. Thus, by measuring the echo amplitude dependence on t_{echo}, the collision rate may be found. In the perturbative case, the time of the peak echo response depends directly on the collision rate,

$$\nu = \frac{1}{(\Delta t)^3_{peak} k_0^2 2\sigma_\varepsilon^2 k^2 |1 - \frac{k}{m}|}$$

Echoes, like all other aspects of beam dynamics, are sensitive to properties of the beam, and to the conditions created by the storage ring in which the beam circulates. Those properties which are variable, and perhaps difficult to measure, are of special interest since echo measurements may help in their determination. In particular, the dependence of the shape and size of longitudinal echoes on wakefields, collisional effects, and the momentum spread of the beam may be useful in various circumstances.

If wakefield effects are too severe, it may be difficult to get a clear echo. On the other hand, if the machine impedances are more benign, they are perhaps more easily determined by doing a transfer function measurement, or by using the damping time of the transient response. However, there may be circumstances where available hardware does not allow an excitation at the frequency of interest, whereas an echo (or higher order echoes) could be generated at the proper frequency through the agency of frequency mixing.

The separation of the peaks around the notch of an echo may be used to determine

the momentum spread of the beam. Although, if there are no significant wakefields present, the landau damping time after a single kick could also be used for this measurement.

Perhaps the best use of echoes is in the measurement of the collision frequency in the beam. A determination of intrabeam scattering is most important for a stored beam, where it is particularly important not to degrade the beam quality. The impedance budget of such a storage ring is normally carefully controlled. So, just when intrabeam scattering becomes an important parameter, echo measurements should be fairly clean. The strength of this technique lies in its speed and sensitivity.

Chapter 8

Accumulator time domain results

8.1 Introduction and overview

The study of echoes in the Fermilab Accumulator was a natural extension of the mode coupling experiments that were done in the Main Ring. Both phenomena are second order frequency mixing effects, whereby existing modes at two different harmonics combine to cause the growth of a third mode at the difference frequency. Echo generation is a time domain analog of parametric coupling. For the echo experiments in the Accumulator, both of the mixing frequencies were applied to the beam externally as a succession of pulses; whereas in the Main Ring parametric coupling experiments, only one external voltage pulse was needed to stimulate the second order coupling. In contrast to the Accumulator, the $h = 1$ mode is already coherent in the Main Ring, and the initially applied pulse spontaneously generated a series of coupling events. A stable low impedance machine such as the Accumulator is better suited to the study of echoes.

The experimental setup for the echo studies is detailed in section 8.2. The following section, section 8.3, begins with the description of a typical echo. Measurements of the frequency and time dependence of the echo are discussed and shown to match the theoretical predictions. The observation of higher order echoes and their relative timing is presented. The purpose of section 8.3 is to show that there is good agreement between the predicted basic properties of echoes, and the experimental results.

Echoes are a potentially useful tool for measuring the diffusion rate in a beam. Diffusion processes are statistical in nature, rather than affecting the beam distribution as a whole. A diffusion mechanism of importance in high energy beams is small angle coulomb scattering, called intrabeam scattering. Intrabeam scattering tends to increase beam size, and in the case of colliding beam physics, can be one of the factors limiting luminosity. Current methods of measuring thermal effects in a beam take on the order of hours. Echoes effectively amplify the effects of scattering, producing a measurement of a small collision frequency in a short time. If echo measurement techniques with sufficient accuracy are developed, these measurements would be on the order of minutes, and could be done quickly and routinely.

The presence of a diffusion mechanism destroys the reversibility of the decoherence of particle bunching. In the absence of diffusion, the phase evolution of the spreading particles depends strictly on their relative energies. The phase development of the particles due to their energy change from the second kick combines with their phase development from the first kick in such a way as to rebunch the particles. The diffusion process breaks down the correlation between energy and phase. Partial decorrelation reduces the echo amplitude, and full decorrelation completely inhibits the echo. A

diffusion process is thus expected to change the dependence of echo amplitude on the time at which the echo occurs, decreasing the amplitude until there is no echo at all. A measurement of echo amplitude versus the time of the echo is presented in section 8.5. This curve is fitted to extract the diffusion rate in the beam. The accuracy of the results and the potential sources of the diffusion are discussed.

Other information besides the diffusion rate lies buried in the echo characteristics. In particular, the echo shape is sensitive to parameters such as the machine impedance at echo-related frequencies, and to the momentum distribution of the beam. In the absence of impedance, the decoherence of particle motion following an applied pulse will happen on a time scale dependent on the energy spread of the beam, the harmonic of the excitation, and on the momentum dispersion characteristics of the storage ring. If there is sufficient machine impedance, the resulting wakefields will extend the duration of coherent particle motion, thus extending the damping time of the beam response to a driving pulse. As demonstrated by O'Neil and Gould [16], this will directly impact the shape of the echo. The echo time depends inversely on the time between coherent excitations at the mixing frequencies. The decay of the beam response after the first driving pulse, rather than the response during the pulse, is closer in time to the second driving pulse. Thus, the shape of the leading edge of the echo is influenced by the damping of the beam response to the first drive pulse. Similarly, the shape of the trailing edge of the echo is influenced by the damping of the beam response to the second pulse. Scattering effects in general could also affect the shape of the echo; but if the diffusion coefficient for the scattering process is independent of energy, then only the amplitude of the echo will be affected by scattering [12].

The Fermilab Accumulator did not have significant impedances at the frequencies used in echo generation. However, the shape of the echo did depend on the momentum distribution of the beam. One of the major features of the observed echoes was a deep notch in the center of the response. As shown in section 7.5, the perturbed current at the echo frequency is dependent on the derivative of the unperturbed beam distribution with respect to energy. Since the slope of the distribution is zero at the center, the perturbed current goes to zero in the middle of the echo. The separation of the peaks on either side of this zero has a predicted dependence on the energy width of the beam. In section 8.4, experimental results and theory are shown to agree to within 20%. More generally, section 8.4 examines the qualitative variation in the character of echoes with beam energy spread.

8.2 Experimental setup

The experimental setup used for time domain measurements in the Accumulator is given in block diagram form in figure 8.1. Two successive approximate impulse excitations were applied to the beam via the ARF2 cavity, which was used as a longitudinal kicker. The frequencies, pulse widths, and time separation of the two pulses were independently controlled parameters. The beam response to the excitations was monitored via the wall current detector, whose amplified output was hooked to an oscilloscope.

The frequency source for the first pulse was an HP 3335A synthesizer/level generator, which has a continuous wave output at a frequency and power level chosen by the user. Typically, the somewhat arbitrary choice for the frequency was $h = 9$, the power level being set between +7-+10 dBm. Using figure 8.3, and the fanback calibration

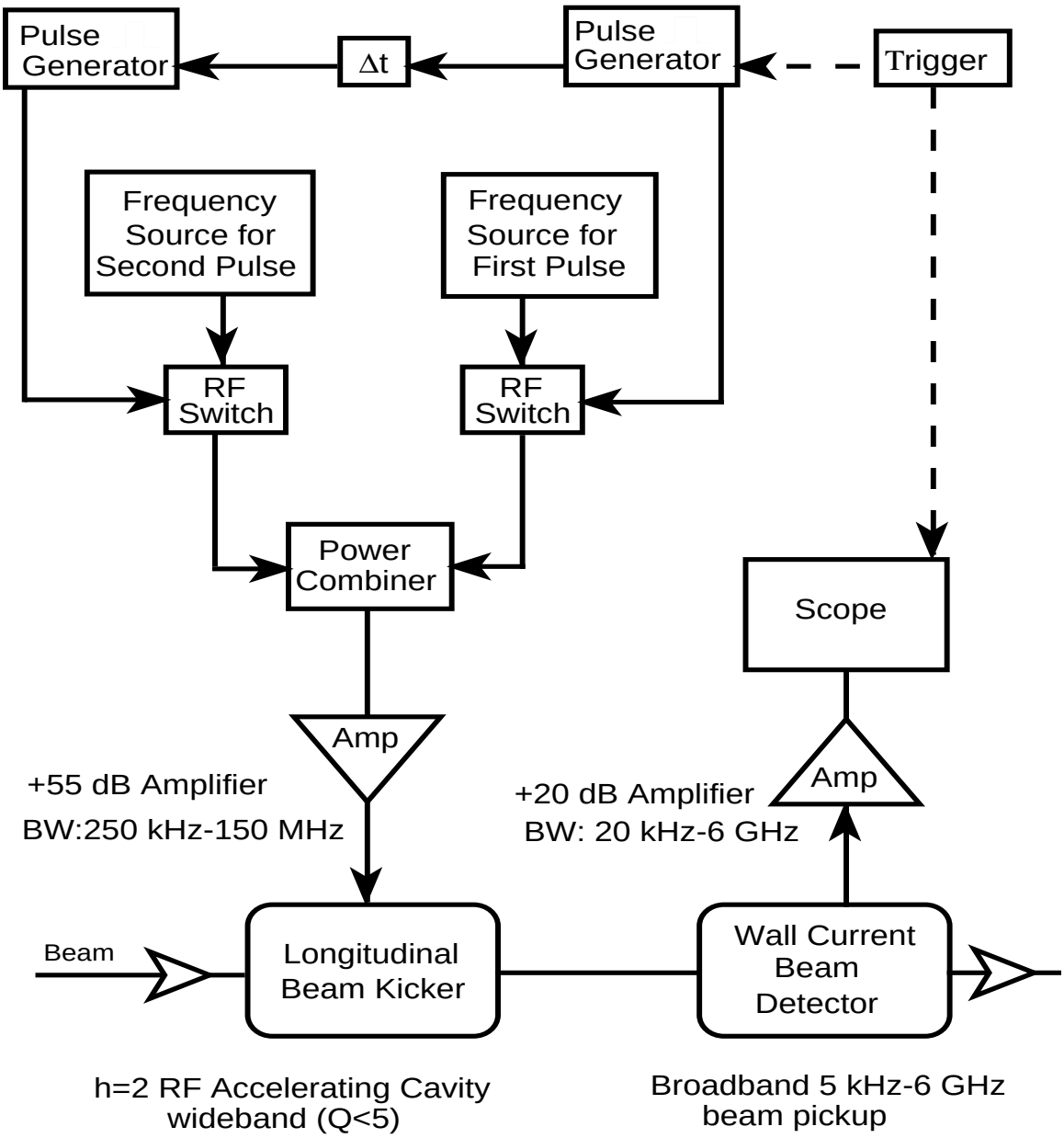

Figure 8.1: Block diagram of Accumulator time domain setup

of 273 cavity volts per fanback volt, a power level setting of +7 dBm would give 43 rms volts on the cavity gap. Similarly, the frequency source for the second pulse was an HP 8656A signal generator. Here, the frequency was usually set to one harmonic above that of the first pulse, and the power level was made to be the same as that of the first pulse. The continuous outputs of the frequency generators were gated onto the beam kicker for a short time using RF power switches with single, triggerable gate pulses supplied by pulse generators. The gate for Pulse 1 was provided by an HP 8011A pulse generator which was manually triggered. The gate for Pulse 2 was provided by an HP 8013A pulse generator, which was triggered by a Systron-Donner 101D pulse generator that was acting as a delay box. The scope used for taking data and the delay box used the manual trigger. The widths of the pulses applied to the beam were controlled by the widths of the gate pulses, both of which were typically set to 5 ms. Pulse widths and power levels were constants during a particular beam study, the delay between pulses being the variable parameter.

The Pulse 1 and Pulse 2 outputs from the two RF switches were sent through a power combiner, so that one signal could be amplified and applied to the longitudinal kicker. The broadband ARF2 cavity was used as the beam kicker. The wall current monitor was used as the beam detector; its amplified output going to the Tektronix DSA 602A digitizing signal analyzer, whose traces were recorded on inserted floppy disks. The kicker, pickup, and the two amplifiers were the same as those used for the frequency domain measurements, and more complete descriptions may be found in section 3.2.

There is no significant distortion of a driving pulse applied to the ARF2 cavity. This can be seen in figure 8.2, which shows the fast rise of the cavity fanback signal

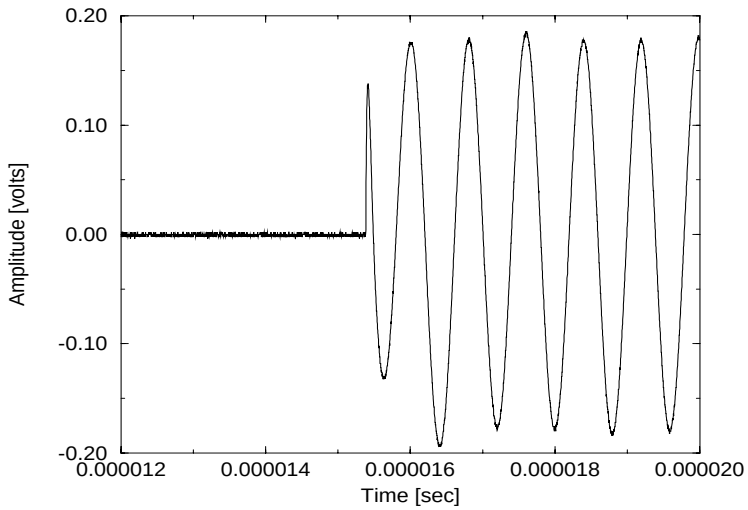

Figure 8.2: Fast rise of a pulse applied to the Accumulator ARF2 cavity, as seen on the fanback signal.

at the initiation of the pulse, as viewed by the signal analyzer.

There is little variation in the amplitude of the response of the cavity when pulsed at adjacent harmonics. The amplitude of the fanback signal was measured at each of the harmonics used during data acquisition. The input power level was kept fixed for all harmonics. The frequency generator output was set at +7 dBm, and the gated signal then sent through the +55 dB amplifier in the usual way. The measured fanback response at the various harmonics is shown in figure 8.3.

8.3 Echo characteristics

A typical view of a longitudinal beam echo in the Fermilab Accumulator is shown in figure 8.4, which displays peak beam current versus time during the echo formation. The beam signal that was used came from the longitudinal wall current monitor.

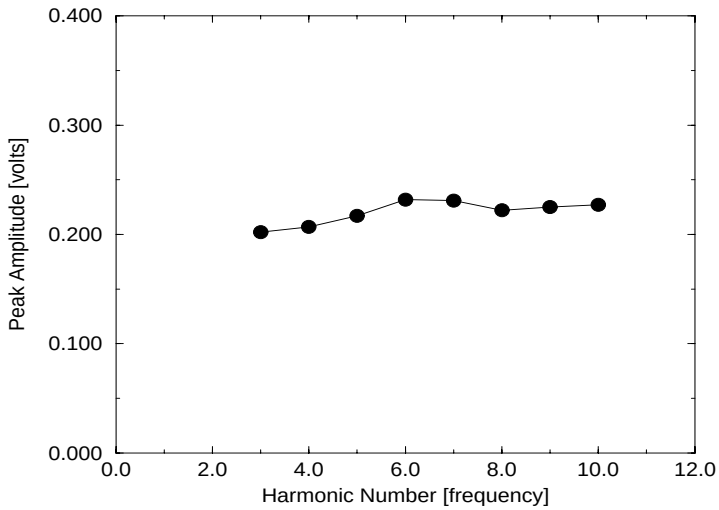

Figure 8.3: ARF2 peak amplitude response at different harmonics, as seen on the cavity fanback signal. The power setting on the frequency source was +7 dBm, and the pulse width was 5 ms. These were typical conditions during echo studies.

Since the total intensity was constant, an increase in the signal reflects a greater instantaneous current due to coherent oscillation. The two large peaks occurring within the first 100 ms are the response to the externally applied pulses. The first 5 ms pulse at the frequency $h = 9$ defines $t = 0$, and is followed 75 ms later by another 5 ms pulse at $h = 10$. By the time of the second excitation, there is no remnant of the bunch structure caused by the first excitation.

The echo is the large coherent signal centered at .75 seconds, and resulted from the frequency mixing of the initial pulses, rather than from direct excitation. The frequency of the echo was measured, and found to be $h = 1$, which is the difference frequency of the applied pulses, $1\omega_0 = (10 - 9)\omega_0$. The shape of the echo is double peaked, with a notch in the center. The echo shape is dependent on the derivative of the unperturbed beam distribution with respect to energy. Since the distribution

peaks in the center, the slope there is zero, and this causes the notch seen in the echo.

The time delay from the first applied pulse to the echo is expected to depend on the pulse separation, Δt, and the mode numbers of the applied pulses as follows,

$$t_{echo} = \frac{|n|}{|n| - |k|}\Delta t$$

where n is the mode number of the second pulse, and k is the mode number of the first pulse. This prediction was checked with two scans, one with initial pulse frequencies of pulse 1 at $h = 9$ and pulse 2 at $h = 10$, and the other with initial pulse frequencies of pulse 1 at $h = 4$ and pulse 2 at $h = 5$. For a given set of frequencies, the echo time was measured as the pulse separation was varied. The results of the two scans conform with expectation, and are shown in figure 8.5.

The additional check of reversing the pulse order was also made. When the frequency of the first pulse was $h = 10$, and that of the second $h = 9$, no echo developed. The frequency of the second pulse must be higher than the first, otherwise the impossible situation arises where the calculated echo time is before the second pulse.

Higher order echoes were clearly seen during the echo studies, an example is shown in figure 8.6. A single pair of driving pulses produced three visible higher order echoes in figure 8.6, which shows signal level versus time on the longitudinal beam detector. The largest part of the signal at approximately .02 seconds was the beam response to the second drive pulse; the scope was triggered between drive pulses. The damping time after the drive pulse is consistent with the expected decoherence time when wakefields are neglected. Using Accumulator parameters at the time of the measurement, and eq. 7.7, the calculated damping time is $\tau_{landau} = .003$ sec.

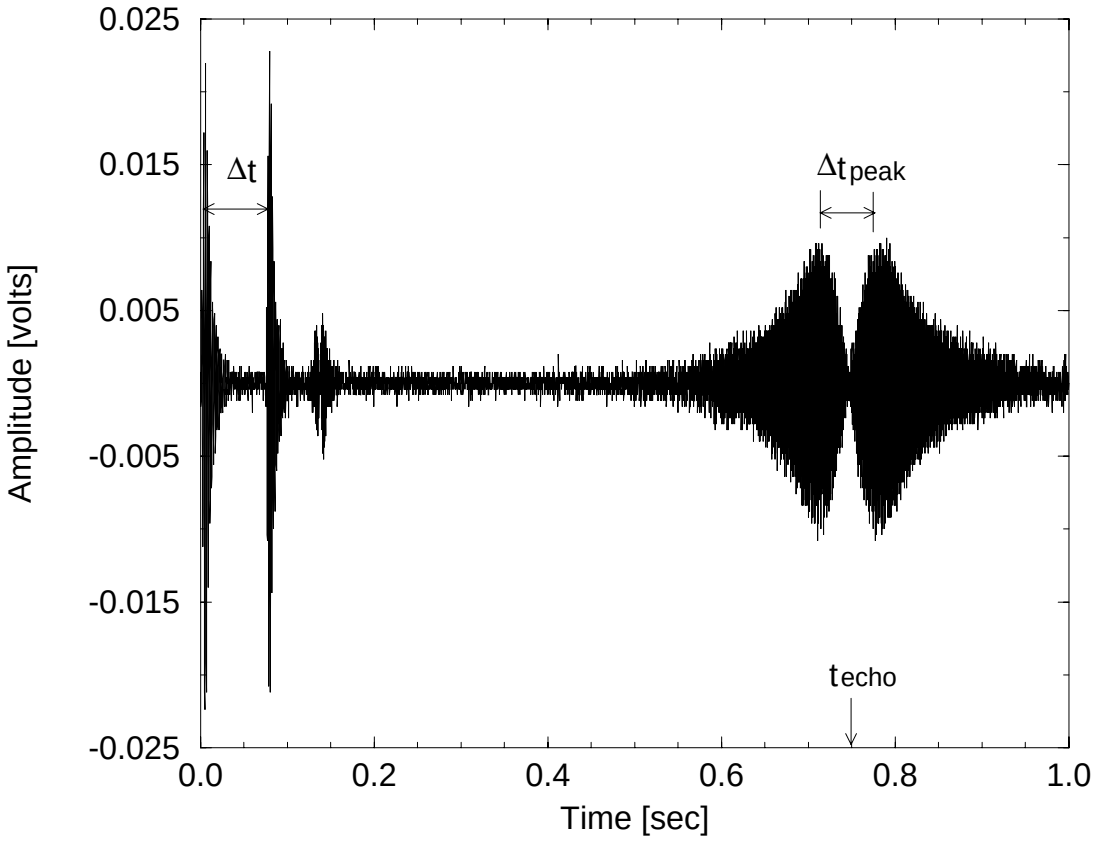

Figure 8.4: Beam response to impulse excitation at $h = 9$, followed by $h = 10$. An echo at $h = 1$ occurs centered at 0.75 seconds after the initial impulse. The beam parameters were: beam current $I_0 = 147$ mA, $\eta = .023$, total beam energy $E_0 = 8696$ MeV, beam energy spread obtained from Schottky pickup $\sigma_\varepsilon = 3.2$ MeV, transverse normalized emittances $\epsilon_H = 1.75\pi$ mm-mrad, $\epsilon_V = .56\pi$ mm-mrad, and peak separation of the echo $\Delta t_{peak} = .07$ sec. Note the presence of a higher-order echo immediately following the second excitation pulse.

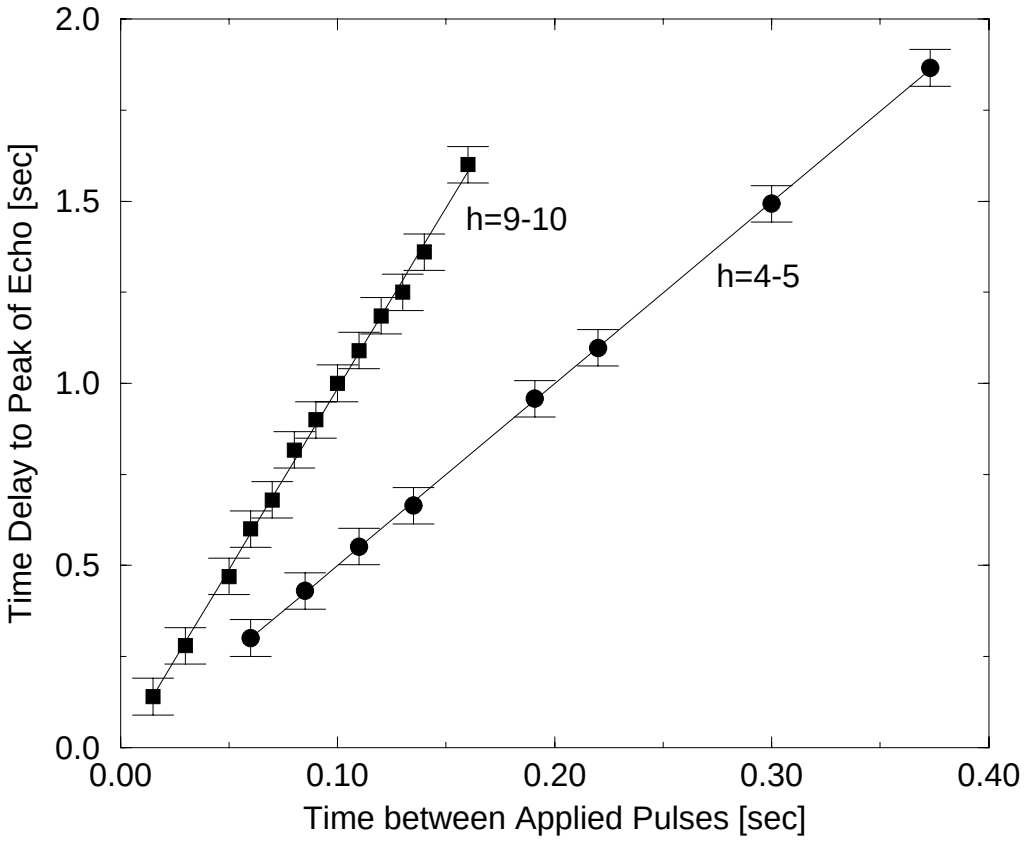

Figure 8.5: Measured echo delay time as a function of separation of the drive pulses. Upper curve: 1st pulse at $h = 9$, 2nd pulse at $h = 10$, giving expected time dependence $t_{echo} = [10/(10-9)]\Delta t = 10\Delta t$. Lower curve: 1st pulse at $h = 4$, 2nd pulse at $h = 5$, giving $t_{echo} = [5/(5-4)]\Delta t = 5\Delta t$.

This is confirmation in the time domain of the stability seen in the transfer function measurements. The three echoes had frequencies $h = 11$, $h = 21$, and $h = 31$; which are $h = (2 \times 10) - 9$, $h = (3 \times 10) - 9$ and $h = (4 \times 10) - 9$. The stronger second order echo at $h = 1$ (not shown in the figure) happened at time $t_{echo} = 10\Delta t$, where $\Delta t = 139$ ms was the driving pulse separation. The higher order echoes were closer to the drive pulses, occurring at $t = 20/11 \times \Delta t$, $t = 30/21 \times \Delta t$, and $t = 40/31 \times \Delta t$.

8.4 Echo shape

The shape of an echo in the free-streaming case is dependent on the energy derivative of the unperturbed distribution function. If the beam distribution varies smoothly and peaks in the center, there should be a notch in the center of any echoes. The echo with a notch has a peak on either side of the notch, and the separation of these two peaks is expected to have the following dependence (see section 7.5),

$$\Delta t_{peak} = \frac{\beta^2}{\pi f_0 |\eta| \frac{\sigma_\varepsilon}{E_0}}$$

For the Accumulator this is, $\Delta t_{peak} = \frac{2.2 \times 10^{-5}}{\frac{\sigma_\varepsilon}{E_0}}$. Information on the echo peak separation versus beam energy width was available from the Accumulator echo studies data, and has been plotted in figure 8.7. Several echo amplitude versus t_{echo} scans were done, each with a beam of different energy width. Each scan in this set used the same stored beam with the same intensity; the beam energy width was controlled using the momentum cooling system. The value for the peak separation of each data point

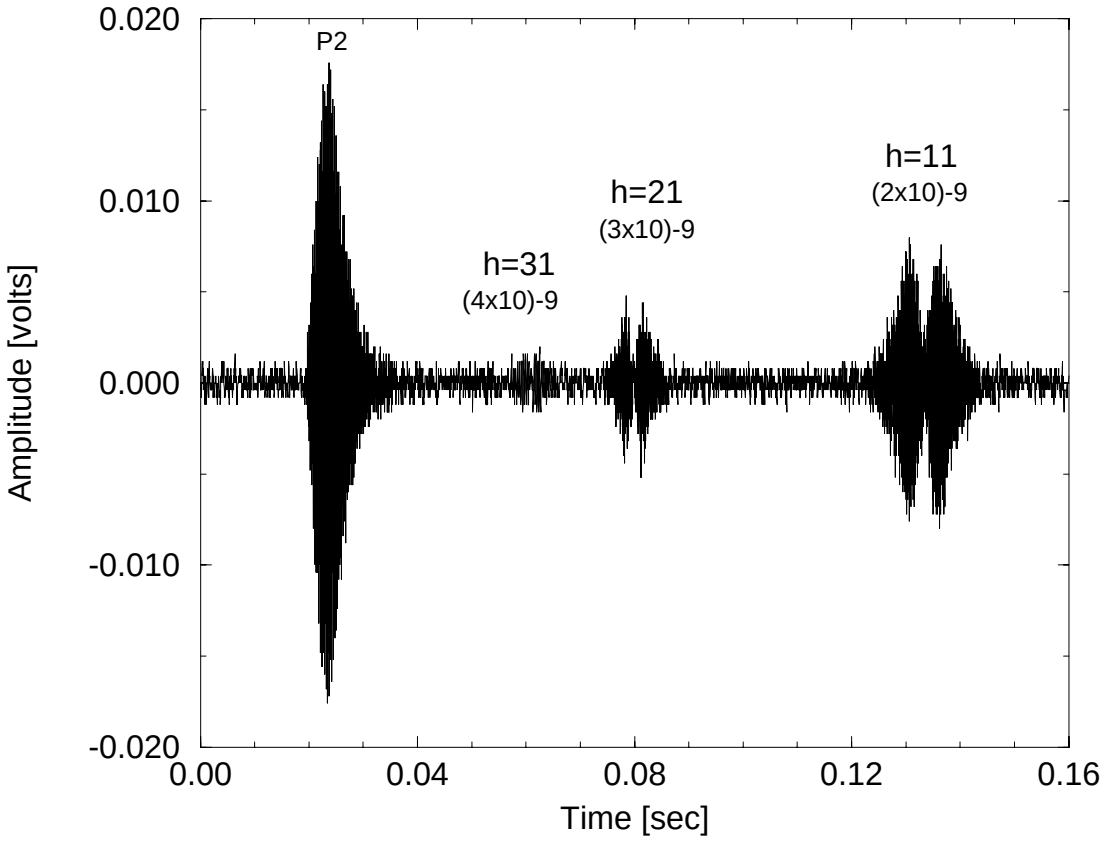

Figure 8.6: Higher order echoes. The leftmost and largest peak is the beam response to the second drive pulse. The other peaks are echoes at $h = 31$, $h = 21$ and $h = 11$. The echo at $h = 31$ is barely visible, but the relative timing verifies that this is also an echo. The delay between driving pulses was 139 ms, and there are $[\frac{30}{21} - \frac{40}{31}].139 = .019$ seconds between the echoes at $h = 31$ and $h = 21$.

in figure 8.7 is an average of all echoes in the scan of the corresponding momentum. The slope of the linear fit is 1.76×10^{-5} which has a 20% error with the prediction.

One interesting result of doing amplitude versus t_{echo} scans at various beam energy spreads, was that for large enough σ_ε the notch in the echo disappeared. Scans were done for σ_ε in the range of 2.3 to 8 MeVc, with no notch in the echoes of the scans done at 7 and 8 MeVc. Figure 8.8 shows echoes from three scans, each with a different σ_ε. The echoes occur at approximately the same time relative to the driving pulses, but their shape is quite distinctive. As the energy spread of the beam goes up, the amplitude and the width of the echoes go down, and the notch begins to fill in, eventually vanishing completely. Although only three echoes are shown in the figure, the trend is assiduously followed in all seven scans which were done.

Another set of scans were done with varying transverse beam sizes, and there was no systematic variation of the echo shape with transverse beam size. The echoes are expected to be much more sensitive to the longitudinal beam size, since they are being driven longitudinally. When the energy width of the beam is narrow, there are more particles directly on the driving frequency. So, it may be expected that there are larger echo amplitudes for energetically narrower beams. However, even a wide beam peaks at the center frequency, so it is not so easy to see why the echo notch vanishes completely. One possibility is that nonlinearities in the η function are mixing the particle distribution in such a way as to destroy the notch. The first term in η which causes a nonlinear dependence of the revolution period on the beam energy spread is $\eta_1 \frac{1}{\beta^2} \frac{\Delta E}{E_0}$ (see section 2.2). In the Accumulator η_1 is approximately .82, which for a large energy error of, say, 8 MeVc is about a 3% correction to η_0.

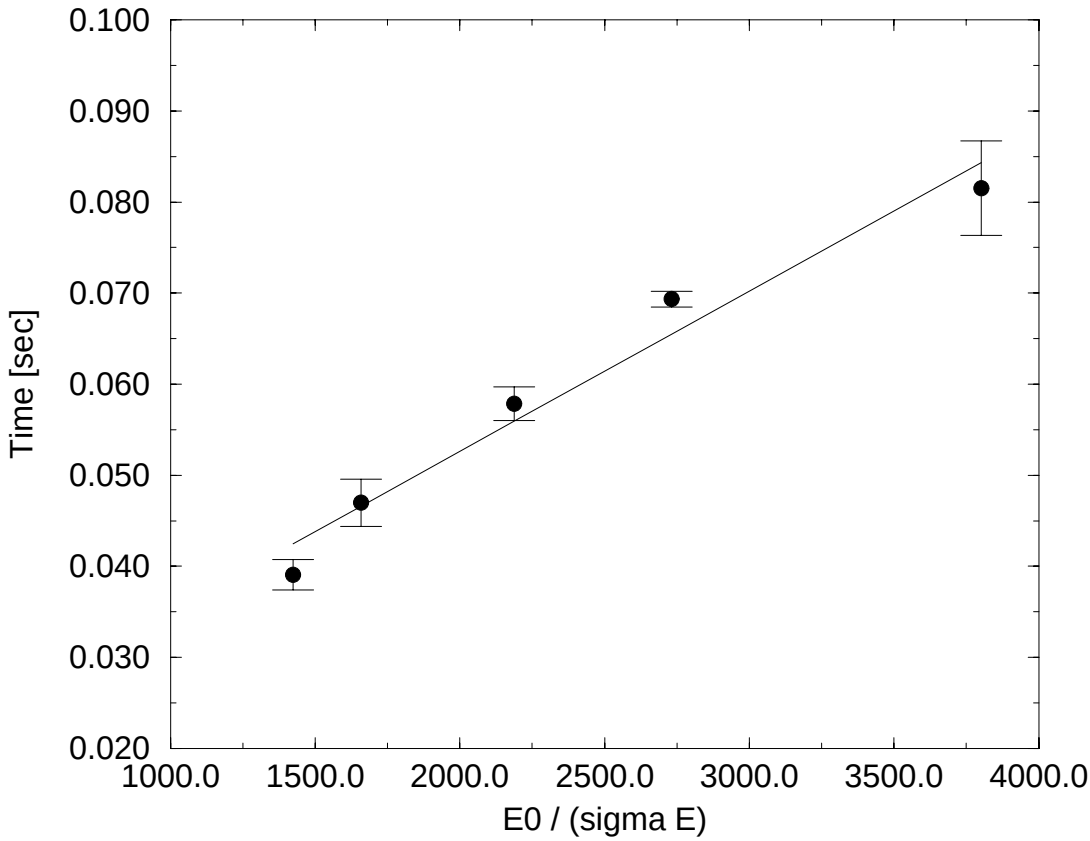

Figure 8.7: Peak separation of double-peaked echoes, Δt_{peak}, versus the inverse of $\frac{\sigma_\epsilon}{E_0}$, the energy spread of the beam. The value of the slope from the linear fit is 1.76E-5. The beam parameters were $I_0 = 147$ mA, $\eta = .023$, and $\beta^2 = .988$

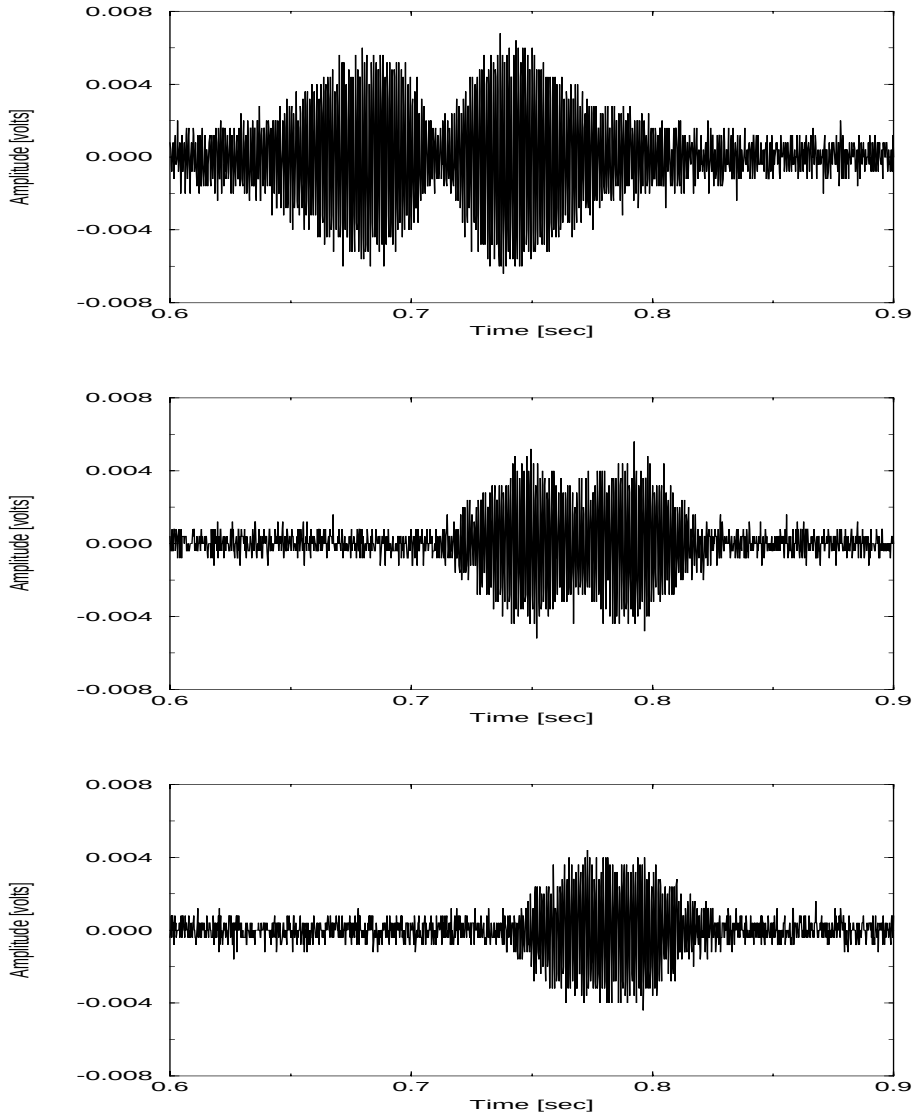

Figure 8.8: Three longitudinal beam echoes occurring in beams with different energy widths. The beam energy sigmas (σ_ε) were from top to bottom, 4.0, 6.1, and 8.0 MeVc. The energy spread was controlled with longitudinal stochastic cooling systems, all other beam conditions were the same. The beam intensity was 147 mA. Echoes which occurred at nearly the same time relative to the driving pulses were chosen for comparison.

8.5 Diffusion rate measurements

The phenomena of beam echoes allows the intriguing possibility of developing a fast method for measuring the diffusion rate in a beam. Processes such as small angle coulomb scattering attenuate beam echoes, by destroying the phase correlation of particles necessary for their growth. As these processes are statistical in nature, their impact will increase as the time delay to the echo increases, eventually obliterating the echo completely. The initial evidence of diffusion effects in the Accumulator was that for sufficiently long pulse separations there were no echoes.

The scattering rate in a beam may be determined by making a measurement of echo amplitude as it varies with time. When there is no diffusion and there are no wakefields, the echo amplitude versus time delay has a Bessel function dependence [16]. The time independent portion of the Bessel function arguments goes as $2\pi \frac{|\eta|}{\beta^2} f_0^2 \frac{eV_0}{E_0} \Delta T_p$, the value of which was about .49 for these studies. Although the more general expression for echo amplitude was used in the data analysis, for times on the order of a few seconds, a perturbative treatment or small kick approximation are valid. The time delay of the echo from the two driving pulses may be varied by changing the pulse separation. The result of one echo amplitude scan is shown in figure 8.9, which shows the superposition of 10 echoes from ten pairs of applied pulses with different separations. The echo amplitude grows nearly linearly until a peak at approximately .65 seconds, and then decays. The large spike at the beginning of the plot is the beam response to the driving pulses during one of the ten measurements, and may be ignored.

A scattering rate for the Accumulator beam was obtained by doing a fit on an echo amplitude scan that was recorded out to $t_{echo} = 3.7$ seconds. The data from this

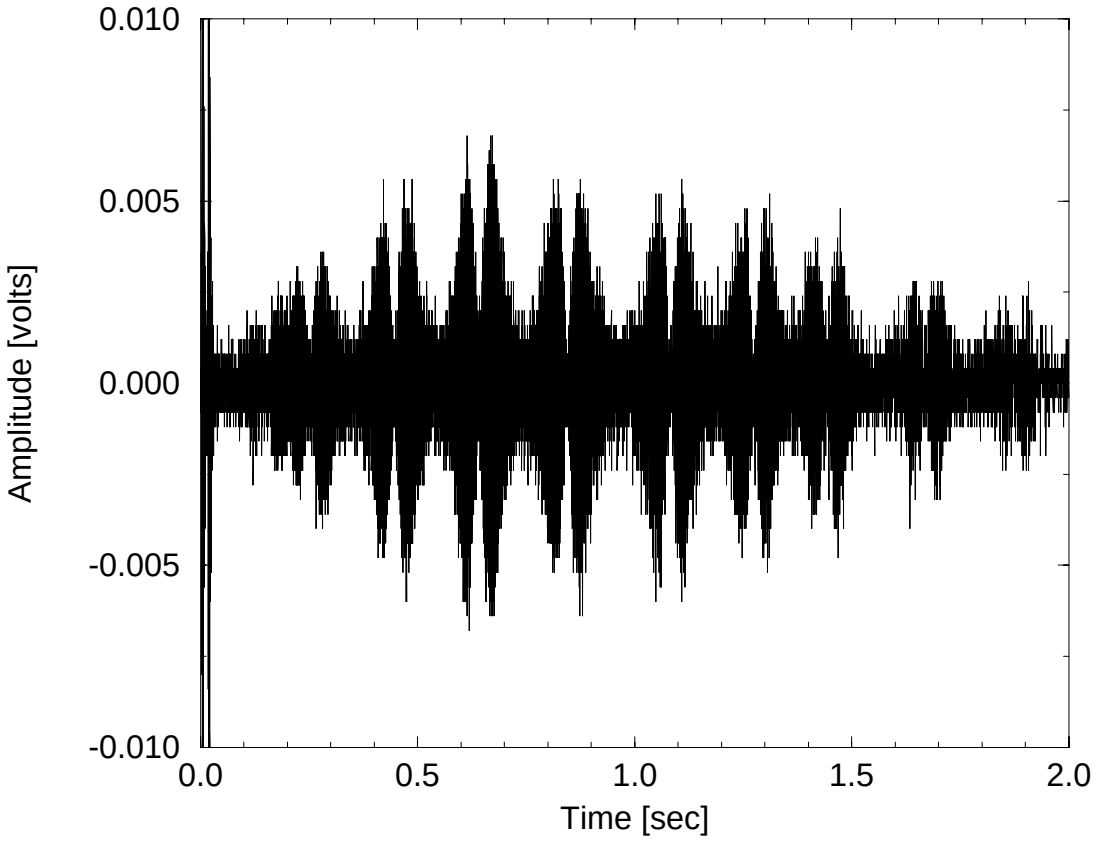

Figure 8.9: Superposition of echoes with varying driving pulse separations. As the initial pulse separation is increased, the echo delay time (t_{echo}) also increases. The echo amplitude is a function of t_{echo}. The beam intensity during this scan was 125 mA.

scan, as well as the theoretical fit is shown in figure 8.10. However, as this was a first attempt at such a measurement, the results were only good to about 30%. This was not sufficient to unequivocally identify the source of diffusion. One source of error was a lack of statistics, usually there was only one measurement for a given pulse separation. There were some instances of multiple measurements at a given pulse separation, allowing for an estimate of the size of the error bars on the data points.

The result of the fit was $\nu = (3.0 \pm 0.8) \times 10^{-4}$ Hz. The theoretical estimate for the intrabeam scattering rate was low by about a factor of 3 [53, 54, 19]. It is possible for other sources of diffusion to dominate, for example the randomizing effect of the cooling systems could be responsible for the phase decorrelation. The gain of the cooling systems have not been completely quantified across the relevant frequency band, so it was not possible to theoretically predict whether these systems have a significant contribution compared to intrabeam scattering. A few other sources of diffusion have been ruled out. Power supply noise has been measured and found to be insignificant [55]. The effect of the damper systems was investigated during these studies. Scans of the echo amplitude versus t_{echo} were done with the damper systems off as well as on. The shape of the curve and location of the peak amplitude did not depend on the state of the damper systems, indicating the contribution of the dampers to the scattering rate is negligible.

Although the first attempt at determining the collision rate in the Accumulator beam did not have the desired accuracy, and in fact did not clearly identify the source of the diffusion, the method employed appears to have the potential of becoming a useful beam diagnostic. It may also be possible to extend the use of echoes to bunched beams [17, 18, 19].

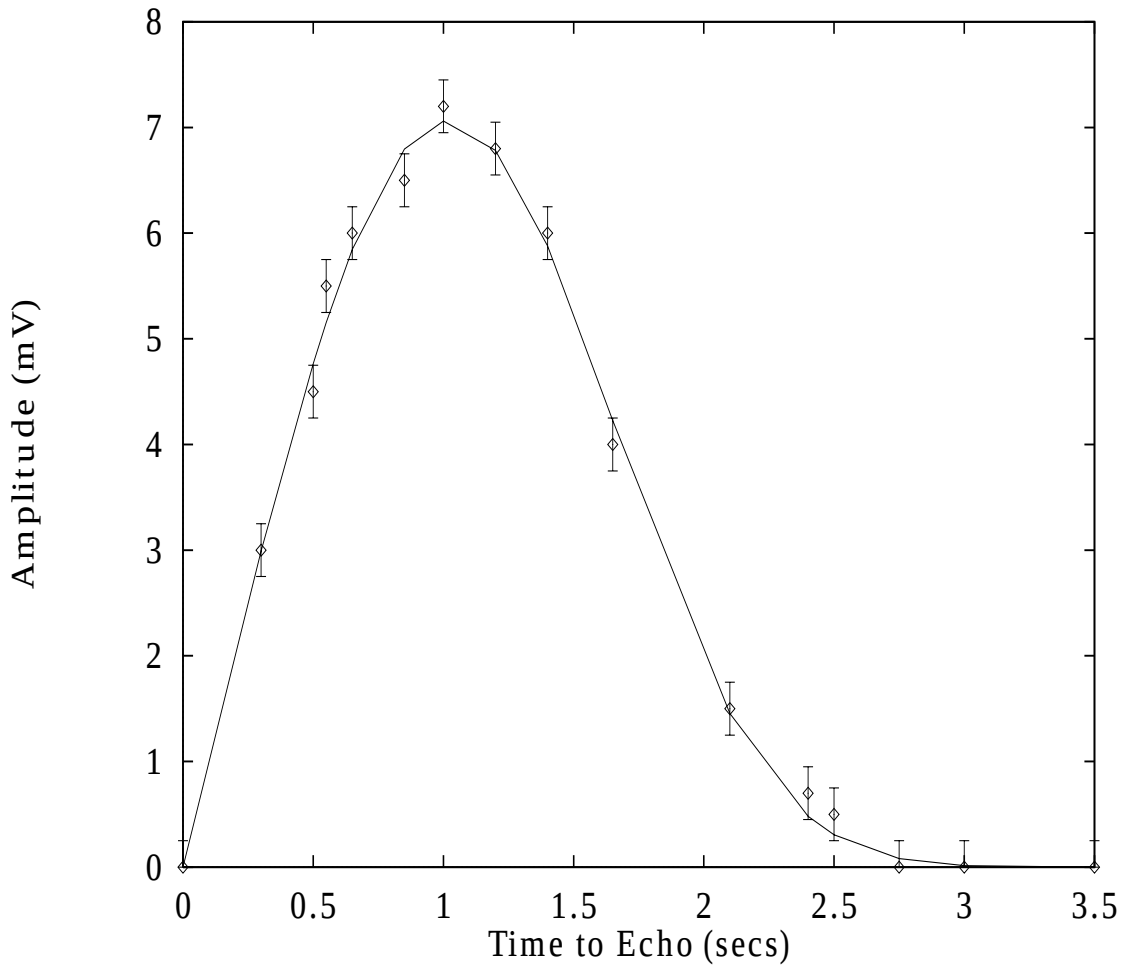

Figure 8.10: Peak echo response as a function of the time to echo following the initial pulse. The solid line represents a theoretical fit corresponding to a collision rate $\nu = (3.0 \pm 0.8) \times 10^{-4}$ Hz. The beam parameters were $I_0 = 147$ mA, $\eta = .023$, $E_0 = 8696$ MeV, beam energy spread obtained from Schottky pickup $\sigma_\varepsilon = 4.0$ MeV, transverse normalized emittances $\epsilon_H = .84\pi$ mm-mrad, and $\epsilon_V = .34\pi$ mm-mrad.

Chapter 9

Conclusions

9.1 The original objective

In the interest of obtaining a value for the machine impedance of the Fermilab Tevatron proton synchrotron, transfer function measurements were made on a coasting, unbunched, 150 GeV beam. The results of the measurement were not linear, as the applied power coupled out of the driven mode in a downward cascade of successive harmonics. The phenomena was recognized as a weakly nonlinear wave-wave coupling phenomena known as parametric coupling. This was the point of departure for this thesis work. The goal was to study the 3-wave coupling of longitudinal modes in unbunched particle beams, with the purpose of learning how to extract the impedance of a machine out of nonlinear data.

9.2 The experimental flow

The first attempt at studying parametric decay was made in the Fermilab Accumulator antiproton storage ring, since this was the first machine available for studies. Here, the experience in the Tevatron could not be duplicated. Conditions in the Main Ring were known to be closer to those in the Tevatron, for the results of transfer function measurements had shown deep notches in the magnitude response of the beam, and these had also been seen in the Tevatron. It turned out that classic parametric coupling was easy to stimulate in the Main Ring.

The next step was to take the measurement into the time domain, applying a short pulse to trigger the cascade of events. The idea was to make a clear determination of the sequential order of the coupling events; and, by knowing how much energy was supplied to the system by the pulse, quantify the machine impedance. The sequence of coupling events was proven to be single-sided, cascading downward in an orderly progression from higher to lower harmonics. This in turn indicated that the $h = 1$ mode was either a partner in parametric scattering, or a product of parametric decay. An examination of power in the $h = 1$ mode indicated the scattering scenario is more likely. That mode was alway coherent, whether or not an external pulse was applied. Since the energy gain or loss during coupling was not detectable, the result is not conclusive, but it certainly suggests that the large coherent energy reservoir at $h = 1$ is at least in part responsible for the cascading behavior of the parametric coupling events.

Although the coherence at $h = 1$ made direct determination of the impedance difficult, repeated studies have outlined the qualitative role of the impedance. It may yet be possible to quantify the process. The major source of impedance at the

frequencies being studied was the broadband RF cavity that was also being used as the kicker during the experiments. The cavity functioned as an amplifier for the decay process, having an integrated effect on the power in the mode progression within the cavity bandwidth. Once the coupling process had moved out of the cavity window, the power of the modal excitation quickly dissipated. Perhaps the impedance may be unfolded from the total harmonic response, using a baseline measurement outside of the cavity bandwidth to account for the natural power flow of the coupling events, and other dissipative sources in the storage ring.

An unexpected observation during the parametric coupling studies was that even with a very short pulse excitation, power in the resulting excited modes decayed too slowly. The time development of the power signals exhibited a 'bouncing' effect characteristic of classic nonlinear Landau damping. A new door had opened, an effort to document moderately nonlinear wave-particle interactions had begun. Increasing the drive pulse width produced much longer nonlinear Landau damping times, together with an increase in the bunch rotation period (due to bigger buckets). Significant higher harmonic generation was also documented. Meanwhile, Colestock and Ostiguy had developed a particle tracking simulation code with a narrow impedance built into the beam dynamics, and the code indicated the possibility of small islands of trapped particles asymmetrically located across the beam distribution. This small subset of particles maintaining a constant relative phase relation was generally suggestive of soliton-like behavior. Indeed, this coherent bunchlet behavior was then also observed experimentally.

The Accumulator had not been forgotten. Eventually it was realized the the failure to produce parametric coupling was due to the stable, low impedance nature of the

Accumulator. The beam energies in the Accumulator and the Main Ring were the same, and not a factor. Two aspects of the Main Ring act to increase the likelihood of coupling. The cavity impedance increases the value of the coupling coefficient, and enhances the coupling process. In addition, the notches in the beam distribution are depopulated regions in phase space, drastically reducing the area of linear stability. The dispersion relation for the 3-wave coupling resonance is built from a combination of linear dispersion relations of the individual modes, and so the area of stability to the coupling resonance is likewise decreased.

The lack of wakefield effects in the Accumulator, evident from the damping time of for coherent motion, and the clean transfer function measurements, make this machine ideal for echo generation, the time domain analog of parametric coupling. Echoes and higher order echoes, complete with theoretically predicted attributes, were easily observed. There was a clear notch in the center of the echoes, which had not been seen in other media. The lack of self-fields in the Accumulator allows free-streaming particle motion away from the drive pulses, and so the notch resulting from the smoothly peaked form of the beam distribution does not deteriorate. Also, the permittivity of the beam allows observation of a clean beam current signal. These notches did fill in, however, if the momentum spread of the beam became very large. Although some possible paths of investigation present themselves, the cause is still undetermined.

Echoes were used to measure the diffusion rate in the beam. The random processes which cause beam heating destroy the correlation between particle energy and phase, which in turn degrades the echo amplitude. Phase decorrelation weakens the echo

more as the time to the echo increases. Therefore, by fitting the functional dependence of echo amplitude on time, the collision rate in the beam may be determined. Following this procedure did indeed yield a collision rate, albeit with a large error bar. It was not possible to pinpoint the source of diffusion with the initial rough measurement. However, the experimental technique may be considerably polished and there is no indication of an intrinsic limitation to the accuracy of the measurement.

9.3 Summary

The formal, theoretical approach of the discipline of plasma physics has been applied to observations of weakly nonlinear to moderately nonlinear effects in particle beams. This has allowed a systematic classification of experimental data, and guidance by the insights gained from the depth of the developed theory. In particular, the weakly nonlinear wave-wave coupling phenomena known as parametric coupling and echo generation have been carefully documented and compared to the theory.

It is now understood that the study and use of echoes is well suited to low impedance machines where there is little interference from wakefields. Echoes may be used to make fast, sensitive measurements of the diffusion rate in a beam, and proof of principal has been shown here. In the era of high intensity, low emittance storage rings, a fast method of obtaining the magnitude of collisional effects such as intrabeam scattering should be a useful addition to the field of accelerator physics. The diagnostic potential of echo generation has just been touched on, there may be a considerable wealth of information in the shape of echoes. Assuming that a machine is not so nonlinear so as to prevent the observation of discernible echoes, any wakefields present will modify the rise and fall of the echoes in a predictable way. The echo

shape is also sensitive to the nature of the diffusion coefficient in the Fokker-Planck operator. If the coefficient is a function of the particle energy, then it also has an effect on the shape of the echo. In addition, there is the issue of the echo notch, which fills in for large energy spreads in the particle distribution. What causes this, and can the cause be quantified?

In contrast, the diagnostic potential of parametric coupling comes into its own in a marginally stable storage ring. The original motivation of quantifying the machine impedance through an examination of the power flow in a coupling cascade has not be met, but the gap has closed somewhat. The role of an impedance as an amplifier for the coupling process is understood, and it remains to find a means of unfolding the various contributions to the total beam response. To this end, it is important to know whether the parametric coupling is a scattering or a decay process so that the power flow between modes may be quantified. It appears that in the Main Ring the coupling is scattering of the excited mode off the continuously coherent $h = 1$ mode, although this is not absolutely conclusive.

Investigation of moderate to strongly non-linear phenomena has begun with the observation of nonlinear Landau damping, higher order harmonic generation, and bunchlet formation which is asymmetric in the particle distribution. Although this exploration is still in the beginning stages, there is already some preliminary information buried in these observations. The bunch rotation period in nonlinear Landau damping time may be used to find the amplitude of the wakefields, and the rate of their decay. The asymmetric bunchlet formation so suggestive of solitons, gives an indication as to the relative phase of a wakefield. There is much more work to be done before this area of study is well understood and exhausted. While inquiry into the

nonlinear regime is still in the exploratory stage, ultimately a deeper understanding of these beam phenomena may allow either the quantization or control of parameters affecting beam dynamics.

Appendix A

Beam transfer function measurements

Beam transfer function measurements are two-port network transmission coefficient measurements using scattering parameters (S-parameters). These S-parameters describe the relations between transmitted and reflected voltage waves at each port of the network, and thus are appropriate for high frequency excitations. A general two-port network is shown schematically in figure A.1. Referring to figure A.1, the

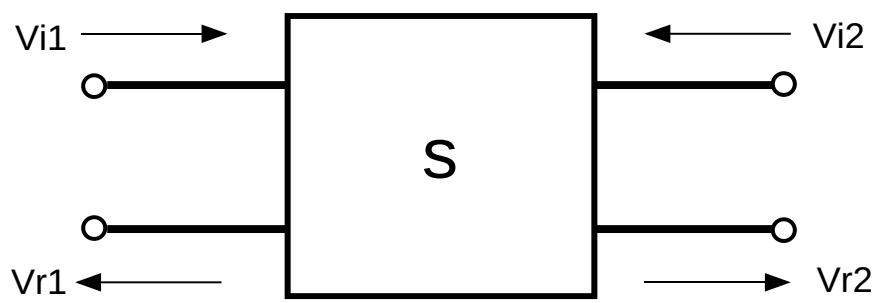

Figure A.1: General two-port network

relation between the traveling waves and the scattering matrix is

$$\begin{pmatrix} V_{r1} \\ V_{r2} \end{pmatrix} = \begin{pmatrix} s_{11} & s_{12} \\ s_{21} & s_{22} \end{pmatrix} \begin{pmatrix} V_{i1} \\ V_{i2} \end{pmatrix}$$

If an incident voltage is applied to port 1 while port 2 is terminated with the characteristic input impedance, then $V_{i2} = 0$, as there is no reflection from the termination. For these cases, s_{11} is the input reflection coefficient, since $V_{r1} = s_{11}V_{i1}$. Similarly, s_{21} is the forward transmission coefficient, since $V_{r2} = s_{21}V_{i1}$. When a two-port network responds linearly to an excitation frequency, it is possible to extract the series impedance, the parallel impedance may be neglected in a particle beam measurement. A representation of a network analyzer set up to measure a series impedance, which is shown as R, is given by figure A.2. The network analyzer is represented by the

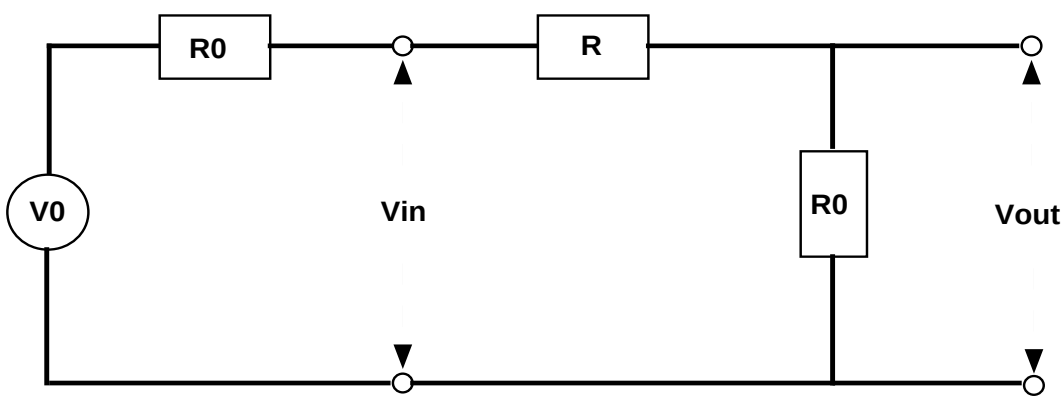

Figure A.2: Network configuration for an impedance measurement

source of excitation $V0$ and a characteristic input impedance $R0$. The impedance being measured is given by R, which is then matched back into the analyzer through the characteristic impedance $R0$. From transmission line theory, the voltage reflection

coefficient is,

$$, = \frac{Z_L - Z_0}{Z_L + Z_0}$$

where Z_L is the impedance of the load, and Z_0 is the characteristic impedance of the line [31]. In figure A.2 the load impedance at port 1 of the two-port network is $R + R0$, so the reflection coefficient becomes,

$$, = s_{11} = \frac{(R + R0) - R0}{(R + R0) + R0} = \frac{R}{2R0 + R}.$$

The transmission coefficient is then,

$$1 - , = s_{21} = 1 - \frac{R}{2R0 + R} = \frac{2R0}{2R0 + R}.$$

The expression for the transmission coefficient can be re-arranged so that R is given in terms of s_{21},

$$R = 2R0 \left(\frac{1}{s_{21}} - 1 \right). \tag{A.1}$$

Network analyzer measurement results are typically displayed using a logarithmic scale in decibels (dB) for the magnitude response and a scale in degrees for the phase response [30]. Amplitude in dB is defined in terms of the power ratio of the transmitted and received signals, $A[dB] = 10 \log \frac{P_r}{P_t}$. When P_r and P_t are due to voltages across equivalent resistances, then the resistances cancel, and this relation can be written $A[dB] = 20 \log \frac{V_r}{V_t}$.

Referring again to figure A.2, suppose a simple circuit device is inserted which has no impedance, $R = 0$. In this case, the ratio $\frac{V_{out}}{V_{in}}$ will be one, and s_{21} will be $0dB$. As the impedance R increases, $\frac{V_{out}}{V_{in}}$ decreases, and the measured amplitude in decibels gets more negative.

When a storage ring with beam is inserted for R, then the interpretation of s_{21} is more subtle. Generally the output port of the network analyzer is connected to a device in the ring which is capable of exciting the beam, while the response of the beam is monitored elsewhere in the ring through the use of a suitable detector. Under normal circumstances, a signal completing the path to the return port of the network analyzer must be transmitted through the particle beam. Thus, there can be power in the response only at frequencies supported by the beam. If the frequency of the external voltage is not a natural frequency of the beam, then there is no mechanism for energy absorption from the voltage source. The particles in the beam do not all move with the same frequency; rather there is a distribution of frequencies, which in the longitudinal case corresponds to the energy distribution of the beam. Barring effects from the hardware comprising the ring, or the measurement itself, the amplitude versus frequency of s_{21} should closely resemble the energy profile of the beam. Only those particles whose frequencies match the frequency of the driving voltage are able to absorb energy from the voltage wave. Thus, the beam response to a voltage source of a given frequency is in direct proportion to the number of particles that move with that frequency. A plot of the magnitude from an s21 measurement and a concurrent beam spectrum are shown in figure A.3. For purposes of comparison, the ratio of the frequency span to the center frequency is the same for both traces. When there is an impedance present in the ring at a frequency within the beam distribution, it may

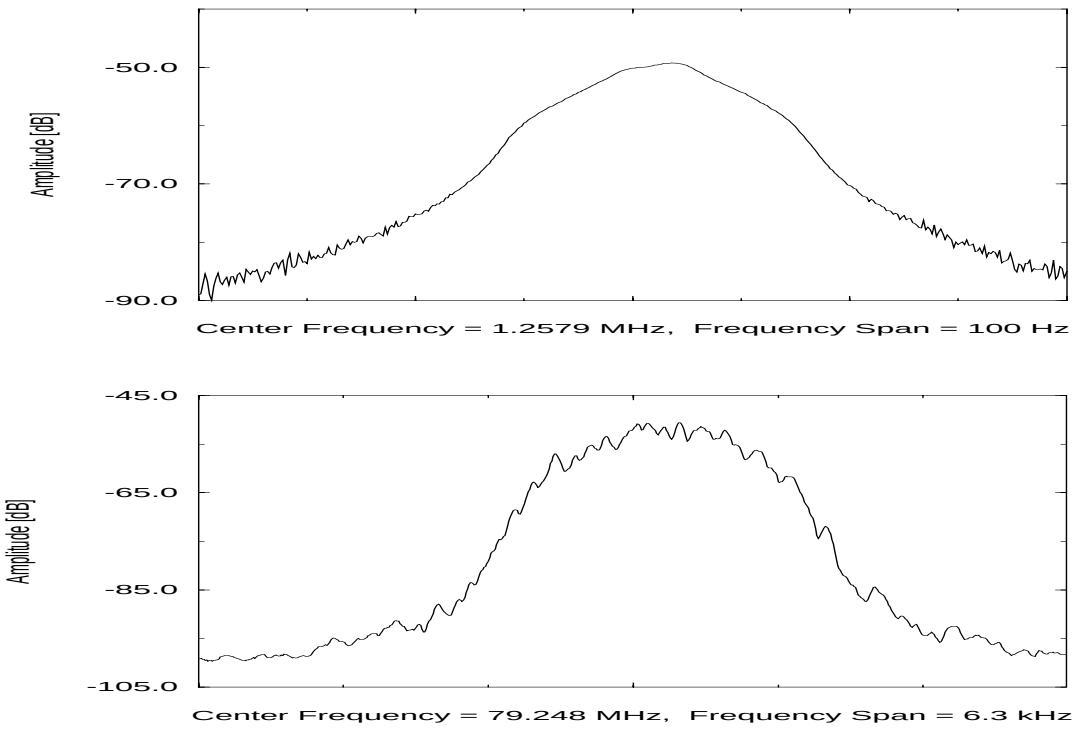

Figure A.3: Comparison of a beam transfer function measurement to the undisturbed frequency distribution of the beam. The top plot is the magnitude response of an S21 measurement, and the bottom plot is the beam spectrum.

enhance the beam response at this frequency, distorting the amplitude of s_{21}. It is this fact which makes beam transfer functions a potentially useful tool for identifying machine impedances.

Appendix B

Alternative derivation of the dispersion relation for parametric coupling

The second order dispersion relation for parametric coupling will be found using a technique derived from D.G. Swanson [43]. The procedure is to do a Fourier transformation of the second order perturbatively expanded Vlasov equation, eq. 5.3. Through the use of direct substitutions, all terms of the equation are written as expressions in the perturbed current, I_m. In addition, non-resonant terms are neglected. Then I_m may be cancelled out of the equation, giving the second order dispersion relation. Once this general dispersion relation is obtained, it is expanded around the resonant frequency in order to get an expression describing the system when it is close to resonance. This resonant form of the dispersion relation is identical to the result obtained in section 5.3, which uses the multiple time scale expansion technique and

normal mode analysis.

Starting with eq. 5.3, consider the response of the beam at a mode m due to the frequency mixing of another mode k with an externally applied voltage. Let U_n be a driving voltage of the form,

$$U_n = V_0 e^{i(n\theta - \Omega_0 t)} + V_0^* e^{-i(n\theta - \Omega_0 t)}$$

where V_0 is the amplitude of the applied voltage, and $\Omega_0 = n\omega_0$ is the frequency of the applied voltage. Then the summation in eq. 5.3 reduces to two terms, and the equation may be written,

$$\frac{\partial f_m}{\partial t} + im\omega(\varepsilon) f_m = -\frac{e\omega_0}{2\pi}\frac{\partial f_0}{\partial \varepsilon} U_m - \frac{e\omega_0}{2\pi} V_0 \frac{\partial f_{m-n}}{\partial \varepsilon} e^{-i\Omega_0 t} - \frac{e\omega_0}{2\pi} V_0^* \frac{\partial f_{m+n}}{\partial \varepsilon} e^{i\Omega_0 t}$$

Taking the Fourier transform,

$$\frac{1}{\sqrt{2\pi}} \int_{-\infty}^{\infty} \frac{\partial f_m}{\partial t} e^{-i\Omega t}\, dt + im\omega(\varepsilon) \frac{1}{\sqrt{2\pi}} \int_{-\infty}^{\infty} f_m e^{-i\Omega t}\, dt =$$

$$\frac{e\omega_0}{2\pi}\frac{\partial f_0}{\partial \varepsilon} \frac{1}{\sqrt{2\pi}} \int_{-\infty}^{\infty} U_m e^{-i\Omega t}\, dt$$

$$\frac{e\omega_0}{2\pi} V_0 \frac{1}{\sqrt{2\pi}} \int_{-\infty}^{\infty} \frac{\partial f_{m-n}}{\partial \varepsilon} e^{-i(\Omega - \Omega_0)t}\, dt - -\frac{e\omega_0}{2\pi} V_0^* \frac{1}{\sqrt{2\pi}} \int_{-\infty}^{\infty} \frac{\partial f_{m+n}}{\partial \varepsilon} e^{-i(\Omega + \Omega_0)t}\, dt \quad \text{(B.1)}$$

The evaluation of eq. B.1 is facilitated by an integration by parts of the first term on the left hand side (LHS), and by applying the modulation property of Fourier

transforms to the last two terms of the right hand side (RHS). Then,

$$\begin{aligned} i[\Omega - m\omega(\varepsilon)]F_m(\Omega) &= \frac{e\omega_0}{2\pi}\frac{\partial f_0}{\partial \varepsilon}U_m \\ &+ \frac{e\omega_0}{2\pi}V_0\frac{\partial F_{m-n}(\Omega-\Omega_0)}{\partial\varepsilon} + \frac{e\omega_0}{2\pi}V_0^*\frac{\partial F_{m+n}(\Omega+\Omega_0)}{\partial\varepsilon} \end{aligned} \quad \text{(B.2)}$$

In order to obtain the dispersion relation, it is necessary to write each term in eq. B.2 as an expression in the same dependent variable, so that it may be cancelled out of the equation. The purpose of most of the remaining analysis in this section is to manipulate eq. B.2 so that I_m may be factored out of the equation. Begin by isolating the F_m on the LHS, and also make the substitution $U_m = -Z_m I_m$,

$$\begin{aligned} F_m(\Omega) &= -\frac{e\omega_0}{2\pi}Z_m(\Omega)I_m(\Omega)\frac{\frac{\partial f_0}{\partial\varepsilon}}{i[\Omega - m\omega(\varepsilon)]} \\ &+\frac{e\omega_0}{2\pi}V_0\frac{\frac{\partial F_{m-n}(\Omega-\Omega_0)}{\partial\varepsilon}}{i[\Omega - m\omega(\varepsilon)]} + \frac{e\omega_0}{2\pi}V_0^*\frac{\frac{\partial F_{m+n}(\Omega+\Omega_0)}{\partial\varepsilon}}{i[\Omega - m\omega(\varepsilon)]} \end{aligned} \quad \text{(B.3)}$$

In order to change the F_m on the LHS into the perturbed current, I_m, multiply eq. B.3 by $e\omega_0$ and integrate over the energy error, ε. If, in addition, an integration by parts is done to the second and third terms on the RHS, then eq. B.3 becomes,

$$\begin{aligned} I_m(\Omega) &= e\omega_0\int_{-\infty}^{\infty} F_m(\Omega)\,d\varepsilon \\ &= -\frac{(e\omega_0)^2}{2\pi}Z_m(\Omega)I_m(\Omega)\int_{-\infty}^{\infty}\frac{\frac{\partial f_0}{\partial\varepsilon}}{i[\Omega - m\omega(\varepsilon)]}\,d\varepsilon \end{aligned}$$

$$+\frac{(e\omega_0)^2}{2\pi}V_0 m k_0 \int_{-\infty}^{\infty} \frac{F_{m-n}(\Omega-\Omega_0)d\varepsilon}{i[\Omega - m\omega(\varepsilon)]^2}$$

$$+\frac{(e\omega_0)^2}{2\pi}V_0^* m k_0 \int_{-\infty}^{\infty} \frac{F_{m+n}(\Omega+\Omega_0)d\varepsilon}{i[\Omega - m\omega(\varepsilon)]^2}$$

Re-arranging so that the terms in I_m are on the same side of the equation,

$$\begin{aligned} I_m(\Omega)D_m(\Omega) &= -\frac{(e\omega_0)^2}{2\pi}V_0 m k_0 \int_{-\infty}^{\infty} \frac{F_{m-n}(\Omega-\Omega_0)}{i[\Omega - m\omega(\varepsilon)]^2}\, d\varepsilon \\ &\quad -\frac{(e\omega_0)^2}{2\pi}V_0^* m k_0 \int_{-\infty}^{\infty} \frac{F_{m+n}(\Omega+\Omega_0)}{i[\Omega - m\omega(\varepsilon)]^2}\, d\varepsilon \end{aligned} \tag{B.4}$$

where D_m is just the linear dispersion relation for mode m,

$$D_m(\Omega) \equiv \left\{ 1 - \frac{i(e\omega_0)^2}{2\pi} Z_m(\Omega) \int_{-\infty}^{\infty} \frac{\frac{\partial f_0}{\partial \varepsilon}}{\Omega - m\omega(\varepsilon)}\, d\varepsilon \right\} \tag{B.5}$$

Note that the closer the dispersion relation is to being satisfied, the more nearly D_m is zero. If both sides of equation B.4 are divided by $D_m(\Omega)$, it can be seen that $I_m(\Omega)$ will be larger as the dispersion relation is closer to zero. The root of the dispersion relation occurs when $\Omega = m\omega_0$, (since $\omega(\varepsilon) = \omega_0 + k_0\varepsilon \simeq \omega_0$), with $m\omega_0$ being the frequency of the mth normal mode. On simple physical grounds, if I_m is large, then an oscillation at $m\omega_0$ must be present in the beam.

Now, to get an alternative expression for F_{m-n}, begin with eq. B.3, letting $m \to m-n$ and $\Omega \to \Omega - \Omega_0$,

$$F_{m-n}(\Omega-\Omega_0) = -\frac{e\omega_0}{2\pi} Z_{m-n}(\Omega-\Omega_0) I_{m-n}(\Omega-\Omega_0) \frac{\frac{\partial f_0}{\partial \varepsilon}}{i[\Omega - \Omega_0 - (m-n)\omega(\varepsilon)]}$$

$$+\frac{e\omega_0}{2\pi}V_0\frac{\frac{\partial F_{m-2n}(\Omega-2\Omega_0)}{\partial\varepsilon}}{i[\Omega-\Omega_0-(m-n)\omega(\varepsilon)]}$$

$$+\frac{e\omega_0}{2\pi}V_0^*\frac{\frac{\partial F_m(\Omega)}{\partial\varepsilon}}{i[\Omega-\Omega_0-(m-n)\omega(\varepsilon)]} \tag{B.6}$$

As seen in eq. B.3, mode m may couple to modes $m-n$, $m+n$, or both by virtue of the existence of the pump at the nth harmonic. Similarly, the pump enables mode $m-n$ to couple with modes m, $m-2n$, or both. Any existing mode may couple to two others via the drive, but for the sake of clarity we are only interested in a single combination of 3-wave coupling. Then the $m-2n$ term in eq. B.6 is not resonant and will phase average to zero.

Substituting the expression for F_{m-n} given by eq. B.6 and a similarly acquired expression for F_{m+n} into eq. B.4,

$$I_m(\Omega)D_m(\Omega) = -\frac{(e\omega_0)^2}{2\pi}mk_0\,\{$$

$$-\frac{e\omega_0}{2\pi}V_0Z_{m-n}(\Omega-\Omega_0)I_{m-n}(\Omega-\Omega_0)\int_{-\infty}^{\infty}\frac{\frac{\partial f_0}{\partial\varepsilon}}{i[\Omega-m\omega(\varepsilon)]^2 i[\Omega-\Omega_0-(m-n)\omega(\varepsilon)]}\,d\varepsilon$$

$$+\frac{e\omega_0}{2\pi}V_0V_0^*\int_{-\infty}^{\infty}\frac{\frac{\partial F_m(\Omega)}{\partial\varepsilon}}{i[\Omega-m\omega(\varepsilon)]^2 i[\Omega-\Omega_0-(m-n)\omega(\varepsilon)]}\,d\varepsilon$$

$$-\frac{e\omega_0}{2\pi}V_0^*Z_{m+n}(\Omega+\Omega_0)I_{m+n}(\Omega+\Omega_0)\int_{-\infty}^{\infty}\frac{\frac{\partial f_0}{\partial\varepsilon}}{i[\Omega-m\omega(\varepsilon)]^2 i[\Omega+\Omega_0-(m+n)\omega(\varepsilon)]}\,d\varepsilon$$

$$+\frac{e\omega_0}{2\pi}V_0V_0^*\int_{-\infty}^{\infty}\frac{\frac{\partial F_m(\Omega)}{\partial\varepsilon}}{i[\Omega-m\omega(\varepsilon)]^2 i[\Omega+\Omega_0-(m+n)\omega(\varepsilon)]}\,d\varepsilon\,\} \tag{B.7}$$

Each of the coupling terms, $m-n$ and $m+n$, may be considered separately, as in general both modes will not be present in the beam. The $m+n$ term will be discarded. The second and forth terms on the RHS may also be discarded, as they represent coupling between mode m and the drive, and it is coupling between different modes which is of interest here. Now we have,

$$\begin{aligned} I_m(\Omega)D_m(\Omega) &= \frac{(e\omega_0)^3}{(2\pi)^2}V_0 m k_0 Z_{m-n}(\Omega-\Omega_0)I_{m-n}(\Omega-\Omega_0) \\ &\times \int_{-\infty}^{\infty} \frac{\frac{\partial f_0}{\partial \varepsilon}}{i[\Omega - m\omega(\varepsilon)]^2 i[\Omega-\Omega_0-(m-n)\omega(\varepsilon)]}\, d\varepsilon \end{aligned} \tag{B.8}$$

In order to get an expression for I_{m-n}, begin with eq. B.4, letting $m \to m-n$ and $\Omega \to \Omega - \Omega_0$ yielding,

$$\begin{aligned} I_{m-n}(\Omega-\Omega_0) &= \frac{1}{D_{m-n}(\Omega-\Omega_0)}\{ \\ &- \frac{(e\omega_0)^2}{2\pi}V_0(m-n)k_0\int_{-\infty}^{\infty}\frac{F_{m-2n}(\Omega-2\Omega_0)}{i[\Omega-\Omega_0-(m-n)\omega(\varepsilon)]^2}\,d\varepsilon \\ &- \frac{(e\omega_0)^2}{2\pi}V_0^*(m-n)k_0\int_{-\infty}^{\infty}\frac{F_m(\Omega)}{i[\Omega-\Omega_0-(m-n)\omega(\varepsilon)]^2}\,d\varepsilon\ \} \end{aligned} \tag{B.9}$$

Again, the $m-2n$ term will be dropped. In the remaining term, F_m may be replaced using eq. B.3, although it is only necessary to use the first term on the RHS for the substitution. The second and third terms would end up being third order in the

coupling coefficient V_0, and so may be neglected. Now I_{m-n} can be written,

$$\begin{aligned} I_{m-n}(\Omega-\Omega_0) &= \frac{1}{D_{m-n}(\Omega-\Omega_0)}\left\{\frac{(e\omega_0)^3}{(2\pi)^2}V_0^*(m-n)k_0 Z_m(\Omega)I_m(\Omega)\right. \\ &\times \left.\int_{-\infty}^{\infty}\frac{\frac{\partial f_0}{\partial\varepsilon}}{i[\Omega-m\omega(\varepsilon)]i[\Omega-\Omega_0-(m-n)\omega(\varepsilon)]^2}d\varepsilon\right\} \qquad \text{(B.10)} \end{aligned}$$

Using the expression for $I_{m-n}(\Omega-\Omega_0)$ given by eq. B.10 in eq. B.8, and then cancelling $I_m(\Omega)$ from both sides, results in the second order dispersion relation,

$$\begin{aligned} D_m(\Omega)D_{m-n}(\Omega-\Omega_0) &= \frac{(e\omega_0)^6}{(2\pi)^4}V_0V_0^*m(m-n)k_0^2 Z_m(\Omega)Z_{m-n}(\Omega-\Omega_0) \\ &\times \int_{-\infty}^{\infty}\frac{\frac{\partial f_0}{\partial\varepsilon}}{[\Omega-m\omega(\varepsilon)][\Omega-\Omega_0-(m-n)\omega(\varepsilon)]^2}d\varepsilon \\ &\times \int_{-\infty}^{\infty}\frac{\frac{\partial f_0}{\partial\varepsilon}}{[\Omega-m\omega(\varepsilon)]^2[\Omega-\Omega_0-(m-n)\omega(\varepsilon)]}d\varepsilon \qquad \text{(B.11)} \end{aligned}$$

It will now be shown that the general dispersion relation given by eq. B.11 is consistent with the result of the multiple time scale technique. This is done by expanding the linear dispersion relations on the LHS around the resonant frequency, $\omega_m = \omega_{m-n}+\Omega_0$. Assume the frequency of the system is nearly resonant, $\Omega = \omega_m - i\nu$, where ν is small compared to ω_m. Then,

$$D_m(\Omega) = 1 - \frac{i(e\omega_0)^2}{2\pi}Z_m(\omega_m)\int_{-\infty}^{\infty} d\varepsilon\frac{\frac{\partial f_0}{\partial\varepsilon}}{[\omega_m - m\omega(\varepsilon)][1-\frac{i\nu}{\omega_m - m\omega}]}$$

$$= 1 - \frac{i(e\omega_0)^2}{2\pi} Z_m(\omega_m) \int_{-\infty}^{\infty} \frac{d\varepsilon \frac{\partial f_0}{\partial \varepsilon}}{\omega_m - m\omega(\varepsilon)} \left\{ 1 + \frac{i\nu}{\omega_m - m\omega} + \left(\frac{i\nu}{\omega_m - m\omega} \right)^2 + \cdots \right\}$$

$$= D_m(\omega_m) + \nu \frac{(e\omega_0)^2}{2\pi} Z_m(\omega_m) \int_{-\infty}^{\infty} d\varepsilon \frac{\frac{\partial f_0}{\partial \varepsilon}}{[\omega_m - m\omega(\varepsilon)]^2} + \mathcal{O}(\nu^2) \tag{B.12}$$

Note that $D_m(\omega_m) = 0$ and may be dropped. Dealing with $D_{m-n}(\Omega - \Omega_0) = D_{m-n}(\omega_{m-n} - i\nu)$ in a similar manner, the second order dispersion relation given by eq. B.11 becomes,

$$\nu^2 \int_{-\infty}^{\infty} \frac{\frac{\partial f_0^0}{\partial \varepsilon}}{[\omega_m - m\omega(\varepsilon)]^2} d\varepsilon \int_{-\infty}^{\infty} \frac{\frac{\partial f_0^0}{\partial \varepsilon}}{[\omega_{m-n} - (m-n)\omega(\varepsilon)]^2} d\varepsilon =$$

$$\frac{(e\omega_0)^2}{(2\pi)^2} V_0 V_0^* m(m-n) k_0^2 \quad \int_{-\infty}^{\infty} \frac{\frac{\partial f_0^0}{\partial \varepsilon}}{[\omega_m - m\omega(\varepsilon)]^2 [\omega_{m-n} - (m-n)\omega(\varepsilon)]} d\varepsilon$$

$$\times \int_{-\infty}^{\infty} \frac{\frac{\partial f_0^0}{\partial \varepsilon}}{[\omega_m - m\omega(\varepsilon)][\omega_{m-n} - (m-n)\omega(\varepsilon)]^2} d\varepsilon \tag{B.13}$$

This is identical to eq. 5.27.

Appendix C

Demonstration of symmetry relations used in section 5.5

The following symmetry relations are needed in section 5.5 to link the frequency and mode selection rules to wave energy and momentum conservation laws,

$$\frac{V_{m,n,k}}{m} = \frac{V_{-n,-m,k}}{-n} = \frac{V_{-k,n,-m}}{-k}$$

where,

$$\frac{V_{mnk}}{m} = \frac{-i\frac{2(\epsilon\omega_0)^3}{\sqrt{\epsilon_0}(2\pi)^2} Z \frac{1}{m} \int_{-\infty}^{\infty} \frac{\partial}{\partial\varepsilon}\left(\frac{\frac{\partial f_0^0}{\partial\varepsilon}}{\omega_k-(k)\omega(\varepsilon)}\right) \frac{1}{[\omega_m - m\omega(\varepsilon)]}\, d\varepsilon}{\left[\left|\frac{\partial D_m}{\partial\omega_m}\right| \left|\frac{\partial D_n}{\partial\omega_n}\right| \left|\frac{\partial D_k}{\partial\omega_k}\right|\right]^{\frac{1}{2}}}$$

The portion which must be shown to be invariant to permutation is:

$$X_{mnk} = \frac{1}{m}\int_{-\infty}^{\infty} \frac{\partial}{\partial\varepsilon}\left(\frac{\frac{\partial f_0^0}{\partial\varepsilon}}{\omega_k - (k)\omega(\varepsilon)}\right)\frac{1}{[\omega_m - m\omega(\varepsilon)]}\,d\varepsilon \tag{C.1}$$

The symmetry relations will be demonstrated using a technique derived from R.C. Davidson [10]. The first step is to write expression C.1 in a more symmetric form:

$$X_{mnk} = \frac{1}{m}\int_{-\infty}^{\infty} \frac{d\varepsilon}{[\omega_m - m\omega(\varepsilon)]}\left\{\frac{\partial}{\partial\varepsilon}\left(\frac{\frac{\partial f_0}{\partial\varepsilon}}{\omega_k - (k)\omega(\varepsilon)}\right) + \frac{\partial}{\partial\varepsilon}\left(\frac{\frac{\partial f_0}{\partial\varepsilon}}{\omega_n - (n)\omega(\varepsilon)}\right)\right\} \tag{C.2}$$

This form of X_{mnk} makes it explicit that the wave interaction $\omega_m = \omega_n + \omega_k$ is the same as the interaction $\omega_m = \omega_k + \omega_n$.

Integrating eq. C.2 by parts,

$$X_{mnk} = -k_0\int_{-\infty}^{\infty} d\varepsilon\frac{\partial f_0}{\partial\varepsilon}\left\{\frac{1}{[\omega_m - m\omega(\varepsilon)]^2[\omega_k - (k)\omega(\varepsilon)]} + \frac{1}{[\omega_m - m\omega(\varepsilon)]^2[\omega_n - (n)\omega(\varepsilon)]}\right\}$$

Adding the fractions in the integrand,

$$X_{mnk} = -k_0\int_{-\infty}^{\infty} d\varepsilon\frac{\partial f_0}{\partial\varepsilon}\left\{\frac{(\omega_n + \omega_k) - (n+k)\omega(\varepsilon)}{[\omega_m - m\omega(\varepsilon)]^2[\omega_k - (k)\omega(\varepsilon)][\omega_n - (n)\omega(\varepsilon)]}\right\} \tag{C.3}$$

However, $\omega_n + \omega_k = \omega_m$ and $n + k = m$, so eq. C.3 may be written,

$$X_{mnk} = -k_0\int_{-\infty}^{\infty} d\varepsilon\frac{\partial f_0}{\partial\varepsilon}\left\{\frac{1}{[\omega_m - m\omega(\varepsilon)][\omega_k - (k)\omega(\varepsilon)][\omega_n - (n)\omega(\varepsilon)]}\right\} \tag{C.4}$$

From the form of eq. C.4, it is now possible to see that making the transformations $m \to -n$ and $n \to -m$ results in no change, since the minus signs cancel. There is also no change under the transformations $m \to -k$ and $k \to -m$.

Bibliography

[1] E.D. Courant and H.S. Snyder, Theory of the alternating-gradient synchrotron, *Annals of physics*, Vol. 3, Academic Press Inc, New York, 1958

[2] R.Z. Sagdeev and A.A. Galeev, *Nonlinear plasma theory*, W.A. Benjamin, Inc., New York, 1969

[3] V.K. Neil and A.M. Sessler, *Review of scientific instruments*, Vol. 36, April 1965.

[4] A. Hofmann, Single-beam collective phenomena - longitudinal, CERN 77-13, Jul 1977.

[5] E. Keil and W. Schnell, CERN report ISR-TH-RF/69-48, Geneva 1969.

[6] J. Dawson, On landau damping, *The physics of fluids*, Vol. 4, Number 7, Jul 1961.

[7] T.M. O'Neil, Collisionless damping of nonlinear plasma oscillations, *The physics of fluids*, Vol. 8, Dec 1965.

[8] A.W. Chao, *Physics of Collective Beam Instabilities in High Energy Accelerators*, Wiley, New York, 1993.

[9] A.G. Sitenko, *Fluctuations and non-linear wave interactions in plasmas*, Pergamon Press, 1982.

[10] R.C. Davidson, *Methods in nonlinear plasma theory*, Academic Press, 1972.

[11] C.H. Su and C. Oberman, Collisional damping of a plasma echo, *Pysical Review Letters*, Vol 20, Number 9, Feb 1968.

[12] T.M. O'Neil, Effect of coulomb collisions and microturbulence on the plasma wave echo, *The physics of fluids*, Vol 11, Number 11, Nov 1968.

[13] K. Nishikawa, Parametric excitation of coupled waves I.General formulation, *Journal of the physical society of Japan*, Vol. 24, 1968.

[14] E.L. Hahn, Spin Echoes, *Pysical Review*, Vol 80, number 4, May 1950.

[15] R.W. Gould, T.M. O'Neil, and J.H. Malmberg, Plasma Wave Echo, *Pysical Review Letters*, Vol 19, Number 5, May 1967.

[16] T.M. O'Neil and R.W.Gould, Temporal and spatial plasma wave echoes, *The physics of fluids*, Vol 11, Number 1, Jan 1968.

[17] G.V. Stupakov, Superconducting supercollider laboratory report No. SSCL-579, 1992.

[18] G.V. Stupakov and K. Kauffmann, Superconducting supercollider laboratory report No. SSCL-587, 1992.

[19] P.L. Colestock and S. Assadi, Private communication.

[20] I.H. Oei and D.G. Swanson, Self-consistent finite amplitude wave damping, *The physics of fluids*, Vol. 15, Number 12, Dec 1972.

[21] J. Canosa and J. Gazdag, Threshold conditions for electron trapping by nonlinear waves, *The physics of fluids*, Vol. 17, Number 11, Nov 1974.

[22] J.H. Malmberg and C.B. Wharton, *Physical review letters*, Vol 17, 175, 1966.

[23] T.M. O'Neil, J.H. Winfrey, and J.H.Malmberg, Nonlinear Interaction of a Small Cold Beam and a Plasma, *The physics of fluids*, Vol 14, Number 6, June 1971.

[24] A.C. Scott, F.Y.F. Chu, and D.W. McLaughlin, The soliton: a new concept in applied science, *Proceedings of the IEEE*, Vol 61, Number 10, Oct 1973.

[25] J.J. Bisognano, Solitons and particle beams, *Particles and fields series 47, High brightness beams for advanced accelerator applications*, AIP conference proceedings 253, College Park MD, 1991.

[26] D.A. Edwards and M.J. Syphers, *An introduction to the Physics of High Energy Accelerators*, Wiley, New York, 1993.

[27] J. Wei, *Longitudinal Dynamics of the Non-adiabatic Regime on Alternating-Gradient Synchrotrons*, Dissertation, State University of New York at Stony Brook, May 1990.

[28] L. Palumbo and V.G. Vaccaro, Wake Fields, Impedances and Green's Function, *Proc. of the CERN Accelerator School - Advanced Accelerator Physics*, CERN 87-03, April 1987.

[29] R.P. Feynman, R.B. Leighton and M. Sands, *The Feynman Lectures on Physics*, Vol. II, Chapter 23, Addison-Wesley, Massachusetts, 1963.

[30] R.A. Witte, *Spectrum and Network Measurements*, Prentice Hall, New Jersey, 1991.

[31] R.E. Collin, *Foundations for Microwave Engineering*, McGraw-Hill, New York, 1992.

[32] G. Jackson, Review of Impedance Measurements at Fermilab, *Proc. of the Fermilab III Instabilities Workshop*, Fermilab Internal Note TM-1696, June 1990.

[33] J. Marriner, et al., Stability Criterion and Wall Impedance for the Antiproton Accumulator, Fermilab Internal Note, Pbar Note 422, 1985.

[34] S. Werkema, Private communication.

[35] I. Kourbanis, Private communication.

[36] D. Peterson, Private communication.

[37] R.C. Webber, Measurement Techniques Including Design of a Wall Current Monitor, *AIP Conference Proceedings No. 212, Accelerator Instrumentation*, American Institute of Physics, New York, 1990.

[38] C.D. Moore, et al., Single Bunch Intensity Monitoring System using an Improved Wall Current Monitor, *Proceedings of the 1989 IEEE Particle Accelerator Conference*, IEEE Cat. No. 89CH2669-0, page 1513, Chicago, 1989.

[39] D. Wildman, Private communication.

[40] J.L. Kirchgessner, et al., The R.F. System for the Princeton-Pennsylvania Accelerator, *IEEE Transactions on Nuclear Science*, NS-9(2):11-18.

[41] W.H. Louisell, *Coupled mode and parametric electronics*, Wiley, New York.

[42] A.H. Nayfeh, *Introduction to perturbation techniques*, Wiley, 1981

[43] D.G. Swanson, *Plasma waves*, Academic Press, 1989

[44] P.L. Colestock, G.P. Jackson, and L. Klamp, Observation and analysis of non-linear parametric coupling of longitudinal modes in synchrotrons, *Proceedings of the 1992 European Particle Accelerator Conference*, Vol. 1, Berlin, Mar 1992.

[45] P.L. Colestock and L. Klamp, A generalized model for parametric coupling of longitudinal modes in synchrotrons, *Proceedings of the 1993 Particle Accelerator Conference*, Vol. 5, Washington DC, 1993.

[46] P.L. Colestock and L.K. Spentzouris, Nonlinear wave phenomena and emittance growth in coasting beams, *The future of accelerator physics, the Tamura symposium proceedings*, AIP conference proceedings 356, Austin Texas, 1994.

[47] P.L. Colestock, L.K. Spentzouris, and F. Ostiguy, Nonlinear wave phenomena in coasting beams, *Proceedings of the 1995 Particle Accelerator Conference*, Dallas Texas, 1995.

[48] E.M. Lifshitz and L.P. Pitaevskii, *Physical Kinetics, Landau and Lifshitz Course of Theoretical Physics, Volume 10*, Pergamon Press, 1981

[49] O. Bruening, On the possibility of measuring longitudinal echoes in the SPS, CERN report SL/95-83, Sept 1995

[50] M. Reiser, *Theory and design of charged particle beams*, Wiley, 1994

[51] V.I. Karpman, "Singular" solutions of the equations for plasma oscillations, *Journal of Experimental and Theoretical Physics (U.S.S.R.)*, Vol 24, Number 3, March 1967.

[52] T.H. Stix, *Waves in plasmas*, AIP, 1992

[53] J.D. Bjorken and S.K. Mtingwa, Intrabeam scattering, *Particle Accelerators*, Vol 13, pp.115-143, 1983.

[54] L. Evans and B. Zotter, CERN/SPS/80-IS(DI), Geneva 1980.

[55] M. Church, Measurement ripple in the accumulator bend bus supply, Fermilab Internal Note, Pbar Note 520, 1992.